



UNIVERSITY OF
LIVERPOOL

**Biocide-Releasing and
Nanostructured Surfaces:
Fabrication, Characterisation
and Bacterial Response**

*Thesis submitted in accordance with the requirements of the
University of Liverpool for the degree of Doctor in Philosophy*

Luca Barbieri

November 2020

Supervisors

Prof. Rasmita Raval

Dr. Joanne L. Fothergill

Dr. Yuri A. Díaz Fernández

Open Innovation Hub for Antimicrobial Surfaces,
Surface Science Research Centre

&

Institute of Infection and Global Health

"There is considerable overlap between the intelligence of the smartest bears and the dumbest tourists."

Yosemite National Park Ranger,
on the challenges of engineering bear-proof garbage cans, circa 1980.

Table of contents

ACKNOWLEDGEMENTS	I
ABSTRACT	II
LIST OF PUBLICATIONS	V
CONFERENCE PARTICIPATIONS	V
GLOSSARY	VI
List of Symbols	VI
List of Abbreviations	VIII
LIST OF FIGURES	IX
LIST OF TABLES	XVII
CHAPTER 1 Introduction	1
1.1 The threat of antimicrobial resistance	1
1.2 Bacterial biofilms	3
1.2.1 The conditioning layer	4
1.2.2 Bacterial adhesion	5
1.2.3 Biofilm growth and maturation	6
1.2.4 Final stages of biofilm development and dispersion	7
1.3 Antimicrobial surfaces	8
1.3.1 Antibiofouling and bactericidal effect of surfaces	9
1.3.2 Biocide-releasing materials	11
1.3.3 Antimicrobial topographic surfaces	13
1.4 Thesis aims	16
1.5 References	17
CHAPTER 2 Experimental Techniques	24
2.1 Introduction	24
2.2 Surface Spectroscopy	25
2.2.1 Vibrational Spectroscopy	25
Attenuated Total Reflection- Infrared Spectroscopy	27
Raman Spectroscopy	29

Raman line mapping	32
2.2.2 Energy Dispersive X-ray Spectroscopy	35
2.3 Microscopy techniques	37
2.3.1 Electron Microscopy	37
Scanning Electron Microscopy	38
Processing of biological samples for SEM imaging	40
Protein fixation	41
Lipid fixation	43
Dehydration	44
Sputter coating	44
2.3.2 Fluorescence Microscopy	45
Confocal Laser Scanning Microscopy	48
Confocal Laser Scanning Microscopy image processing	52
2.3.3 Atomic Force Microscopy	55
2.4 Physical characterisation techniques	59
2.4.1 Contact angle	59
The effect of surface roughness on contact angle	62
2.4.2 Ultraviolet-visible-near infrared (UV-Vis-NIR) Spectroscopy	64
2.5 References	68
CHAPTER 3 Antimicrobial activity of biocide-releasing PDMS substrates	75
3.1 Introduction	75
3.1.1 Polydimethylsiloxane (PDMS)	75
PDMS surface modifications	77
Bulk modifications of PDMS	78
Blending	78
Co-polymerisation	79
PDMS swelling	80
3.1.2 Salicylic Acid	82
3.2 Experimental section	84
3.2.1 Fabrication of PDMS-Salicylic acid samples	84
3.2.2 Surfaces analysis of PDMS-SA samples	84
Raman analysis	85

Raman cross section analysis	83
ATR-FTIR analysis	86
Contact angle measurements	86
Atomic force microscopy analysis	87
3.2.3 Release tests	87
3.2.4 Antimicrobial response	88
Determination of MIC and MBC	88
Determination of <i>S. aureus</i> and <i>E. coli</i> viability on PDMS-SA	88
Investigating pH effect on bacterial growth	89
Imaging sessile bacteria	90
Scanning electron microscopy	90
Confocal fluorescence microscopy	90
3.3 Results and discussion	92
3.3.1 Sample fabrication	92
3.3.2 Material characterization	93
Raman analysis	94
Atomic force microscopy analysis	97
Static contact angle analysis	99
3.3.3 Release of Salicylic Acid from PDMS-SA samples	101
ATR-FTIR analysis	105
Raman analysis	108
Contact angle analysis	111
Atomic force microscopy analysis	112
3.3.4 Antimicrobial activity of PDMS-SA samples	112
CFUs counting of planktonic bacterial cells	115
Viability of surface-attached bacterial cells	117
CFUs counting of bacterial cells at the surface	119
3.4 Conclusions	120
3.5 Annex	122
3.6 References	126

CHAPTER 4 Insights on the first stages of biofilm formation of staphylococcal cells on nanostructured Silicon surfaces	133
4.1 Introduction	133
4.1.1 The first stages of biofilm formation on surfaces	133
Reversible attachment (docking stage)	135
Irreversible attachment (locking stage)	136
Biofilm maturation	137
4.1.2 Bacterial division	138
Peptidoglycan synthesis during cell division in <i>Staphylococci</i>	139
Successive divisions in <i>Staphylococci</i> : planktonic growing mode	142
4.1.3 <i>Staphylococci</i> response to nanostructured surfaces	143
4.1.4 Silicon	146
Nanostructured Si surfaces	147
4.2 Experimental Details	150
4.2.1 Fabrication and functionalisation of Silicon NanoWire arrays	150
Fabrication of silicon nanowires (SiNW)	150
Imaging of sessile bacteria on flat Si and SiNWs	151
Viability of sessile bacteria	151
Scanning Electron Microscope (SEM) imaging	152
Characterisation of SiNW arrays by EDS mapping	152
4.3 Results and discussion	154
4.3.1 Characterisation of SiNWs surfaces	154
4.3.2 Viability of sessile bacteria on flat Si and SiNWs	155
4.3.3 Scanning electron microscope configurations	158
4.3.4 Biofilm formation of <i>S. aureus</i> cells on flat Si and SiNWs	160
4.3.5 Biofilm formation of <i>S. epidermidis</i> cells on flat Si and SiNWs	169
4.4 Division modes of <i>Staphylococci</i> at the surface	174
4.5 Conclusion	180
4.6 References	182

CHAPTER 5 Insights on the effect of nanostructured Silicon on the first stages of biofilm formation of rod-shaped bacteria	189
5.1. Introduction	189
5.1.1 Why do bacteria form biofilms?	189
Surface attachment of rod-shaped bacteria and the role of adhesins	190
Surface sensing and stimulation of adhesin production	193
5.1.2 Cell division in rod-shaped bacteria	195
The Min system	195
The nucleoid occlusion system	196
<i>Caulobacter crescentus</i> cell cycle	198
5.1.3 The effect of nanostructured topography on the attachment of rod-shaped bacteria	200
5.2 Experimental Details	208
5.2.1 Fabrication and Functionalisation of SiNW arrays	208
Fabrication of Silicon nanowires (SiNW)	208
Viability of sessile bacteria	210
Scanning Electron Microscope imaging	210
5.3 Results	212
5.3.1 Viability of sessile bacteria on flat Si and SiNWs	212
5.3.2 Attachment and division of <i>E. coli</i> cells on flat Si and SiNWs	216
5.3.3 Attachment and division of <i>A. baumannii</i> on flat Si and SiNWs	224
5.3.4 Attachment and division of <i>B. subtilis</i> on flat Si and SiNWs	230
5.3.5 Attachment and division of <i>C. crescentus</i> on flat Si and SiNWs	234
5.4 Division modes of rod-shaped bacteria at the surface	236
5.4.1 Effect of nanostructured Si on the division modes of <i>E. coli</i> , <i>A. baumannii</i> and <i>B. subtilis</i>	236
5.4.2 Cell cycle of <i>Caulobacter crescentus</i> on nanostructured Si	241
5.5 Conclusion	245
5.6 Future Work	247
5.7 References	248
CONCLUSIONS	258

Acknowledgements

I would like to thank my supervisors, Prof. Rasmita Raval, Dr. Jo Fothergill and Dr. Yuri Diaz-Fernandez for providing me with the opportunity to complete my PhD, as well as welcoming me to their research groups. I am also thankful to the School of Physical Sciences and the Institute of Infection and Global Health for providing me with the funding for my PhD. I would also like to express my gratitude to all my supervisors for their precious guidance and concise critique throughout the course of my PhD.

I would also like to thank everyone who was, in one way or another, involved in the research within this thesis: Dr. Ioritz Sorzabal Bellido, for his advice and support on tackling some issues and in general on improving my thesis; Dr. Sam Haq, for his selfless helping efforts, adaptable working nature, and the endless advices, the kind I knew I could trust; A sincere thank you to Gareth P. Morris for his help and support in several aspects of research, but most importantly for the laughs we had through the whole course of the PhD.

I am grateful to all the members of Dr. Jo Fothergill's research group, especially Dr. Laura Wright, Dr. John Newman and Dr. Yasmin Hilliam, for their welcome, support and help during my stay at the Institute of Infection and Global Health. I would like to thank the team at the Centre for Cell Imaging, especially Dr. Marco Marcello, Dr. Dave Mason and Jen Adcott for their teaching, time and support during my work at the confocal laser microscope.

Last, but not least, I sincerely thank my family, especially my parents, Maria Grazia and Mario Barbieri, for always believing in me and whose support, encouragement and love are invaluable.

Abstract

Bacterial colonisation is one of the main causes of disease in humans, particularly when extended to medical devices. Understanding and preventing the initial stages of biofilm formation on surfaces is essential to save millions of lives and to reduce the economic impact on the healthcare sector. This thesis presents a novel approach on the functionalisation and characterisation of bactericidal surfaces based on PDMS with potential applications in catheters and wound dressing, as well as an in-depth study on the first stages of biofilm formation of a wide range of bacteria on nanostructured substrates.

Chapter 2 gives an overview of the main characterisation techniques used throughout this work to investigate the surface chemistry and topography of the samples, as well as the mechanism and dynamics of biocide release. This chapter presents ATR-FTIR and Raman amongst the vibrational spectroscopy techniques used to unravel the chemical fingerprint of the biocide-releasing samples. The bacterial response at the surfaces was investigated via high-resolution SEM and confocal fluorescence microscopy, allowing to assess both the antimicrobial effect of the released biocide and the effect of the nanotopography on the division modes of the bacterial cells.

Chapter 3 presents a post-fabrication functionalisation method to create a reservoir of salicylic acid, a biocide approved for use on humans, within biocompatible polydimethylsiloxane (PDMS) creating surfaces able to inhibit biofilm formation and planktonic proliferation. Surface analysis via atomic force microscopy, contact angle measurements and Raman spectroscopy showed that the functionalisation method had minimal effect on the roughness and chemistry of the surface of PDMS samples. Vibrational and UV-vis spectroscopy were used to monitor the release of SA from the material's bulk into the surrounding media, which was sustained for 72h. The antimicrobial performance of the samples was tested on *Staphylococcus aureus* and *Escherichia coli* strains associated to medical device biofilms. Viability assays showed

that bactericidal concentrations were reached in the supernatants within the first 24h for both tested bacterial strains and bacterial attachment was reduced by four orders of magnitude. The simplicity and versatility of this approach may allow translation into existing medical devices and be used to prevent surface colonisation by Gram-positive and Gram-negative bacteria.

Chapter 4 focuses on the study of the first stages of biofilm formation of *S. aureus* and *Staphylococcus epidermidis* on nanopatterned silicon nanowire (SiNWs) surfaces. The selected bacteria are the main responsible for prosthetic infections, while silicon is widely used in medical implants, often in combination with topographic surfaces to promote osteogenesis. While confocal images of Live/Dead assay showed no intrinsic killing effect of the nanostructured substrates, high definition SEM images suggested that the uneven surface topography and the high rigidity of the staphylococcal cell wall prevented in some cases the bacteria from dividing parallel to the substrate, generating daughter cells with few attachment points to the substrate and bacterial colonies growing with out-of-plane morphologies. These data suggested that the nanostructured topography of SiNWs has an impact on the biofilm formation of staphylococcal cells, enabling the engineering of materials able to effectively control bacterial adhesion and proliferation, with potential biomedical and industrial applications.

Chapter 5 follows a similar approach, studying the impact of SiNWs on the first stages of biofilm formation of the rod shaped bacteria *E. coli*, *Bacillus subtilis* and *Acinetobacter baumannii*. SEM images showed that the characteristic polar growth of these bacteria was not affected by the nanostructured topography, with the colonies displaying similar morphologies on both flat silicon and SiNWs arrays, indicating that SiNWs arrays do not alter the first stages of biofilm formation for the tested strains. Special attention was dedicated to *Caulobacter crescentus*, a bacterium with a unique cell cycle and attachment mechanism. The presented SEM images allowed to identify the specific stages of cell cycle and the different cell configurations adopted. Remarkably, the ability of *C. crescentus* to attach and differentiate at the surface was not affected by the topography of the SiNWs arrays.

These findings could lead to a better understanding of the attachment and division of rod-shaped bacteria on surfaces with controlled nanotopography.

List of Publications

Publications arising during the course of this thesis

One-step preparation of antimicrobial materials based on PDMS and salicylic acid: insights from spatially and temporally resolved techniques.

Barbieri L, Sorzabal-Bellido I, Beckett AJ, Prior IA, Fothergill JL, Diaz-Fernandez YA, Raval R

Manuscript submitted to *Nature Publishing Journals - Biofilms and Microbiomes, Special Collection: Translational Research in Biofilms*, awaiting peer review.

Conference participations

- **CMD (Condensed Matter Division)** 26, 4th -9th September 2016, *Groningen, The Netherlands*.
- **RSC Biomaterials Chemistry Annual Conference**, 9th – 11th January 2019, *Liverpool, UK*.
- **Eurobiofilms**, 3rd – 6th September 2019, *Glasgow, UK*
(poster presentation: **Antimicrobial activity of biocide-releasing PDMS substrates** Barbieri L, Sorzabal-Bellido I, Fothergill JL, Diaz-Fernandez YA, Raval R)

Glossary

List of Symbols

Å	Angstrom
K _a	Acid dissociation constant
~	Approximately
ν_{as}	Asymmetric stretch mode (ATR-IR)
δ	Bending mode (ATR-IR)
cm	Centimetre
$C(t)$	Concentration over time
pH	Concentration of hydrogen ions, $\text{pH} = -\text{Log}_{10} [\text{H}^+]$
C _φ	Carbon atom in the benzene ring
°	Degrees
°C	Degrees Celsius
eV	Electron Volt
ν	Frequency
ϕ	Good–Girifalco interaction parameter
g	Grams
μg	Micrograms
μm	Micrometres
mg	Milligrams
ml	Millilitre
mm	Millimetre
N	Number of cells attached to the surface
NA	Numerical aperture
nm	Nanometres
nmol	Nanomole
pK _a	$\text{pK}_a = -\text{Log}_{10} K_a$
% (w/w)	Percentage (Weight/ Weight)

h	Plank's constant
r	Ratio of the rough surface area to the projected ideal smooth surface
Rq	Root Mean Square Roughness
μ	Reduced mass
d	Resolution
π_e	Spreading pressure
s	Seconds
cm ²	Square Centimetres
μm^2	Square Micrometres
Ra	Surface roughness average
γ	Surface tension
σ	Standard Deviation
ν_s	Symmetric stretch mode (ATR-IR)
T	Temperature
v/w	Volume/ Weight
λ	Wavelength
$\bar{\omega}$	Wavenumber (ATR-IR)/ Raman Shift (Raman)
w/v	Weight/ Volume
w/w	Weight/ Weight

List of Abbreviations

AFM	Atomic force microscopy
AMR	Antimicrobial resistance
ATR-FTIR	Attenuated total reflectance – Fourier transform infrared
CFUs	Colony forming units
CLSM	Confocal laser scanning microscopy
DEPs	Differentially expressed proteins
DI	Deionised
EDS	Energy Dispersive X-ray Spectrometry
EPS	Extracellular polymeric substances
FRET	Fluorescence/Förster resonance energy transfer
IR	Infrared
LB	Luria-Bertani broth
MBC	Minimum bactericidal concentration
MIC	Minimum inhibitory concentration
NB	Nutrient broth
NO	Nucleoid occlusion
PBPs	Penicillin-binding proteins
PDMS	Polydimethylsiloxane
PI	Propidium iodide
SA	Salicylic acid
SEs	Secondary electrons
SEM	Scanning electron microscopy
SiNWs	Silicon nanowires
TEM	Transmission Electron Microscopy
UV-vis	Ultraviolet–visible

N.B. The symbols and abbreviations stated above only relate to the most common occurring symbols and abbreviations encountered throughout the thesis. Additional symbols and abbreviations have been described within the thesis content.

List of Figures

Chapter 1

Fig. 1.1	Scanning electron microscopy (SEM) image of <i>C. albicans</i> biofilm developed in vitro on polystyrene discs.	3
Fig. 1.2	Schematisation of the bacterial biofilm life cycle	5
Fig. 1.3	Schematisation of the main strategies on which antibiofouling materials are based on.	9
Fig. 1.4	Schematisation of the main strategies on which bactericidal materials are based on	10
Fig. 1.5	Antibiofilm efficacy of PU-Auranofin catheters. The bioluminescence (radiance) of MRSA was examined using an <i>in vivo</i> imaging system.	12
Fig. 1.6	SEM images showing <i>S. aureus</i> and <i>P. aeruginosa</i> cells retained on surfaces of defined topography.	14
Fig. 1.7	MRSA cells on nanostructured Ti surfaces after 18 h of incubation, showing altered cell morphology.	15

Chapter 2

Fig. 2.1	Schematic representation of an infrared spectrometer in attenuated total reflectance infrared (ATR) configuration	27
Fig. 2.2	Infrared spectrum of polydimethylsiloxane (PDMS) between 1200 and 3200 cm ⁻¹ .	28
Fig. 2.3	Jablonski diagram representing elastic Rayleigh scattering (a), inelastic Stokes (b) and anti-Stokes scattering (c)	30
Fig. 2.4	Raman spectrum of Salicylic Acid, Salicylate monoanion and Salicylate dianion.	31
Fig. 2.5	Above: an example of Raman line mapping across the depth of a functionalised PDMS sample, the red dashed line represents the scanning path. Below: Raman spectroscopy analysis of the SA presence through the section of a functionalised PDMS sample.	33
Fig. 2.6	Layout of Renishaw inVia confocal Raman microscope.	34

Fig. 2.7	Schematic representation of the EDS process that leads to an energy emission in the form of x-rays.	35
Fig. 2.8	Schematic representation of the interaction volume of a 20kV electron beam with a poly(methyl methacrylate) sample, displaying the different classes of radiation emerging at increasing probe depths.	39
Fig. 2.9	Schematic representation of an electron beam scanning a rough surface, encountering a sharp peak (A) which results in high emission of SEs, a flat area (B) and a deep valley (C), which results in low emission of SEs.	40
Fig. 2.10	Schematisation of the sample processing protocol for the imaging of bacterial cells via SEM.	41
Fig. 2.11	A Reaction of depolymerisation of paraformaldehyde into formaldehyde, followed by hydration of formaldehyde in the presence of water. B Reaction of methanediol with amines, forming an imine group via N-methylol intermediate. The imine furtherly reacts with other amines forming a methylene bridge leading to the irreversible crosslinking of protein residues.	42
Fig. 2.12	A Depolymerisation of glutaraldehyde. B A proposed reaction mechanism of glutaraldehyde (and poly(glutaraldehyde)) crosslinking two protein residues	43
Fig. 2.13	Schematisation of osmium tetroxide reacting with unsaturated bonds in lipids. OsO ₄ acts as a crosslinker and is reduced in the process.	44
Fig. 2.14	Jablonski diagram schematising the process that leads to emission of fluorescence.	46
Fig. 2.15	Excitation (green, solid) and emission (red, dashed) spectra of Acridine Orange. Insert shows the molecular structure of the fluorophore.	47
Fig. 2.16	Schematic representation of an upright confocal laser scanning microscope.	49
Fig. 2.17	Absorbance and emission spectra of SYTO 9 and propidium iodide. The insert displays the molecular structure of PI, while the molecular structure of SYTO 9 has not been disclosed by Thermofisher™.	50
Fig. 2.18	Representative merged CLSM image of <i>E. coli</i> cells on flay Si. Green cells are stained with SYTO 9 and while cells with a damaged membrane are stained with propidium iodide and are displayed as red.	51
Fig. 2.19	Overview of the image processing using Fiji macro of CFM images stained with Live/Dead viability kit.	54
Fig. 2.20	SEM image of a Bruker™ diamond coated AFM tip, specific for applications that require increased wear resistance and a conductive tip. Tip height: 10 - 15 μm. Tip radius: 10 nm.	55

Fig. 2.21	Schematisation of the working mode of an AFM.	56
Fig. 2.22	Schematisation of the experimental set-up required to measure bacterial adhesion forces and example of the force–extension curves obtained.	58
Fig. 2.23	Liquid – vapor interface and balance of forces on molecules of liquids.	59
Fig. 2.24	Equilibrium of a liquid drop on a horizontal solid surface.	60
Fig. 2.25	Illustration of contact angles formed by a liquid drop on solid surfaces with different degrees of wettability.	60
Fig. 2.26	UV-Vis spectrum of Salicylic Acid in aqueous medium.	65
Fig. 2.27	Jablonski diagram representing the relative energies of molecular orbitals and possible transitions between them.	66

Chapter 3

Fig. 3.1.1	Dimethylsiloxane backbone.	76
Fig. 3.1.2	Schematic depiction of the method used by Fisher et al. to produce antimicrobial catheters.	81
Fig. 3.1.3	Molecular structures of Salicylic Acid, Salicylate and Oxidobenzoate	82
Fig. 3.3.1	Schematic representation of the post-fabrication modification method proposed to load SA within pristine PDMS.	92
Fig. 3.3.2	Photographs of PDMS and PDMS-SA samples on dark background.	93
Fig. 3.3.3	Raman spectra of pristine PDMS and PDMS-SA.	94
Fig. 3.3.4	Raman spectra of pristine PDMS and PDMS-SA, taken at the surface of the samples, in the region between 950 and 1200 cm^{-1} .	95
Fig. 3.3.5	Raman spectroscopy investigation of the SA presence through the section of the material.	96
Fig. 3.3.6	AFM analysis of pristine PDMS and PDMS-SA Left: 3D AFM height mode images.	99
Fig. 3.3.7	The optimization of the citrate model buffer allowed to obtain a pH response comparable to the one of the LB media used in the biological tests. Figure shows the titration curves of LB medium and of the 11.5 mM citrate model buffer.	101
Fig. 3.3.8	Calibration curve used to assess the extinction coefficient of SA in 11.5 mM citrate model buffer.	102

Fig. 3.3.9	Concentration of SA released from PDMS-SA samples monitored at different time points measuring the UV-vis absorbance peak at 299 nm.	103
Fig. 3.3.10	Concentrations of Salicylic Acid and Salicylate calculated using the Henderson-Hasselbalch equation based on the release data over 72 h, and corresponding pH decrease.	104
Fig. 3.3.11	ATIR spectra of PDMS- SA left for 24 h in model buffer, PDMS – SA, PDMS left for 24 h in model buffer, pristine PDMS.	106
Fig. 3.3.12	ATR-IR spectrum resulting from the subtraction of the spectrum of PDMS left for 24 h in model buffer and PDMS-SA in the same condition.	107
Fig. 3.3.13	Schematic representation of the SA release mechanism: the water-based media penetrating the sample, reaching the biocide in the bulk, dissolving it and allowing it to diffuse outside of the sample.	108
Fig. 3.3.14	Raman spectra taken 500 μm within the bulk of PDMS-SA before release, PDMS-SA after 24 hours release and PDMS after 48 hours release.	109
Fig. 3.3.15	Raman spectroscopy investigation of the SA presence through the section of the material.	110
Fig, 3.3.16	AFM analysis of PDMS-SA after 24h in release conditions Left: 3D AFM height mode images.	112
Fig. 3.3.17	Absorbance of bacterial suspensions measured after 24 hours in physiological conditions.	115
Fig. 3.3.18	Viable planktonic <i>E. coli</i> J96 and <i>S. aureus</i> SH1000 cell counts cultured for 24 hrs on PDMS-SA samples and pristine PDMS.	116
Fig. 3.3.19	Representative SEM images showing bacteria cultured for 24 h on PDMS-SA samples and pristine PDMS.	117
Fig. 3.3.20	Representative merged confocal scanning microscopy images of live and dead bacteria cultured for 24 h on the surface of PDMS-SA samples and pristine PDMS.	118
Fig. 3.3.21	Sessile <i>E. coli</i> J96 and <i>S. aureus</i> SH1000 cell counts cultured for 24 h on PDMS-SA samples and pristine PDMS.	119
Fig. 3.5.1	Time-dependent static contact angle of pristine PDMS and PDMS-SA measured over 2 hrs. Measurements were taken using model buffer.	122
Fig. 3.5.2	Contact angle of PDMS measured using model buffer with different concentrations of Salicylic acid.	123

Fig. 3.5.3 Static contact angle of pristine PDMS and PDMS-SA measured on dry samples (0 hrs) and on samples left for 3 and 24 hrs in model buffer. Measurements were taken using model buffer. 124

Fig. 3.5.4 Absorbance of bacterial suspensions measured over 24 hours. 125

Chapter 4

Fig. 4.1.1 Scanning electron microscopy image of a staphylococcal biofilm on the surface of a medical device. 134

Fig. 4.1.2 Schematisation of biofilm development in *Staphylococcus epidermidis*. 138

Fig. 4.1.3 Localisation microscopy image of a *S. aureus* cell labelled with ADA (azido D-alanine) clicked to Alexa Fluor 647, highlighting the sites of peptidoglycan insertion during cell division. 139

Fig. 4.1.4 Schematisation of cell wall synthesis in spherical cocci 141

Fig. 4.1.5 *Staphylococci* growing mode: the schematic shows a cell forming the septum at the equatorial plane of division. 143

Fig. 4.1.6 SEM image showing *S. aureus* morphology on nanopillar Ti surface NW-850-5 following 3 h incubation. 145

Fig. 4.1.7 SEM image showing *S. aureus* adhesion on hydrophilic nanostructured surfaces. 146

Fig. 4.1.8 MG-63 osteoblast culture on a silica rough surface ($R_a = 16.6$ nm) showing a highly spread, random distribution and dispersion (SEM, 1440x). 147

Fig. 4.1.9 Top-view SEM image of *S. aureus* cells after 8 h of culture on unfunctionalised SiNWs. 148

Fig. 4.3.1 Scanning electron microscopy images of a silicon nanowire arrays. 154

Fig. 4.3.2 Representative high resolution SEM image with relative EDS mapping of the SiNWs surfaces. 155

Fig. 4.3.3 Representative merged confocal laser scanning microscopy images for live and dead *S. aureus* and *S. epidermidis* cells attached to flat Si and SiNWs after 8 h of culture. 156

Fig. 4.3.4 Schematic representation of the two configurations used to acquire SEM images for this work, with representative SEM images. 159

Fig. 4.3.5	Representative SEM images of <i>S. aureus</i> biofilm formation on flat Si (A, B, C) and SiNWs (D, E, F).	161
Fig. 4.3.6	Representative SEM images of <i>S. aureus</i> aggregates on flat Si (A, B, C) and SiNWs (D, E, F).	162
Fig. 4.3.7	Representative SEM images of <i>S. aureus</i> colonies on flat Si (A, B, C) and SiNWs (D, E, F).	164
Fig. 4.3.8	Representative SEM images of <i>S. aureus</i> microcolonies on flat Si (A, B, C) and SiNWs (D, E, F).	165
Fig. 4.3.9	Representative SEM images of <i>S. aureus</i> single cells on flat Si (A, B, C) and SiNWs (D, E, F).	167
Fig. 4.3.10	Representative SEM images of <i>S. aureus</i> single cells and division events on flat Si (A, B, C) and SiNWs (D, E, F).	169
Fig. 4.3.11	Representative SEM images of <i>S. epidermidis</i> aggregates on flat Si (A, B, C) and SiNWs (D, E, F).	170
Fig. 4.3.12	Representative SEM images of <i>S. epidermidis</i> cells and small clusters on flat Si (A, B, C) and SiNWs (D, E, F).	172
Fig. 4.3.13	Representative SEM images of <i>S. epidermidis</i> cells and microcolonies on flat Si (A, B, C) and SiNWs (D, E, F).	173
Fig. 4.4.1	Schematic representation of <i>Staphylococci</i> dividing on flat Si, showing the available orientations for the daughter cells.	175
Fig. 4.4.2	SEM images and relative schematic representation of <i>Staphylococci</i> attached to flat Si dividing parallel to the surface and out of plane.	176
Fig. 4.4.3	Schematic representation of <i>Staphylococci</i> dividing on SiNWs, with focus on the available orientations range for the daughter cells to assume.	178
Fig. 4.4.4	SEM images and relative schematic representation of <i>Staphylococci</i> attached to SiNWs surfaces and their division effected by the uneven topography.	179

Chapter 5

Fig. 5.1.1	Representation of events and factors enabling bacteria to transition from a planktonic to a sessile state.	191
Fig. 5.1.2	Schematisation of the process and the components involved in the interaction between the surface and the bacterium.	192

Fig. 5.1.3	In <i>E. coli</i> and other rod-shaped bacteria, initial surface contact is mediated by flagellae and pili, which leads to the cell adhering to one of its poles. The transition from reversible to irreversible attachment involves the repositioning of the cell parallel to the substrate.	194
Fig. 5.1.4	Schematisation of the role of the Min system and the Nucleoid occlusion in driving the division at the middle of the cell.	197
Fig. 5.1.5	The life cycle of <i>C. crescentus</i> begins with the stalked cell with an adhesive holdfast at the tip of the stalk.	199
Fig. 5.1.6	False colour FE-SEM images of <i>E. coli</i> cells grown on static and in steady flow conditions on nanopillared aluminium surfaces.	201
Fig. 5.1.7	SEM images of <i>E. coli</i> cells cultured for 2 h on untreated and plasma-treated (2 and 10 min) Monosyn and Miralene sutures.	202
Fig. 5.1.8	SEM images of <i>E. coli</i> cells cultured for 3 h on flat titanium alloy (control) and TiO ₂ nanopillar surface (NW-850-5).	203
Fig. 5.1.9	SEM images of <i>E. coli</i> and <i>P. fluorescens</i> cells attached to nanostructured silica substrates after 24 h culture.	205
Fig. 5.1.10	SEM images of <i>E. coli</i> adhering to flat Si and NSS. The stretching of the cells on NSS increases their projected surface area compared to the on flat Si surfaces.	206
Fig. 5.1.11	SEM images of <i>B. subtilis</i> adhering to black silicon. The cell membrane appears to be significantly disrupted through interaction with the nanostructured surface.	206
Fig. 5.3.1	Representative merged confocal laser scanning microscopy images for live (green) and dead (red) bacterial cells adhering to flat Si and SiNWs after 8 h of culture.	215
Fig. 5.3.2	Representative SEM images of colonies of <i>E. coli</i> cells adhering to flat Si (A, B, C) and SiNWs (D, E, F).	217
Fig. 5.3.3	Representative SEM images of small colonies of <i>E. coli</i> cells adhering to flat Si (A, B, C) and SiNWs (D, E, F).	219
Fig. 5.3.4	Representative SEM images of <i>E. coli</i> cells adhering to flat Si (A, B, C) and SiNWs (D, E, F).	221
Fig. 5.3.5	Representative SEM images, taken in upright configuration, of <i>E. coli</i> cells adhering to flat Si (A, B, C) and SiNWs (D, E, F).	223
Fig. 5.3.6	Representative SEM images of colonies of <i>A. baumannii</i> cells adhering to flat Si (A, B, C) and SiNWs (D, E, F).	225

Fig. 5.3.7	Representative SEM images of <i>A. baumannii</i> cells adhering to flat Si (A, B, C) and SiNWs (D, E, F).	227
Fig. 5.3.8	Representative SEM images of <i>A. baumannii</i> cells adhering to flat Si (A, B, C) and SiNWs (D, E, F).	229
Fig. 5.3.9	Representative SEM images of colonies of <i>B. subtilis</i> adhering to flat Si (A, B, C) and SiNWs (D, E, F).	231
Fig. 5.3.10	Representative SEM images of <i>B. subtilis</i> cells adhering to flat Si (A, B, C) and SiNWs (D, E, F).	233
Fig. 5.3.11	Representative SEM images of <i>C. crescentus</i> cells attaching to flat Si (A, B, C) and SiNWs (D, E, F).	235
Fig. 5.4.1	Schematic representation of rod-shaped bacteria dividing on flat Si parallel to the surface and tilted.	237
Fig. 5.4.2	SEM images and relative schematic representation of rod-shaped bacteria attached to flat Si dividing parallel to the surface and out of plane.	238
Fig. 5.4.3	Schematic representation of rod-shaped bacteria attached to SiNWs surfaces and their division effected by the uneven topography. Below: SEM images of <i>E. coli</i> , <i>B. subtilis</i> and <i>A. baumannii</i> dividing on SiNWs.	240
Fig. 5.4.4	Schematic representation of <i>C. crescentus</i> attaching and dividing on flat Si and SiNWs.	243
Fig. 5.4.5	Representative SEM images of <i>C. crescentus</i> cells dividing on flat Si (A, B, C) and SiNWs (D, E, F).	243

List of tables

Chapter 2

Table 2.1	Vibrational modes of functional chemical groups in IR spectroscopy encountered in this work, with their commonly assigned symbol and a schematic representation of the atomic movement involved	26
Table 2.2	Characteristic infrared vibrational frequencies of the Methyl group.	28
Table 2.3	Raman vibrational frequencies for the functional groups related to Salicylate bianion, Salicylate monoanion and Salicylic Acid.	32

Chapter 3

Table 3.1.1	List of solvents and the degree of swelling they cause when in contact with PDMS.	78
Table 3.3.1	Contact angles measurements of pristine PDMS, SA pellet and PDMS-SA.	98
Table 3.3.2	Salicylic acid concentration inhibiting growth by 50% (MIC 50), 90% (MIC 90) and minimum bactericidal concentration (MBC) for <i>E. coli</i> J96 and <i>S. aureus</i> SH1000.	110

Chapter 4

Table 4.3.1	Percentage (%) alive <i>S. aureus</i> and <i>S. epidermidis</i> sessile bacteria on flat Si and SiNWs surfaces.	156
--------------------	---	-----

Chapter 5

Table 5.3.1	Percentage (%) of alive <i>E. coli</i> , <i>A. baumannii</i> , <i>B. subtilis</i> and <i>C. crescentus</i> sessile bacteria on flat Si and SiNWs surfaces after 8 h of culture.	210
--------------------	---	-----

Chapter 1

Introduction

1.1 The threat of antimicrobial resistance

Micro-organisms are the oldest life form on earth, over millions of years of existence they have evolved to overcome several obstacles to their survival, the last of which are artificial antibiotics [1]. Used to prevent and treat bacterial infections, antibiotics have led to an increase of resistance in bacteria due to their over- and misuse on humans and animals. Antibiotics-resistant bacterial strains cause infections harder to treat than those caused by non-resistant bacteria, leading to higher medical costs, prolonged hospital stays, and increased mortality [2]. A recent report to the Secretary-General of the United Nations estimated that antimicrobial resistance (AMR) causes the death of 700,000 people globally a year, and it is predicted to cause 10 million deaths per year by 2050 if the current situation is not improved [3]. The challenge of AMR is not exclusively related to human healthcare; it has a considerable impact also on several strategic sectors, including food security, sustainable farming, paints, coatings, and the marine industry [4, 5].

As the majority of pharmaceutical companies are no longer investing in the research for new antibiotics [3], new approaches are needed to prevent multi-drug resistant infections, ending the increase of AMR and reducing human and economic losses. A promising strategy in this respect is the engineering and development of antimicrobial surfaces: prokaryotes have developed versatile mechanisms to attach and multiply onto solid interfaces [1] and humans are everyday in contact with various surfaces of communal use that are often subject of bacterial colonisation.

This problem has been traditionally overcome with the use of antibacterial detergents, a strategy that introduced a tremendous selective pressure on microorganisms that has ultimately led to an increase in AMR.

Amongst the materials most sensitive to this issue are medical devices, defined by the World Health Organisation as any instrument, apparatus, implement, machine, appliance, implant or material intended to be used, alone or in combination, for human beings, for one or more of the specific medical purpose(s) [6]. Such materials, if exposed to the attachment of microorganisms, constitute a perfect substrate for their proliferation, especially when in direct contact with living tissues, a condition that leads ultimately to infection and failure of the device [7]. These issues have focused the interest of scientists and engineers on the development of new strategies to prevent bacterial colonisation at surfaces and to control the release of biocides to the environment.

This introductory chapter presents a critical discussion on the recent and most representative scientific literature on bacterial colonisation of surfaces, analysing the biological processes that cause the formation of bacterial colonies on abiotic surfaces. The discussion includes some general strategies and recent examples on the functionalisation of artificial surfaces with antimicrobial properties, focusing on two main research areas: biocide-releasing materials and antibiofouling surface topographies.

1.2 Bacterial biofilms

The advances in microbiology over the past 50 years have allowed the scientific community to realise of the extent to which microbial attachment and colonisation occurs on surfaces [8]. High resolution imaging techniques (**Fig. 1.1**), specific molecular fluorescent dyes, molecular-reporter technology and cell-culturing apparatus have been applied over the years to unravel the structural and dynamic complexity of this biological system, referred to as biofilm [8, 9].

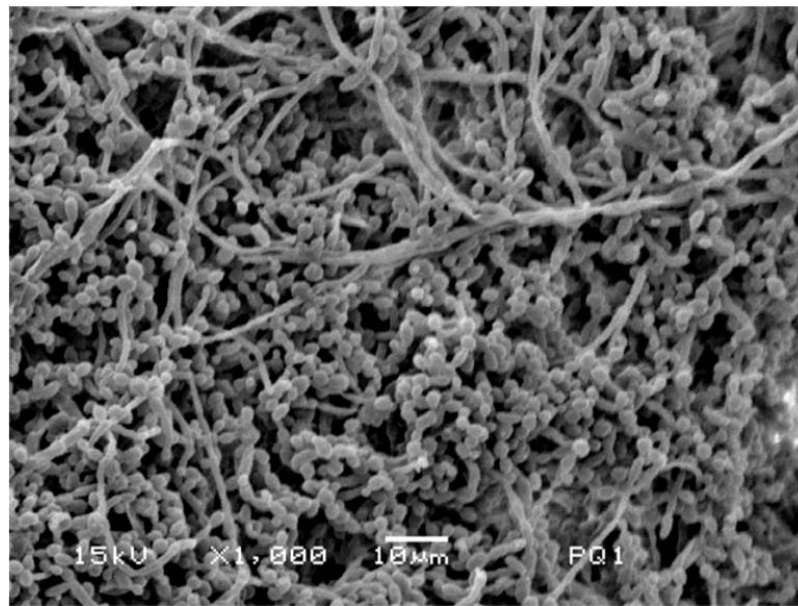


Fig. 1.1 Scanning electron microscopy (SEM) image of *C. albicans* biofilm developed in vitro on polystyrene discs. Image adapted from [13].

Biofilms are defined as ‘aggregates of microorganisms in which cells are frequently embedded in a self-produced matrix of extracellular polymeric substances (EPS) that are adherent to each other and/or a surface’ [10]. These complex systems have density of cells ranging from 10^8 to 10^{11} cells g^{-1} (wet weight) [12] and provide numerous advantages for their survival, from improved mechanical stability against shear forces to increased expression of beneficial genes and protection from antimicrobial agents [11], detergents and protozoa [14].

Biofilm growth is a highly dynamic process governed by numerous physical, chemical and biological factors [18]. Attachment of a cell to a substrate is defined as *adhesion*, while cell-to-cell attachment is named *cohesion*, the mechanisms behind these processes ultimately determine the adhesive and cohesive properties that a biofilm will exhibit [18]. Characklis and Marshal [19] described biofilm formation as a multi-step process which starts from the formation of a conditioning layer on the substrate, which enables the reversible and irreversible adhesion of bacteria, followed by biofilm growth and the subsequent detachment of cells from a mature biofilm for colonisation of a different site, as shown schematically in **Fig. 1.2**.

1.2.1 The conditioning layer

The conditioning layer constitutes the base on which a biofilm develops and grows, its role is to facilitate the accessibility of a substrate to bacterial adhesion. This layer is composed of organic and inorganic particles, as any molecule within the bulk fluid can settle onto the substrate and become part of a conditioning layer through gravitational force or flow movement. Conditioning films, for example, often form on medical devices due to exposure to human fluids, such as blood, urine or tears [21]. The interactions between the conditioning layer and substrate can alter the surface charge, wettability, potential and surface tension, favouring adhesion and providing anchorage and nutrients to enable the growth of the bacterial community [18, 19].

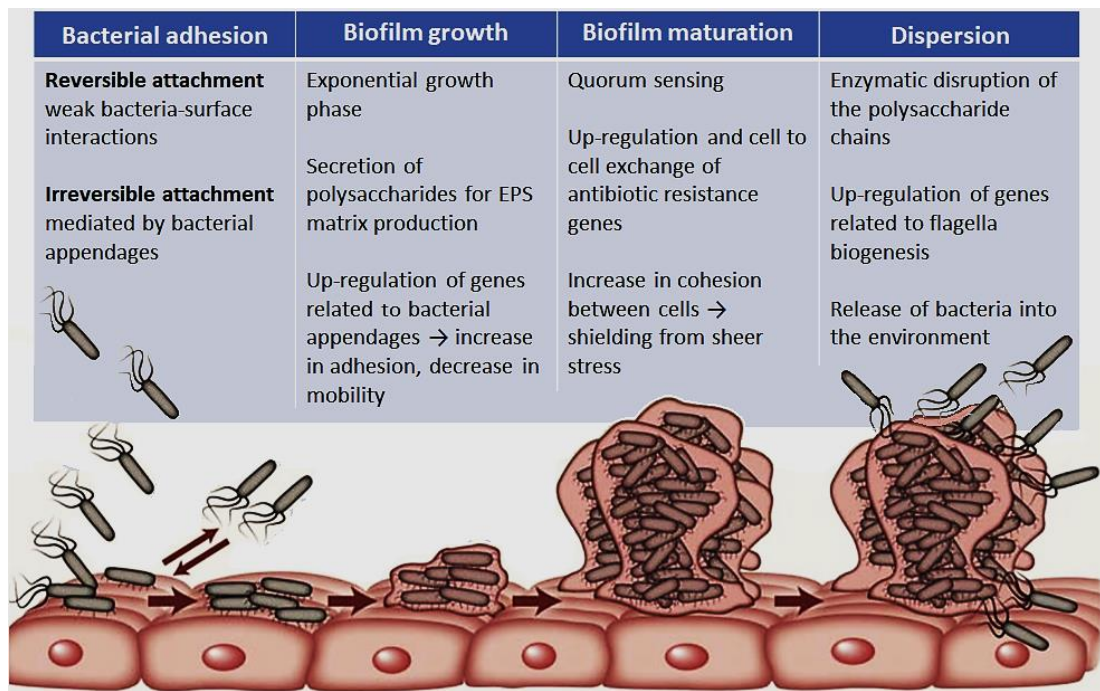


Fig. 1.2 Schematic of the bacterial biofilm life cycle: after the formation of a conditioning layer, bacterial cells adhere to the surface; if the attachment becomes irreversible, the biofilm grows and matures until the EPS matrix is disrupted and the cells are dispersed in the environment. Image adapted from [31].

1.2.2 Bacterial adhesion

Initially, the mobility of planktonic bacteria within the bulk liquid relies on physical forces and cell appendages such as flagella. A fraction of the bacteria that comes in contact with the surface reversibly adsorbs, influenced by local environmental variables such as surface microtopography and chemistry, bacterial orientation, temperature and pressure of the medium [18]. Bacterial adhesion on surfaces is often described as a two-step process consisting of reversible and irreversible attachment [20]. Reversible attachment refers to the initial adhesion of bacteria to the substrate, it relies on weak bacteria-surface interactions, such as van der Waals attractive forces and repulsive electrostatic forces generated by the overlap between the charges of the bacterial membrane and the substrate [20]. Further investigations into this process highlighted how acid-base forces and hydrophobic interactions between bacteria and surfaces may play a critical role in the reversible attachment [23]. If the repulsive forces prevail over the attractive ones, reversible

adhesion is followed by detachment and the cell returns to the planktonic state, a phenomenon more likely to occur before the formation of the conditioning layer [18]. Extracellular bacterial appendages, such as *flagella* and *pili*, have a key role in overcoming the repulsive forces of the electrical double layer and in consolidating the attachment, making it irreversible [22]. Most of these appendages display, at their probing end, proteins referred to as *adhesins*, some of which are essential in mediating cell adhesion to abiotic surfaces, while others bind to specific sites in biomolecules of host cells [22]. The transition from planktonic to sessile state causes a shift in gene expression, leading, for example, to an increase in the production of *pili* to comply with the adhesive needs of the bacterial population, while genes related to the biogenesis of *flagella* are downregulated due to the decreased motility [28]. Bacterial appendages make contact with the conditioning layer, initialising chemical reactions such as oxidation and hydration, essential in consolidating the bacteria– surface bond [18].

1.2.3 Biofilm growth and maturation

Once attachment is irreversible and after an initial lag phase, a rapid increase in bacterial population at the surface is observed, usually referred to as the exponential growth phase, a process influenced by the physical and chemical characteristics of both the substrate and the medium [24]. When the sessile cells divide, the daughter cells usually form clusters with a mushroom-like structure, which allows nutrients to reach the cells deep within the biofilm [18, 24]; in the case of *Escherichia coli* K-12, these structures are characterised by water channels and heterogeneous architectures aimed at delivering nutrients to the entire bacterial community [28]. The biofilm maturation stage is associated with an increased expression of genes involved in the production of cell surface proteins and excretion products [18]. For example, strong bonds between cells are formed due to the excretion of polysaccharide intercellular adhesion (PIA) polymers and the presence of divalent cations [25]. The secreted polysaccharides are fundamental in the production of the EPS matrix that surrounds and connects the bacteria in the

biofilm, the matrix also includes proteins, lipids and extracellular DNA (eDNA) [14, 15]. The electric charge of the EPS ranges from neutral or polyanionic in the case of Gram-negative bacteria [16] to primarily cationic for some Gram-positive strains [17]. This structure grants mechanical stability and is essential to the cohesion and adhesion of the biofilm, shielding the cells from harsh dynamic environmental conditions [18]. It has been reported that during the maturation stage, the bacterial community develops other features, such as increased tolerance to UV light and an increase in the DNA exchange rate which leads to antimicrobial resistance [26, 27].

1.2.4 Final stages of biofilm development and dispersion

Following exponential growth, the cells enter the stationary phase, in which the division rate matches the rate of cell death. For cells that are part of a biofilm, this process involves a series of cell signalling mechanisms, collectively referred to as *quorum sensing* [29]. This process involves several chemical and peptidic signals (e.g. homoserine lactones) secreted to induce the genetic expression of mechanical and enzymatic processors of alginates, fundamental in the formation of the extracellular matrix [18]. The final stage is initiated by the breakdown of the biofilm: enzymes are secreted by the bacterial community to disrupt the polysaccharides chains holding the biofilm together, actively releasing cells into the medium to colonise fresh substrates. Simultaneously, the genes related to flagella biogenesis are up-regulated to increase the motility of the microorganisms, thus closing the cycle for biofilm adhesion and growth [18]. The factors that trigger the dispersion of bacteria embedded in biofilms are still unclear, it is hypothesised, however, that starvation and rise of local bacterial concentration could play a central role [30].

The human body harbours trillions of bacterial cells that coexist in symbiosis with the host, granting mutual benefits for both organisms [32]. In some cases the human host has even evolved to facilitate the colonisation of prokaryotes and biofilm growth: in the gut for example, the abundant and diverse bacterial population plays an essential role in breaking down food substances into nutrients that otherwise wouldn't be accessible to the host, in ATP production, vitamin synthesis, in promoting host cell differentiation, and in stimulating/modulating the immune system, protecting the host from the colonisation of harming organisms such as pathogenic strains of *E. coli* [32, 33].

In some instances, however, bacterial growth can become uncontrolled and harmful to the human body, leading to infection [34]. According to the National Institute of Health, biofilms are estimated to cause up to 80% of the total number of microbial infections in humans [35], which include endocarditis, cystic fibrosis, periodontitis, rhinosinusitis, osteomyelitis, non-healing chronic wounds, meningitis, kidney infections, and prosthesis [34, 36].

1.3 Antimicrobial surfaces

A specific instance in which bacterial colonisation and biofilm formation become harmful to the host is when they involve medical devices. Both Gram-positive and Gram-negative bacteria lead to this problem; for example, *Staphylococcus aureus* and *Staphylococcus epidermidis* are indicated as the main pathogens causing 40-50% of prosthetic heart valve infections and 50-70% of catheter infections [36]. *E. coli* has shown to be the cause of infections related to medical devices such as orthopaedic prostheses, urinary and cardiovascular catheters, intraocular lenses and dentures [37]. The strategy employed to overcome this issue traditionally involves the use of oral or intravenous antibiotics; in the last decades however, the rise in antimicrobial resistance has caused this approach to fail on numerous occasions, particularly as biofilms-associated bacteria can tolerate up to 1000-fold

higher antibiotics concentrations compared to planktonic cells [38]. This issue often leads to severe device-associated infections to be treated with the complete replacement of the device, which involves high risks for the health of the patients and high social costs [39]. Promising results in the prevention of the bacterial colonisation of medical devices arise from aseptic techniques, such as the control of environmental sterility, the use of electric and electromagnetic fields and the employment of antimicrobial surfaces [40-44]. Antimicrobial surfaces preserve the performance of medical devices by preventing or substantially decreasing the initial adhesion of bacteria, their multiplication and the subsequent biofilm formation. Due to the complexity of the issue, a broad variety of solutions have been proposed and employed; the following sections we will give an overview of the different categories of antimicrobial surfaces and their mode of action against bacterial attachment and colonisation.

1.3.1 Antibiofouling and bactericidal effect of surfaces

An effective antimicrobial material aims at repelling or killing adhering bacteria. They are classified into two main categories according to the strategy adopted to prevent their colonisation: antibiofouling and bactericidal. In this context, antibiofouling implies the prevention or removal of adhering bacteria, due to the effect of the surface topography or of the physical/chemical environment (**Fig. 1.3**).

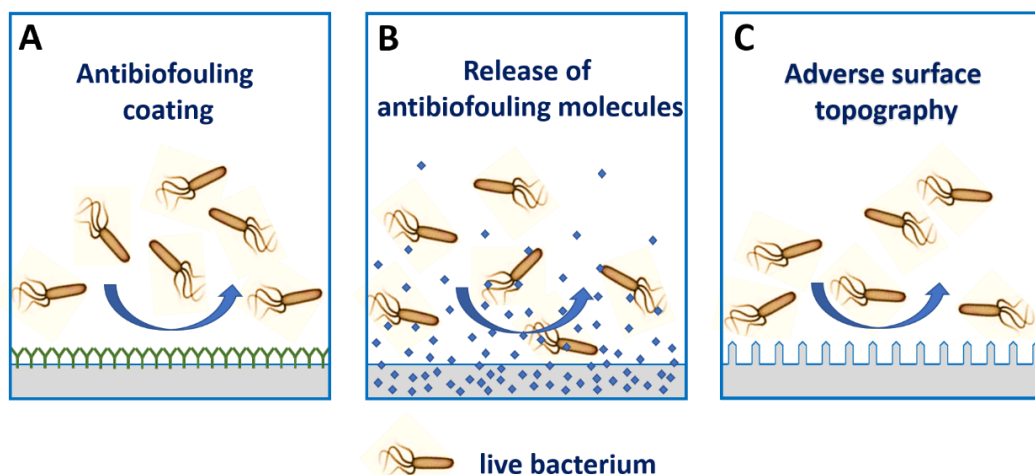


Fig. 1.3 Schematisation of the main strategies on which antibiofouling materials are based on: **A** surface coatings, **B** release of antibiofouling molecules and **C** adverse surface topographies.

The second category features materials that prevent initial bacterial colonisation by causing cell death, either due to bacteria coming in contact with a bactericidal coating or topography, or by the material actively releasing biocides into the environment (**Fig. 1.4**). Some of these strategies are currently in use in the biomedical field: hydroxyapatite coatings are applied to artificial prostheses to stimulate osteogenesis and can be further functionalised by immersion in antibiotic solutions, creating a biocidal coating, this approach presents significant drawbacks as sublethal doses of antibiotics have been shown to increase AMR and biofilm formation [45, 46].

Several strategies to grant antimicrobial properties to a substrate can be found in the literature, either focusing on the antibiofouling approach or the bactericidal one or, in some cases, combining the two. For the purpose of this work, we will focus on materials releasing bactericidal compounds and antimicrobial topographic surfaces.

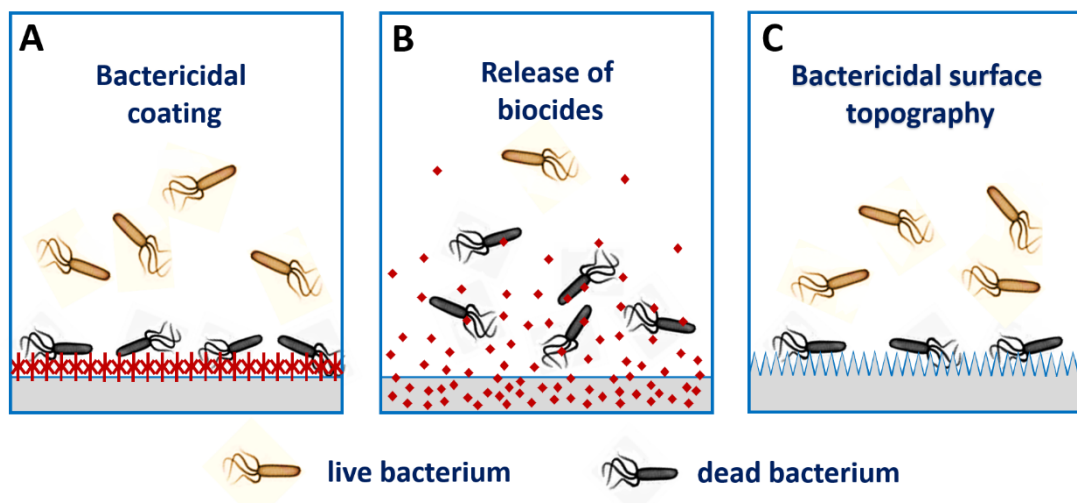


Fig. 1.4 Schematisation of the main strategies on which bactericidal materials are based on: **A** bactericidal surface coatings, **B** release of biocides and **C** bactericidal surface topographies.

1.3.2 Biocide-releasing materials

One of the most effective approaches to improve the efficacy of conventional antibiotic, extending their effect over time, is to deliver the biocide in a controlled, time dependent manner from the material itself or with the aid of a coating. The latter approach was recently exploited by Goudie *et al.* [47], who created an antimicrobial substrate by grafting nitric oxide (NO)-releasing molecules to a silicone surface; the biocide reservoir was shown to last ca. 1 month in the tested release conditions, leading to a 4 fold decrease of the concentration of *Staphylococcus aureus* in the supernatants over 24 h. The coating also improved the antibiofouling nature of the material, decreasing protein adhesion by $65.8 \pm 8.9\%$ compared to pristine silicone.

Drug delivery systems capable of releasing compounds *in vivo* have been studied in combination with orthopedic implants to promote and accelerate osteogenesis and prevent common issues including infection, bone resorption, and implant loosening [48-51]. A commonly used strategy to prevent infection in orthopedic implants relies on embedding antibiotics into bone cement, polymethylmethacrylate (PMMA). This polymer, selected for the role due to its mechanical properties, can be tuned for *in situ* delivery of several biocides and bioactive anti-osteoporotic agents, proteins (model protein, albumin) and growth factors. The release profile of biocides from bone cement takes place in two phases, with an initial burst followed by a slow release that can last for days up to months [51]. This process is influenced by the relative loaded amount within the material [52], bulk porosity [53], surface area and surface roughness of the PMMA material [51]. Despite the optimisation of these parameters though, the biocide release is often largely incomplete [48]. A recent work by Cyphert *et al.* [54] described how insoluble Cyclodextrin (CD) microparticles were embedded within PMMA; these particles can form inclusion complexes with a variety of antibiotics, for a more consistent and prolonged release of rifampicin (RMP), a biocide particularly efficient against *S. aureus* and *S. epidermidis*. CD polymers showed to be able to be re-loaded with RMP *in situ* after the implant, even in the presence of a mature biofilm, and refilled CD microparticles

within a PMMA matrix have shown to extend their release window and antimicrobial activity when compared to systems governed by diffusion alone (e.g. pristine PMMA) [54, 55].

Research on intravascular catheters is focused on solving the issue of catheter-related bloodstream infections (CRBSIs). Every year over 250,000 cases of CRBSIs are reported in the U.S. alone, prolonging hospital stays by ~10–20 days and with reported mortality rates of 12–25 % [56, 57]. In a recent work, Liu *et al.* [57] developed a novel Auranofin-releasing biocidal Polyurethane (PU) catheter for future use in preventing CRBSIs. The carrier, PU, already successfully used for intravascular catheter applications [58], acts as matrix for the biocide, Auranofin, extending its release window and improving the long-term antibacterial effects of the device. The tested catheters were able to inhibit the growth of methicillin-resistant *S. aureus* (MRSA) from 8 up to 26 days, depending on the amount of biocide loaded within the matrix. The PU catheters loaded with Auranofin showed to completely inhibit MRSA biofilm formation *in vitro*, an effect that was not observed with auranofin alone or pristine PU (**Fig. 1.5**).

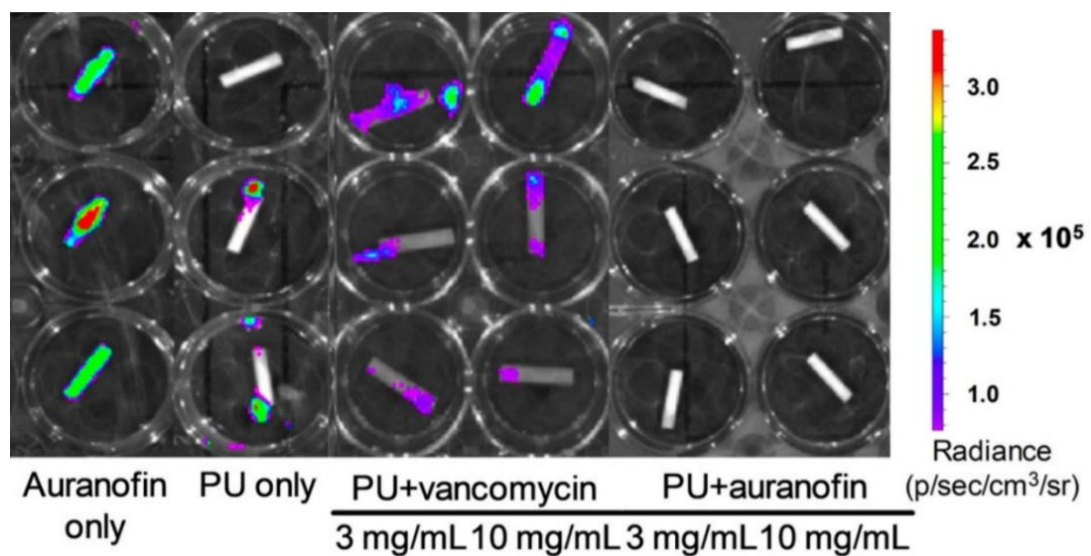


Fig. 1.5 Antibiofilm efficacy of PU-Auranofin catheters. The bioluminescence (radiance) of MRSA was examined using an *in vivo* imaging system (IVIS), samples were either pristine PU, coated with auranofin (at a 3 mg/mL coating concentration), loaded with Vancomycin, or with Auranofin at 3 and 10 mg/mL concentration of dip coating solution. Samples were exposed to MRSA, rinsed, and the potentially attached bacteria were incubated for 48 h prior to measurement. Image adapted from [57].

1.3.3 Antimicrobial topographic surfaces

An alternative approach to solving the issue of bacterial attachment on medical devices is via surface modification techniques that enhance the biocompatibility, functionality of the materials and their antimicrobial properties, while preserving their bulk properties and structural integrity [59]. Several solutions have been studied in recent years to modify the surface topography at the nanoscale level and enhance its antibiofouling and/or bactericidal activity. Many natural surfaces have served as inspiration in this context, as through billions of years they evolved characteristics that allow them to resist or prevent bacterial colonisation; some of the most commonly studied include gecko foot, shark skin, cicada wings, fish scale, and spider silk [60, 61, 62]. An important role in bacterial attachment and biofilm formation is played by the surface topography, as properties like surface area, surface roughness, surface energy, and hydrophilicity strongly influence protein adsorption and consequently prokaryotes adhesion [63, 64]. Yet, the extent to which the topography affects bacterial attachment and subsequent biofilm formation remains a subject of dispute, especially when focusing on the length scale of the topographic features at which the influence is most profound [65, 66]. In 2004, Katsikogianni and Missirlis [67] reported that the substrates with features comparable to the cells in size allowed bacteria to maximise their contact area with the surface, hence enhancing their binding potential. Edwards and Rutenberg [68], studying the attachment patterns and attachment strength of *Thiobacillus caldus* on mineral pyrite, found strong correlations between the crystallographic axes and predominant bacterial cell alignments.

In their work, Whitehead *et al.* [69] coated silicon wafers with titanium, combining physical vapour deposition and template techniques. The obtained substrates showed a variety of features, from irregularly spaced, ranging from 0.2 to 0.5 μm in size, to regularly spaced pits with regular features characterised by 1-2 μm diameters. The antimicrobial activity of the modified surfaces was tested via microbial retention assays, using unrelated, differently sized bacterial strains. As shown in scanning electron microscope images (**Fig. 1.6**), the highest number of *S.*

aureus cells, 0.5–1 μm in size, were retained in the 0.5 μm sized pits and accumulated within larger surface features. The rod-shaped *Pseudomonas aeruginosa* cells (1 $\mu\text{m} \times 3 \mu\text{m}$) preferentially adhered to the 1 μm surface features. For both strains, the highest number of cells was retained within the largest (2 μm) surface features.

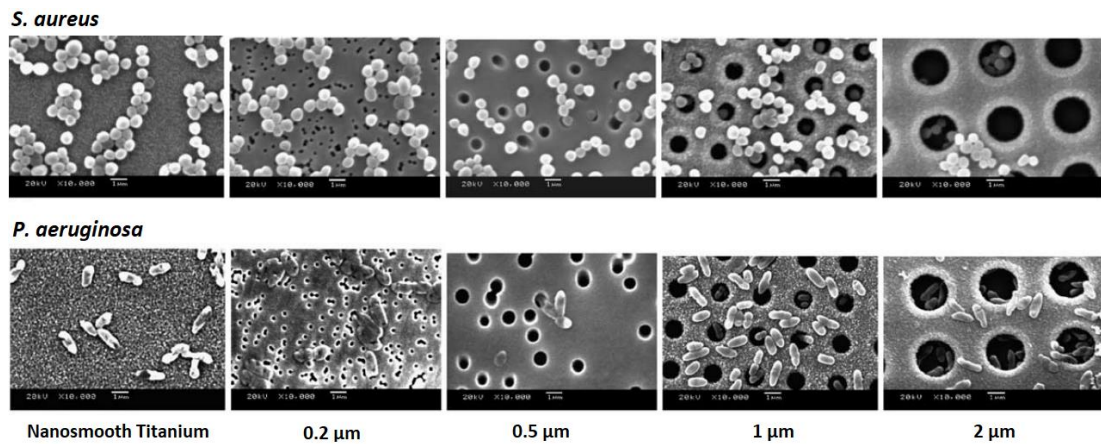


Fig. 1.6 SEM images showing *S. aureus* and *P. aeruginosa* cells retained on surfaces of defined topography. The spherical staphylococcal cells are retained in the 0.5 μm sized pits, and accumulate in the larger surface features. The larger *P. aeruginosa* cells are mostly retained in the 1 μm surface features. Image adapted from [69].

The group of Elena P. Ivanova has in recent years pioneered the studies on bacterial attachment on topographic surfaces: in a 2019 paper [70] they focused on the interactions between MRSA strains and nanostructured titanium substrates, fabricated via hydrothermal etching. The surfaces proved to be bactericidal against the tested *S. aureus* strains, with killing efficiencies higher than 80% on the attached cells. SEM images (**Fig. 1.7**) showed evident disrupted integrity of the bacterial membranes of MRSA strains due to the interaction with the etched Ti surfaces.

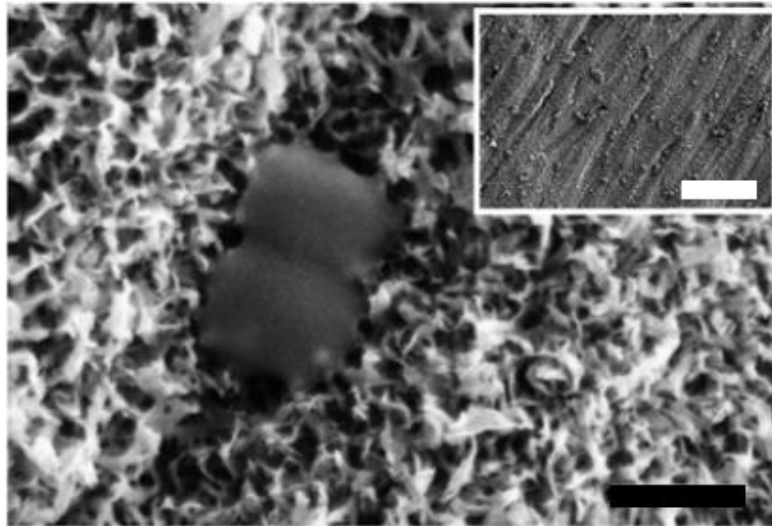


Fig. 1.7 MRSA cells on nanostructured Ti surfaces after 18 h of incubation, showing altered cell morphology. The inset displays an overview of the cell attachment pattern. Scale bar is 400 nm, inset scale bar is 10 μm . Image adapted from [70].

In some cases the antibiofouling and the biocide-releasing approaches can be combined for an enhanced antimicrobial effect. Brammer *et al.* [71] fabricated silicon nanowire (SiNW) arrays via electroless etching, obtaining 1-3 μm tall surface features with 10-40 nm diameters. The substrates were functionalised with penicillin and streptomycin via vacuum vapor deposition. The antibiotic-loaded SiNWs showed to be able to maintain high levels of release for 42 days when incubated in simulated body fluid. At the surface, the suppressed cell and protein adhesion caused by the adverse topography indicated a reduced probability for biofouling and bacterial attachment.

1.4 Thesis aims

This Ph.D. thesis presents a multidisciplinary approach on the functionalisation and characterisation of biocompatible surfaces for antimicrobial purposes, combining surface science, material chemistry, and microbiology. We focused on the events and material properties that lead to bacterial attachment and consequent biofilm formation, aiming at the prevention or alteration of these processes.

Two separate approaches are presented in this work: first, we developed a post-fabrication method to functionalise a polymeric biocompatible material with a reservoir of commercially available biocide within its bulk, allowing for sustained release over 72h. We used advanced spectroscopic techniques to provide insights on the biocide loading and release mechanisms, while microbiology assays assessed the antimicrobial effect of the released compound, both on sessile and planktonic bacteria. We aim at demonstrating the feasibility of this post-fabrication modification approach in the context of materials currently used for the fabrication of medical devices, exemplified by PDMS.

The second approach focuses on the study of the attachment and cell-division at the surface of a wide range of bacteria on flat and nanostructured silicon substrates, aiming to probe some mechanisms that allow the surface topography to influence the initial stages of biofilm formation. The use and optimisation of high resolution imaging techniques allows for an in depth analysis, down to the single cell level, on the viability, division modes and extracellular appendices of the bacteria adhering to the substrates, highlighting similarities and differences between the different species and correlating biological responses to the local surface topography. With this approach we aim to assess how nanotopography affects biofilm development on materials relevant for orthopaedic prostheses applications.

1.5 References

[1] **Adaptive evolution in single species bacterial biofilms**

Kraigsley AM, Finkel SE
FEMS Microbiol. Lett. 293 (2009) 135–140

[2] **World Health Organization. WHO. Antibiotic resistance**

<https://www.who.int/news-room/fact-sheets/detail/antibiotic-resistance>
(accessed 15 August 2020)

[3] **No Time To Wait: Securing The Future From Drug-Resistant Infections**

Report To The Secretary-General Of The United Nations, April 2019

[4] **Review of Antimicrobial Food Packaging**

Appendini P, Hotchkiss JH
Innov. Food Sci. Emerg. Technol. 3(2) (2002) 113–126

[5] **Antimicrobial Polymers for Antibiofilm Medical Devices: State-of-Art and Perspectives**

Francolini I, Donelli G, Crisante F, Taresco V, Piozzi A
Advances in Experimental Medicine and Biology 831 (2015) 93–117

[6] **World Health Organization. WHO. Medical Device – Full Definition**

https://www.who.int/medical_devices/full_definition/en/ (accessed 15 August 2020)

[7] **In Vitro Biofilm Models for Device-Related Infections**

Buhmann MT, Stiefel P, Maniura-Weber K, Ren Q
Trends in Biotechnology 34(12) (2016) 945-948

[8] **Bacterial Biofilms: From The Natural Environment To Infectious Diseases**

Hall-Stoodley L, Costerton JW, Stoodley P
Nat. Rev. Microbiol. 2 (2004) 95

[9] **Microbial growth in biofilms: developmental and molecular biological aspects**

Doyle R
Methods Enzymol., 1st Edition, 2001, 336-337

[10] **Terminology for biorelated polymers and applications (IUPAC Recommendations 2012)**

Vert M, et al.
Pure Appl. Chem. 84 (2012) 377–410

[11] **Microbiological Aspects of Biofilms and Drinking Water**

Percival SL, Walker JT, Hunter PR
CRC Press, 1st Edition, 2010

[12] **Characterization of the loosely attached fraction of activated sludge bacteria**

Morgan-Sastume F, Larsen P, Nielsen JL, Nielsen PH
Water Res. 42 (2008) 843–854

[13] Essential oil of *Melaleuca alternifolia* for the treatment of oral candidiasis induced in an immunosuppressed mouse model

Rasteiro V, Costa A, Araujo C, Barros P, Rossoni R, Anbinder AL, Jorge A Junqueira J
BMC Complementary and Alternative Medicine 14 (2014) 489

[14] Biofilms: an emergent form of bacterial life

Flemming HC, Wingende J, Szewzyk U, Steinber P, Rice SA, Kjelleberg S
Nat. Rev. Microbiol. 14 (2016) 563

[15] The biofilm matrix

Flemming HC, Wingende J
Nat. Rev. Microbiol. 8 (2010) 623–633

[16] Biofilm Exopolysaccharides: A Strong and Sticky Framework

Sutherland IW
Microbiology 147(1) (2001) 3–9

[17] The Slime of Coagulase-Negative Staphylococci: Biochemistry and Relation to Adherence

Hussain M, Wilcox MH, White PJ
FEMS Microbiol. Lett. 104 (3–4) (1993) 191–207

[18] Bacterial adhesion and biofilms on surfaces

Garrett TR, Bhakoo M, Zhang Z
Progress in Natural Science 18 (2008) 1049–1056

[19] Biofilms

Characklis WG, Marshal KC
John Wiley and Sons, New York, 1st Edition, 1990

[20] Theory of the Stability of Lyophobic Colloids

Verwey EJW, Overbeek JTG
J. Colloid Sci. 10(2) (1955) 224–225

[21] Molecular and Ecological Diversity

Fletcher M
John Wiley and Sons, New York, 1st Edition, 1996

[22] Bacterial Adhesion: From Mechanism to Control.

Hori K, Matsumoto S
Biochemical Engineering Journal 15 (2010) 424–434.

[23] Adhesion of *Paenibacillus Polymyxa* on Chalcopyrite and Pyrite: Surface Thermodynamics and Extended DLVO Theory

Sharma PK, Hanumantha Rao K
Colloids Surfaces B Biointerfaces 29(1) (2003) 21–38

[24] Developmental regulation of microbial biofilms

Hall-Stoodley L, Stoodley P
Curr Opin Biotechnol 13 (2002) 228–233

[25] Bacterial adhesion: seen any good biofilms lately?

Dunne WM

Clin Microbiol Rev 15 (2002) 155–166

[26] Gene Transfer among Bacteria under Conditions of Nutrient Depletion in Simulated and Natural Aquatic Environments

Goodman AE, Marshall KC, Hermansson M

FEMS Microbiol. Ecol. 15(1) (1994) 55–60

[27] In Situ Gene Expression in Mixed-Culture Biofilms: Evidence of Metabolic Interactions between Community Members

Møller S, Sternberg C, Andersen JB, Christensen BB, Ramos JL, Givskov M, Molin S

Appl. Environ. Microbiol. 64 (2) (1998) 721– 732

[28] Abiotic Surface Sensing and Biofilm-Dependent Regulation of Gene Expression in Escherichia Coli

Prigent-Combaret C, Vidal O, Dorel C, Lejeune P

J. Bacteriol. 181(19) (1999) 5993–6002

[29] How bacteria talk to each other: regulation of gene expression by quorum sensing

Bassler BL

Curr Opin Microbiol 2 (1999) 582–587

[30] Extracellular Products as Mediators of the Formation and Detachment of Pseudomonas Fluorescens Biofilms

Allison DG, Ruiz B, Sanjose C, Jaspe A, Gilbert P

FEMS Microbiol. Lett. 1998, 167 (2), 179–184

[31] Bacterial Biofilms: Development, Dispersal, and Therapeutic Strategies in the Dawn of the Postantibiotic Era

Kostakioti M, Hadjifrangiskou M, Hultgren SJ

Cold Spring Harb Perspect Med 3(4) (2013) a010306

[32] The First Microbial Colonizers of the Human Gut: Composition, Activities, and Health Implications of the Infant Gut Microbiota

Milani C, Duranti S, Bottacini F, Casey E et al.

Microbiol Mol Biol Rev 81 (2017) e00036-17

[33] Gut Biogeography of the Bacterial Microbiota

Donaldson GP, Lee SM, Mazmanian SK

Nat. Rev. Microbiol. 14(1) (2015) 20–32

[34] The role of bacterial biofilms in chronic infections

Bjarnsholt T

Apmis 121 (2013) 1-58

[35] Understanding biofilm resistance to antibacterial agents

Davies D

Nat. Rev. Drug Discov. 2(2) (2003) 114-122

- [36] **Novel strategies for the prevention and treatment of biofilm related infections**
Chen M, Yu Q, Sun H
Int. J. Mol. Sci. 14(9) (2013) 18488-18501
- [37] ***Escherichia coli* biofilm: development and therapeutic strategies**
Sharma G, Sharma S, Sharma P, Chandola D, Dang S, Gupta S, Gabrani R
Journal of Applied Microbiology 121 (2016) 309-319
- [38] **Biofilm-specific antibiotic tolerance and resistance.**
Olsen I
Eur. J. Clin. Microbiol. 34 (2015) 877–886
- [39] **Health care-associated infections: a meta-analysis of costs and financial impact on the US health care system.**
Zimlichman E, et al.
JAMA Intern. Med. 173 (2016) 2039–2046
- [40] **Prevention of Surgical Site Infections in Orthopaedic Surgery and Bone Trauma: State-of-the-Art Update**
Uçkay I, Hoffmeyer P, Lew D, Pittet D
J. Hosp. Infect. 84 (1) (2013) 5–12
- [41] **Diagnosis, Management, and Prevention of Prosthetic Joint Infections.**
Yin JM, Liu ZT, Zhao SC, Guo YJ
Front. Biosci. Landmark Ed. 18 (2013) 1349–1357
- [42] **Biofilm Formation in Staphylococcus Implant Infections. A Review of Molecular Mechanisms and Implications for Biofilm-Resistant Materials**
Arciola CR, Campoccia D, Speziale P, Montanaro L, Costerton JW
Biomaterials 33 (26) (2012) 5967–5982
- [43] **A Review of the Biomaterials Technologies for Infection-Resistant Surfaces**
Campoccia D, Montanaro L, Arciola CR
Biomaterials 34 (34) (2013) 8533–8554
- [44] **Bacterial biofilm formation on implantable devices and approaches to its treatment and prevention**
Khatoun Z, McTiernan CD, Suuronen EJ, Mah TF, Alarcon EI
Heliyon 4(12) (2018) e01067
- [45] **Bacterial adherence and biofilm formation on medical implants: a review**
Veerachamy S, Yarlagadda T, Manivasagam G, Yarlagadda PK
Proc. Inst. Mech. Eng. H 228(10) (2014) 1083-1099
- [46] **Antimicrobial and Antifouling Strategies for Polymeric Medical Devices**
Zander ZK, Becker ML
ACS Macro Lett. 7 (2018) 16–25

[47] Active Release of an Antimicrobial and Antiplatelet Agent from a Nonfouling Surface Modification

Goudie MJ, Singha P, Hopkins SP, Brisbois EJ, Handa H
ACS Appl. Mater. Interfaces 11(4) (2019) 4523–4530

[48] Biologic fixation and bone ingrowth

Sporer SM, Paprosky WG
Orthop Clin North Am 36(1) (2005) 105–111

[49] Mechanisms of failure of total hip replacements: lessons learned from retrieval studies

Hirakawa K, Jacobs Joshua J, Urban R, Saito T
Clin Orthop 420 (2004) 10–17

[50] Failures and successes in total hip replacement—why good ideas may not work

Morscher EW
Scand J Surg 92(2) (2003) 113–120

[51] Drug/device combinations for local drug therapies and infection prophylaxis

Wu P, Grainger DW
Biomaterials 27 (2006) 2450–2467

[52] Gentamicin release from modified acrylic bone cements with lactose and hydroxypropylmethylcellulose.

Virto MR, Frutos P, Torrado S, Frutos G
Biomaterials 24(1) (2002) 79–87

[53] Surface roughness, porosity and wettability of gentamicin-loaded bone cements and their antibiotic release.

Van de Belt H, Neut D, Uges DRA, Schenk W, van Horn JR, van der Mei HC, et al.
Biomaterials 21(19) (2000) 1981–1987

[54] An Additive to PMMA Bone Cement Enables Post-implantation Drug Refilling, Broadens Range of Compatible Antibiotics, and Prolongs Antimicrobial Therapy

Cyphert HL, Learn GD, Hurley SK, Lu CY, Von Recum HA
Adv. Healthcare Mater. 7 (2018) 1800-1812

[55] Affinity interactions drive post-implantation drug filling, even in the presence of bacterial biofilm

Cyphert EL, Zuckerman ST, Korley JN, Von Recum HA
Acta Biomater. 57 (2017) 95

[56] The risk of bloodstream infection in adults with different intravascular devices: a systematic review of 200 published prospective studies

Maki DG, Kluger DM, Crnich CJ
Mayo Clin. Proc. 81 (2006) 1159–1171

[57] Auranofin Releasing Antibacterial and Antibiofilm Polyurethane Intravascular Catheter Coatings

Liu H, Shukla S, Vera-González N, et al.
Front Cell Infect Microbiol. 9 (2019) 37

- [58] **Polyurethane versus silicone catheters for central venousport devices implanted at the forearm**
Wildgruber M, Lueg C, Borgmeyer S, et al.
European Journal of Cancer 59 (2016) 113-124
- [59] **Efficient surface modification of biomaterial to prevent biofilm formation and the attachment of microorganisms**
Bazaka K, Jacob MV, Crawford RJ, Ivanova EP
Appl. Microbiol. Biotechnol. 95 (2012) 299–311
- [60] **Antibacterial surfaces: the quest for a new generation of biomaterials**
Hasan J, Crawford RJ, Ivanova EP
Trends in Biotechnology 31(5) (2013) 295-304
- [61] **Purity of the sacred lotus, or escape from contamination in biological surfaces**
Barthlott W, Neinhuis C
Planta 202 (1997) 1–8
- [62] **Bio-inspired design of multiscale structures for function integration**
Liu K, Jiang L
Nano Today 6 (2011) 155–175
- [63] **Bacterial biofilm formation on implantable devices and approaches to its treatment and prevention**
Khatoun Z, McTiernan CD, Suuronen EJ, Mah TF, Alarcon EI
Heliyon 4 (2018) e01067
- [64] **Biomaterials Associated Infection: Immunological Aspects and Antimicrobial Strategies**
Moriarty TF, Zaat SAJ, Busscher HJ
Springer New York, New York, NY, 2nd Edition, 2013
- [65] **The interaction of cells and bacteria with surfaces structured at the nanometre scale**
Anselme K, Davidson P, Popa AM, Giazzon M, Liley M, Ploux L
Acta Biomater 6 (2010) 3824–3846
- [66] **Rapid quantification of staphylococci adhered to titanium surfaces using image analyzed epifluorescence microscopy**
An YH, Friedman RJ, Draughn RA, Smith EA, Nicholson JH, John JF
J Microbiol Methods 24 (1995) 29–40
- [67] **Concise review of mechanisms of bacterial adhesion to biomaterials and of techniques used in estimating bacteria–material interactions**
Katsikogianni M, Missirlis YF
Eur Cells Mater 8 (2004) 37–57
- [68] **Microbial response to surface microtopography: the role of metabolism in localized mineral dissolution**
Edwards KJ, Rutenberg AD
Chem Geol 180 (2001) 19–32

[69] Retention of microbial cells in substratum surface features of micrometer and sub-micrometer dimensions

Whitehead KA, Colligon J, Verran J
Colloids Surf B 41 (2005) 129–138

[70] Outsmarting superbugs: bactericidal activity of nanostructured titanium surfaces against methicillin- and gentamicin-resistant *Staphylococcus aureus* ATCC 33592

Wandiyanto JV, Cheeseman S, Truong VK, Kobaisi MA, Bizet C, Juodkasis S, Thissen H, Crawford RJ, Ivanova HP
Mater. Chem. B 7 (2019) 4424-4431

[71] Antibiofouling, sustained antibiotic release by Si nanowire templates

Brammer KS, Choi C, Oh S, et al.
Nano Lett. 9(10) (2009) 3570-3574

Chapter 2

Experimental Techniques

2.1 Introduction

Any deep investigation of the chemical and physical characteristics of a sample, and of the biological processes taking place at the liquid-solid interface, requires the use of a wide range of techniques spanning from microbiology to spectroscopy to high resolution imaging. The following chapter will describe the experimental techniques and the instruments used to characterise the materials studied in this work and their antimicrobial activity.

The fields of surface chemistry and material science provide us with established characterisation methods to assess the physicochemical properties of functionalised and topographic substrates. Due to the complex challenges emerged during the characterisation of biological interfaces, the optimisation of some of these methods was required in terms of probing speed and spatial resolution, while their combination with microbiology techniques allowed us to unravel the modes of action of model bacterial species on nanostructured surfaces, providing a better understanding of the complex biological processes occurring at the interfaces.

2.2 Surface Spectroscopy

2.2.1 Vibrational Spectroscopy

The term vibrational spectroscopy commonly refers to two main analytical techniques: infrared (IR) and Raman spectroscopy. In the characterisation of polymers and biointerfaces, these techniques are essential and complementary in providing information on the chemical fingerprint of a sample, assessing the molecular composition and interactions at the surface and within the bulk of the material, by measuring vibrational frequencies associated with specific chemical bonds and functional groups [1]. The vibrational modes of chemical groups are characterised by harmonic oscillations whose frequency, expressed in wavenumbers ($\bar{\omega}$, cm^{-1}), can be calculated using **Eq. 2.1**:

$$\bar{\omega} = \frac{1}{2\pi c} \sqrt{\frac{k}{\mu}}$$

Equation 2.1

In which c is the velocity of light ($3 \times 10^{10} \text{ cm s}^{-1}$), k is the force constant, measured in N/m, associated with the strength of chemical bonds and μ refers to the reduced mass [2, 3, 4] which can be calculated as follows for a diatomic molecule (**Eq. 2.2**).

$$\mu = \frac{m_1 \times m_2}{m_1 + m_2}$$

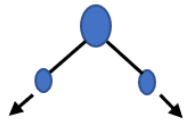


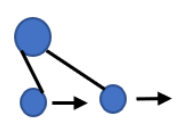
Equation 2.2

Where m_1 and m_2 are the atomic masses of the atoms in the diatomic molecule [4].

Infrared Spectroscopy

Infrared spectroscopy is based on the absorption of photons in the infrared region of the spectrum, in a wavelength range of 2.5 μm to 25 μm . Energy absorption occurs when the oscillation frequency of the incident photons matches the characteristic frequency of a specific vibrational mode. The selection rules of quantum mechanics imply that, for a vibrational mode to be infrared active, it must induce a change in the dipole moment of the molecule due to a vibration or rotation caused by the interaction with the incident photons [3, 4]. Infrared absorption only occurs when the energy of incoming IR photons ($E = h\nu$) is sufficient to transition the molecule to the next allowed vibrational state [4]. As represented in **Table 2.1**, vibrations can cause changes in bond length (stretching) or bond angle (bending), both symmetrically and asymmetrically [4].

Table 2.1 Vibrational modes of functional chemical groups in IR spectroscopy encountered in this work, with their commonly assigned symbol and a schematic representation of the atomic movement involved.

Vibrational mode	Assigned symbol	
Symmetric stretch	ν_s	
Asymmetric stretch	ν_{as}	
Symmetric bend	δ_s	
Asymmetric bend	δ_{as}	

Attenuated Total Reflection - Infrared Spectroscopy

Attenuated Total Reflection - Infrared Spectroscopy (ATR-IR) is a surface-sensitive technique that relies on the penetration of a photon beam from a prism with higher refractive index into a sample with lower refractive index (**Fig. 2.1**).

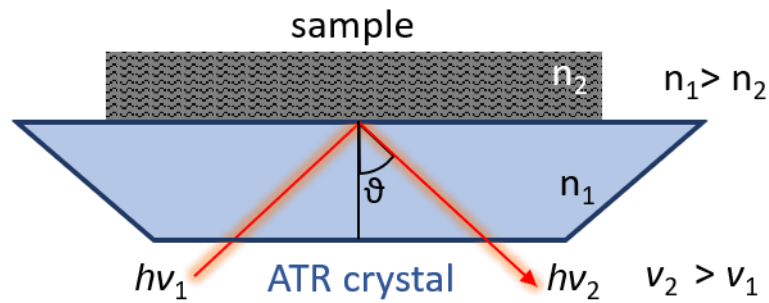


Fig 2.1 Schematic representation of an infrared spectrometer in attenuated total reflectance infrared (ATR) configuration. n_1 and n_2 represent the refractive indices of the ATR crystal (or prism) and the sample, respectively, while ϑ represents the angle of incidence of the photon beam.

The energy ($h\nu_1$) of the incident light is absorbed by the IR-active chemical groups of the sample's molecules within probe depth (d). As shown in **Eq. 2.3**, d is related to the refractive indices of the prism (n_1 , typically 2.4 for diamond ATR prisms) and the sample (n_2), to the wavenumber of the studied band (λ) and can be controlled changing the angle of incidence of the photon beam (ϑ) [5].

$$d = \frac{\lambda}{4\pi\sqrt{n_1^2 \sin^2 \vartheta - n_2^2}}$$

Equation 2.3

The intensity of the evanescent wave reflected from the sample is measured by a detector and processed via Fourier transformation, obtaining a plot of the absorbance as a function of the wavelength.

An ATR-IR spectrum provides information on the chemical species and the molecular structure of a sample, as specific functional group vibrations can be matched with their characteristic absorption bands, often referred to as fingerprints, allowing to assess the chemical composition of the sample. An example can be found in **Table 2.2** where the vibrational modes of the methyl group are identified by specific absorption bands [6].

Table 2.2 Characteristic infrared vibrational frequencies of the Methyl group.

Origin Group	Frequency, wavenumber (cm^{-1})	Functional Group
C-H ₃	2970-2950	C-H asymmetric stretching
C-H ₃	2880-2860	C-H symmetric stretching
C-H ₃	1470-1430	C-H asymmetric bending
C-H ₃	1380-1370	C-H symmetric bending

An example of methyl-related bands can be found in the IR spectrum of polydimethylsiloxane (PDMS), shown in **Fig. 2.2**.

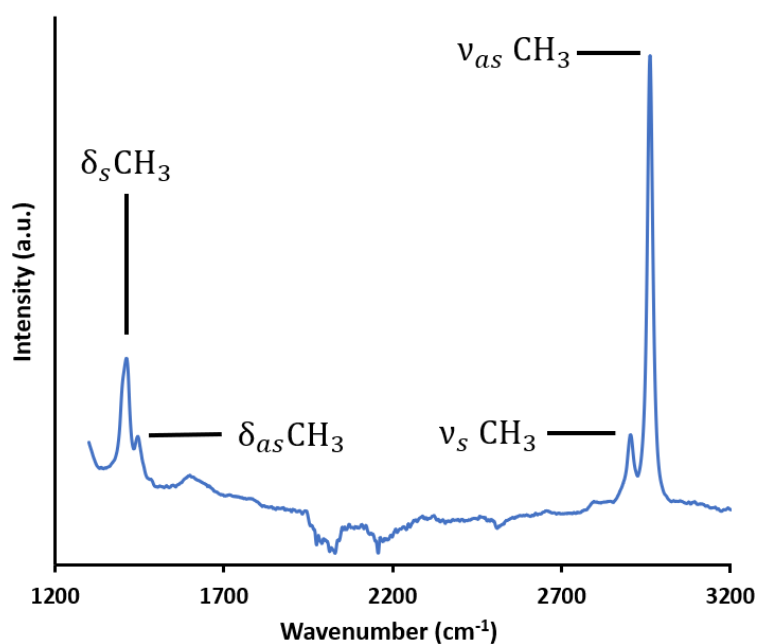


Fig. 2.2 Infrared spectrum of polydimethylsiloxane (PDMS) between 1200 and 3200 cm^{-1} .

In this work, infrared measurements were performed using a Bruker Alpha FTIR equipped with an ATR module. ATR-FTIR measurements allowed the assessment of the chemical fingerprint of biomaterial interfaces used in this work, as well as in the investigation of the biocide release mechanisms in Chapter 3.

Raman Spectroscopy

Raman spectroscopy is a technique complementary to IR spectroscopy, as in many instances, vibrational modes that are not observed by IR absorption can be detected by Raman spectroscopy. When incident photons collide with a sample, most of them are elastically scattered, retaining the same energy and wavelength after collision, a process known as Rayleigh scattering (**Fig. 2.3 A**). The small portion of incident photons inelastically scattered when colliding with the sample generates what is referred to as Raman scattering. In this process energy can be transferred from the photons to a molecule, leading to scattered light of lower energy and higher wavelengths (Stokes scattering, **Fig. 2.3 B**); anti-Stokes scattering refers to the process in which energy is transferred from a molecule in an excited vibrational state to an incident photon, resulting in scattered light of higher energy and lower wavelength (**Fig. 2.3 C**) [7, 8].

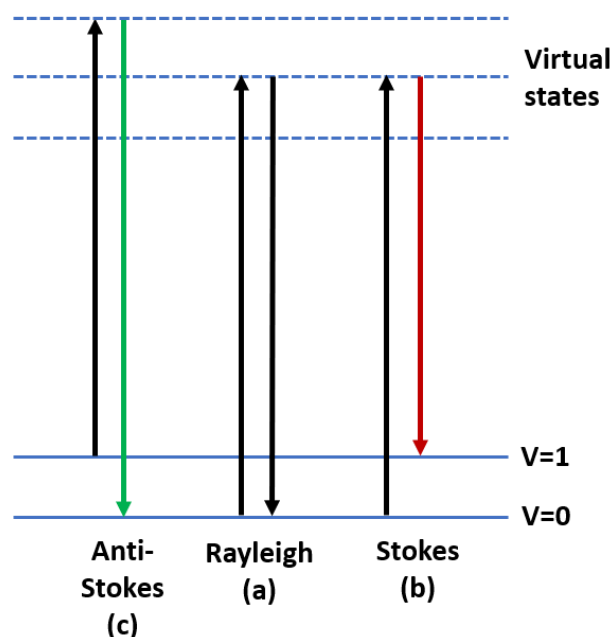


Fig. 2.3 Jablonski diagram representing elastic Rayleigh scattering (a), inelastic Stokes (b) and anti-Stokes scattering (c).

A vibrational mode will be active and visible in the Raman spectrum if it induces a change in the polarizability of the molecule, which is the measure of the ability of the electron cloud around a molecule to be distorted by an external electromagnetic field [7]. Since Raman and infrared spectroscopy differ in their selection rules and consequently in the vibrational transitions of molecules and functional groups they detect, the two spectroscopic techniques are highly complementary in assessing the molecular structure of the chemical species present in a sample. As a general rule, molecules with polar groups are more visible in IR spectroscopy, while vibrations of symmetric vibrations of a-polar, electron rich moieties like aromatic groups are Raman active [7].

Fig. 2.4 shows the evolution of the Raman spectra of Salicylic Acid (SA) with pH conditions, while **Table 2.3** identifies the bands related to the vibration modes of SA (**Fig. 2.4 C**), Salicylate monoanion (**Fig. 2.4 B**) and Salicylate dianion (**Fig. 2.4 A**) [9].

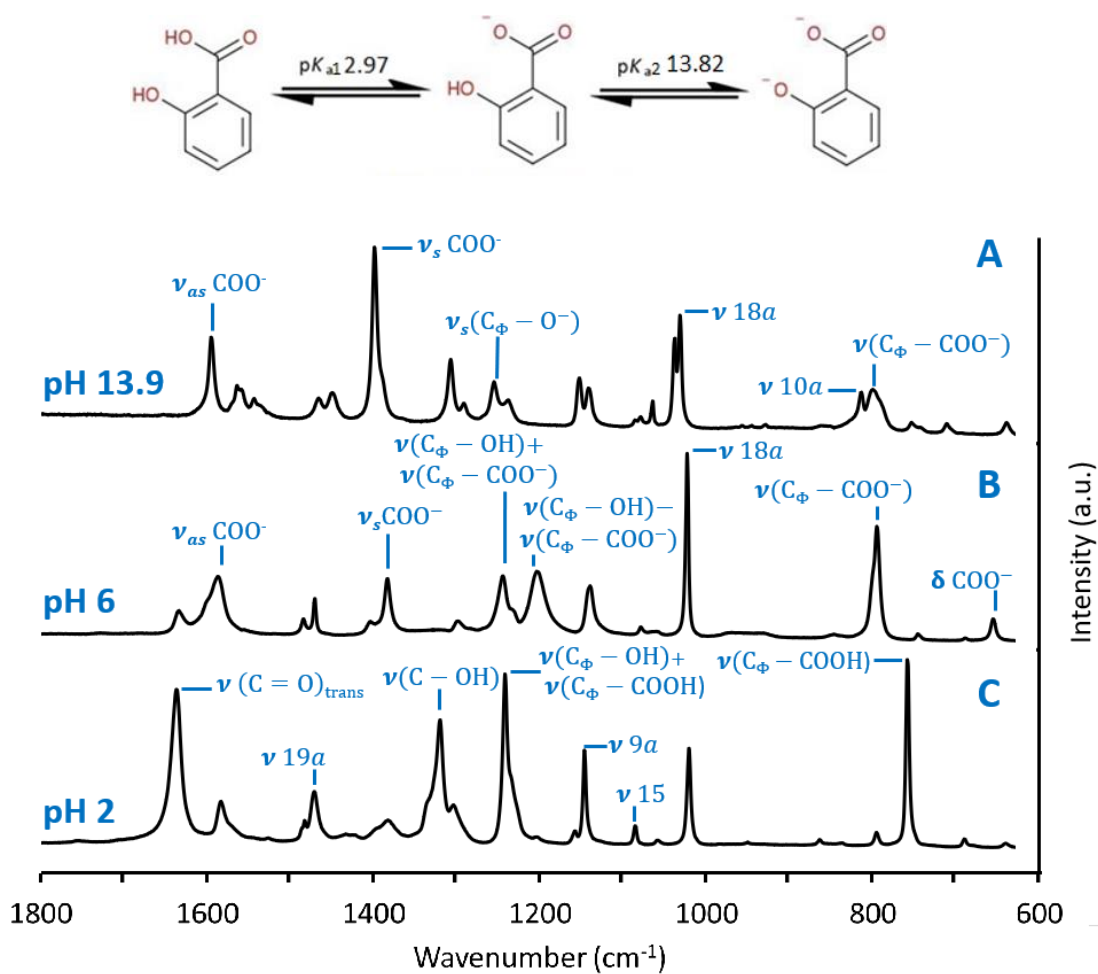


Fig. 2.4 Raman spectrum of Salicylic Acid (C), Salicylate monoanion (B) and Salicylate dianion (A). *as* stands for asymmetric, *s* for symmetric; +: in-phase movement; -: out-of-phase movement C_ϕ indicates a C atom in the benzene ring. The modes derived from benzene are indicated by the Wilson's numbering [9]. For more detailed peak assignments please refer to **Tab. 2.3**.

Table 2.3 Raman vibrational frequencies for the functional groups related to Salicylate bianion, Salicylate monoanion and Salicylic Acid. Adapted from Humbert *et al.* [9]; + (in-phase movement); - (out-of-phase movement); C_ϕ indicates a C atom in the benzene ring. The modes derived from benzene are indicated by the Wilson's numbering.

Wavenumbers (cm ⁻¹)	Salicylate Bianion	Salicylate Monoanion	Salicylic Acid
1610	/	/	$\nu_{8a} + \nu(C-O) - \nu(C_\phi-OH) + \delta(C_\phi-OH)$
1593	ν_{8a}	$\nu_{8b} + \nu_{as}(COO^-) + \delta(C_\phi-OH)$	$\nu_{8b} + \nu(C-O) + \delta(C_\phi-OH)$
1570	/	$\nu_{as}(COO^-) + \nu_{8b} + \delta(C_\phi-OH)$	/
1556	$\nu_{as}(COO^-)$	/	/
1535	ν_{8b}	/	/
1487	/	/	ν_{19a}
1468	ν_{19}	ν_{19}	/
1459	/	/	ν_{19b}
1390	$\nu_s(COO^-)$	$\nu_{14} + \nu_s(COO^-) + \delta(C_\phi-OH) + \nu(C_\phi-OH)$	/
1345	/	/	$\delta(C_\phi-OH)$
1265	$\nu(C_\phi-O)$	/	/
1254	/	$\nu(C_\phi-OH) + \nu(C_\phi-COO^-)$	/
1246	/	/	$\nu(C_\phi-OH) + \nu(C_\phi-COOH)$
1226	/	/	$\nu(C_\phi-OH) - \nu(C_\phi-COOH) + \delta(C_\phi-OH)$
1093	ν_{15}	ν_{15}	ν_{15}
1038	ν_{18a}	ν_{18a}	ν_{18a}
920	ν_{17a}	/	/
870	ν_{10a}	ν_{10a}	/
822	$\nu(C_\phi-COO^-)$	/	/
814	/	$\nu(C_\phi-COO^-) + \delta(C_\phi-OH) + \delta_s(COO^-)$	/
664	/	$\delta_s(COO^-) + \nu_4$	$\delta(COOH) + \nu_4$

Raman line mapping

By properly adapting the configuration of the instrument, it's possible to use Raman spectroscopy for mapping the chemicals within the bulk of a sample. An accurate profile of the concentration of a specific compound across a cross section of a specimen can be obtained by scanning across a selected line and processing the spectra obtained at each point, each time integrating a specific peak, associated to a vibrational mode characteristic of the compound to investigate. Fig. 2.5 displays

the relative amount of SA along the cross-section of a functionalised PDMS sample
~ 1mm thick.

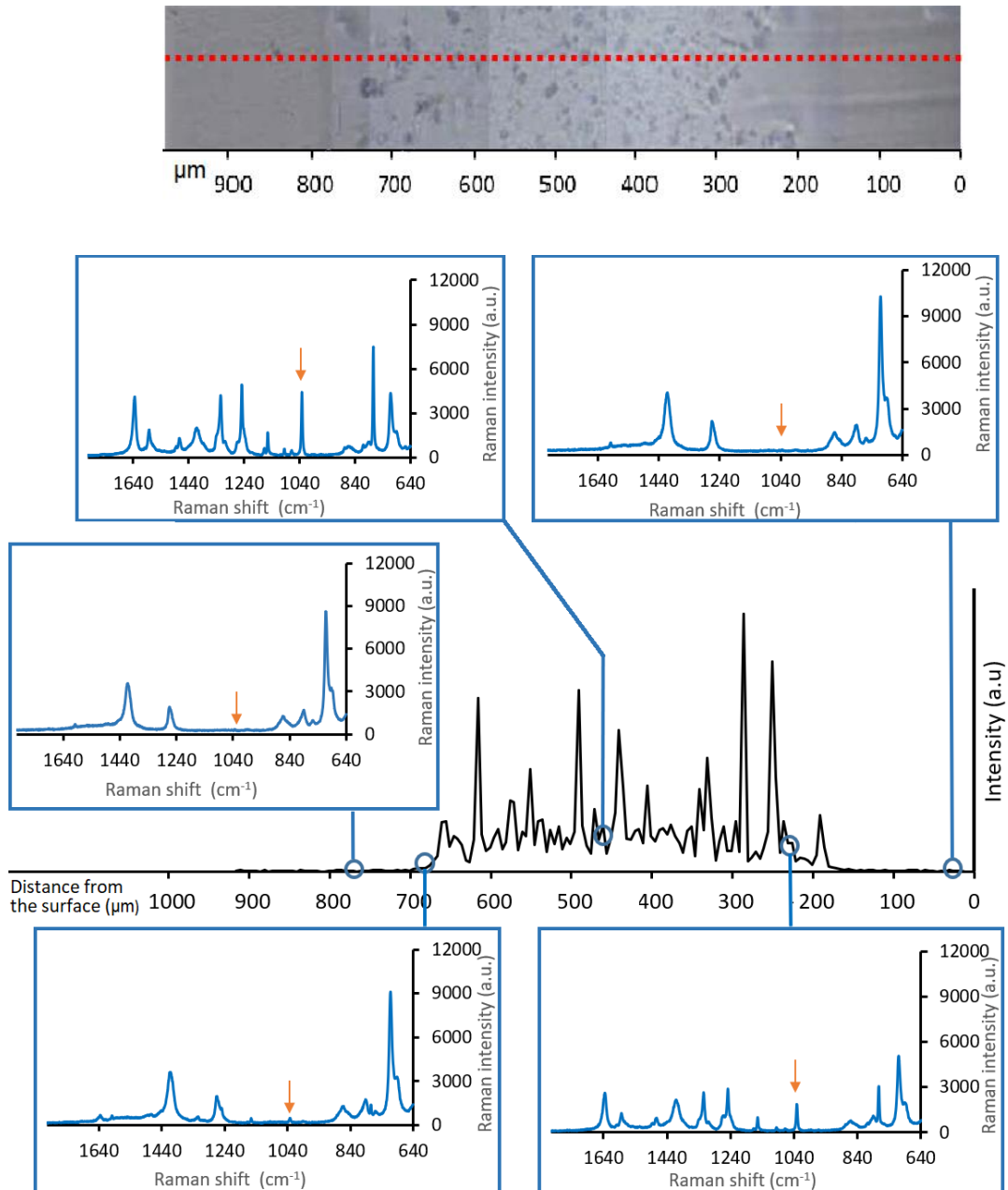


Fig. 2.5 Above: an example of Raman line mapping across the depth of a functionalised PDMS sample, the red dashed line represents the scanning path. **Below:** Raman spectroscopy analysis of the SA presence through the section of a functionalised PDMS sample. Inserts show representative Raman spectra acquired along at a specific distance from the surface of the sample, while the orange arrow identifies the peak that was integrated in order to obtain the concentration profile.

In this work, Raman spectroscopy in combination with Raman line mapping was essential in the characterisation of samples discussed in chapter 3 and in the investigation of the mechanism of biocide release from said samples. All Raman data were collected with the use of a Renishaw inVia confocal Raman microscope (Fig. 2.6). The confocality (<2 micron axial, depending on the objective and laser used) feature of this instrument allowed to decrease the sampling volume from which the spectroscopic signal is collected, leading to an increase in spatial resolution

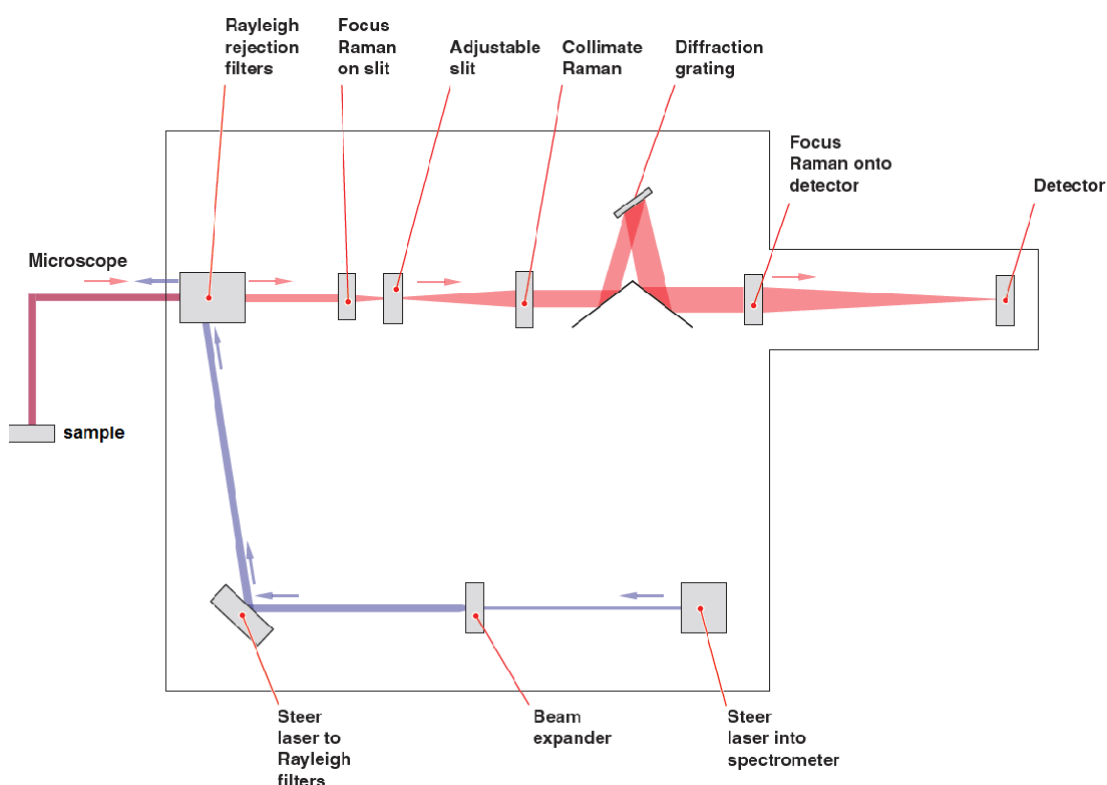


Fig. 2.6 Layout of Renishaw inVia confocal Raman microscope. The instrument mainly consists of a microscope coupled with a laser for sample irradiation; the photons scattered from sample then pass through a Rayleigh reflection filter, and a set of slits to exclude out of focus light. The component wavelengths of the scattered light are split with the use of a diffraction grating and directed to a detector. Image adapted from [10].

2.2.2 Energy Dispersive X-ray Spectroscopy (EDS)

EDS is an analytical technique that allows the analysis of the elemental composition of samples by detecting the energy emitted as result of an electron transition. As schematised in **Fig. 2.7**, the initial excitation, caused by a beam of primary electrons colliding with the atoms comprising the surface of the sample, leads to an emission of an electron from a low energy level, leaving a vacancy soon to be filled by an electron from a shell of higher energy [11, 12, 13].

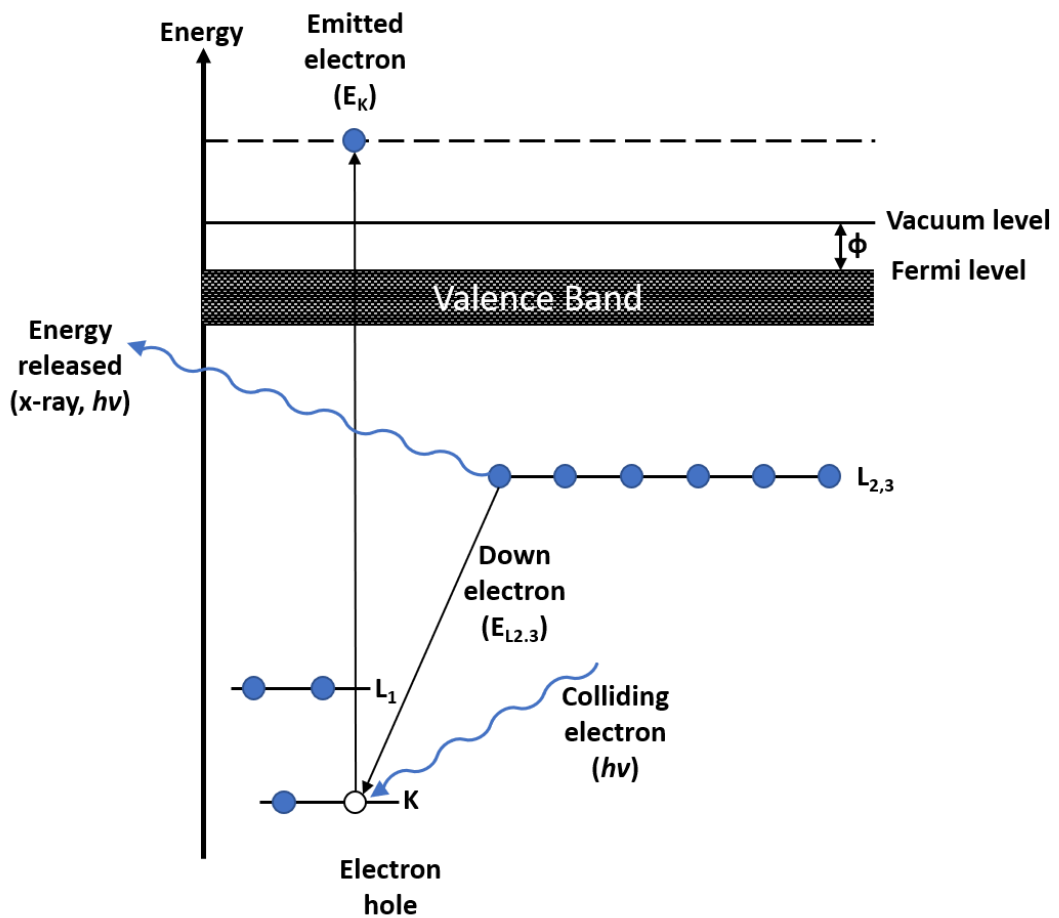


Fig. 2.7 Schematic representation of the EDS process that leads to an energy emission in the form of x-rays.

Referring to **Fig. 2.7**, the energy released in the form of X-ray photons (E_{hv}) is equal to the difference between the binding energy of the down electron ($E_{L2,3}$) and the one of the emitted electron (E_k) (**Eq. 2.4**):

$$E_{hv} = E_{L2,3} - E_K$$

Equation 2.4

The values of E_{hv} (related to ν = frequency of the X-ray emitted) are characteristic to the specific compounds and therefore, once the photons have been detected and analysed by an energy-dispersive spectrometer (EDS), the spectrum of the emitted X-ray wavelengths can be used for elemental and compositional analysis [11, 12, 13].

EDS is a technique often used in conjunction with scanning electron microscopy (SEM), as it utilises the same electron beam used in the acquisition of SEM images [14]; similarly to SEM, its probing depth is dependent on the applied accelerating voltage and the specimen density [15]. In this work, EDS was essential in the chemical analysis at the surface of the materials in chapters 4 and 5, the data was collected using an EDAX Octane T Optima windowless 60 mm² SDD EDS detector coupled to a JEOL 2100F S/TEM. For further experimental details and examples of EDS data please refer to chapter 4.

2.3 Microscopy techniques

2.3.1 Electron Microscopy

Electron microscopy is a technique performed in vacuum conditions and allows to obtain detailed images of biological and abiotic samples [15]. The high resolution of this technique derives from the use of electrons as excitation source, characterised by very short De Broglie wavelengths. Louis De Broglie, introducing the concept of wave–particle duality, proposed that electrons exhibit wave-like behaviour and can be diffracted just like a beam of light or a water wave [16]. The characteristic wavelength λ of an electron is related its momentum p , via Plank’s constant ($h=6.626 \times 10^{-34}$ Js) as show in **Eq. 2.5** [24].

$$\lambda = \frac{h}{p} = \frac{h}{mv}$$

Equation 2.5

The momentum p is the product of the mass of an electron m and its velocity v . As a result, electrons display shorter wavelengths than photons and therefore allow to reach nanometer-scale imaging, according to the Abbe diffraction limit, which states that the smallest distance between two points (resolution), resolvable with an optical technique, can be calculated using **Eq. 2.6** [17].

$$d = \frac{\lambda}{n \sin \alpha}$$

Equation 2.6

Where d is the resolution, n the index of refraction of the medium through which wave passes and α is half the angular aperture of a given objective in radians. Electron microscopy is characterised by a low fixed value of α and by an index of refraction close to 1, being a technique performed in vacuum. The resolution d in electron microscopy is almost solely dependent on the wavelength of the incident

electrons, which can be optimised by adjusting the acceleration voltage, delivering exceptionally high resolution images [17], up to the point that recent advancements in this technique have allowed the imaging of atoms and crystallographic planes [18, 19].

Scanning Electron Microscopy

Scanning electron microscopy (SEM) is a powerful and widely used technique to investigate the morphology and the topography of biological and abiotic samples [15]. In SEM, the electron source, often referred to as electron gun, can be of two types : field emission gun, which funnels electrons out of the atom by generating a strong electric field, and thermionic gun, in which electrons stream away from a heated tungsten filament [20]. The emitted electrons are accelerated by an applied voltage, which can be adjusted and determines λ in **Eq. 2.6**; magnetic lenses then converge them into a focused beam, which hits the sample surface in a fine, precise spot, the size and shape of which determine the resolution of the measurement, potentially reaching the nanoscale [15]. SEM can generate three-dimensional-like images by tuning its depth of focus, an important feature that enables the characterisation of microvolumes [15].

When the electron beam collides with a sample, it causes the emission of a variety of signals: Auger electrons, secondary and backscattered electrons, characteristic x-rays and photons of various energies [15] (**Fig. 2.8**).

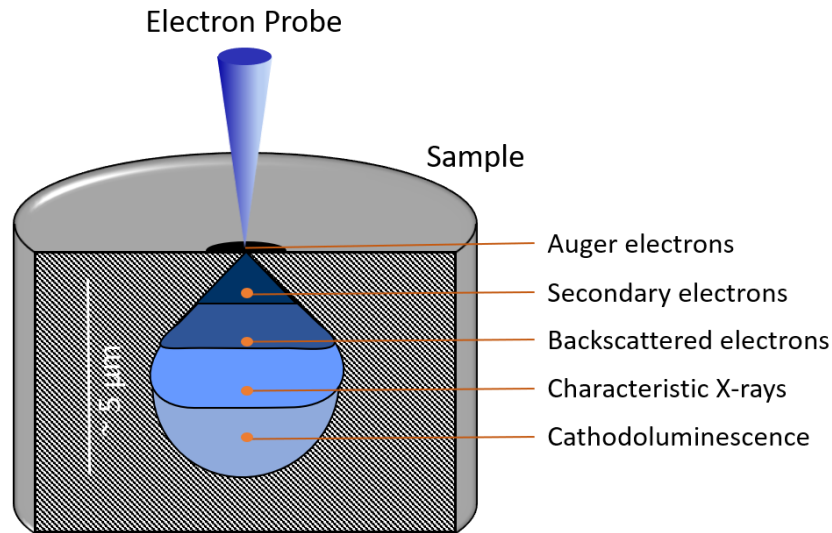


Fig. 2.8 Schematic representation of the interaction volume of a 20kV electron beam with a poly(methyl methacrylate) sample [15], displaying the different classes of radiation emerging at increasing probe depths.

The signal that mainly contributes to the generation of topographic SEM images is the one emerging from the secondary electrons. As shown in **Fig. 2.8**, the emission of secondary electron (SEs) is confined to a very small volume of sample below the beam impact area. SEs are outer shell electrons that are ejected from the sample atoms when they receive sufficient kinetic energy from inelastic scattering collisions [21]. Characterised by energies lower than 50 eV, SEs can propagate through the material for very short distances to escape from the sample surface and reach the secondary electron detector, a feature that makes them particularly fit to investigate the topography of samples [15], they highlight the surface topography by representing the edges as bright areas and the recesses as dark regions [20]. The brightness of a specific pixel in the image is proportional to the number of SEs reaching the detector when the electron beam collides with the corresponding location on the surface; this number is mostly determined by the surface topography: as represented in **Fig. 2.9**, when the beam encounters a sharp peak (**A**), the surface area (and corresponding sample volume) interacting with the electron probe is much greater than when it scans a flat region (**B**), resulting in the emission of a higher number of SEs from the sample. Conversely, when the electron beam

scans the bottom of a deep valley (C), a low number of SEs successfully escapes the sample, resulting in dark region in the forming image [22].

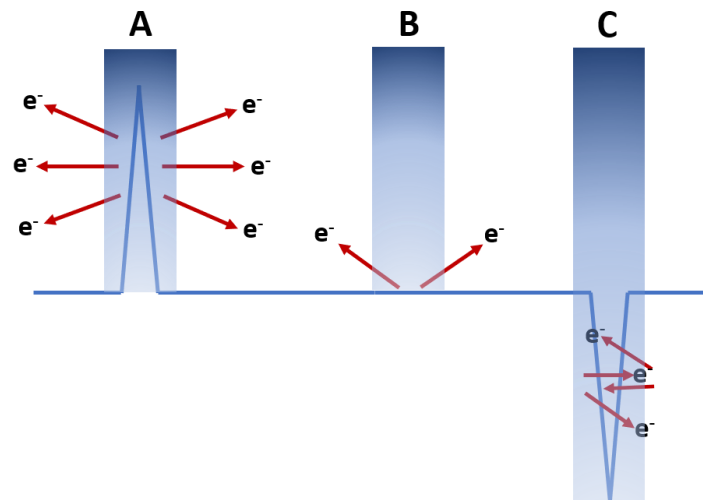


Fig. 2.9 Schematic representation of an electron beam scanning a rough surface, encountering a sharp peak (A) which results in high emission of SEs, a flat area (B) and a deep valley (C), which results in low emission of SEs.

Processing of biological samples for SEM imaging

SEM is commonly used to characterise surface of metallic and inorganic materials, but this technique has proven to be a powerful tool in the investigation of the morphology of biological samples. While light microscopy is limited by the diffraction limit and the wavelength of the photons to a resolution of hundreds of nanometres, SEM allows to resolve features down to 100 Å [21]. The superior resolution of this technique allows to investigate the micro and nano-size features of microorganisms like prokaryotic and eukaryotic cells, with a precision unreachable by traditional light microscopy. The challenges of this technique reside in the preservation of the biological structures during sample preparation and imaging: (a) typically, the images are acquired in high vacuum conditions (10⁻⁵ Torr), causing the dehydration of biological specimens. (b) The collision of the electron beam with the sample can cause the local temperature to increase considerably and leads to sample damage by ionising radiation. (c) The non-

conductive nature of biological samples can cause the accumulation of static charge which quickly leads to the degradation of image quality due to charging effects (**d**) Low-atomic number elements present in biological samples can lower the signal-to-noise ratio of the signal.

In order to overcome these challenges it is necessary to apply a modification protocol to allow the sample to withstand the SEM imaging conditions. An effective preservation of the delicate biological structures of the sample determines the success of the SEM characterisation, allowing us to investigate the morphology of the bacterial membranes, assessing their integrity to evaluate the bactericidal effect of the materials studied in this work; the preservation of the extracellular structures secreted by prokaryotic cells in the adhesion process gives us insights on the strategies adopted by bacteria to attach to substrates with an adverse topography.

The experimental protocol described in the following paragraph is divided in four stages that preserve the original morphology of biological samples and allow the examination of bacterial cells via SEM: Protein fixation (**Fig. 2.10 A**) followed by lipid fixation (**Fig. 2.10 B**), dehydration (**Fig. 2.10 C**) and sputter coating the sample with a conductive metal layer (**Fig. 2.10 D**).

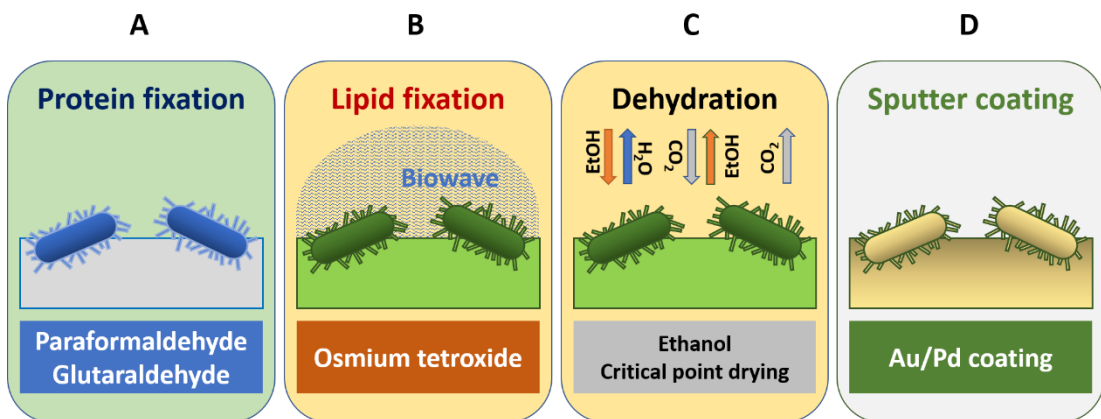


Fig. 2.10 Schematisation of the sample processing protocol for the imaging of bacterial cells via SEM. **A** Fixation of membrane proteins with a solution of paraformaldehyde and glutaraldehyde in water-based buffer. **B** Fixation of bacterial lipid membrane with solutions of osmium tetroxide in water (OsO_4) with the use of Biowave Pro Microwave system. **C** Sample dehydration via gradual dilutions in EtOH followed by CO_2 critical point drying (CPD). **D** Deposition of a 10 nm layer of Au/Pd via sputter coating.

Protein fixation

The term fixation refers to the process that grants irreversible chemical and morphological stability to macromolecules and supramolecular assemblies in biological samples [15]. A mixed solution of paraformaldehyde and glutaraldehyde in phosphate buffer allows to fix proteins in bacterial cells. In physiological conditions ($T = 37\text{ }^{\circ}\text{C}$, $\text{pH} \approx 7.4$), paraformaldehyde polymers are hydrolysed and hydrated leading to the formation of formaldehyde monohydrate, commonly known as methanediol [23] (**Fig. 2.11 A**), this molecule easily penetrates bacterial membranes and its reaction with the amine groups in proteins leads to the formation of a N-methylol group (bond between secondary amine and hydroxymethyl groups). The N-methylol group subsequently condenses to an imine and forms an irreversible methylene bridge with a second amine from nucleophilic addition [23] (**Fig. 2.11 B**).

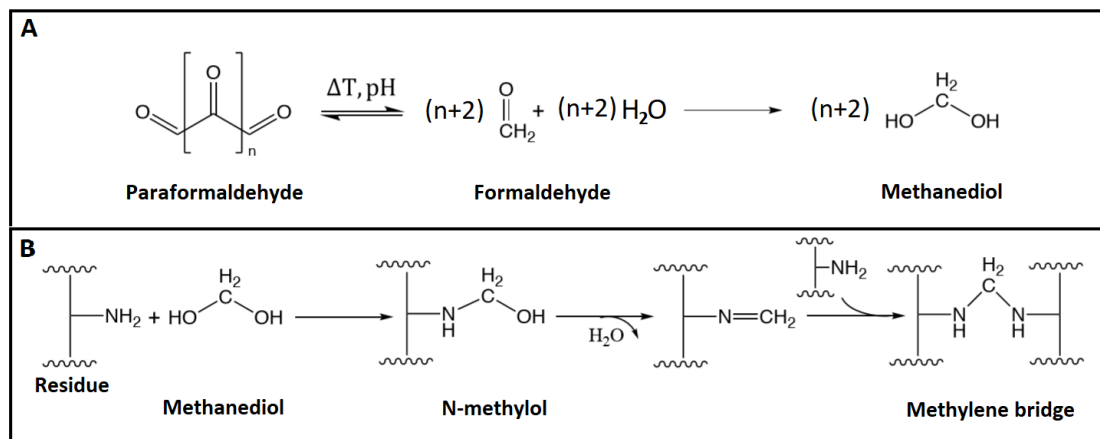


Fig. 2.11 A Reaction of depolymerisation of paraformaldehyde into formaldehyde, followed by hydration of formaldehyde in the presence of water. **B** Reaction of methanediol with amines, forming an imine group via N-methylol intermediate. The imine furtherly reacts with other amines forming a methylene bridge leading to the irreversible crosslinking of protein residues [23]. Image adapted from [24].

As shown in **Fig. 2.12 A**, glutaraldehyde is a molecule characterised by an aldehyde group at both ends, when one reacts with an amino group in a protein, the other can react to form a direct crosslink with another protein, acting as a direct

crosslinker [25] (**Fig. 2.12 B**). Although glutaraldehyde penetrates tissues slowly, it reacts faster with isolated proteins than formaldehyde [26].

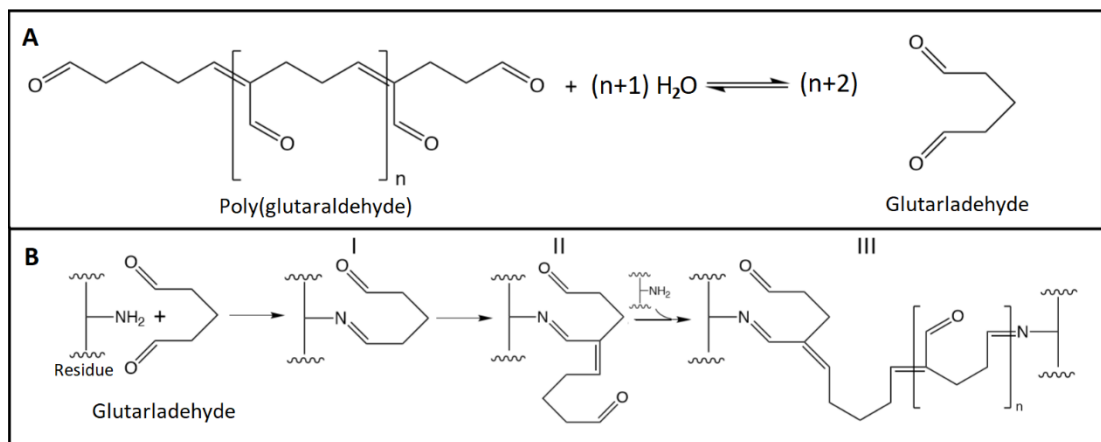


Fig. 2.12 A Depolymerisation of glutaraldehyde. **B** A proposed reaction mechanism of glutaraldehyde (and poly(glutaraldehyde)) crosslinking two protein residues. Image adapted from [24].

As several factors, including diffusion, pH and temperature, affect the fixation speed and the degree of crosslinking of formaldehyde and glutaraldehyde, both are used in combination, ensuring fast and efficient protein fixation. Additionally, glutaraldehyde and formaldehyde forming intra- and inter- molecular crosslinks effectively freezes the conformation of proteins, preserving their secondary and tertiary structure and ceasing every metabolic process within the cell [26].

Lipid fixation

The fixation of lipids is essential in achieving chemical and mechanical stability of biological samples for SEM imaging. Bacterial membranes are in fact mainly constituted by phospholipids, which play a major role in determining the morphology of the cell [27]. The crosslinking of lipids is therefore another effective strategy to preserve the integrity and morphology of bacterial membranes, this was achieved with the use of solution of osmium tetroxide in water. As shown in **Fig. 2.13**, the fixation mechanism of osmium tetroxide relies to the reaction with alkene

bonds in unsaturated lipids, in which Os^{VIII} is reduced to Os^{IV}, crosslinking two unsaturated bonds in its proximity [27, 28]. Osmium tetroxide has also shown to improve fixation of proteins and to enhance contrast of bacterial cells in SEM imaging [15].



Fig. 2.13 Schematisation of osmium tetroxide reacting with unsaturated bonds in lipids. OsO₄ acts as a crosslinker and is reduced in the process. Image adapted from [24].

Dehydration

The imaging of a biological sample in high vacuum conditions requires the removal of the water within, this procedure must be performed carefully and slowly, as rapid dehydration can cause major disruption in the biological structures of the sample [15]. In this work, dehydration of bacteria was performed washing the sample with ethanol solutions at increasing concentration (i.e. from 30% to 100%) in order to extract the water molecules within the cells. The samples were then transferred to the critical point dryer (CPD), which substitutes the dehydrating compound, in this case EtOH, with liquid CO₂, which consequently is slowly heated under pressure, reaching its critical point where the density of the gas phase and liquid one are equal. The purpose of this process is to minimise any damage that could be caused by surface tension effects [15].

Sputter coating

SEM imaging of non-conductive samples can cause accumulation of static electric charges on the specimen surface, leading to charging effects. An established strategy to overcome this issue is to coat the surface of the sample with a thin

metal layer, preventing accumulation of electrons, that can potentially create image artefacts [15]. In addition, the presence of a thin metal coating improves the thermal conductivity at the sample, reducing heat-induced damage. For these reasons, in this work the processing of biological samples for SEM imaging was concluded with a 10 nm layer of gold-palladium alloy coating of the specimen. Although the thin metal layer could conceal some of the small features, it allows high resolution imaging of biological specimens protecting the sample from the damaging effects of the incident electron beam.

In this work, scanning electron microscopy was used to investigate the morphology of bacterial cells adhering to the materials discussed in chapters 3, 4 and 5. The imaging was performed using a JEOL7001F field emission scanning electronic microscope in secondary electron detection mode. The sample set up for SEM imaging included mounting the specimen on aluminium stub holders using double sided carbon tape and applying silver paint between the sample and the holder to ensure the electrical conductivity. The images were acquired at 10 kV acceleration voltage, which showed to be the best compromise between signal to noise ratio and surface charging effect.

2.3.2 Fluorescence Microscopy

Fluorescence is a photophysical phenomenon characteristic of some atoms and molecules, in which, after excitation by incident light ($h\nu$) and decay between singlet electronic states, light of higher wavelengths is emitted. Molecules that display this quality are known as fluorescent probes or fluorophores [29]. A singlet state is defined as the molecular electronic state in which all electron spins are paired ($\uparrow\downarrow$) [30]. After initial excitation, the fluorophore retains its excited state for an interval of time, then regains the ground energy state by emitting light at higher wavelengths (lower energy). This process can be represented in a Jablonski energy diagram (**Fig 2.14**).

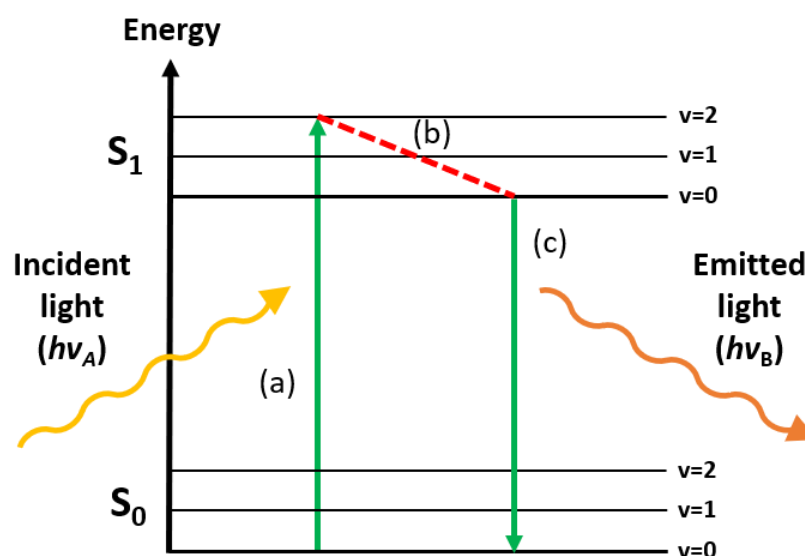


Fig. 2.14 Jablonski diagram schematising the process that leads to emission of fluorescence: (a) the absorption of incident light of energy $h\nu_A$ causes excitation of a fluorophore from the ground state S_0 to the excited singlet state S_1 , (b) non-radioactive relaxation (red dashed line) brings the molecule to the lowest vibrational state of S_1 , (c) the molecule relaxes back to S_0 by emitting of light of energy $h\nu_B$ ($\nu_A > \nu_B$).

The emission of fluorescence can be associated with multiple relaxation processes, the most common one is known as internal conversion and refers to the molecule relaxing to the lowest vibrational energy state ($v=0$) of the excited singlet (S_1). This is caused by the wavefunctions of the excited vibrational states ($v=0, 1, 2$) being very close in terms of energy, naturally causing non-radiative transition to the lowest vibrational state of the excited singlet. For this reason the wavelength of the exciting photons does not have an effect on the shapes of emission spectra [31]. Following this process, the excited fluorophore relaxes from the lowest vibrational excited singlet ($v=0; S_1$) to its ground state (S_0) by emission of fluorescence, releasing a photon of energy $h\nu_B$. Importantly, the fluorescence emission occurs at higher wavelengths compared to the excitation source. As mentioned in the paragraph on Raman spectroscopy, the shift in maximum wavelengths between the excitation light and the emitted one is known as the Stokes shift. This shift can range from a few nanometres (**Fig. 2.15**) to several hundreds, depending on the chemical structure of the fluorophore and environmental conditions. Although the Stokes shift is mainly caused by the fast internal conversion, other factors that

contribute to the energy loss include emission to higher vibrational levels of S_0 and solvent orientation effects [31].

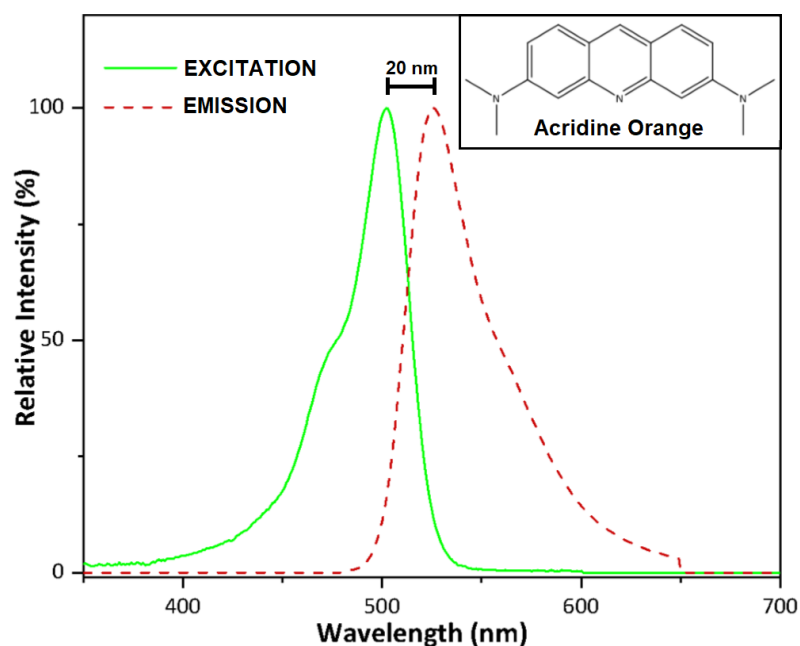


Fig. 2.15 Excitation (green, solid) and emission (red, dashed) spectra of Acridine Orange. Insert shows the molecular structure of the fluorophore. Image adapted from [32].

The importance of the Stokes shift in fluorescence sensing is related to peaks resolving and resolution: if excitation and emission peaks are well separated (wide Stokes shift), the frequency of the exciting light can be tuned to match the one of the maximum excitation of the fluorophore, obtaining the maximum emission. However, if the Stokes shift is too narrow, causing the two bands to overlap, elastic scattering of the exciting light can interfere with the detection of the emission peak. This issue requires the adjustment of the exciting light wavelength, resulting in a less intense fluorescent emission [29]. Fluorophores with wide Stokes shifts are therefore preferred for most applications.

Other properties must be taken into account when selecting the proper fluorophore for fluorescence spectroscopy or imaging: some dyes substantially increase their fluorescence quantum yield (ratio between photons emitted through fluorescence and photons absorbed from excitation) after binding to nucleic acids [29]. Other

fluorophores can undergo quenching (a process that decreases the fluorescence intensity of a given substance) upon interaction with specific chemical species in the environment, such as iodide ions and acrylamide, decreasing the emitted fluorescence signal [29].

The phenomenon known as fluorescence resonance energy transfer (FRET) can occur when more than one type of fluorophore is present simultaneously in a sample. FRET involves a donor fluorophore, initially in the excited state, transferring energy to an acceptor fluorophore via non-radiative dipole-dipole coupling. The acceptor molecule subsequently emits fluorescence at a higher wavelength than the one that would have been emitted by the donor [32]. It is fundamental to consider these limitations when interpreting fluorescence images, as well as to using the appropriate combination of fluorophores to avoid any possible artefacts.

Confocal Laser Scanning Microscopy

Confocal fluorescence microscopy (CFM) was optimised to partially overcome the biggest challenges in light microscopy, associated with low contrast and poor resolution. The capability of this technique to produce images free of out-of-focus light is related to the confocality, which refers to the optical arrangement where both illumination and detection spots are focused to the same focal plane, with the use of a pinhole. The pinhole is a small diaphragm aperture located after the light source and at the image plane, just before the detector [31]. Adjusting the aperture at the light source varies the size and the shape of the incident light, while the pinhole located before the detector blocks the out of focus light coming from above and below the focal plane, therefore allowing only light at the focal point to be detected, drastically increasing the contrast and resolution of the images, delivering highly detailed images [31]. Another feature of CFM, essential in delivering high resolution imaging, is the association of the specific wavelengths of the illumination sources (lasers), with the excitation wavelengths of the fluorophores, allowing for high contrast and detail in the imaging of a wide range of fluorescent specimens.

Fig. 2.16 shows a schematic representation of a confocal laser scanning microscope (CLSM), an instrument based on this type of set-up. In this configuration, the illumination source consists in a laser light that reaches the illumination pinhole, which alters the size and shape of the laser spot, narrowing the beam. The laser light then reflects on a dichromatic mirror and gets focused by the objective lens to finally collide with the sample. The fluorescent light is emitted from the sample, back through the objective lens, reflected by the dichromatic mirror and is focused at the detector pinhole, which excludes out-of-focus light. A photomultiplier then detects the light emitted from the focal plane and converts the photons into an electric signal that can be interpreted by the computer [33].

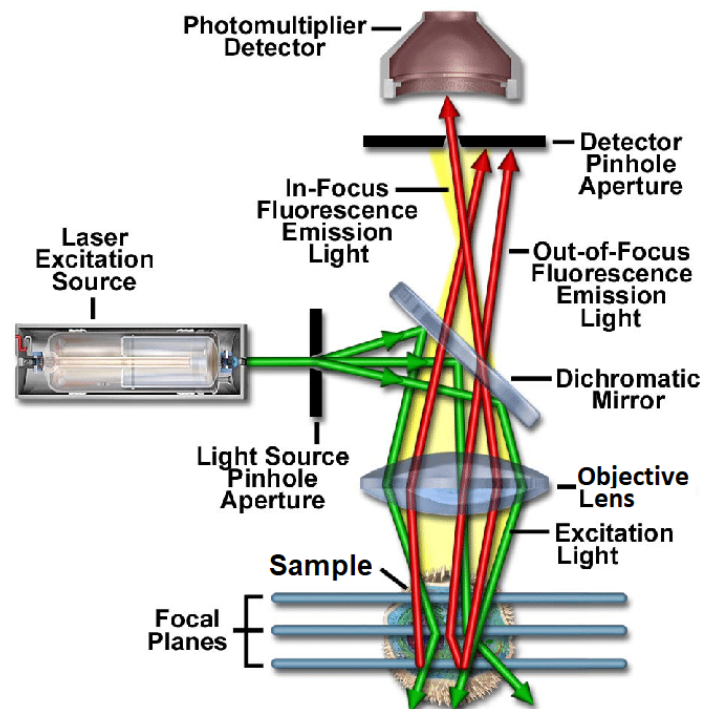


Fig. 2.16 Schematic representation of an upright confocal laser scanning microscope. Image adapted from [34].

CLSM can be optimised to obtain space and time resolved information on complex biological processes, such as protein expression or the differentiation of live and dead bacteria. In fluorescence microscopy, an image is obtained by collecting the signal emitted from the fluorophores naturally present in the sample or introduced as labelling stains. The combination of the nucleic acid stains SYTO 9 and propidium

iodide (PI) (**Fig. 2.17**) enables to assess the viability of bacteria due to their distinct spectral characteristic and their differences in the ability to penetrate bacterial membranes: SYTO 9 typically penetrates all bacterial cells in a population, with both damaged and intact membranes while Propidium Iodide (PI) is only able to penetrate compromised cell membranes. When both fluorophores are present in a cell (i.e. in a bacterium with damaged membrane), PI displaces SYTO 9 from the nucleic acid chains as it strongly intercalates between bases in the DNA chain with little or no sequence preference [35]. Their spectral characteristics enable to easily differentiate between the two by selecting lasers with appropriate characteristic wavelengths: SYTO 9 exhibits absorbance/emission maxima at around 480/500 nm (**Fig. 2. 17 A**), while these values are around 535/620 nm in the case of PI (**Fig. 2. 17 B**), whereas the background remains virtually nonfluorescent [35]. Environmental conditions and the bacterial species in the specimen can affect the optimum SYTO 9 and PI ratio necessary to obtain high definition imaging.

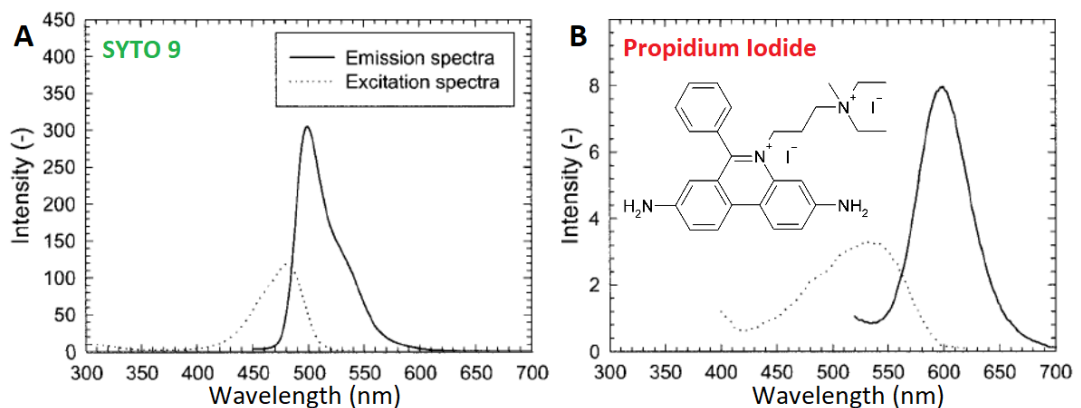


Fig. 2.17 Absorbance and emission spectra of SYTO 9 (**A**) and propidium iodide (**B**). The insert in (**B**) displays the molecular structure of PI, while the molecular structure of SYTO 9 has not been disclosed by Thermofisher™ [35]. Image adapted from [35].

Observing the spectra in **Fig. 2.17**, we can notice that the emission spectrum for SYTO 9 and excitation spectrum of PI overlap. It is important therefore to note that FRET may occur in specific conditions [35].

The Live/dead BacLight bacterial viability kit, which comprises of the SYTO 9 and PI dyes, has found wide use in the assessment of bacterial viability in solution and on

surfaces, showing good correlation with traditional plate counting assays. It is important however to bear in mind that the distinction between live and dead cells determined by Live/dead BacLight bacterial viability assay is based on the permeability of bacterial membranes, not on the ability to reproduce; this may lead to the mislabelling of cells with a damaged membrane capable of undergoing division, while bacteria with intact membranes but unable to reproduce may be categorised as live [35].

SYTO 9 and PI dyes can be used with a wide range of planktonic and sessile bacterial organisms. **Fig. 2.18** shows a representative CLSM image of the Live/dead assay performed on *Escherichia coli* cells attached on a flat Si surface. The image shows live bacteria labelled green, whereas dead bacteria are displayed in red.

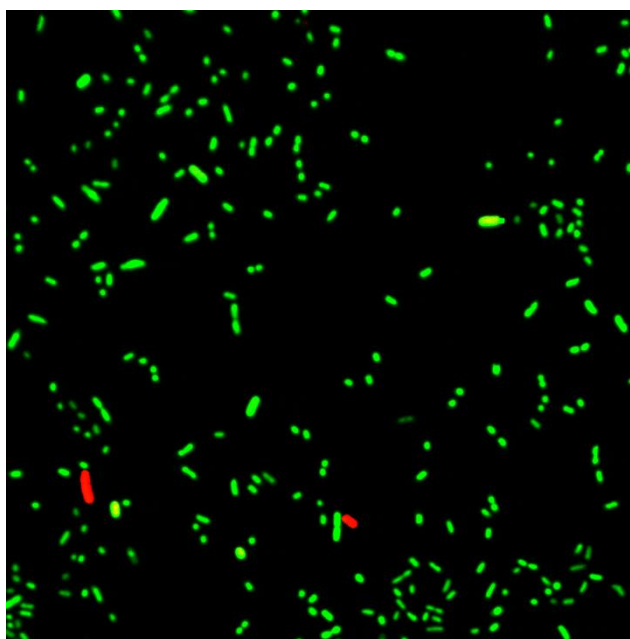


Fig. 2.18 Representative merged CLSM image of *E. coli* cells on flay Si. Green cells are stained with SYTO 9 and while cells with a damaged membrane are stained with propidium iodide and are displayed as red. Image size: 71.8 x 71.8 μm^2 .

CLSM was used in this work in conjunction with SYTO 9 and PI stains to perform viability assay on the prokaryotic cells adhering to the investigated materials. The data collected was essential in the determination of the biocidal effect of the substrates. All images were collected using a confocal upright Zeiss LSM 880

Multiphoton microscope with excitation wavelengths of 488 nm for SYTO 9 and 561 nm for PI.

Confocal Fluorescence Microscopy image processing

The determination of the fraction of live or dead cells in a bacterial population, using propidium iodide and SYTO 9 staining, requires an image processing software package, such as Fiji. Fiji is software based on ImageJ, with a large number of built-in plugins and algorithms, that can be optimised and automated (with the use of a macro function) to process large sets of data [36]. The analysis of the green and red channels allows to calculate the number (N) of green and red stained cells in the image, keeping in mind that all bacteria will be stained green by SYTO 9, while only the ones with a damaged membrane, which we assume dead for the purpose of the analysis, will be stained red by PI. Therefore, the fraction of live or dead cells in the population is calculated with the use of **Eq. 2.7** or **Eq. 2.8**:

$$Live\ Ratio = \frac{N_{Green\ only}}{N_{Green\ only} + N_{Red}}$$

Equation 2.7

$$Dead\ Ratio = \frac{N_{Red}}{N_{Green\ only} + N_{Red}}$$

Equation 2.8

Where $N_{Green\ only}$ refers to the number of cells on the green channel that don't appear also on the red one. The macro in used in Fiji to calculate the fraction of live or dead cells was adapted by the Centre for Cell Imaging at the University of Liverpool and further modified by Dr. Ioritz Sorzabal-Bellido; the first step consists in the creation of two images from the two channels (red and green) and in the removal of the background from each of them (**Fig. 2.19 A**). A *Threshold* is then applied, an algorithm used to classify the pixels forming an image into two or more

classes, typically labelling them as "foreground" (the features of interest) and "background" [37]. As the contrast between the features of interest and the background depends on the specimen, on environmental and protocol-related factors, Fiji offers a selection of thresholds and the user is required to use a heuristic approach to apply the most appropriate one to each sample. The following step of the macro is the segmentation and is achieved using *Watershed*, a feature that separates two connected objects (i.e. two adjacent bacteria) by creating *Watershed* lines (**Fig. 2.19 B**) [37]. Following segmentation, the macro creates a binary image (mask) with only live cells (**Fig. 2.19 C**) by subtracting the generated red mask from the green one. The *Analyse Particles* function provides the count of the green only ($N_{Green\ only}$) and red (N_{Red}) cells with areas ranging from $0.3\ \mu\text{m}^2$ to $5\ \mu\text{m}^2$. The values obtained can be implemented in **Eq. 2.7** and **Eq. 2.8** to obtain the fraction of live or dead cells in the population.

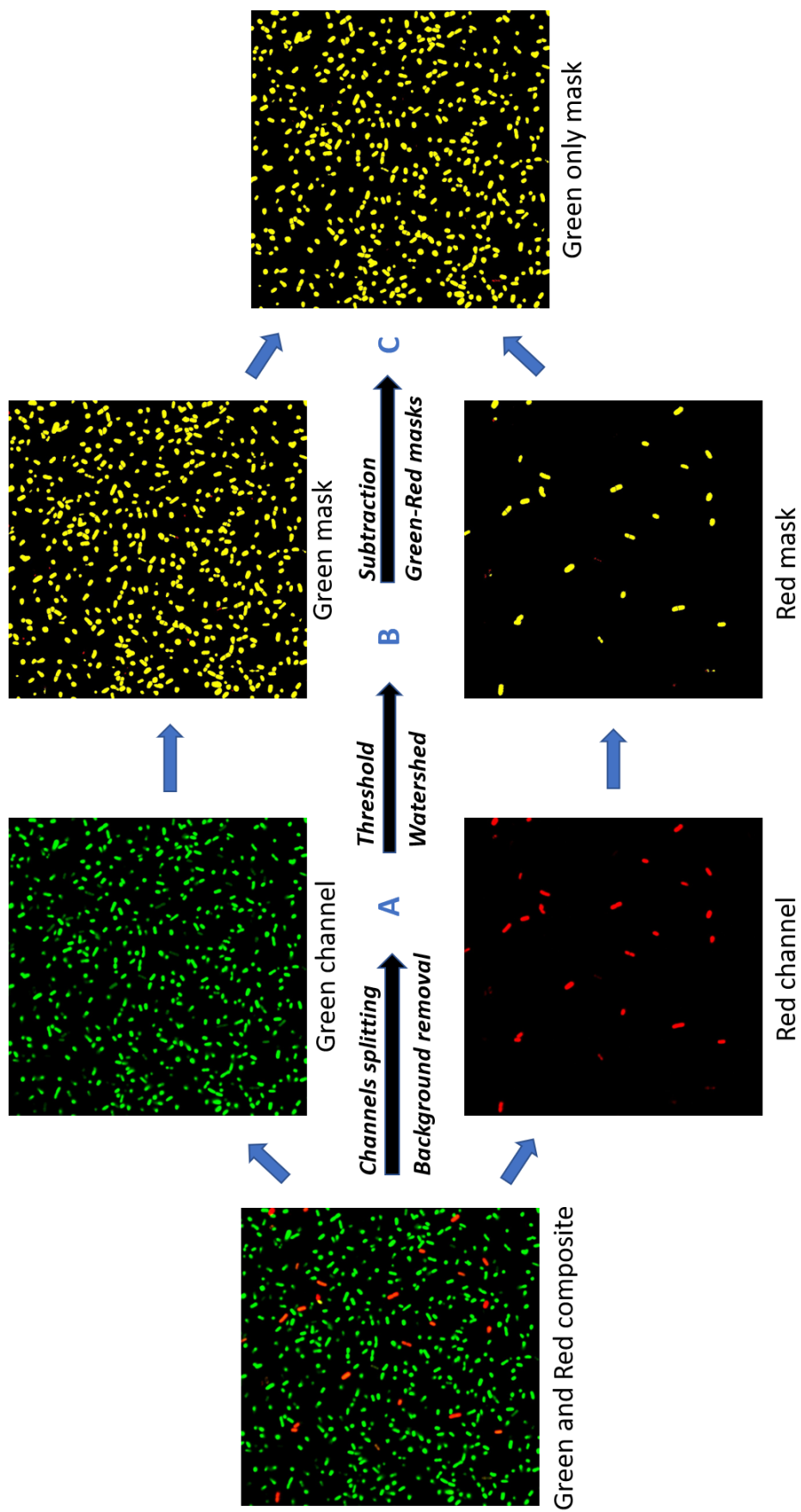


Fig. 2.19 Overview of the image processing using Fiji macro of CFM images stained with Live/Dead viability kit. Example shown is a CLSM image of *E. coli* cells grown for 24 hours on a flat alumina surface. **A:** The composite image is split into green and red channels and the backgrounds are removed. **B** The images undergo segmentation with the application of the *Threshold* and *Watershed* functions. **C** Green only mask is obtained by subtracting the red mask (dead cells) from the green mask (all cells). Images size is 71.8x71.8 μm^2 .

2.3.3 Atomic Force Microscopy (AFM)

Since its invention in 1986, the atomic force microscope has evolved to become one of the most important instruments for the imaging and characterisation of surfaces; nowadays it's employed in various research fields including physics, chemistry, biology and engineering [38, 39]. Its remarkable versatility allows to obtain three-dimensional renditions of the surface topography, structural details of biological samples [40], as well as quantifiable measurements of the attractive and repulsive forces between atoms at the tip and the sample. The attractive forces include van der Waals interactions, electrostatic forces and chemical forces, while the repulsive forces between the tip and the sample can be classified as hard sphere repulsion, Pauli-exclusion interaction and electron–electron Coulomb interaction [38]. These repulsive forces are generally very short-ranged (0.1- 100nm) with an exponential decay in intensity as the surface-tip distance increases [38].

The AFM tip (**Fig 2.20**), at the probing end of a cantilever, scans the sample, measuring the topographic height of the surface, and acts as a force sensor when pulled from the substrate.

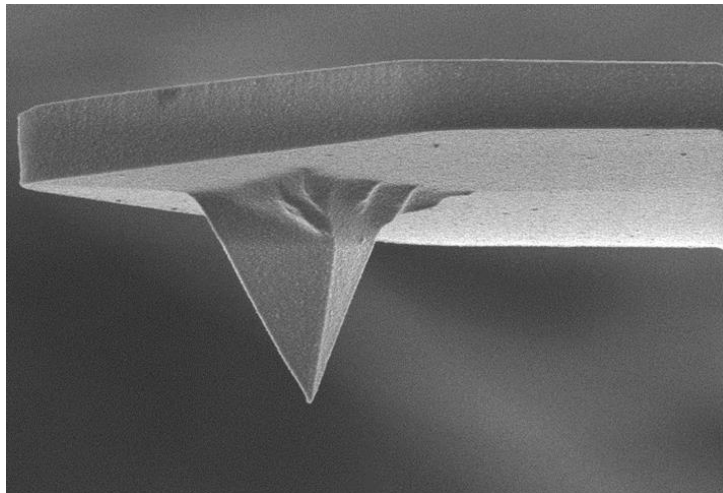


Fig. 2.20 SEM image of a Bruker™ diamond coated AFM tip, specific for applications that require increased wear resistance and a conductive tip. Tip height: 10 - 15 μm . Tip radius: 10 nm. Image adapted from [41].

As schematised in **Fig 2.21**, as the tip scans across the surface, the deflections of the cantilever in response to surface features are detected by a laser aligned with the cantilever tip. The laser beam is reflected onto a position-sensitive photodiode detector (PSPD), the beam displacements from the centre of the PSPD reach a PI controller in a feedback loop that adjusts the cantilever's vibration via a piezo Z-actuator [39]. The topographic data can be provided by the signal reaching the PI controller [42] or through the piezo Z-actuator motion [43]. The vibration of the cantilever is characterised by its amplitude, phase and frequency, the variation of these three parameters, due to interaction or repulsions forces with the sample, can be measured and the force can be extrapolated a theoretical formalism from the registered signals [43].

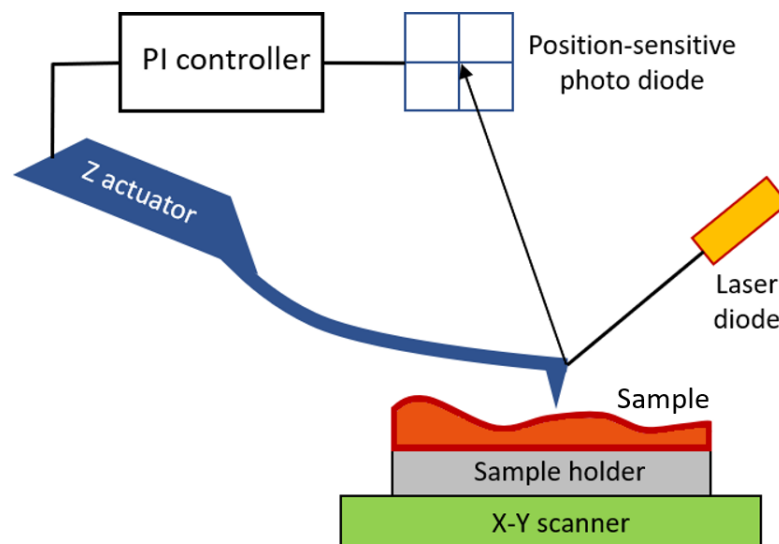


Fig. 2.21. Schematisation of the working mode of an AFM: a laser beam from a laser diode is focused on the end of the cantilever, the reflected beam is aligned at the centre of a PSPD. The signal of the PSPD changes according to the deflections of the cantilever and reaches the PI controller to control the cantilever's vibration and distance from the sample via the piezo Z-actuator.

The two most common modes of operation to investigate the topography of a sample via AFM are static and dynamic mode. The operational mode is selected according to the characteristics of the substrate to scan and the type of information that needs to be obtained from the experiment.

The **static mode**, or contact mode, is the most common and simple mode to operate an AFM. In this configuration the tip is dragged over the substrate and the cantilever maintains its deflection (the feedback parameter in this mode) at a constant rate, set by the user. The mechanical contact force can be estimated according to Hooke's law from the detected variations of the cantilever bending, the displacement being the controllable parameter ($F = kx$, with k = spring constant of the cantilever and x = displacement from the equilibrium position). In the static mode, both tip and sample at risk of being damaged, and the use of low stiffness cantilevers is advised.

In **dynamic mode**, also referred to as "tapping mode", the scanning probe "taps" along the surface at a frequency close to the resonance frequency of the cantilever, which changes due to the interaction or repulsion forces between tip and the surface [44]. The gentle interaction with the surface relative to the static mode allows to preserve the sharpness of the tip and the integrity of the sample [43]. In the most common dynamic imaging mode, referred to as amplitude modulation mode (AM-AFM), the oscillation amplitude functions as the feedback parameter. The user sets the oscillation amplitude, selecting a larger amplitude to scan stiff, robust materials and a smaller amplitude for softer ones [43]. The instrument's feedback loop on the z piezo maintains the cantilever's amplitude of oscillation constant throughout the sample's imaging.

In the past 20 years, the AFM has undergone constant upgrades, increasing its sensitivity, resolution and granting it new actuating features. These performance optimisations have found important applications in microbiology, allowing new techniques to emerge, such as single-molecule force spectroscopy (SMFS), single-cell force spectroscopy (SCFS), and chemical force microscopy (CFM) [40]. Remarkable advances allowed to use AFM to manipulate membrane proteins, to map microorganisms surface properties and receptor sites, up to quantify the forces involved of bacterial adhesion [40, 45, 46, 47]. To simplify, this technique involves attaching to the AFM tip a single microsphere (**Fig. 2.22**), coated with an adhesive compound (i.e. polydopamine), once the probe is brought into contact with an isolated bacterium and proper attachment is achieved, the surface-bacterium

adhesion force can be measured as a function of the distance by pulling the probe away from the sample [40].

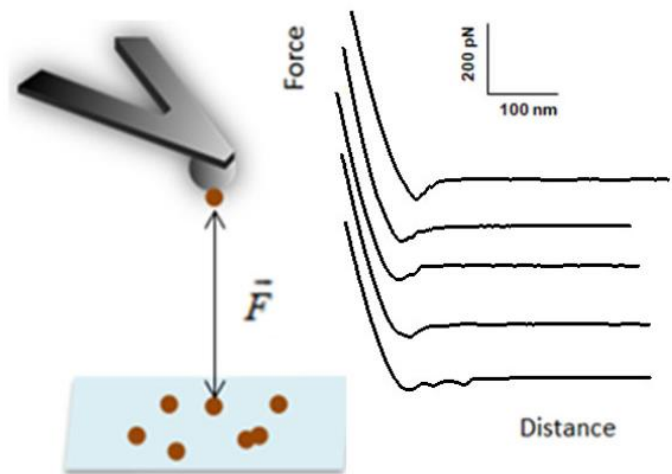


Fig. 2.22 Schematisation of the experimental set-up required to measure bacterial adhesion forces (left) and example of the force–extension curves obtained (right). Image adapted from [48]

In this work, AFM was used in Chapter 3 and was essential to evaluate the effect of the biocide incorporation (and its subsequent release) on the sample's surface topography. For more insights on the processing of AFM data, including surface roughness analysis, please refer to Chapter 3.

2.4 Physical characterisation techniques

2.4.1 Contact Angle

Contact angle measurements investigate the angle formed at the intersection of the liquid-solid interface and the liquid-vapour interface by a drop of liquid resting on a substrate [49]. This value is strictly related to the surface tension of the liquid and the surface energy of the solid sample. Surface tension is defined as the work necessary to increase the area of a surface isothermally and reversibly by unit amount, is commonly expressed as the surface energy per unit area or alternatively as the force per unit length (e.g. the surface tension of water is 72 dynes per cm) [50]. Surface tension and the interactions of the liquid with the substrate determine the shape of the sessile droplet: the molecules of a liquid are subject to attraction forces on the molecules in the bulk of the liquid, the sum of which averages zero (**Fig 2.23**) [50]. On a surface molecule though, the net force (also known as cohesion force) is a non-zero quantity in the direction of the bulk, a force that causes liquid droplets to adopt a spherical shape, which guarantees the lowest possible free energy by minimising the surface area. The energy necessary to counteract this force and to increase the surface area is called surface energy, which coincides with

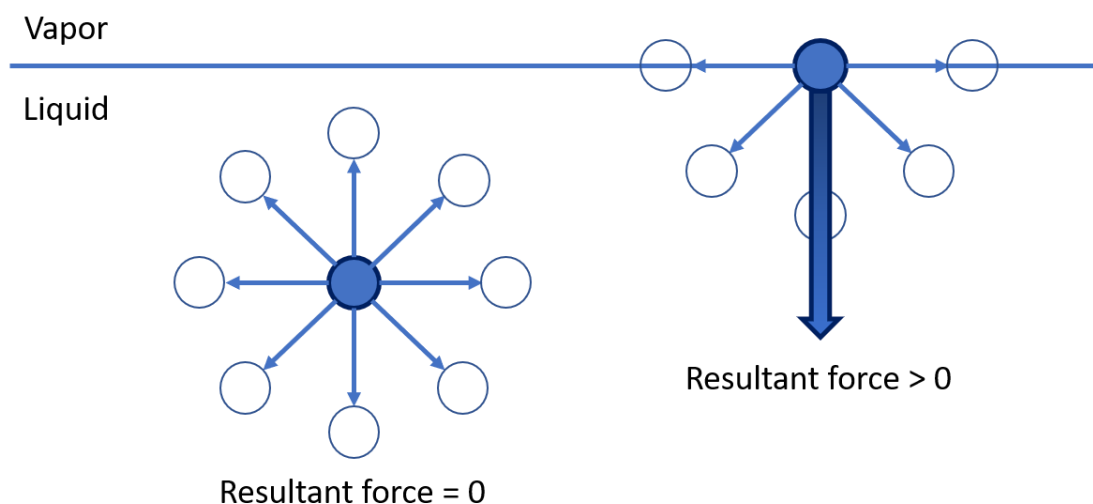


Fig. 2.23 Liquid – vapor interface and balance of forces on molecules of liquids.

the surface tension in the case of a liquid while the same is not true for a solid surface [50].

When a liquid drop rests on a horizontal solid surface, the equilibrium of forces at the intersection of the liquid-solid interface and the liquid-vapour interface dictates the shape of the droplet and consequently the contact angle, following Young's equation (Eq. 2.9):

$$\gamma_{sv} - \gamma_{sl} = \gamma_{lv} \cos\theta$$

Equation 2.9

where γ_{sv} , γ_{sl} and γ_{lv} are respectively the tensions of the solid-vapor, solid-liquid, and liquid-vapor interfaces (Fig. 2.24) and θ is the contact angle for a liquid drop on

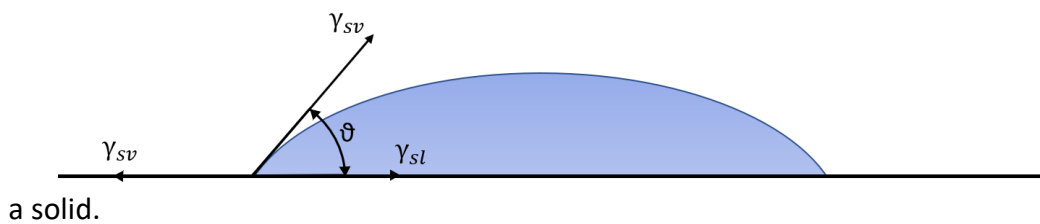


Fig. 2.24 Equilibrium of a liquid drop on a horizontal solid surface

In this work, contact angle measurements were used in the investigation of the wettability of surfaces: as shown in Fig. 2.25, contact angles lower than 90° indicate a substrate susceptible to wetting (hydrophilic), while contact angles higher than 90° suggest the surface is less susceptible to wetting (hydrophobic) [51].

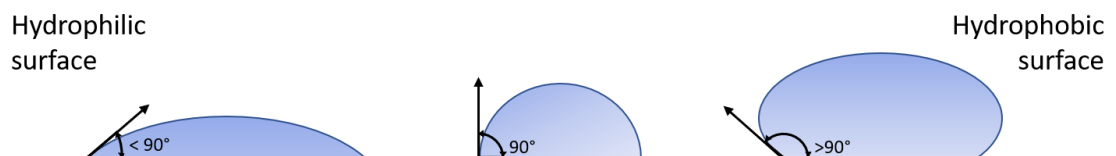


Fig. 2.25 Illustration of contact angles formed by a liquid drop on solid surfaces with different degrees of wettability.

Contact angle measurements of a series of test liquids on a solid flat surface can be used to calculate the different surface energy components, assuming that the relationship between γ_{sl} , the solid γ_s in vacuum and γ_{lv} is known [52]. The value of γ_{sl} can be obtained via the Good and Girifalco equations (**Eq. 2.10**, **Eq. 2.11**) [53, 54]:

$$\gamma_{sl} = \gamma_s + \gamma_{lv} - 2\phi\sqrt{\gamma_s\gamma_{lv}}$$

Equation 2.10

$$\gamma_s - \gamma_{sv} = \pi_e$$

Equation 2.11

where ϕ is referred to as the Good–Girifalco interaction parameter and π_e as the spreading pressure. The spreading pressure value is commonly neglectable for low energy, nonpolar solids [52]; this assumption allows to combine Young’s and Good and Girifalco equations, obtaining **Eq. 2.12**.

$$\gamma_{lv}(1 + \cos\theta) = 2\phi\sqrt{\gamma_s\gamma_{lv}}$$

Equation 2.12

The issue with **Eq. 2.10** and **Eq. 2.12** is that the value of ϕ is generally unknown, over past decades various theoretical models have been proposed to overcome the problem, each with their own advantages or disadvantage [52]; the most commonly used are the Owens–Wendt–Rabel–Kaelble (*OWRK*) method (**Eq. 2.13**) [55].

$$\gamma_{lv}(1 + \cos\theta) = 2\sqrt{\gamma_s^d\gamma_{lv}^d} + 2\sqrt{\gamma_s^p\gamma_{lv}^p}$$

Equation 2.13

Where γ^d refers to the dispersion component of the surface energy and γ^p to the polar one.

Souheng Wu, in 1973 [56] proposed the model shown in **Eq. 2.14**, in which the interactions between the solid, liquid and vapor phase are interpreted as the harmonic mean of a disperse part γ^d and a polar part γ^p of the surface tension.

$$\gamma_{lv}(1 + \cos\vartheta) = 4(\gamma_s^d \gamma_{lv}^d)/(\gamma_s^d + \gamma_{lv}^d) + 4(\gamma_s^p \gamma_{lv}^p)/(\gamma_s^p + \gamma_{lv}^p)$$

Equation 2.14

In this case the determination of the free energy of the surface requires at least two liquids in which the disperse and polar parts of the surface tension are known, with at least one of the two with a polar part > 0 .

In 1992, Good *et al.* [57], proposed the model shown in **Eq. 2.15**:

$$\gamma_{lv}(1 + \cos\vartheta) = 2\sqrt{(\gamma_s^{LW} \gamma_{lv}^{LW})} + 2\sqrt{(\gamma_s^+ \gamma_{lv}^-)} + 2\sqrt{(\gamma_s^- \gamma_{lv}^+)}$$

Equation 2.15

Which takes into account the Lifshitz-Van der Waals (γ^{LW}), acidic (γ^+) and basic (γ^-) components of the surface tension. All these methods imply π_e to be neglectable and each of them is more suitable for specific types of surfaces, depending on which components of their surface energy are more prominent [52].

The effect of surface roughness on contact angle measurements

Surface roughness significantly influences the wettability of flat surfaces, affecting the hysteresis in contact angle measurements [58]. The extent of this contribution is not obvious and was first quantified by Robert N. Wenzel in 1949 [59] in **Eq. 2.16**, where ϑ_A is the apparent contact angle, ϑ is the contact angle corresponding to an ideal smooth surface, while r is the ratio of the rough surface area to the projected ideal smooth surface, proportional to the extension of surface area caused by the roughness [59, 60].

$$\cos\vartheta_A = r \times \cos\vartheta$$

Equation 2.16

The validity of Wenzel's modification of the Young Equation has been questioned over the years [58, 61], Bartell and Shepard [62] showed in 1953 that the drop shape and resulting contact angle measurement are determined at the solid-liquid-air interface and the increase in the surface area beneath the liquid caused by roughness does not alter the drop shape. An attempt to theorise the wettability of a heterogeneous surface has been made by Cassie and Baxter [63]. Their model, shown in **Eq. 2.17**, describes the apparent contact angle as the sum, for each component of the substrate, of the product of ϕ , referred to as the fraction of interface length, and the cosine of the contact angle ϑ .

$$\cos\vartheta_A = \phi_1 \cos\vartheta_1 + \phi_2 \cos\vartheta_2$$

Equation 2.17

In the specific case of a porous surface in which the pores create gas pockets ($\vartheta_2 = 180^\circ$), **Eq. 2.17** can be simplified to [60]:

$$\cos\vartheta_A = \phi_{LS} [\cos\vartheta + 1] - 1$$

Equation 2.18

where ϕ_{LS} is the fraction of the liquid–solid interface (making the fraction of the liquid–air interface equal to $1-\phi_{LS}$). For practical applications, the contact angle of a heterogeneous and complex rough surface is sometimes approximated combining **Eq. 2.17** and **Eq. 2.18**, obtaining **Eq. 2.19** [60]:

$$\cos\vartheta_A = r \times \sum \phi_n \cos\vartheta_n$$

Equation 2.19

Contact angles can be defined as static or dynamic depending on whether the liquid-solid-air intercept is stationary or in movement during the measurement [64]. The contact angle is referred to as *advancing* when the measurement is taken as the droplet expands, it investigates the effect of a freshly wetted surface on the fluid mechanics. On the other hand, the effect of the surface's de-wetting can be studied by continuously removing liquid from the measured droplet, the resulting dynamic contact angle is referred to as *receding* [65]. During dynamic measurements, the contact angle value is limited between the static advancing contact angle and the static receding contact angle; between these two values, increasing and decreasing the amount of liquid in the drop, rate-dependent hysteretic behaviour is observed [66]. These data provide additional information on the properties of the surface and the liquid: contact angle *hysteresis* reflects the chemical and topographical heterogeneity of the substrate, the surface forces and the alterations caused by the interaction with the solvent, as in dynamic conditions the contact angle is not only influenced by surface characteristics, but also the physical properties of fluid flow [66, 67].

2.4.2 Ultraviolet-visible-near infrared (UV-Vis-NIR) Spectroscopy

UV-Vis-NIR spectroscopy is an extinction spectroscopic technique, which relies on the measurement of the light absorbed in the 200 to 1100 nm wavelength range when transmitted across a sample or reflected from it. UV-Vis-NIR measurements result in a spectrum displaying the values of absorbance of light at different wavelengths, as shown in **Fig. 2.26**, which displays the UV-Vis spectrum of Salicylic Acid in aqueous medium, with maximum absorbance at 299 nm.

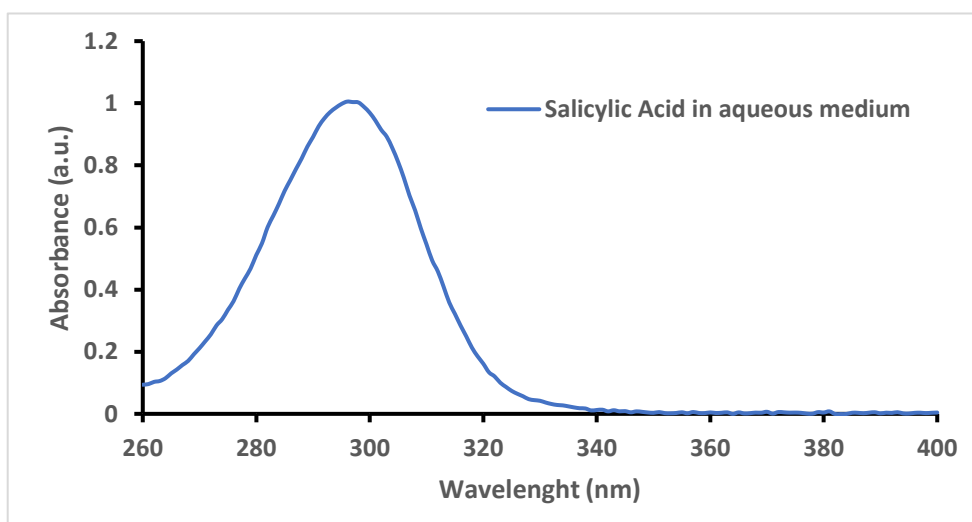


Fig. 2.26 UV-Vis spectrum of Salicylic Acid in aqueous medium.

Transmittance (**T**) is defined as the ratio of the intensity of the transmitted light (**I**) and the incident light (**I₀**) (**Eq. 2.20**) [68]:

$$T = \frac{I}{I_0}$$

Equation 2.20

The absorbance (**A**) is related to the transmittance according to **Eq. 2.21** [68]:

$$A = \text{Log}_{10}T$$

Equation 2.21

The absorbance can be used to calculate the concentration (**c**) of a compound in solution, following Lambert-Beer's law (**Eq. 2.22**), which states that the amount of light absorbed by a material is directly proportional to **c**, to how strongly a chemical species attenuates light at a given wavelength (molar extinction coefficient, **ε**) and to the path length of the light beam (**l**):

$$A = \epsilon cl$$

Equation 2.22

The absorbance is sometimes referred to as optical density (OD), implying a path length (l) of 1 cm [68].

An absorbance band in a UV-Vis spectrum carries information on the structure of organic molecules. The formation of a covalent bond between atoms creates bonding orbitals, which may be of the σ type or of the π type, depending on the nature of the overlapping atomic orbitals [68]. According to molecular orbital theory, the formation of a bonding molecular orbital also creates an orbital of different shape and energy, referred to as an anti-bonding orbital. These orbitals can be of type σ^* or π^* , mirroring the bonding ones, and in most cases are vacant of electrons, being less energetically favourable than the original atomic orbitals and the newly formed bonding molecular ones. **Fig. 2.27** schematises the relative energies of these orbitals and the one of a non-bonding orbital n , which may contain the electrons not participating in bonding [68].

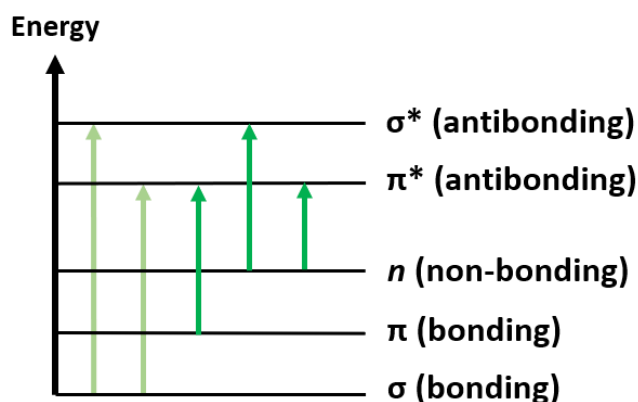


Fig. 2.27 Jablonski diagram representing the relative energies of molecular orbitals and possible transitions between them.

When light passes through a compound, some of its energy is absorbed by the electrons in non-bonding orbitals, promoting them to the anti-bonding ones. Observing the Jablonski diagram in **Fig. 2.27** we can notice that the transition

requiring the lowest energy is the one from the n orbital to the π^* one, followed by $n \rightarrow \sigma^*$ and $\pi \rightarrow \pi^*$. The wavelengths related to these energy values are in the near UV and visible regions of the spectrum and they vary from compound to compound, depending on the elements involved, the molecular structure the extent of delocalisation [64]. The absorbance spectrum in the UV-vis region is therefore unique for each molecule, making this a powerful technique for both the qualitative and quantitative determination of organic molecules in solution [69].

In this work, UV-Vis-NIR infrared spectroscopy was used for assessing the release over time of a biocide from the samples discussed in Chapter 3 into the surrounding water-based medium. The absorbance measurements were performed using a Shimadzu UV-1800, for further experimental details see Chapter 3.

2.5 References

[1] **Interpretation of Infrared Spectra, A Practical Approach.**

Coates J

In Encycl. Anal. Chem. 1st Edition, 2006

[2] **Encyclopedia of Analytical Chemistry**

Coates J

John Wiley & Sons, 1st Edition, 2006

[3] **Challenges in Molecular Structure Determination**

Reichenbacher M, Popp J

Springer, Heidelberg, 1st Edition, 2012, pp. 63–143

[4] **Fundamentals of molecular spectroscopy**

Banwell CN, McCash EM

McGraw-Hill, Berkshire, 4th Edition, 1994, pp. 55–99

[5] **Attenuated total reflection Fourier-transform infrared (ATR-FTIR) imaging of tissues and live cells**

Andrew Chana KL, Kazarian SG

Chem. Soc. Rev. 45 (2016) 1850

[6] **Raman, mid-infrared, near-infrared and ultraviolet–visible spectroscopy of PDMS silicone rubber for characterization of polymer optical waveguide materials**

Cai D, Neyer A, Kuckukb R, Heise HM

Journal of Molecular Structure 976 (2010) 274–281

[7] **Infrared and Raman Spectroscopy: Principles and Spectral Interpretation**

Larkin P

Elsevier, Stamford, 2nd Edition, 2018

[8] **Fundamentals of molecular spectroscopy**

Banwell CN, McCash EM

eds. C. N. Banwell and E. M. McCash, McGraw-Hill, Berkshire, 4th Edition, 1994, 308

[9] **Infrared and Raman spectroscopical studies of salicylic and salicylate derivatives in aqueous solution**

Humbert B, Alnot M, Quile`s F

Spectrochimica Acta Part A 54 (1998) 465–476

[10] **Capturing Irradiation with Nanoantennae: Plasmon-Induced Enhancement of Photoelectrolysis.**

Daccache L, Zeller S, Jacob T

Chem phys chem. (12) (2018) 1578-1585

- [11] **Microscopy Methods in Nanomaterials Characterization**
Mishra RK, Zachariah AK, Thomas S, Thomas R
Elsevier, 1st Edition, 2017, 383–405
- [12] **Handbook of Silicon Wafer Cleaning Technology**
Hues SM, Lovejoy L, Reinhardt KA, Kern K
Elsevier, Oxford, 3rd Edition, 2018, 728
- [13] **Fuel Cell Degradation and Failure Analysis**, chapter 11
Zhang J, Wu J, Zhang J
Elsevier, Oxford, 1st Edition, 2013
- [14] **Energy Dispersive X-ray (EDX) microanalysis: A powerful tool in biomedical research and diagnosis**
Scimeca M, Bischetti S, Lamsira HK, Bonfiglio R, Bonanno E
Eur. J. Histochem., 62 (2018) 2841
- [15] **Scanning Electron Microscopy and X-Ray Microanalysis**
Goldstein J
Kluwer Academic/Plenum Publishers, 2003
- [16] **The reinterpretation of wave mechanics**
De Broglie L
Foundations of Physics 1(1) (1970) 5–15
- [17] **Physical principles of electron microscopy: An introduction to TEM, SEM, and AEM**
Egerton RF
Springer International Publishing, Switzerland, 2nd Edition, 2016
- [18] **Strain mapping of a triple junction in nanocrystalline Pd**
Rösner H, Kübel C, Ivanisenko Y, Kurmanaeva L, Divinski SV, Peterlechner M, Wilde G
Acta Mater. 59 (2011) 7380–7387
- [19] **Imaging and dynamics of light atoms and molecules on graphene**
Meyer JC, Girit CO, Crommie MF, Zettl A
Nature 454 (2008) 319–322
- [20] **Scanning Electron Microscopy Working Principle**
<https://www.thermofisher.com/uk/en/home/global/forms/industrial/sem-working-principle.html> (accessed 19th September 2020)
- [21] **Cathodoluminescence and Transmission Cathodoluminescence**
Pendse DR, Chin AK
Encyclopedia of Materials: Science and Technology, 1st Edition, 2001
- [22] **A rapid technique for the determination of secondary electron emission yield from complex surfaces**
Ottaviano A, Banerjee S, Raites Y
J. Appl. Phys. 126 (2019) 223-301

- [23] **Formaldehyde Stress Responses in Bacterial Pathogens**
Chen NH, Djoko KY, Veyrier FJ, McEwan AG
Front. Microbiol. 7 (2016) 257
- [24] **Fabrication and Characterisation of Antimicrobial Surfaces**
Sorzabal-Bellido I
PhD thesis (2018) University of Liverpool, DOI:10.17638/03022760
- [25] **Glutaraldehyde as a Crosslinking Agent for Collagen-Based Biomaterials**
Olde Damink LHH, Dijkstra PJ, Van Luyn MJA, Van Wachem PB, Nieuwenhuis P, Feijen J
Journal of Materials Science: Materials in Medicine 6 (1995) 460–472
- [26] **Theory and Practice of Histological Techniques**
Bancroft JD, Gamble M
Churchill Livingstone, 8th Edition, 2019
- [27] **Membrane Lipid Homeostasis in Bacteria**
Zhang, YM, Rock CO
Nat. Rev. Microbiol. 6(3) (2008) 222–233
- [28] **The Use of Osmium in the Fixation and Staining of Tissues**
Wigglesworth VB
Proc. R. Soc. B Biol. Sci. 147(927) (1957) 185–199
- [29] **Fundamentals of Fluorescence Microscopy**
Mondal PP, Diaspro A
Springer, 2nd Edition, 2016
- [30] **Organic Light-Emitting Diodes (OLEDs)**
D’Andrade B
Materials, Devices and Applications, in Electronic and Optical Materials, 1st Edition, 2008, 143-169
- [31] **Acridine Orange – Thermofisher**
<https://www.thermofisher.com/order/catalog/product/A1301#/A1301> (accessed 19th September 2020)
- [31] **Basic Confocal Microscopy: A Tutorial**
Jerome WGJ, Price RL
Springer, 2002, Vol. 8
- [32] **Fluorescence microscopy**
Herman B
Bios Scientific Publishers, Oxford, 2nd Edition, 1998.
- [33] **Basic Confocal Microscopy**
Price RL, Jerome WG
Springer, New York, 1st Edition, 2011

- [34] **Laser Scanning Confocal Microscopy**
Claxton NS, Fellers TJ, Davidson MW
Der Hautarzt; Zeitschrift für Dermatologie, Venerologie, und verwandte Gebiete 61 (2010) 421-428
- [35] **Mechanism and Use of the Commercially Available Viability stain, BacLight.**
Stocks SM
Cytometry 61A(2) (2004) 189–195
- [36] **Fiji: an open-source platform for biological-image analysis**
Schindelin J, Arganda-Carreras I, Frise E, et al.
Nat. Methods 9 (2012) 676–682
- [37] **Handbook of Biological Confocal Microscopy**
Pawley JB
Springer New York, 1st Edition, 1995
- [38] **Atomic Force Microscopy, a Powerful Tool in Microbiology**
Dufrene YF
J Bacteriol. 184(19) (2002) 5205-13
- [39] **Atomic force microscopy and spectroscopy**
Seo Y, Je W
Rep. Prog. Phys. 71 (2008) 016101
- [40] **Application of Atomic Force Microscopy in Bacterial Research**
Dorobantu LS, Gray MR
Scanning 32(2010) 74–96
- [41] **Bruker AFM Probes - DDESP-V2**
<https://www.brukerafmprobes.com/p-3884-ddesp-v2.aspx> (accessed 17th October 2020)
- [42] **Bruker - Atomic Force Microscopes**
<https://www.bruker.com/products/surface-and-dimensional-analysis/atomic-force-microscopes/campaigns/afm-microscopes.html> (accessed 17th October 2020)
- [43] **Nanosurf – AFM operating principle**
<https://www.nanosurf.com/en/support/afm-operating-principle> (accessed 20th October 2020)
- [44] **Amplitude Modulation (AM) Mode in Dynamic Atomic Force Microscopy**
Voigtländer B
In: *Scanning Probe Microscopy. NanoScience and Technology.* Springer, 1st Edition, 2015, 187-204
- [45] **Atomic force microscopy measurements of bacterial adhesion and biofilm formation onto clay-sized particles**
Huang Q, Wu H, Cai P *et al.*
Sci Rep 5 (2015) 16857

- [46] **Bacterial recognition of mineral surfaces: nanoscale interactions between *Shewanella* and α -FeOOH**
Lower SK, Hochella MF, Beveridge TJ
Science 292 (2001) 1360–1363
- [47] **Cell adhesion of *Shewanella oneidensis* to iron oxide minerals: effect of different single crystal faces**
Neal AL, Bank TL, Hochella MF, Rosso KM
Geochem. T. 6 (2005) 77–84
- [48] **Analysis of Homotypic Interactions of *Lactococcus lactis* Pili Using Single-Cell Force Spectroscopy**
Dramé I, Formosa-Dague C, Lafforgue C, Chapot-Chartier MP, Piard JC, Castelain M, Dague E
ACS Appl. Mater. Interfaces 12(19) (2020) 21411–21423
- [49] **Contact Angle And Solid-Liquid-Vapor Equilibrium**
Liu Y, German RM
Acta mater. 44(4) (1996) 1657-1663
- [50] **Surface Tension and Its Measurement**
Ebnesajjad S, Landrock AH
In: Adhesives Technology Handbook, 1st Edition, 2009, pp. 21-36
- [51] **Contact Angle and Wetting Properties**
Yuan Y, Lee TR
Surface Science Techniques 51 (2013) 3-34
- [52] **Surface energy, surface topography and adhesion**
Packham PE
International Journal of Adhesion & Adhesives 23 (2003) 437–448
- [53] **A Theory for the Estimation of Surface and Interfacial Energies. I. Derivation and Application to Interfacial Tension**
Girifalco LA, Good RJ
J Phys Chem 61(7) (1957) 904–909
- [54] **A Theory for the Estimation of Surface and Interfacial Energies. III. Estimation of Surface Energies of Solids from Contact Angle Data**
Girifalco LA, Good RJ
J Phys Chem 64(5) (1960) 561–565
- [55] **Estimation of the surface free energy of polymers**
Owens DK, Wendt RC
J Appl. Polym. Sci. 13 (1961) 1741–1747
- [56] **Polar and Nonpolar Interactions in Adhesion**
Wu SJ
The Journal of Adhesion 5(1) (1973) 39-55

[57] Modern approaches to wettability

Good RJ, Van Oss CJ

Editors: Schrader ME, Loeb GI, New York: Plenum, 1st Edition, 1992, p. 12

[58] Physical chemistry of surfaces

Adamson AW, Gast AP

Wiley-Interscience, New York, 6th Edition, 1997

[59] Surface Roughness and Contact Angle

Wenzel RN

J. Phys. Chem. 53(9) (1949) 1466–1467

[60] Wettability versus roughness of engineering surfaces

KJ Kubiak, Wilson MCT, Mathis PG, Carval P

Wear 271(3-4) 2011 523-528

[61] A review of factors that affect contact angle and implications for flotation practice

Chau TT, Bruckard WJ, Koh PTL, Nguyen AV

Advances in Colloid and Interface Science 150 (2009) 106–115

[62] Surface Roughness as Related to Hysteresis of Contact Angles. II. The Systems Paraffin–3 Molar Calcium Chloride Solution–Air and Paraffin–Glycerol–Air

Bartell FE and Shepard JW

J Phys Chem 57 (1953) 455-458

[63] Wettability of porous surfaces

Cassie ABD, Baxter S

Trans. Faraday Soc. 40 (1944) 546

[64] Dynamic contact angles and contact angle hysteresis

Johnson RE, Dettre RH, Brandreth DA

Journal of Colloid and Interface Science 62(2) 1977 205-212

[65] Microfluidics: Modeling, Mechanics and Mathematics

Rapp BE

Elsevier, 1st Edition, 2016

[66] Dynamic contact angle hysteresis in liquid bridges

Zhang Shi, Yi Zhang, Mingchao Liu, Dorian A.H. Hanaor, Yixiang Gan

Colloids and Surfaces A: Physicochemical and Engineering Aspects 555 (2018) 365-371

[67] What is contact angle hysteresis?

Susanna Laurén

<https://www.biolinscientific.com/blog/what-is-contact-angle-hysteresis> (accessed on the 20th of February 2021)

[68] Principles and Practice of Analytical Chemistry

Fifield FW, Kealey D

Blackwell Science, Oxford, 5th Edition, 2000

[69] **Analytical Chemistry: An Introduction**
Skoog DA, West DM, Holler FJ
Saunders Golden Sunburst Series, 7th Edition, 1999

Chapter 3

Antimicrobial Activity of Biocide-Releasing PDMS Substrates

3.1 Introduction

3.1.1 Polydimethylsiloxane (PDMS)

Polydimethylsiloxane (PDMS) is a silicon based polymer commonly used in the fabrication and prototyping of microfluidic chips, as a food additive (E900), in shampoos, and as an anti-foaming agent in beverages or in lubricating oils [1]. It is elastic, thermally stable, transparent, chemically robust, and with high oxygen permeability [2]. The surface of PDMS is highly hydrophobic and almost unreactive due to the presence of surface-oriented methyl groups from the dimethylsiloxane moiety.

Siloxanes are some of the most flexible polymers, of paramount importance in most organic and semi-organic polymers due to their particular chemical structure (**Fig. 3.1.1**) where the Si-O skeletal bond (1.64 Å) is longer than the C-C bond (1.53 Å). As a result, PDMS has lower steric hindrance between adjacent molecules, allowing torsional rotations that occur with low energy cost [3].

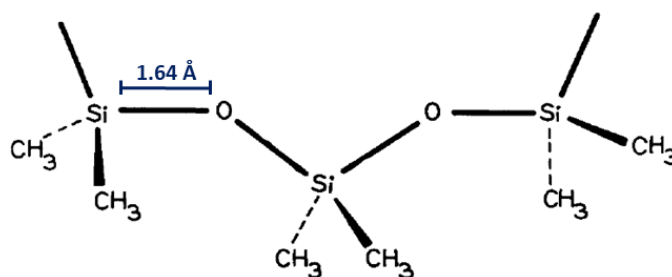


Fig 3.1.1 Dimethylsiloxane backbone. Image adapted from [3].

The mechanical properties of PDMS are also influenced by the length of the dimethylsiloxane chains, which determines the molecular weight of the polymer, and by the degree of crosslinking, which can be tailored by engineering the curing process [4]. The most common method for the preparation of PDMS is very simple and consists in mixing a pre-polymer (base) and a crosslinker (curing agent) in specific ratios that determine the properties of the final material.

PDMS exhibits remarkable biocompatibility, and from the clinical perspective it can be associated with: a) the absence of thrombogenic, toxic, allergic or inflammatory reactions; b) no change in plasma proteins or enzymes; c) no immunological reactions d) no carcinogenic effects; e) no deterioration of adjacent tissues [5]. Consequently, PDMS has found a wide range of applications in medical products [6], including venous catheters [7], urinary catheters [8], and voice prostheses [6], it is also used to fabricate lab-on-a chip devices and microarrays for DNA analysis [4]. One major drawback of pristine PDMS for some applications is its high hydrophobicity which may cause the adsorption of significant amounts of proteins from the surrounding biological environment, followed by bacterial attachment, which can lead to biofilm formation [9].

Bacterial attachment has serious consequences for human health especially when extended to implanted medical devices, artificial prostheses and catheters [10]. Bacterial communities, after initial adhesion to the surface, change their metabolic activity and form multicellular structures known as biofilms. Biofilms are defined as “aggregates of microorganisms in which cells are frequently embedded in a self-

produced matrix of extracellular polymeric substances (EPS) that are adherent to each other and/or a surface” [11]. They enhance bacterial resistance to mechanical forces, antibiotics, disinfectants and phagocytosis due to the barrier function of the EPS, the presence of dormant cells within the matrix and the upregulation of several antibiotic resistance genes [12].

PDMS surface modifications

One strategy to tackle the issue of biofilm formation on PDMS devices is modifying the surface chemistry of the material. However, the low chemical reactivity of the PDMS restricts the strategies to strong oxidising processes. Oxidation of PDMS surfaces provides a route to improve reactivity by replacing the surface methyl groups with hydroxyl groups, able to bind other functional molecules. A simple and cost-effective way to oxidise the PDMS surface is by reactive plasma treatment using oxygen or air [13].

In the work of Bodas *et al.* [14], grafting of hydrophilic functional groups onto PDMS using oxygen plasma treatment allowed the functionalisation the surface with 2-hydroxyethyl methacrylate (HEMA), leading to an increase in hydrophilicity over 10 days and effectively decreasing protein fouling and bacterial attachment [13].

A different strategy to modify the PDMS is via layer by layer coatings. In the work of Lopez *et al.* [15] mild CO₂ plasma was used to activate the PDMS surface followed by simple attachment of generation 5 (G5) poly(amidoamine) (PAMAM) creating an amino-terminated surface that reduced the adherence of the uropathogenic *Enterococcus faecalis* by 4 orders of magnitude after 72 hours.

Other strategies to change the surface properties of PDMS involve coatings with compounds such as poly(carboxybetaine methacrylate) [13], polyacrylamide [16] or metals [17]; or grafting hydrophilic monomers by laser [18], plasma [19] or chemical treatment [14].

Plasma treatment can be a highly effective method to functionalise PDMS surfaces with hydrophilic hydroxyl groups, however plasma treated surfaces can be unstable. These functionalized surfaces can recover their original hydrophobicity after several hours of exposure to air [20]. Therefore, oxidised PDMS surfaces require additional functionalisation immediately after plasma treatment.

Bulk modifications of PDMS

Contrary to surface modification techniques, where the surface composition is modified by external treatments such as grafting, modifying the bulk of PDMS alters the surface composition as a result of the presence of the new components in the material. PDMS bulk modification allows tailoring the polymer design to have a specific surface composition and to display specific properties related to the application [21].

Blending

Blending of polymers is a versatile strategy for producing materials with improved bulk and surface properties, combining different characteristics of individual polymers and leading to synergistic effects that may enhance the structure and chemistry of the material. Many polymeric materials of great technological and commercial value owe their superior performances to the combination of two or more blended parent polymers [21].

A PDMS-based composite material was studied by Hron *et al.* [22] and was prepared by blending a silicone rubber matrix and lightly crosslinked polyacrylamide (poly(AAm)). The mechanical properties of the composite materials in the equilibrium-swollen state were found to be even better than those of either the unfilled silicone matrix alone or of the methacrylate-type hydrogel with the same water content. In the implantation tests, cytotoxicity tests and cell cultivation tests

detected no difference between the silicone rubber/poly(AAm) composite materials and the standard poly(AAm) hydrogel biomaterial demonstrating that the composite materials were suitable for biological and medical use.

Wang *et al.* followed a similar approach in their 2016 work [23], in which they described the functionalisation of PDMS with small molecule antibiotics: Gentamicin Sulphate (GS) and Triclosan (TCA) were added into the mixed solution of elastomer base and curing agent in the stirring process, blending the biocides with the PDMS carrier. Interestingly, the resulting materials displayed different release kinetics depending on the antibiotic involved: PDMS-GS blends completed 11.8% (9.0 µg/mL) and 13.5% (20.5 µg/mL) of its drug release within 8 h, while PDMS-TCA displayed to be releasing 6.7% (8.7 µg/mL) of the total loaded biocide in the same amount of time. The different release profiles of GS and TCA could be explained with their opposite hydrophilic-hydrophobic properties. GS is easily dissolvable in water, which facilitates its diffusion into the supernatants, while the hydrophobicity of TCA could explain its slower release. Live/Dead staining on *S. aureus* cells incubated for 4 h with pristine PDMS, PDMS-TCA and PDMS-GS blends demonstrated the antimicrobial effect of the blends, which displayed fewer attached bacteria and lower cells viability than pristine PDMS. This biofilm inhibition effect was shown to persist after 72 h of exposure.

The main drawbacks of PDMS physical blends include poor interfacial adhesion between the two phases and leaching out of the hydrogel particles into the biological media [21].

Co-polymerisation

A different approach for the bulk modification of PDMS is the co-polymerisation with other materials.

Let *et al.* [24] created tri-block copolymers grafting onto PDMS quaternary ammonium salts (QAS), widely used as epidermal and topical antimicrobial agents in

medical treatments. The drawbacks of pure QAS include considerable toxicity caused by transdermal delivery which burdens the systemic circulation [25] and even damaging of organs caused by local allergic contact dermatitis (ACD) on skin [26] or drug-induced liver injury (DILI) [27]. The resulting copolymer proved to effectively inhibit growth of epidermal pathogenic microbes like *Escherichia coli*, *Staphylococcus albus* and *Candida albicans*. Moreover, the antimicrobial agent grafted to the PDMS backbone showed no skin penetration. These findings indicate that introducing hydrophobic moieties into polymeric antimicrobial agents helps their application in epidermal use.

PDMS swelling

An interesting property of PDMS is its capacity to swell in contact with non-polar solvents, which are able to penetrate the material increasing the volume. This process is partially reversible and once the solvent evaporates PDMS returns to the original size [28]. The volume swelling ratio (Q_v) can be defined as the ratio of the volume of swollen PDMS to its dry volume [28]. **Table 3.2.1** shows a list of different solvents and the degree of swelling they cause when in contact with PDMS [30]. The PDMS swelling process is believed to be associated with partially cross-linked macromolecules within the polymer (sol macromolecules) which, when in contact with a solvent of low molecular weight, participate in the swelling process acting as an athermal solvent (a solvent in which the polymer chains occupy a larger volume than an ideal chain of the same length). Sol macromolecules diffuse out of the polymer into the surrounding solution while the volume they previously occupied is replaced by solvent molecules until an equilibrium is reached, increasing the gel fraction [31].

During the swelling process, small solutes can also be incorporated into PDMS, and one can envision the transition of this phenomenon into a simple and cost-effective fabrication method for new functionalised material.

Table 3.1.1 List of solvents and the degree of swelling they cause when in contact with PDMS. Table adapted from [30].

No Swelling	≤5% volume	<5% to 30% <	≥30%
Water, Glycol, Ethylene Glycol, DMSO, Nitromethane.	Dimethyl carbonate, Acetone, Pyridine, NMP, Acetonitrile, Methanol, Ethanol, Phenol, Propylene Alcohol.	Ethyl acetate, Benzene, Chloroform, 2-Butanone, Chlorobenzene, DCM, Dioxane, Propanol and <i>tert</i> -butyl alcohol.	Pentane, Hexane, Heptane, Triethyl amine, Ether, Cyclohexane, Xylene, Toluene, THF. Diisopropylamine will swell up to 2.1 times.

In their work, Fisher *et al.* [32] exploited the ability of silicone polymers to swell upon contact with non-polar solvents to introduce three different antimicrobial agents, rifampicin, sparfloxacin and triclosan, within the material's bulk. As shown in **Fig. 3.1.2** the three antimicrobials were dissolved in chloroform and silicone cylinders were left in the solution for 1h, swelling to approximately twice their initial volume and taking in the biocides within their bulk. The materials were then removed from the solution, rinsed and allowed to dry overnight. In flow experiments, the antimicrobial cylinders were able to prevent colonization by the common uropathogens *Proteus mirabilis*, *Staphylococcus aureus* and *E. coli* for 7 to 12 weeks *in vitro*. Drug release profiles, distribution in the polymer and surface analysis were also performed and the process showed no deleterious effect on the topography or mechanical performance of the materials. Despite the effectiveness of the loading method described in this study, the use of antibiotics could possibly lead to an increase in the antimicrobial resistance of the tested uropathogens and the use of chloroform to swell the polymer raises biocompatibility concerns in applying this method for human use.

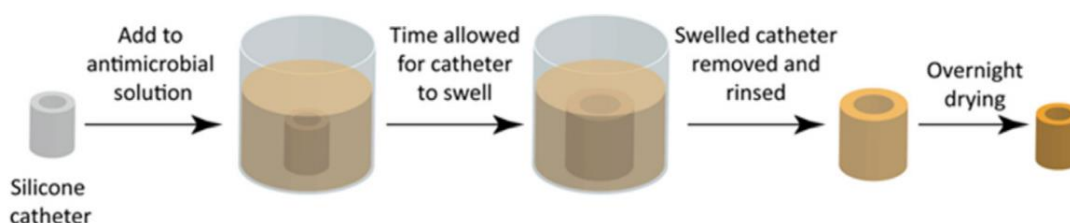


Fig. 3.1.2 Schematic depiction of the method used by Fisher *et al.* [23] to produce antimicrobial catheters. Catheters were added to a solution of antimicrobials and given time to allow the solvent to swell the catheter (1 h). Catheters were then removed from solution and allowed to dry overnight, returning to their original size. Image adapted from [32].

3.1.2 Salicylic Acid

Salicylic acid (SA) is a phenolic compound naturally present in plants as an endogenous signal, mediating local and systemic plant defence responses against pathogens [33]. SA is also a metabolic product of aspirin (acetylsalicylic acid) and its role as an antibacterial agent has been used in the food preservation industry [33]. In addition, SA has been approved for use on humans and is present in pharmaceutical preparations and cosmetic products as the active component to treat bacteria-related skin conditions like *acne vulgaris* [35, 36].

SA can be found in acidic and salt forms (**Fig. 3.1.3**) with dissociation constants (pKa) of $pK_{a1} = 2.98$ for the carboxylic group and $pK_{a2} = 13.6$ for the phenolic group [37].

SA has a wide range of antimicrobial effects [38] and it has been reported to affect the membrane proteome of *Pseudomonas aeruginosa* down-regulating the expression of many outer-membrane pore-forming proteins (OMPs) [39] and inhibiting the *las* quorum sensing system, which regulates gene expression of virulence factors [40]. SA has also been reported as an inhibitor of biofilm formation of *Staphylococcus epidermidis* [41], *Bacillus subtilis* [42] and *S. aureus* [41], being able to reduce adhesion of various micro-organisms to catheters [43].

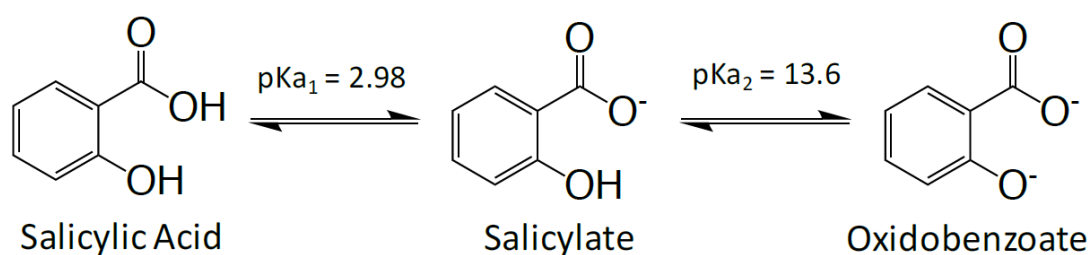


Fig. 3.1.3 Molecular structures of Salicylic Acid, Salicylate and Oxidobenzoate (Salicylate dianion).

A study by Kunin *et al.* [44] showed that salicylates were able to block the synthesis of flagellin in *E. coli*, disabling the production of fimbriae and flagella and consequently decreasing considerably the mobility of said bacterium.

A similar effect was reported on *P. aeruginosa* by Chow *et al.*, in their study [45] motility assays were conducted on wild-type strains (PAO1, PA14), flagella (PAO1 fliC, PA14 fliC) and type IV pili (PAO1 pilB, PA14 pilB) mutants, showing that sub-inhibitory concentrations of 25 and 50 mM SA significantly decreased bacterial swarming motility. These findings correlated with a significant reduction in biofilm formation when incubated with SA concentrations of 10 mM or above.

The controlled release of SA from materials to inhibit biofilm formation has been studied to some extent: SA-releasing poly(anhydride-ester) polymers have been shown to considerably inhibit *P. aeruginosa* biofilm formation [46]. In this case, the SA release was due to the hydrolysis of the main chain bonds of the polymer, a process that caused the materials to lose mechanical strength and structural integrity as they degrade, precluding *in vivo* applications.

In this chapter we present a post-fabrication modification method, exploiting the PDMS ability to swell in contact with non-polar solvents, leading to incorporation of SA in high concentrations within the bulk material while preserving the surface chemistry and topography of PDMS. Here we also investigate the ability of the loaded PDMS samples to release SA under physiological conditions, inhibiting surface colonisation and planktonic proliferation of both Gram-positive and Gram-negative bacteria. This approach avoids introducing blends of the polymer and the biocide, with the consequent change on the mechanical properties of the material, or by oxidising the PDMS surface to functionalise it with the antimicrobial agent, risking to compromise its biocompatibility.

3.2 Experimental section

3.2.1 Fabrication of PDMS-Salicylic acid samples

PDMS (Sylgard 184 silicone elastomer kit, Dow Corning) disks were fabricated mixing 10 parts of base and 1 part of curing agent, 1.1 g of the resulting mixture were poured to individual wells of a 6 well plate and cured overnight at 50°C.

The disks were then removed from the 6 well plate and left overnight at 4°C in a 500 mg/ml solution of Salicylic Acid (SA) (A12253, Alfa Aesar) in Tetrahydrofuran (THF) (401757, Sigma-Aldrich) to allow the swelling of the PDMS samples and the diffusion of SA within the material's bulk.

After removing the samples from the loading solution, SA was secreted from the material as a consequence of the PDMS de-swelling and THF evaporation. The excess of SA was scraped off their surface with the use of a plastic spatula for about 1h, the samples were then sonicated in a saturated solution of SA (to avoid release of biocide during the washing procedure) in DI water for 30 min at room temperature, the washing procedure was repeated 3 times changing the SA solution each time. The materials were then removed from the solution, dried and cut in 2.5 cm diameter disks.

All tests reported in this work were started the day following the cleaning procedures.

3.2.2 Surfaces analysis of PDMS-SA samples

The changes in the surface chemistry, topography and wettability after the SA loading process were analysed by Raman spectroscopy, atomic force microscopy (AFM) and Contact angle analysis, respectively.

Raman spectroscopy also allowed to assess the effective loading of SA in the PDMS, its distribution within the sample and its release at different time points when in contact with a water-based medium.

Raman analysis

Surface Raman spectra were recorded on a Renishaw inVia Confocal Raman microscope using an excitation wavelength of 532nm and focused using a 20x Leica objective. 4 types of samples were analysed: PDMS-SA, irradiated with 50% laser power corresponding approximately to 125 mW, for 5 seconds; PDMS-SA after a 24h release experiment, irradiated with 100% laser power, corresponding approximately to 250 mW, for 20 seconds; PDMS-SA after a 48h release experiment irradiated with 100% laser power for 10 seconds. Pristine was analysed as control PDMS, irradiated with 100% laser power for 20 seconds. Prior to each measurement, the power/time settings were optimised to have the best signal/noise ratio without damaging the sample.

The same measurements were repeated at a depth of 500 μm within the sample. The depth resolution of the instrument, associated to the laser with 532nm excitation wavelength, was estimated to be just below 1 μm , consequently the irradiation time was increased to 50 seconds for PDMS-SA and for PDMS-SA after a 24h release experiment, while for PDMS-SA after a 48h release experiment the irradiation time was 10 seconds, 100% laser power was used for all samples. Pristine PDMS, which was irradiated for 30 seconds, was analysed as control.

Raman cross section analysis

In order to assess the distribution of SA after the loading process and at different time point of a release experiment, the cross-section of PDMS-SA and PDMS-SA after a 12, 24 and 48h release experiment were analysed. The Raman spectra of these cross sections were taken using map image acquisition mode. A spectrum was

taken every 20 μm starting from the surface to 1.1 mm within the material, for each measurement, an excitation wavelength of 532 nm at 100% power was selected, focused with a 20x Leica objective and acquisition time of 10 seconds. Using the Wire 4.4 analysis software (Renishaw), the presence of SA through the sample was monitored by integrating one characteristic peak of Salicylic acid, from 1020 to 1045 cm^{-1} . 3 measurements were taken per sample, then averaged and normalised in respect to the average of the integral of a characteristic peak of PDMS, from 690 to 720 cm^{-1} , 100 μm before and after the region in which SA was concentrated.

The Raman spectra were processed using WiRE 4.4 software (Renishaw)

Attenuated total reflectance – Fourier transform infrared (ATR-FTIR)

In order to assess the mechanism of SA release, the presence of water in PDMS-SA and pristine PDMS was investigated by attenuated total reflectance. The samples were analysed in 2 conditions: dry and after 24h submerged in 4 ml of release media at 37°C. Fourier transform infrared (ATR-FTIR), Infrared measurements were performed using a Bruker Alpha FT-IR with Platinum ATR module with a resolution of 4 cm^{-1} . Each spectrum was the average of 24 scans. Sample spectra were collected in the 400-4000 cm^{-1} range and analysed using OPUS Spectroscopy Software (Bruker).

Contact angle measurements

In order to monitor any change at the surface wettability of the samples after loading of SA, contact angle (WCA) measurements were performed using of a contact angle meter (CAM 100, KSV Instruments) and using the same model buffer employed in the release experiments as probing liquid (see section 3.2.3). The WCA was calculated with a drop shape analysis software using curve fitting based on the Young–Laplace equation with an inaccuracy of 0.1 degrees. At least three measurements in different areas within each PDMS and PDMS-SA disk were taken,

giving reproducible results. The contact angle of a pellet of compressed SA was also measured, in order to evaluate the biocide's effect on the PDMS wettability.

Atomic force microscopy analysis

AFM was used to monitor any topographical changes of the PDMS surface topography after loading of SA. A Bruker Multimode 8 AFM fitted with a NanoScope controller operating in a ScanAsyst mode and equipped with a silicon tip and a cantilever operating at a scan rate of 0.977 Hz. Images were taken with a 512 x 512 pixels resolution and were analysed using Nanoscope analysis software. The average roughness (Ra) and root-mean-squared roughness (Rq) were measured from the analysis of the images at a 0.5 μm x 0.5 μm scan size using Microsoft Excel.

3.2.3 Release tests

The release of SA from the samples was evaluated at 299 nm using UV-VIS Spectrophotometry in conditions reproducing those of the bacterial viability experiments. It was found necessary to replace Luria-Bertani (LB) nutrient broth with a chlorine free phosphate buffer to prevent absorption in the UV region in which SA can be detected. The model buffer was prepared by dissolving 4.6 mM citric acid, 6.9 mM sodium citrate tribasic dehydrate in DI water to produce a pH 4.8, 11.5 mM citrate buffer solution. The final pH of this model buffer was adjusted to pH 7 using a 1M NaOH solution (Sigma Aldrich). Each PDMS-SA sample was incubated in well of a 6 well plate at 37 °C in 4 ml of model buffer and the SA concentration was assessed at different time points in order to obtain a release profile. The relationship between the absorbance and the SA concentration was determined by analysing the derivate of a calibration curve that was obtained by measuring the absorbance of solutions of SA at known concentrations in release buffer.

3.2.4 Antimicrobial response

All biotests were performed with *S. aureus*, SH1000 strain and *E. coli*, J96 strain.

Determination of minimum inhibitory concentration (MIC) and minimum bactericidal concentration (MBC)

In order to perform planktonic and surface viability test, bacteria were transferred from the frozen stock to a fresh nutrient agar plate using a sterile plastic loop and incubated overnight at 37°C. 3 colonies were then transferred from the agar plate to 5 ml of fresh Luria-Bertani (LB) nutrient broth medium (Fisher Scientific, 244620) and grown overnight in a shaking incubator at 37°C and 180 rpm. After the incubation, the bacterial concentration in sterile LB was adjusted to 3×10^4 CFUs mL⁻¹ and 50 µL of this solution were added to the microwells of a sterile 96-well plate containing 150 µL of different concentrations of SA in a 3.49 % mixture of EtOH in LB. The plates were placed in a FilterMax F5 Multimode Plate Reader (Molecular Devices) and the light scattering was screened at 595 nm for 24 h at 37 °C. The 595 nm value was set due to the low absorbance of the culture medium (yellow in colour) at the said wavelength. The MIC 50 and MIC 90 were calculated as the minimum SA concentration that prevented an optical density increase above 50% and 10%, respectively, compared to bacteria grown in a solution of 3.49 % EtOH in LB medium. After incubation, 30 µL of the bacterial solutions from the non-growing microwells were transferred to a fresh agar plate and incubated for 24 h. The MBC was calculated as the minimum concentration that did not allow bacterial growth on the agar plate.

Determination of *S. aureus* and *E. coli* viability on PDMS-SA

E. coli and *S. aureus* were grown as stated above, their concentration was then diluted 10^5 times in sterile LB. PDMS – SA samples and pristine PDMS samples of the same diameter and thickness, used as controls, were sterilised under UV light for 30 min and placed in a sterile 6 well plate, 4 ml of bacteria suspension at a concentration of 10^4 CFUs mL⁻¹ were then added to each well and the plate was left to incubate for 24 hours at 37°C. At the end of the incubation period a sample of bacterial suspension was taken from each well and underwent serial dilutions, a sterile LB agar plate was then inoculated 3 times with 10 µl of each dilution, the plates were left overnight at 37°C to allow the colonies to grow.

In order to assess the viability of sessile bacteria, the samples were washed 3 times in sterile 1x phosphate-buffered saline (PBS), 4 ml of sterile LB medium were then added to each well and the biofilm formed on the surface of the samples was disrupted by strong pipetting, dispersing the bacteria in the solution. A sample of bacteria suspension underwent the same dilution and plating process as the one of planktonic bacteria.

The CFU concentration was calculated by counting the number of colonies grown from 10µl of bacteria suspension and multiplying by the correspondent diluting factor. Viability assays of attached bacteria were performed in biological and technical triplicate.

Investigating pH effect on bacterial growth

In order to determine the effect that the low pH caused by the release of SA has on bacteria viability, *E. coli* and *S. aureus* were grown in SA in LB at different concentrations, following the same procedure used to assess the MIC and MBC of bacteria. In a parallel experiment *E. coli* and *S. aureus* were grown in solutions of Hydrochloric Acid in LB, at concentrations that allowed the solution to match the pH

value of the corresponding wells containing SA. The bacterial growth was evaluated measuring their optical density of the suspension at 595 nm for 24 h at 37 °C.

Imaging sessile bacteria

The concentration and viability of bacteria attached to PDMS-SA surfaces were studied by confocal fluorescence and scanning electron microscopy (SEM). For both techniques, *E. coli*, *S. aureus* were initially incubated over pristine PDMS and PDMS-SA for 24 h, as described in the previous section.

Scanning electron microscopy

The sample preparation for scanning electron microscopy (SEM) analysis started by washing the surfaces 3 times in 1x PBS and fixed overnight at 4°C with 4% paraformaldehyde and 2.5% glutaraldehyde in 0.1 M phosphate buffer. Sample fixation was completed in four sequential steps using 2% osmium tetroxide, 1% tannic acid, 2% osmium tetroxide and 1% uranyl acetate solutions in water. Every step was assisted by a Biowave Pro Microwave system (Pelco). For each step, samples were exposed to 100W microwave radiation for 20 s and subsequently cooled down for 20 s. This process was repeated three times per microwaving step. Between each staining step, the samples were thoroughly rinsed with DI-water. After the final uranyl acetate staining, the samples were rinsed with DI-water, and progressively dehydrated with different volumetric ratios of EtOH (i.e. 30%, 50%, 70%, 90% and 100%). After dehydration, modified and control PDMS samples were critical-point dried in CO₂ (Quorum Technologies K850) and sputter coated with 10 nm of Au/Pd (Quorum Technologies Q150T) for SEM imaging at 10 kV using a JEOL SEM 6610 system.

Confocal fluorescence microscopy

Prior to confocal fluorescence imaging, each PDMS-SA and pristine PDMS sample was washed 3 times with sterile 0.85% (w/w) NaCl solution, cut in a square < 1cm per side and placed in individual wells of a 24 well plate. The staining was performed using Live/dead BacLight bacterial viability kit (Molecular Probes, L7012). In detail, SYTO 9 (green-fluorescent nucleic acid stain for live cells), and propidium iodide (red-fluorescent nucleic acid stain for dead cells) were diluted in 1 mL of a sterile 0.85% NaCl solution which was added to each sample in the 24-well plate and incubated for 15 min in the dark at room temperature. After staining, the samples were imaged in 0.85% (w/w) NaCl solution using a confocal upright Zeiss LSM 880 Multiphoton microscope. Collected confocal fluorescence images were processed using Fiji software.

3.3 Results and discussion

3.3.1 Sample fabrication

The post-fabrication modification method we propose relies on the ability of PDMS to swell in contact with polar solvents. In our work Tetrahydrofuran (THF) was selected since, diversely to other solvents like Chloroform, it was demonstrated to not induce skin sensitization or developmental reproductive toxicity. It has also showed not to pose a concern for adverse impact on the environment [59].

Our approach to load a biocide within the PDMS matrix without altering the surface chemistry or topography of the material is described in **Fig. 3.3.1**. A pristine PDMS disk (**a**) was placed in a 500 mg/ml solution of Salicylic Acid (SA) in THF (**b**) and left overnight at 4°C to allow the swelling of the PDMS and the diffusion of SA within the material's bulk (**c**). After removing the samples from the loading solution (**d**), SA was secreted from the material as a consequence of the PDMS de-swelling and THF evaporation. The excess of SA was scraped off their surface with the use of a plastic spatula and the samples were sonicated in a saturated solution of SA in DI water to clean the surface from biocide residuals without inducing release of the biocide. The resulting material appeared to have retained high concentrations of SA within the bulk (**e**), consequently acquiring a white, opaque appearance.

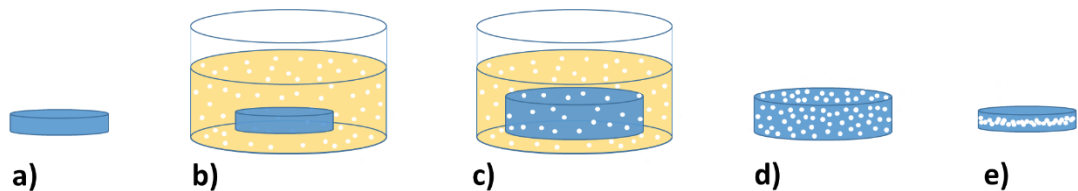


Fig. 3.3.1 Schematic representation of the post-fabrication modification method proposed to load SA within pristine PDMS. **a**) a pristine PDMS sample is submerged in a 500 mg/ml solution of Salicylic Acid (SA) in THF **b**), allowing it to swell and intake the biocide **c**), after removing the samples from the loading solution **d**) and cleaning and washing procedures the PDMS returned to its de-swelled configuration showing high concentration of SA in the bulk of the samples **e**), acquiring a white opaque appearance as a consequence.

PDMS is sufficiently soft and flexible to be cut in any desired shape and size, these properties were retained after the loading and washing process and the samples were cut in 2.5 cm diameter disks. The final concentration of SA within the PDMS was calculated to be 4.5 ± 0.1 % (w/w) via gravimetric measurements. **Fig 3.3.2** shows pristine PDMS (**A**) and a SA-loaded sample (PDMS-SA), with a white appearance, due to the high concentration of biocide introduced in the loading process (**B**).

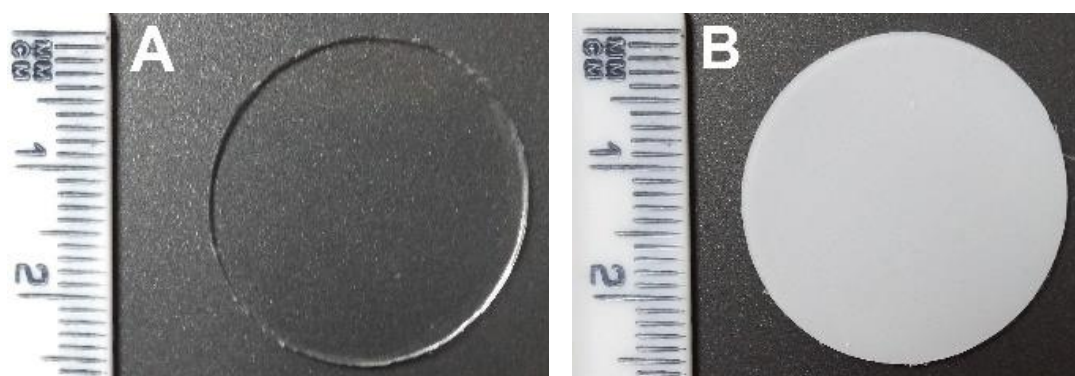


Fig. 3.3.2 Photographs of (**A**) PDMS and (**B**) PDMS-SA samples on dark background. Pristine PDMS is optically transparent, while PDMS-SA appears opaque/white.

3.3.2 Material characterization

The success of the biocide-loading process and its effects on the chemistry and topography of the sample's surface were evaluated via atomic force microscopy (AFM), contact angle measurements and Raman spectroscopy, while attenuated total reflectance – Fourier transform infrared (ATR-FTIR) and UV-vis spectroscopy allowed the monitoring of the release of SA from the material's bulk into the surrounding media.

Raman analysis

In order to investigate the changes in the sample's chemistry caused by the SA-loading process, Raman analysis was performed on pristine PDMS and PDMS-SA samples. **Fig 3.3.3** shows Raman spectra taken at the surface of the samples (**above**) and at 500 μm within the bulk (**below**). The spectra related to pristine PDMS show a characteristic band at 1412 cm^{-1} corresponding to the asymmetric bending of the methyl group, the Si-C stretch band of Si-CH₃ at 711 cm^{-1} [47]. As expected, no change in the spectra is observed increasing the probing depth.

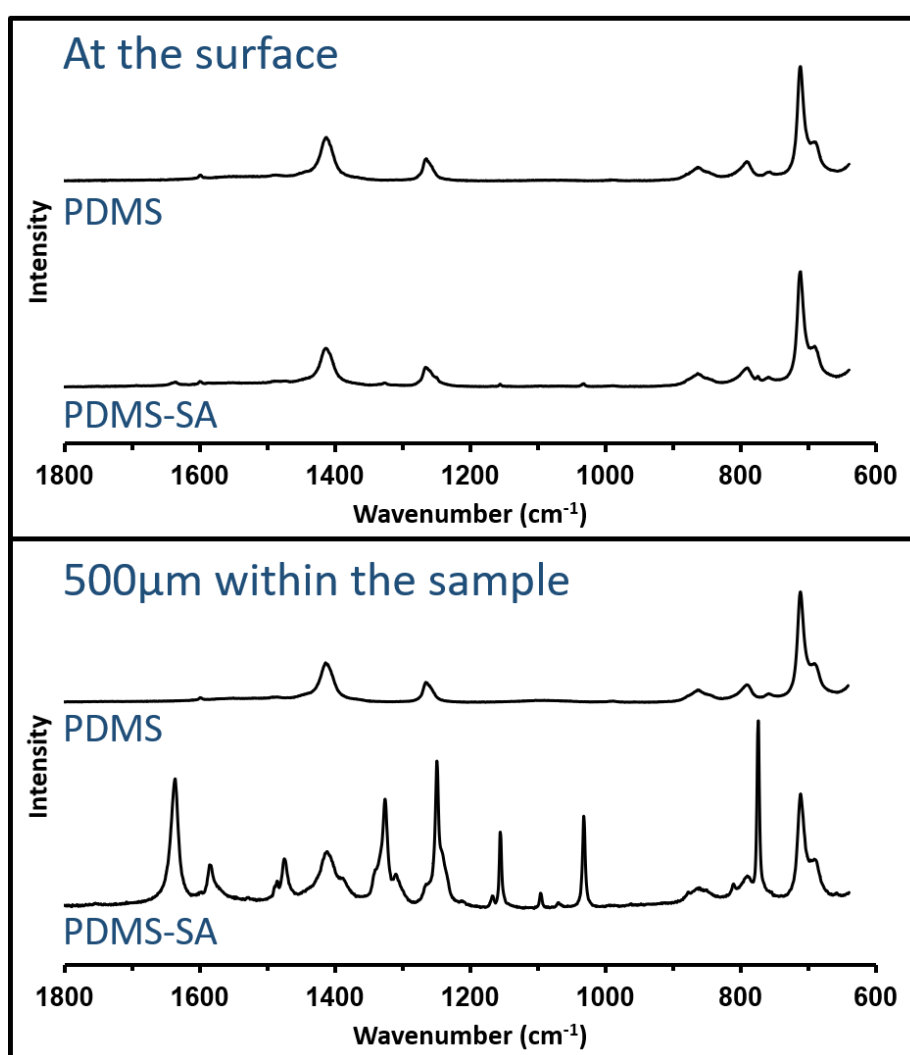


Fig 3.3.3 Raman spectra of pristine PDMS and PDMS-SA. **Above:** spectra taken at the surface of the sample. **Below:** spectra taken 500 μm within the bulk.

A subtle difference between the pristine PDMS and the PDMS-SA spectra taken at the surface is noticeable in the region between 950 and 1200 cm^{-1} , shown in **Fig 3.3.4**. In the PDMS-SA spectrum two small peaks, absent in the pristine PDMS one, are visible at 1170 and 1033 cm^{-1} related to the stretching of the C atoms in the aromatic ring of the SA molecule [37]. The concentration of SA in the bulk was calculated to be >10 times higher than on the surface.

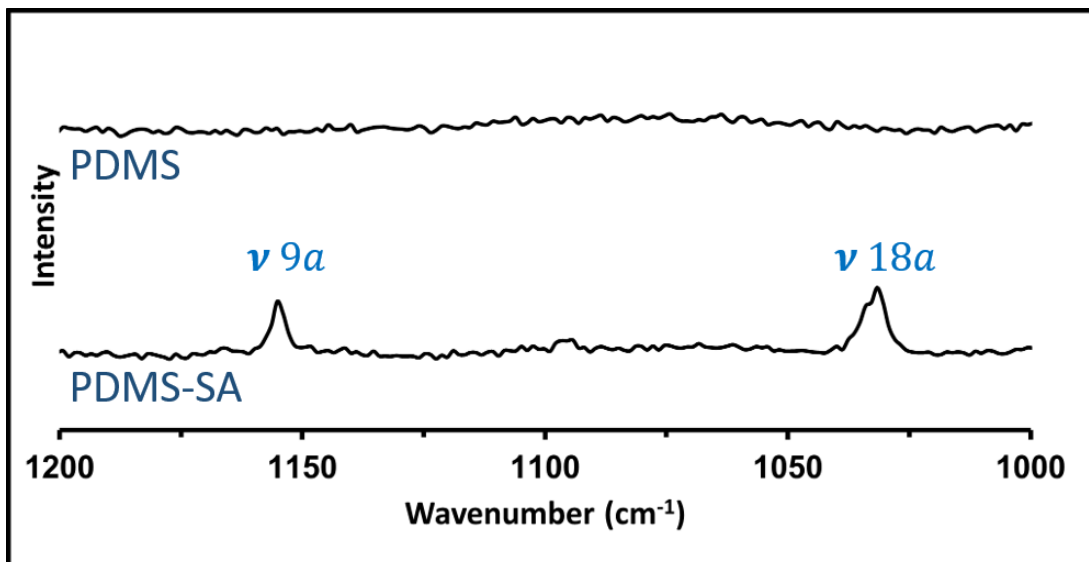


Fig 3.3.4 Raman spectra of pristine PDMS and PDMS-SA, taken at the surface of the samples, in the region between 950 and 1200 cm^{-1} . The nomenclature $\nu 9a$ and $\nu 18a$ indicates that the peaks are related to the stretching of the C atoms in the aromatic ring.

A clear difference between the two samples is visible in the spectra taken 500 μm within the bulk of the material (**Fig 3.3.3**, below), where the PDMS-SA shows prominent additional peaks compared to the pristine PDMS one. The previously described peaks at 1170 and 1033 cm^{-1} appear much more intense while additional characteristic SA bands can be observed at 1478 and 774 cm^{-1} , associated with the symmetric stretching and bending modes of the carboxylic group, plus another band at 1637 cm^{-1} , related to stretching of C=O in the carboxylic group [37].

The distribution of SA along the depth cross-section of PDMS-SA was evaluated using confocal Raman microscopy (**Fig 3.3.5**). No shift in peaks was noticed comparing the SA in the bulk to pristine SA at pH 2.0 (**Fig. 2.4**), indicating that the compound remains unaltered during the loading process. The intensity of the Raman peak at 1032 cm^{-1} , characteristic of SA, was mapped across the sample-air interface by integrating the Raman intensity values from 1020 to 1045 cm^{-1} . The results showed that the SA-loading process leaves a reservoir of biocide hundreds of microns within the bulk, as the SA peak was detected from $\approx 170\text{ }\mu\text{m}$ to $\approx 720\text{ }\mu\text{m}$ within material. The lack of biocide in the proximity of the surface is likely due to the evaporation of THF after the loading process, which lead to release of excess SA from the sample top and bottom surfaces. The non-homogeneity of the SA concentration through the material cross-section, with visible peaks in Raman intensity, is due to the presence of SA crystals within the PDMS bulk, which leads to spikes in the signal.

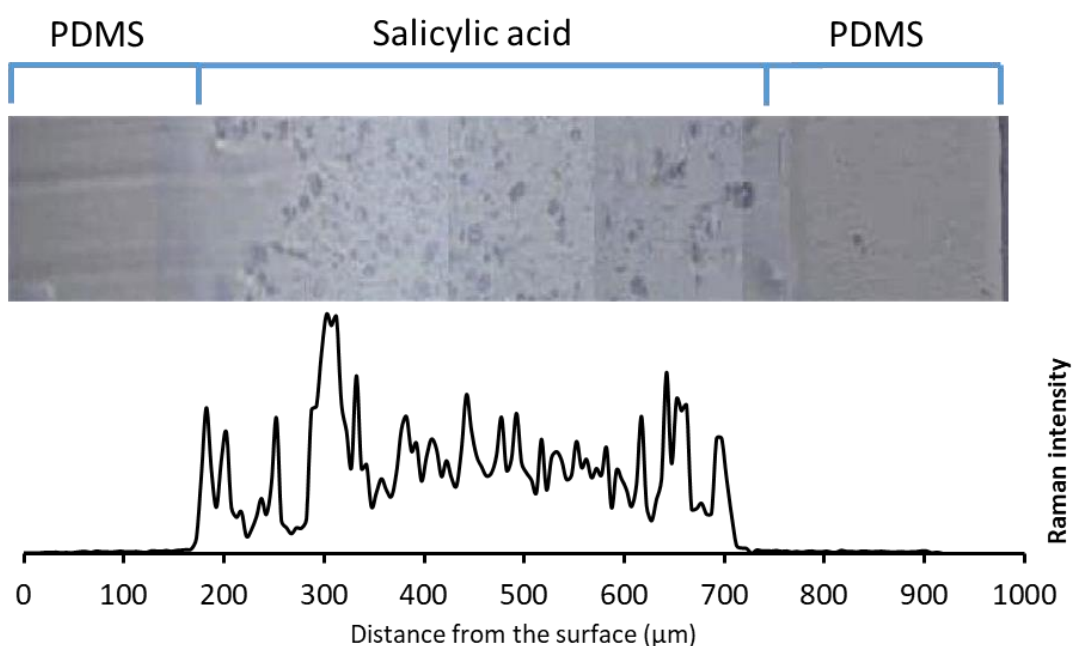


Fig 3.3.5 Raman spectroscopy investigation of the SA presence through the section of the material. Above: representative image of the PDMS-SA cross section taken using a 20x Laica objective, the represented inclusions in the bulk of the sample appear to be SA crystals. Below: intensity of the Raman peak at 1032 cm^{-1} , related to SA, mapped across the sample-air interface, obtained by integrating the Raman intensity values from 1020 to 1045 cm^{-1}

These results demonstrate the successful creation of a reservoir of biocide in high concentration within the bulk of the samples, while leaving minimal traces of SA at the surface.

Atomic force microscopy analysis

Surface roughness (Ra) is considered to be a key factor on the wettability and protein adsorption on materials, which can lead to bacterial colonisation [60]. It is defined as the average deviation of the profile from the mean line over the length of assessment and is determined by **Eq. 3.3.1**:

$$Ra = \frac{1}{l} \int_0^l |y - y_{cl}| dl$$

Equation 3.3.1

Where y is the height measurement of the surface, y_{cl} is defined as the center line, chosen such that the areas above and below the line are equal, and l is the length of assessment [61].

The Root Mean Square Roughness (Rq) gives a measure of microscopic peaks and valleys of a surface and is essentially the standard deviation or second moment of the height distribution [62]. Like Ra , Rq is a measure of the surface roughness but a single large peak or valley within the microscopic surface texture will affect the Rq value more than Ra [63]. Rq is calculated as shown in **Eq. 3.3.2**:

$$Rq = \sqrt{\frac{1}{l} \int_0^l (y - y_{cl})^2 dl}$$

Equation 3.3.2

In a study by Kerr *et al* [66] the accumulation of bacterial biofouling was assessed on surfaces with Rq values ranging from 5 to 25 nm. The samples were exposed to

different experimental regimes: a purely static exposure, static exposure followed by dynamic removal of the attached cells and fully dynamic exposure where the bacterial suspensions were allowed to flow across the surface of the samples. The results suggest that the effect of surface roughness on bacterial adhesion is almost instantaneous, with surfaces with $Rq \sim 10$ nm compared to 5 nm and 15 nm leading to a more pronounced biofilm formation.

A study by Singh *et al.* [64] compared the biofilm formation of *S. aureus* and *E. coli* on nanostructured titania thin films fabricated with controlled nanoscale morphology with Rq values ranging from 16 to 32 nm. Results showed significantly higher mean biofilm formation for *S. aureus* compared to *E. coli* species, with higher bacterial cells attached on surfaces with Rq values of 16 and 21 nm than on the samples with Rq of 25 and 32 nm. The glass control with $Rq \sim 5$ nm exhibited significantly less biofilm formation in respect to nanostructured surfaces by several orders of magnitude. Quantification revealed that lower surface roughness induces more EPS productions, henceforth thicker biofilm structure.

The surface topography of pristine PDMS and PDMS-SA was analysed by atomic force microscopy (AFM). Representative AFM images are presented in **Fig 3.3.6**, pristine PDMS is relatively smooth, with a Ra value of 3.97 nm and a Rq value of 2.97 nm. After SA loading only a slight increase in surface roughness ($Ra = 5.51$ nm) and root mean square roughness ($Rq = 4.28$ nm) was observed, probably due to swelling and de-swelling process of PDMS during SA loading or the mechanical scraping of the surface during the sample cleaning process.

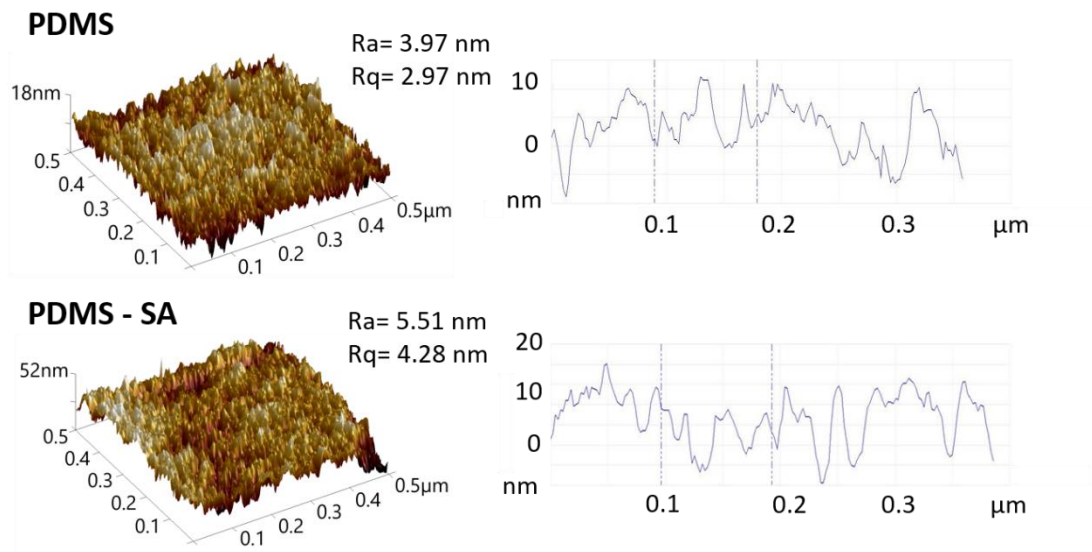


Fig 3.3.6 AFM analysis of pristine PDMS and PDMS-SA Left: 3D AFM height mode images. Image size= 0.5 x 0.5 μm^2 . Right: examples of roughness profile taken from the same images. Ra = Surface Roughness, Rq = Root Mean Square Roughness.

These results show that the post-modification fabrication method we described has a negligible effect on the topography of the samples, as the detected $\sim 1.5\text{nm}$ increase in Ra cannot significantly cause an increase in protein adsorption that would lead to bacterial colonization [64], while surfaces with an Rq values around 5 nm were reported not to induce bacterial attachment [66, 64].

Static contact angle analysis




Theoretical predictions on the propensity of bacteria to adhere to different substrates are based on physicochemical characteristics of the bacterial membranes such as their wettability and surface charge [67, 68]. According to this concept, *E. coli* cells are expected to exhibit a greater tendency than *S. aureus* to populate hydrophilic substrates [72, 68], due to the thermodynamic preference of hydrophilic cells to adhere to hydrophilic surfaces and of hydrophobic cells for hydrophobic surfaces [67, 68]. The results of the study by Mitik-Dineva *et al.* [68] conformed to this theory, showing higher hydrophobicity in the *S. aureus* cells than *E. coli* ones,

which led to lower attachment of the Gram-positive species than the Gram-negative one to hydrophilic (water contact angle = $45\pm 4^\circ$) glass surfaces.

A recently a study by Yuan *et al.* [69] showed that a hydrophobic (water contact angle = $\sim 115^\circ$) or hydrophilic (water contact angle = $\sim 28^\circ$) surface reduces *E. coli* adhesion, while moderate hydrophobicity with water contact angle of $\sim 90^\circ$ increases it.

The wettability of PDMS before and after loading SA was determined by static contact angle measurements. C.A. data in water, resumed in **Table 3.3.1**, confirmed the hydrophobicity of pristine PDMS with a contact angle of $\sim 110^\circ$. The contact angle of the biocide was measured on a pellet of compressed SA and resulted to be $\sim 43^\circ$. Measuring the contact angle of PDMS-SA, no significant difference was found to pristine PDMS, indicating that the wettability of the material is not influenced by the SA loading process and consequently that it would not play a role in a difference in bacterial adhesion between pristine PDMS and SA-loaded samples.

Table 3.3.1 Contact angles measurements of pristine PDMS, SA pellet and PDMS-SA. Measurements expressed as average value \pm standard deviation.

PDMS	Salicylic acid	PDMS - SA
		
$101.5 \pm 2.3^\circ$	$43.3 \pm 2.6^\circ$	$101.7 \pm 4.3^\circ$

3.3.3 Release of Salicylic Acid from PDMS-SA samples

The release over time of SA from PDMS-SA samples was evaluated at 299 nm using UV-VIS spectrophotometry in conditions reproducing those of the bacterial viability experiments. Due to the intrinsic absorption of LB in the UV-Vis region in which SA can be detected, it was necessary to optimise a model pH buffer based on citrate, which is optically transparent in that UV region of interest for SA. The model buffer also required a pH response comparable to the one of the LB medium used in the biological tests, a characteristic that was achieved at citrate concentration of 11.5 mM, as shown by the titration curves in **Fig 3.3.7** (SA was used as titrant).

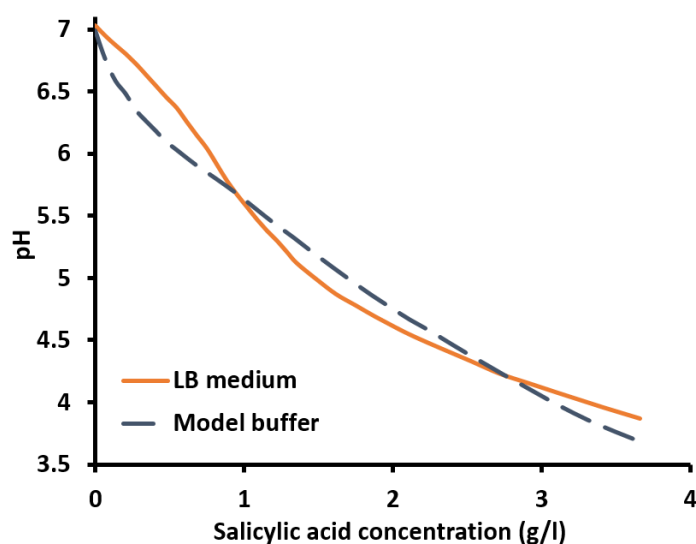


Fig 3.3.7 The optimization of the citrate model buffer allowed to obtain a pH response comparable to the one of the LB medium used in the biological tests. Figure shows the titration curves of LB medium (orange) and of the 11.5 mM citrate model buffer (dotted blue). The titration was performed using SA.

In order to calculate of the extinction coefficient of SA at 299 nm in citrate model buffer, it was necessary to measure the absorbance at said wavelength of different known concentrations of SA in model buffer via UV-Vis spectrophotometry. The calibration curve obtained is shown in **Fig. 3.3.8**, the extinction coefficient was calculated to be 24.785, with and R^2 coefficient of 0.99.

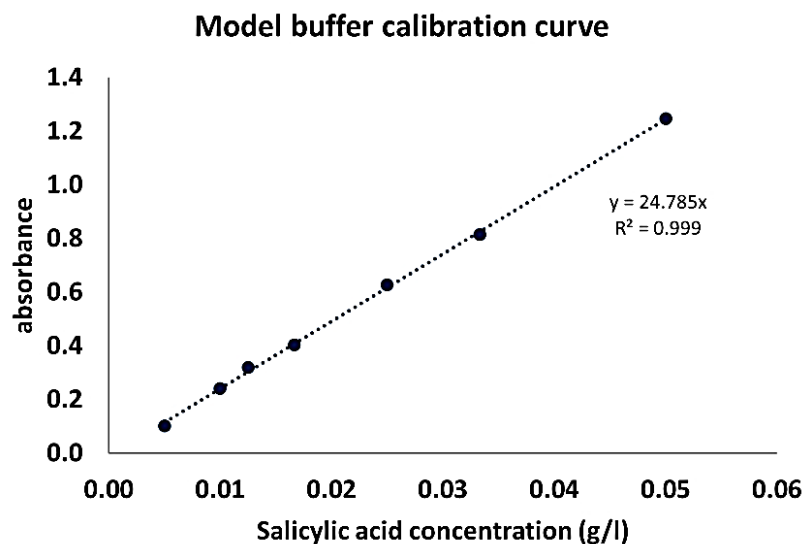


Fig 3.3.8 Calibration curve used to assess the extinction coefficient of SA in 11.5 mM citrate model buffer.

In order to evaluate the release of SA from PDMS-SA samples under physiological conditions, the samples were placed in individual wells of a 6 well plate and 4 ml of model buffer solution were added to each well, the samples were then incubated at 37°C and the concentration of SA was assessed over 72 h at different time points via UV-Vis spectroscopy by monitoring the absorbance of the SA peak at 299 nm. Under these model buffer conditions, the concentration of SA released from PDMS-SA samples after 24 h was 2.79 (± 0.20) mg mL⁻¹, rising to 3.07 (± 0.11) mg mL⁻¹ after 48 h and reaching 3.55 (± 0.22) mg mL⁻¹ after 72 h.

The release profile, shown in **Fig. 3.3.9**, can be described empirically by two regimes: the concentration of SA in the first 24h of release can be estimated, using the experimental data, with a saturation-limited model described in **Eq. 3.3.3** The solubility limit of SA in model buffer was found experimentally to be 5.43 mg mL⁻¹ and was set as the horizontal asymptote of the model, while 0.03 is the time constant found to fit empirically the experimental data.

$$C(t) = 5.43(1 - e^{-0.03t})$$

Equation 3.3.3

From 24 to 72 h the release regime was slower, **Eq. 3.3.4** was found to fit the experimental data, until the SA concentration reached 3.55 mg mL^{-1} after 72 h of release.

$$C(t) = 0.016t + 2.371$$

Equation 3.3.4

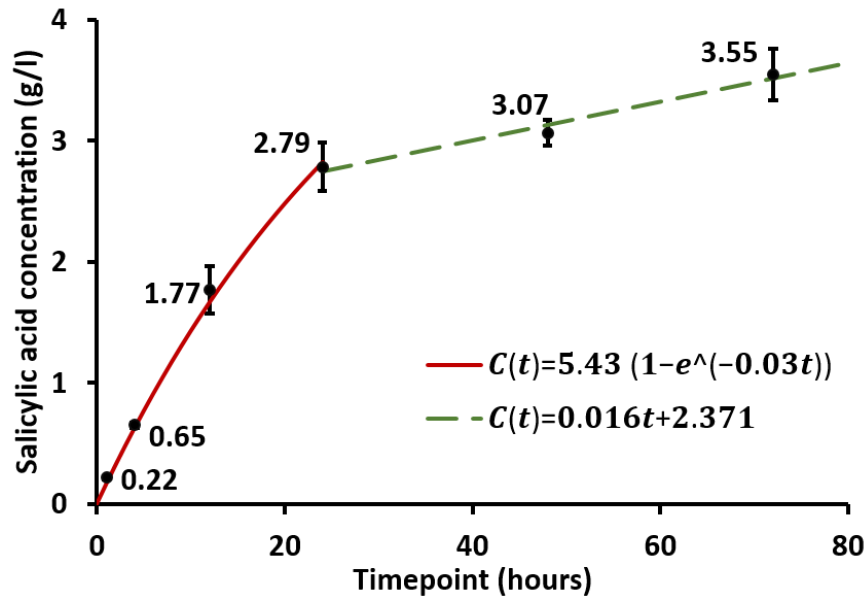


Fig. 3.3.9 Concentration of SA released from PDMS-SA samples monitored at different time points measuring the UV-vis absorbance peak at 299 nm. The equations represented describe the double regime mathematical model fitting the SA release profile.

The two dynamic regimes observed for the release data can be rationalized considering the change in the pH in the buffer solution. As shown in **Fig 3.3.10**, during the first 24 h of release the pH solution decreases due to the increase in SA concentration, reaching $\text{pH} \sim 4.2$ after 24 h of release, with a SA concentration of 2.79 mg mL^{-1} , similarly to the behaviour of the LB medium (**Fig. 3.3.7**) used for the biological tests. Salicylic Acid has a pKa of 2.97 [37], consequently during the first 24 h of release it deprotonates in solution and is mostly present in its deprotonated form. At increasing time points the Salicylate concentration increases along with the concentration of H^+ in solution, decreasing the pH to 4 after 48h, and to 3.7 after 72 h. At low pH the high concentration of protons in solutions decreases the

percentage of Salicylic Acid dissociating into Salicylate, the concentration of the protonated and de-protonated form in solution at different pH values can be calculated by re-arranging the Henderson-Hasselbalch equation:

$$pH = pKa + \log \frac{[\text{Salicylate}]}{[\text{Salicylic Acid}]}$$

Obtaining Eq. 3.3.5:

$$[\text{Salicylic Acid}] = \frac{[\text{Salicylic Acid} + \text{Salicylate}]}{1 + 10^{(pH-pKa)}}$$

Equation 3.3.5

As shown in Fig. 3.3.10, after 48 h of release the percentage of Salicylic Acid in solution was calculated to be 8.5%; after 72 h of release, when the pH reached 3.7, 15% of the biocide was released in its protonated form.

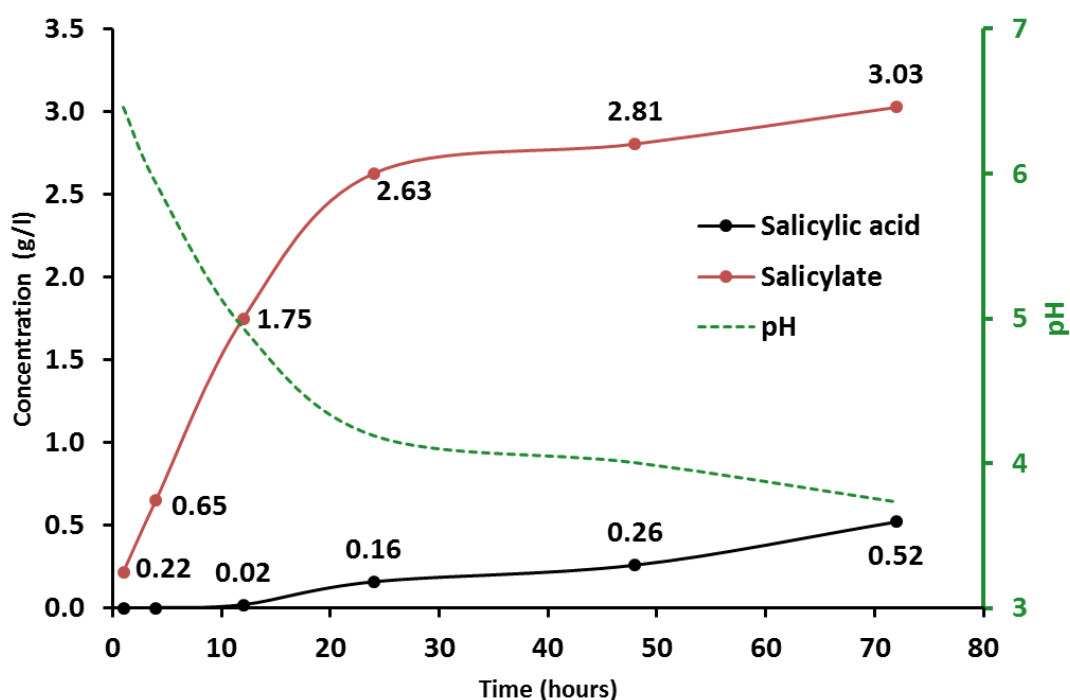


Fig. 3.3.10 Concentrations of SA (black) and Salicylate (red) calculated using the Henderson-Hasselbalch equation based on the release data over 72 h, and corresponding pH decrease (green dotted line).

An explanation of the slower regime in the release after the first 24h could be found in the intrinsic non-polar character of SA [70] which grants high solubility in non-polar solvents like THF but has the opposite effect in polar solvents. The rise in the degree of ionization of SA increases its polarity and therefore grants higher solubility in water. This effect was also observed by Otto *et al.* in a recent work [71].

Attenuated total reflectance – Fourier transform infrared (ATR-FTIR) analysis

ATR-FTIR analysis was performed on PDMS-SA and pristine PDMS samples in two conditions: dry and being submerged for 24h in 4 ml of citrate buffer at 37°C, matching the conditions in which the release tests were performed.

As shown **Fig. 3.3.11**, the IR spectra of pristine PDMS in dry conditions and after 24h in model buffer at 37°C don't show significant differences, they are both characterised by the vibrational band of the PDMS methyl groups asymmetric bending at 1450, while the characteristic bands related to the symmetrical and asymmetrical stretching of the methyl groups are visible at 2905.9 and 2964.4 cm^{-1} , respectively (the absorbance of the latter was measured to be circa 0.21 a.u.) [47]. It is interesting to notice that the IR spectrum of the SA-loaded sample in dry conditions (**PDMS-SA**) matches those related to pristine PDMS samples (**PDMS** and **PDMS wet**), suggesting that SA in the loaded samples is present near the surface in amounts not detectable by ATR-FTIR analysis.

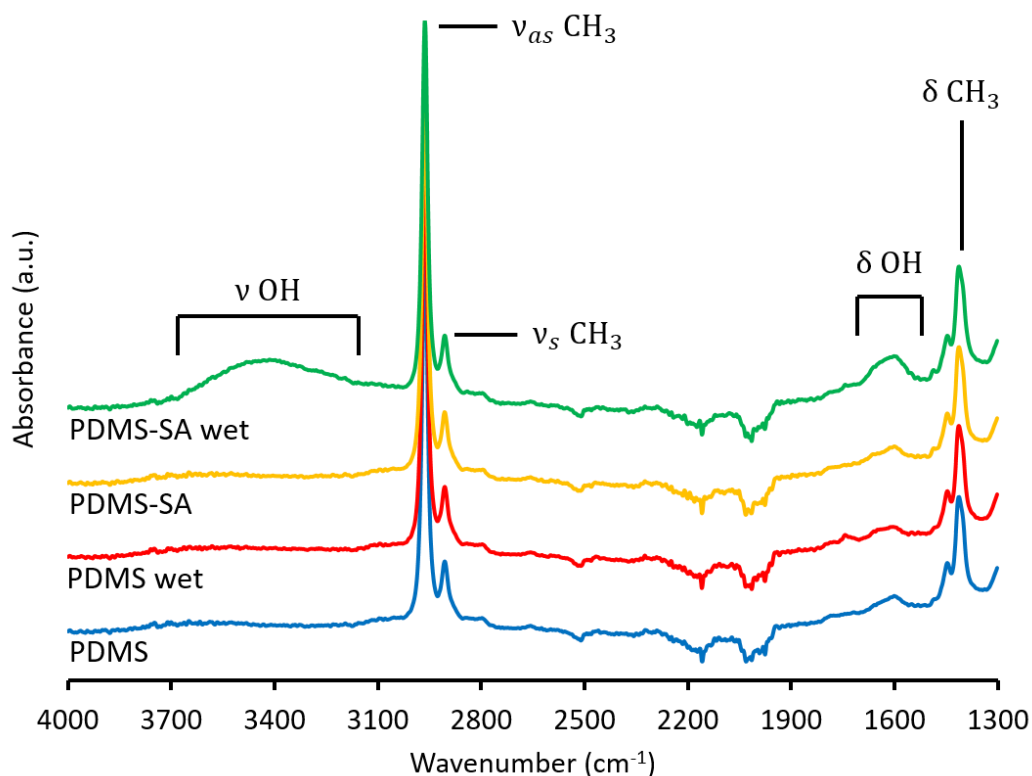


Fig. 3.3.11 ATIR spectra of PDMS- SA left for 24 h in model buffer (green), PDMS – SA (yellow), PDMS left for 24 h in model buffer (red), pristine PDMS (blue).

The spectrum of the PDMS-SA sample submerged for 24h in release media (**PDMS-SA wet**) presents a broad band centered at 3500 cm^{-1} , attributed to the stretching of the hydroxyl groups of water molecules and the band related to the scissoring of the hydroxyl groups at 1635 cm^{-1} [49]. These bands are evident when subtracting the spectrum of the PDMS sample submerged for 24h in citrate buffer from the spectrum PDMS-SA sample under the same condition, the resulting spectrum is shown in **Fig. 3.3.12**. No shift in the PDMS related picks is highlighted from this spectrum, indicating that the material did not undergo structural changes during the biocide-loading or the buffer-intaking processes.

It is interesting to notice that the spectrum of pristine PDMS submerged for 24h in release media does not show water-related bands in its IR spectrum, suggesting that the SA-loading process allows water to penetrate the sample in the conditions of the release experiments.

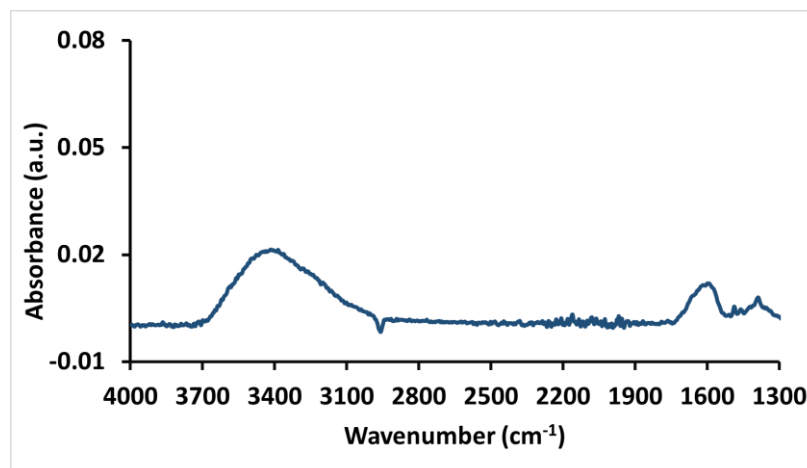


Fig. 3.3.12 ATR-IR spectrum resulting from the subtraction of the spectrum of PDMS left for 24 h in model buffer and PDMS-SA in the same condition.

These results demonstrate the presence of water in the PDMS-SA samples, within the probe depth of the spectrometer (circa 1 μm), when they are submerged for 24h in model buffer at 37°C, suggesting (**Fig. 3.3.13**) that SA release is associated with penetration of water-based media into the sample.

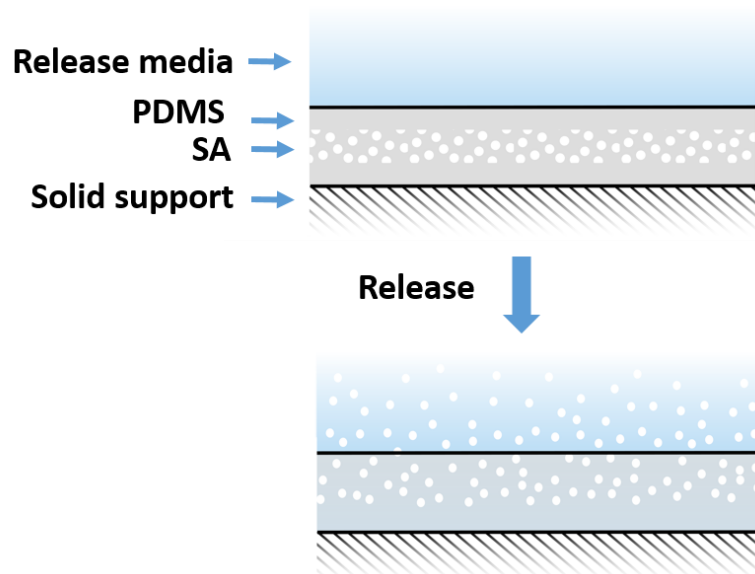


Fig. 3.3.13 Schematic representation of the SA release mechanism: the water-based media penetrating the sample, reaching the biocide in the bulk, dissolving it and allowing it to diffuse outside of the sample.

Raman analysis

In order to assess the change in the SA concentration in the bulk of the sample at different time points of the release experiment, Raman analysis was performed 500 μm within the bulk of PDMS-SA and PDMS-SA after a 12, 24 and 48h release experiment (**Fig 3.3.14**). As discussed previously, in the PDMS-sample before the release the presence of SA is defined by prominent peaks at 1478 and 774 cm^{-1} , associated with the symmetric stretching and bending modes of the carboxylic group, and the band at 1637 cm^{-1} , related to stretching of C=O in the carboxylic group. PDMS related bands are present at 1412 cm^{-1} , corresponding to the asymmetric bending of the methyl group, the Si-CH₃ symmetric stretch band at 711 cm^{-1} and the band corresponding to the Si-CH₃ symmetric rocking at 616 cm^{-1} [47].

After 24 h in release conditions the bands characteristic of SA showed distinctively lower intensity compared to the same bands before release. After 48 h no SA related bands were detected 500 μm within the samples.

These results demonstrate that the SA content within the bulk decreased after 24 and 48 h in release conditions, supporting the hypothesis that SA is released into the supernatant.

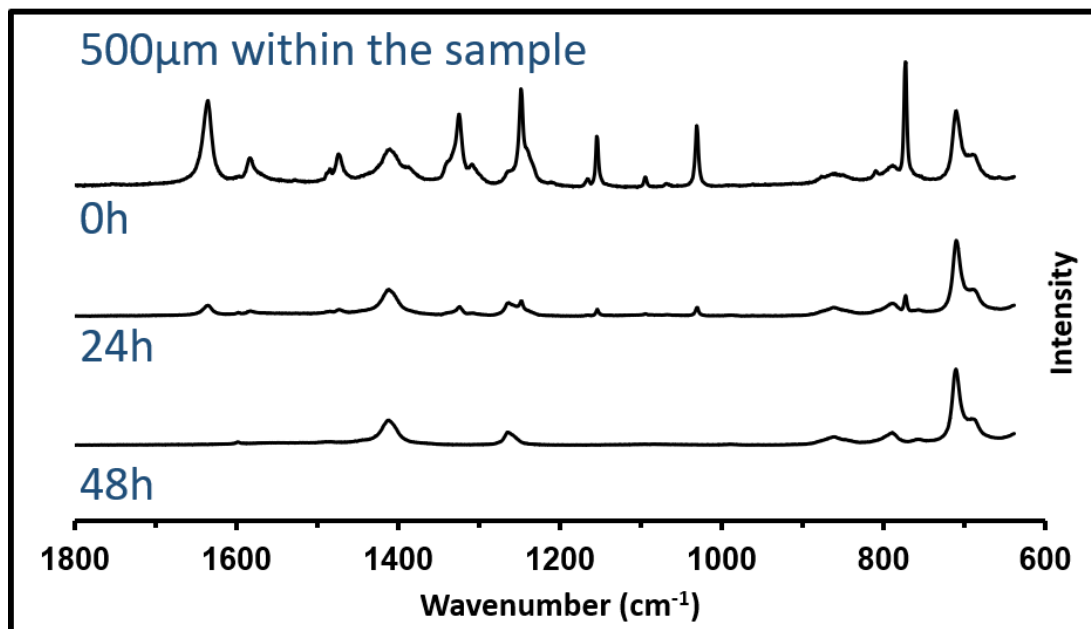


Fig 3.3.14 Raman spectra taken 500 μm within the bulk of PDMS-SA before release, PDMS-SA after 24 hours release and PDMS after 48 hours release.

To assess the distribution of SA at different time points of a release experiment, the cross-sections of PDMS-SA after the loading process and PDMS-SA after 12, 24 and 48h in release conditions were analysed. The presence of SA was determined by monitoring the intensity of the SA-related peak at 1032 cm⁻¹, which was done by integrating the Raman intensity values from 1020 to 1045 cm⁻¹. **Fig. 3.3.15** shows the intensity of the SA peak through the cross section of the sample. Comparing the data related to the PDMS-SA sample after the loading process (**0h**) with those related to samples at different time points of the release experiment (**12h**, **24h**, **48h**), it can be assessed that, as the release experiment proceeded, the SA signal was detected at increasing depth from the surface exposed to the media.

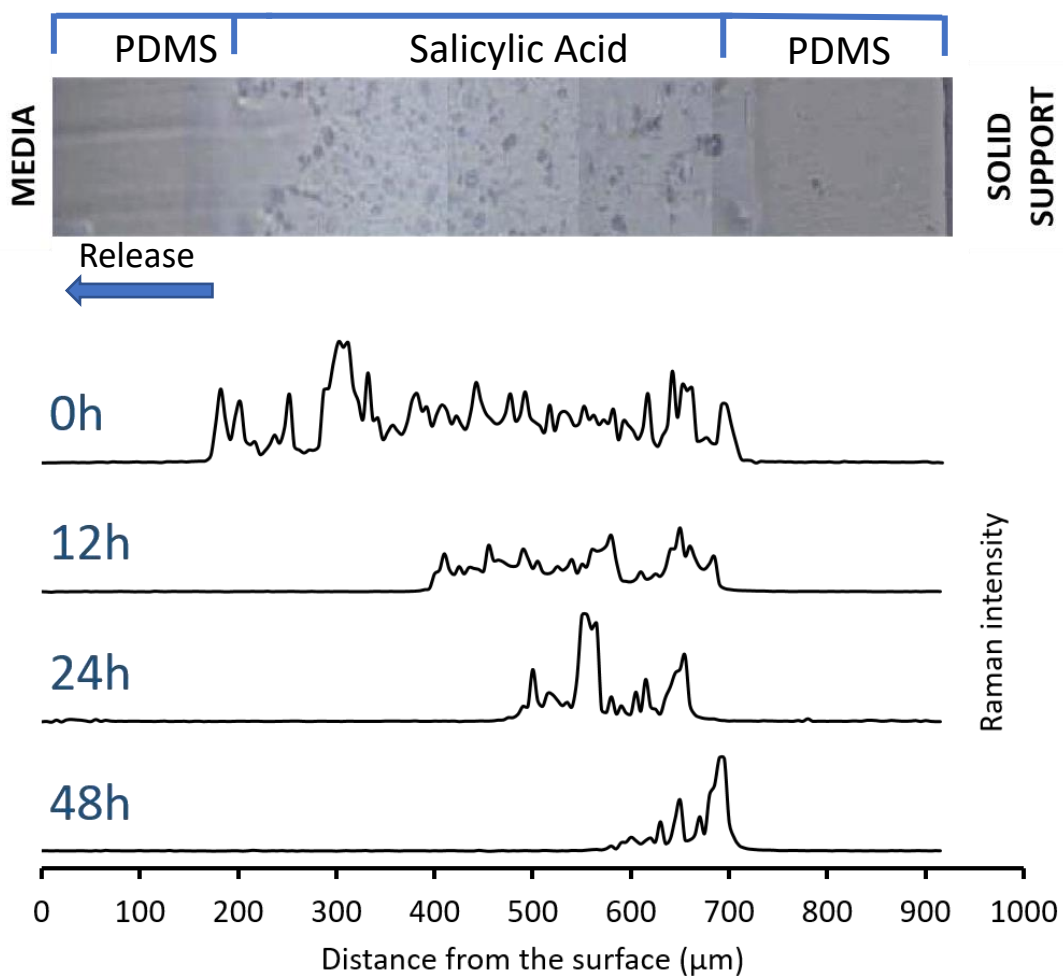


Fig. 3.3.15 Raman spectroscopy investigation of the SA presence through the section of the material. **Above:** representative image of the material's cross section taken using a 20x Laica objective. **Below:** Raman cross section of PDMS-SA before release experiment (**0h**), PDMS-SA after 12 hours release(**12h**), PDMS-SA after 24 hours release (**24h**) and PDMS after 48 hours release (**48h**).

These findings, along with the presence of water 1 μm within the surface assessed by the ATR-IR spectra in the previous section, support the hypothesis that the PDMS-SA samples allow the medium to penetrate into the material, dissolving the SA and releasing it into the surrounding environment by diffusion.

Contact angle analysis

In order to gain further insights on the mechanism that allows the medium to penetrate only the SA-loaded PDMS, an experiment was carried out in which a drop of model buffer was left in contact with pristine PDMS and PDMS-SA and the contact angle was measured every 30 min.

The results (**Fig 3.5.1**) showed, on both samples, a starting contact angle of $\sim 101^\circ$, as the liquid of which the drop is composed slowly evaporated, the contact angle remained stable on pristine PDMS up to 1 h, while it decreased to $63.3 (\pm 1.7)^\circ$ on PDMS-SA. After 2 h the contact angle of the model buffer droplet on pristine PDMS decreased to $95.6 (\pm 2.3)^\circ$ and to $58.8 (\pm 1.9)^\circ$ on PDMS-SA.

To investigate the hypothesis that the decrease of the contact angle of model buffer on PDMS-SA over time was due to SA release, leading to a decrease in the surface tension of the droplet, the contact angle on pristine PDMS was measured using solutions of SA in model buffer at increasing concentrations. The results (**Fig. 3.5.2**) showed no significant difference between any of the solutions, with a contact angle of $102 (\pm 7.4)^\circ$ for a 1 mg mL^{-1} solution of SA in model buffer and $106.5 (\pm 5.8)^\circ$ for a 3 g/l solution, the highest concentration tested.

In order to assess a possible change in the topography of the samples due to contact with model buffer that might affect the capacity of PDMS to intake water, the contact angle of model buffer on pristine PDMS and PDMS-SA that had been in release conditions for 3 and 24h was measured. Results (**Fig. 3.5.3**) show no significant difference between the contact angle of the tested samples and those that had never been in contact with model buffer. Also no significant difference was measured between the contact angles on pristine PDMS and PDMS-SA, in any condition.

Atomic force microscopy analysis

To further investigate a possible change in the topography of the samples due to contact with model buffer and SA release, the surface of PDMS-SA samples after 24 h in release conditions was analysed via atomic force microscopy. The results summarised in **Fig 3.3.16** show an increase in Ra of ~ 1 nm compared to PDMS-SA before release, not sufficient to cause a change in the wettability of the sample or to facilitate bacterial attachment.

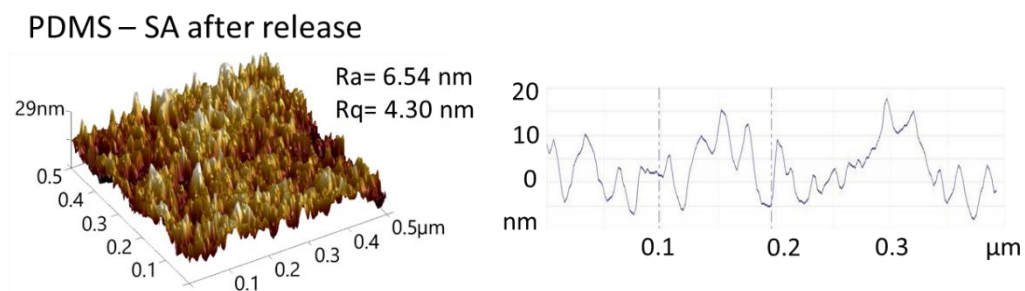


Fig 3.3.16 AFM analysis of PDMS-SA after 24h in release conditions. Left: 3D AFM height mode images. Image size= $0.5 \times 0.5 \mu\text{m}^2$. Right: examples of roughness profile taken from the same images. Ra = Surface Roughness, Rq = Root Mean Square Roughness.

3.3.4 Antimicrobial activity of PDMS-SA samples

Pathogens related to urinary tract infections [49] were used in this study to test the antimicrobial activity of SA released from PDMS-SA samples. The tested strains were a Gram-negative clinical isolate of uropathogenic *E. coli* J96 [50] and a Gram-positive model strain used extensively in laboratory research [51]: *S. aureus* SH1000. The antimicrobial activity of the PDMS-SA samples was evaluated both on sessile and planktonic cells, with imaging techniques and biological assays.

All biological experiments were performed in triplicates for each bacterial species.

Planktonic cells viability

The minimum inhibitory concentration (MIC) and the minimum bactericidal concentration (MBC) related to SA were assessed by growing the tested strains at increasing concentrations of SA in LB.

The bacterial growth was measured by screening the optical density of the solutions at a wavelength of 595 nm for 24 h at 37 °C. MIC 50 and MIC 90 are defined as the minimum SA concentrations preventing an optical density increase above 50% and 10%, respectively, compared to bacteria grown in absence of SA after 24 h. The MBC was calculated as the minimum SA concentration preventing bacterial growth on the agar plate.

The MIC and MBC values found in this work were higher for *E. coli* than those for *S. aureus* (**Table 3.3.2**). This result was expected since *E. coli* is a Gram-negative bacterium and the presence of an outer membrane increases its resistance to antimicrobials compared to Gram-positive bacteria like *S. aureus* [52, 53].

In comparison with previous studies with SA, different *E. coli* and *S. aureus* strains showed more resistance to the biocide, with an MBC of 5 g/l for *E. coli* CETC 434 and 3.2 g/l for *S. aureus* CETC 976 [54]. In a study by Muroi *et al.* [54], SA was used in combination with methicillin against methicillin resistant *S. aureus* ATCC 33591 (MRSA). Results showed a MIC of said strain related to SA to be 0.4 g/l and related to methicillin of 0.8 g/l, while combining the two it was possible to completely inhibit the *S. aureus* growth with a concentration of 0.2 g/l for both compounds.

Table 3.3.2 SA concentration inhibiting growth by 50% (MIC 50), 90% (MIC 90) and minimum bactericidal concentration (MBC) for *E. coli* J96 and *S. aureus* SH1000.

	<i>E. coli</i>	<i>S. aureus</i>
MIC 50	0.75 g/l	0.75 g/l
MIC 90	1 g/l	1.25 g/l
MBC	2 g/l	1.75 g/l

Crossing the MIC and MBC values shown in Table 4.3.2 with the data related to the release experiments in **Fig 3.3.9**, it appears that the MIC 50 and MIC 90 for both species are reached within the first 10 h of release, while the MBCs are reached within the first 20 h.

In order to evaluate the effect that the low pH of the bacterial suspensions caused by SA has on bacteria viability, *E. coli* and *S. aureus* were grown at different concentrations of SA in LB and in solutions of Hydrochloric Acid (HCl) in LB, at concentrations that allowed the solution to match the pH value of the corresponding suspensions containing SA. The results shown in **Fig. 3.3.17** display the growth after 24 h of *E. coli* and *S. aureus* in solutions at decreasing pH values due to increasing SA concentrations in LB and at the corresponding pH in HCl solutions in LB.

In the case of *E. coli*, a decrease in the pH from of 7.2 to 4.2 in the HCl solutions led surprisingly to a ~ 18% increase in the absorbance of the bacterial suspension. The corresponding pH decrease, caused by an increase in SA concentration, completely inhibited bacterial growth, showing an intrinsic antimicrobial effect of SA.

In the case of *S. aureus*, the MBC of SA in model buffer corresponded to a pH of 5 and, as expected, in this condition no bacterial growth was detected. In a pH 5 solution of HCl in LB bacteria showed a 61% decrease in growth after 24h (**Fig. 3.5.4**) in comparison to bacteria grown in the absence of HCl, showing a synergy in inhibiting bacterial growth between the intrinsic antimicrobial effect of SA and the low pH conditions.

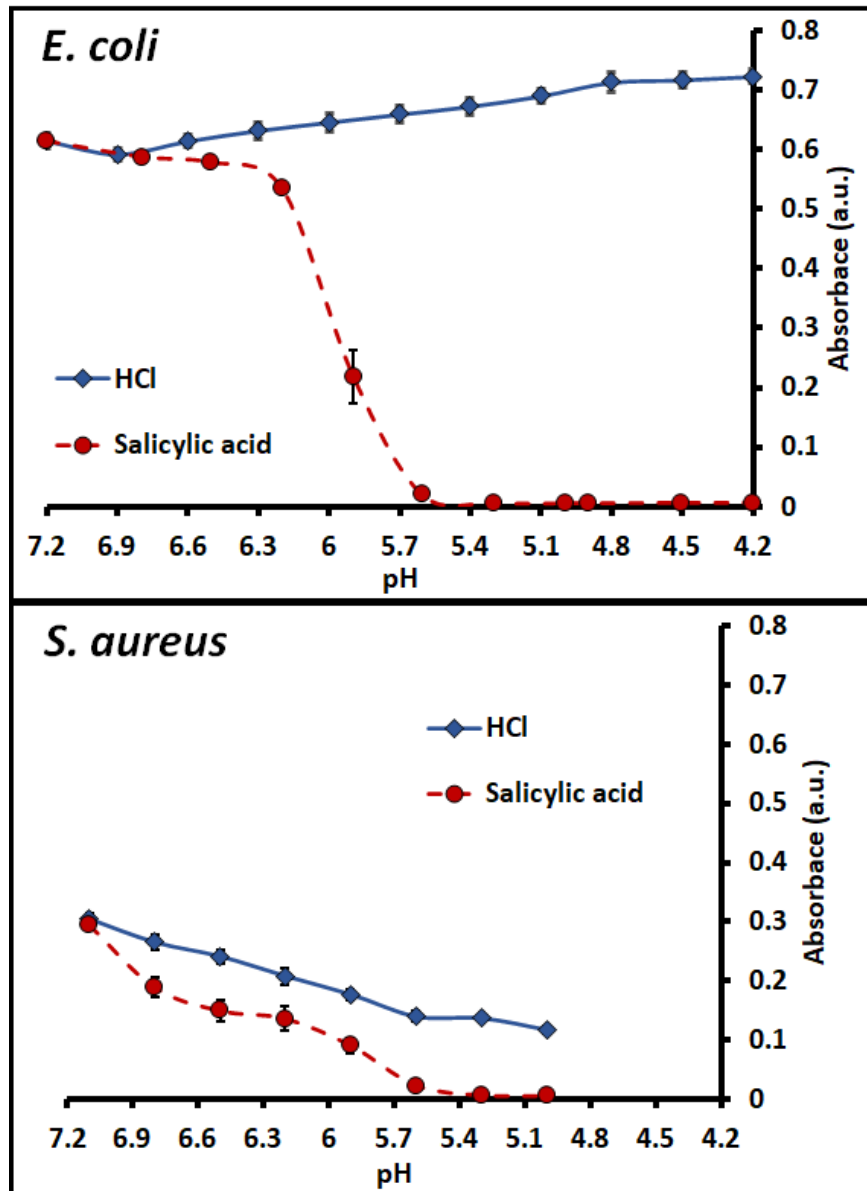


Fig. 3.3.17 Absorbance of bacterial suspensions measured after 24 hours in physiological conditions. *S. aureus* SH1000 (above) and *E. coli* J96 (below) were grown in LB medium at the different concentrations of SA (dashed red line) and at the corresponding pH in the presence of HCl (continuous blue line).

CFUs counting of planktonic bacterial cells

In order to compare the antibacterial effect of the SA released from the loaded samples with the pure one used in the MIC and MBC tests, bacterial suspension with a starting concentration of 10^4 CFUs/ml in LB were incubated at 37°C for 24 h with PDMS-SA samples and pristine PDMS samples as control. Results of the colony

forming units (CFUs) counting are summarised in **Fig 3.3.18** and show high bacterial proliferation in suspensions in contact with pristine PDMS, reaching a concentration of 3.2×10^9 CFUs/ml for *E. coli* and 1.7×10^8 CFUs/ml for *S. aureus* after 24h. For bacterial suspensions in contact with PDMS-SA samples, it was not possible to detect any live bacteria by CFUs counting, an assay with a detection limit of 33 CFUs/ml [56].

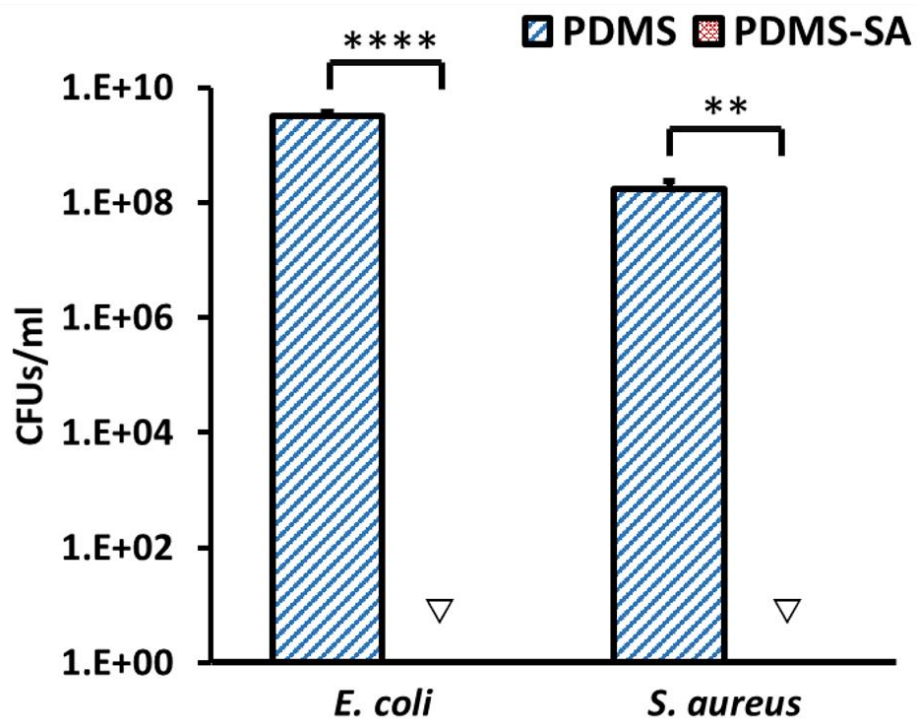


Fig. 3.3.18 Viable planktonic *E. coli* J96 and *S. aureus* SH1000 cell counts cultured for 24 hrs on PDMS-SA samples and pristine PDMS. ∇ signifies that the CFUs concentration was below the detection limit of 33 CFUs/ml. **** signifies p -value ≤ 0.0001 , ** signifies p -value ≤ 0.01 .

These results indicate a strong antimicrobial effect of the SA released from the loaded samples, comparable with the one of pure SA, used in the MIC and MBC assay, resulting in inhibition of proliferation and death of planktonic cells.

Viability of surface-attached bacterial cells

In the previous section, it was shown that the SA released from PDMS-SA samples were able to induce death of planktonic bacterial cells. However, it has been demonstrated that bacteria growing as a biofilm can display enhanced resistance to the action of biocides [56, 57]. Therefore, the concentration and viability of bacterial cells at the surface of the samples was evaluated under the same experimental conditions, using fluorescence scanning electron microscopy imaging and viability assessment by counting colony forming units.

SEM imaging allows to assess the bacterial concentration and the morphology of bacterial colonies grown on pristine PDMS and PDMS-SA samples (Fig. 3.3.19). The images show a high number of bacterial cells attached to pristine PDMS, with *E. coli* homogeneously distributed on the surface while *S. aureus* assembled in large three dimensional aggregates. In contrast, the number of cells on the PDMS-SA surfaces appears distinctively lower after 24 h, with only sporadic bacteria visible on the samples, indicating an anti-biofouling effect for both Gram-negative and Gram-positive species.

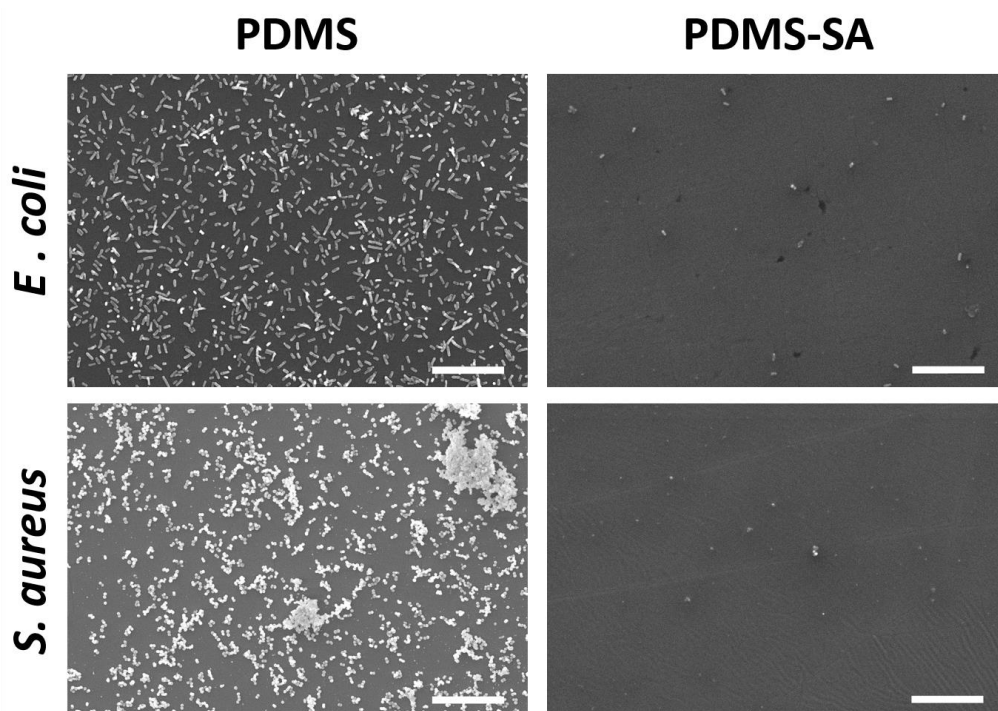


Fig. 3.3.19 Representative SEM images showing bacteria cultured for 24 h on PDMS-SA samples and pristine PDMS. Scale bars = 20 μ m.

Live/Dead assay of bacteria attached to PDMS-SA surfaces

Confocal laser scanning microscopy (CLSM) images of bacteria stained with Live/dead viability kit allowed the investigation of the viability of the sessile cells. This was achieved with the use of SYTO 9, a cell-permeant dye that shows a large fluorescence enhancement upon binding nucleic acids, and Propidium Iodide, a nucleic acid binding dye unable to permeate the intact membrane of live cells, commonly used to detect dead cells in a population [58]. Live/dead viability assays shows dead cells as red or yellow and live cells in green.

The CLSM images (**Fig. 3.3.20**) show a high coverage of bacterial cells on pristine PDMS with 92.9 (± 2) % viability in the case of *E. coli* and 99.1 (± 0.2) % in the case of *S. aureus*.

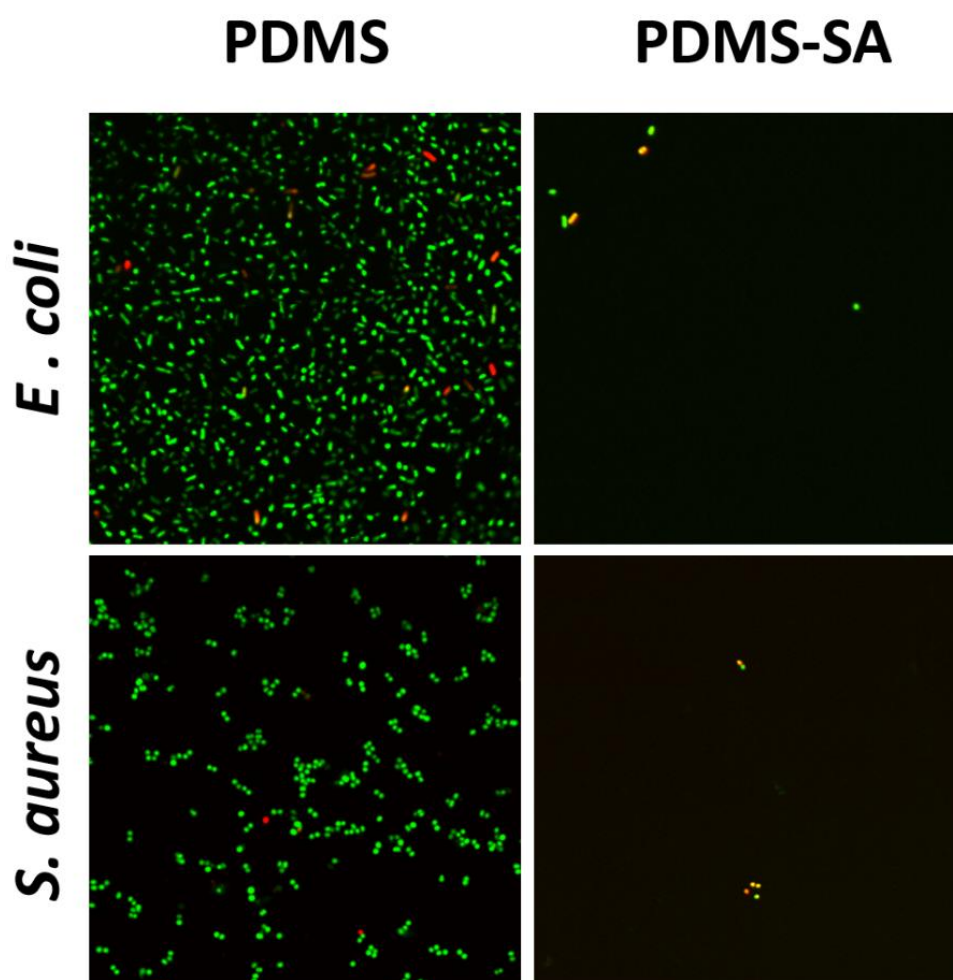


Fig. 3.3.20 Representative merged confocal scanning microscopy images of live (green) and dead (red or yellow) bacteria cultured for 24 h on the surface of PDMS-SA samples and pristine PDMS. Images size = 71 x 71 μm^2

Confirming the SEM imaging findings, confocal images of PDMS-SA samples show a dramatic reduction of bacterial density. Persistent cells display lower viability compared those attached to pristine PDMS, with 73.3 (\pm 3.4) % *E. coli* and 31.6 (\pm 11.5) % *S. aureus* alive sessile cells. These findings suggest a bactericidal effect of SA released from PDMS-SA samples following initial bacterial attachment.

CFUs counting of bacterial cells at the surface

The concentration of live bacterial cells attached to PDMS-SA and pristine PDMS was assessed via CFUs counting on *E. coli* and *S. aureus* and results are displayed in Fig 3.3.21. The extreme inhibition of bacterial attachment and viability at the surface of the SA-loaded samples was measured in a 3.85 fold reduction in cell concentration for *E. coli* and 4.01 in the case of *S. aureus*. These results show that PDMS-SA samples are able to sensibly reduce the concentration of viable bacteria adhering to the surface, demonstrating significant antibacterial activity of the released SA against sessile cells.

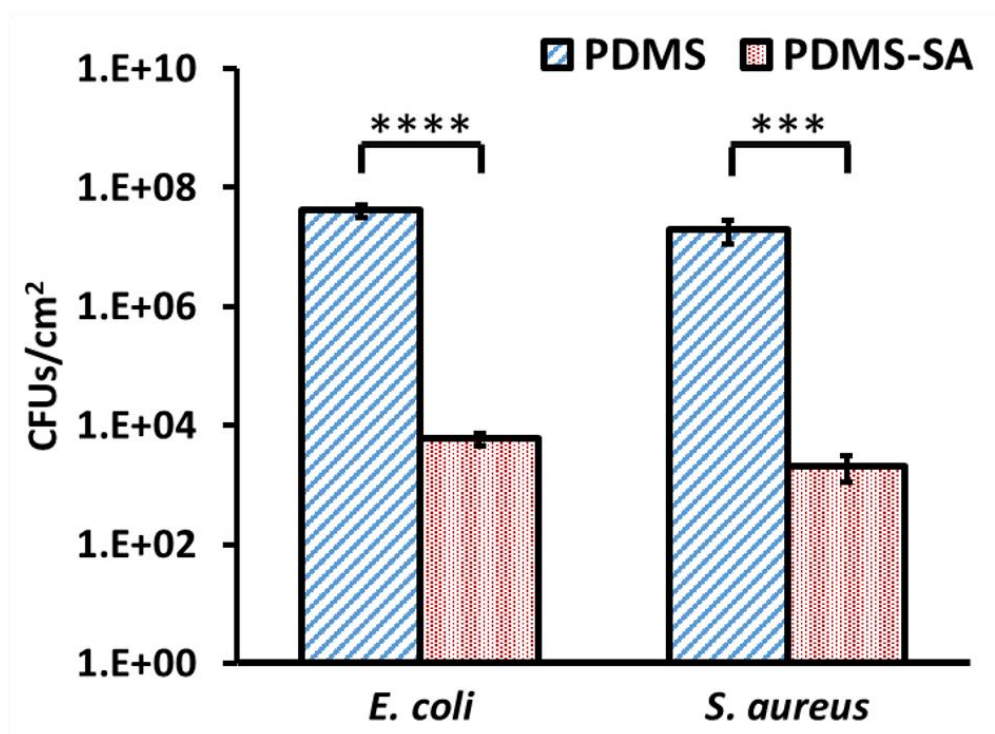


Fig. 3.3.21 Sessile *E. coli* J96 and *S. aureus* SH1000 cell counts cultured for 24 h on PDMS-SA samples and pristine PDMS. **** signifies *p*-value \leq 0.0001, *** signifies *p*-value \leq 0.001.

3.4 Conclusions

In this study, we presented a post fabrication-modification method to create a reservoir of biocide, Salicylic Acid (SA), approved for human use, within the bulk of biocompatible polydimethylsiloxane (PDMS). Atomic force microscopy and contact angle analysis showed no significant difference in topography or wettability between pristine PDMS and SA-loaded samples (PDMS-SA). Raman analysis confirmed the presence of SA in high concentration within the material's bulk, at hundreds of microns from the surface. Release experiments showed that the biocide was released in physiological conditions in a water-based buffer over a period of 72 h, with a faster release regime in the first 24 h.

AFT-IR analysis was used to investigate the mechanism of release and showed the presence of water-related bands within $\sim 1\mu\text{m}$ from the surface of a PDMS-SA sample after a 24 h release experiment, suggesting that the water-based media penetrates the sample reaching the biocide in the bulk, dissolving it and allowing it to diffuse outside of the sample.

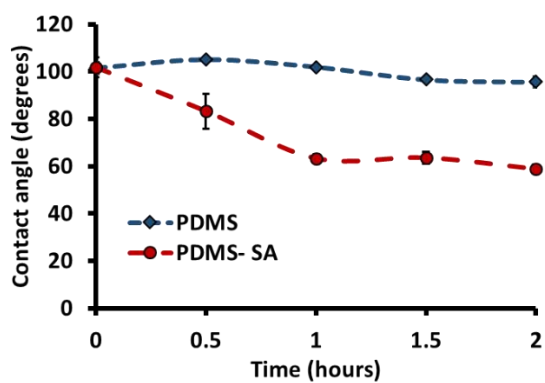
The antimicrobial effect of the released SA was tested over 24 h on Gram-positive (*S. aureus*) and Gram-negative (*E. coli*) bacteria. The minimum bactericidal concentration (MBC) of the tested species for SA was reached within the first 20 h of release, the effect of the low pH of the supernatants caused by the released SA was evaluated by incubating bacterial suspensions in the presence of HCl. The results showed that both species were able to grow in HCl solutions at the pH values matching the ones related to their MBC in SA, indicating an intrinsic antimicrobial effect of the released biocide.

Furthermore, these results were confirmed by viability tests, in which there were no detectable bacteria following 24h incubation with PDMS-SA samples, while bacteria incubated with pristine PDMS proliferated, reaching concentrations higher than 10^8 CFUs/ml.

SEM imaging and viability tests conducted on bacterial cells attached to PDMS-SA samples showed a dramatic reduction in the density of bacterial cells attached to PDMS-SA samples when compared to pristine PDMS, with a 3.85 fold reduction in sessile cells concentration for *E. coli* and 4.01 for *S. aureus*.

In conclusion, the post fabrication-modification method we implemented created a reservoir of biocide in an inert polymeric material, giving it antimicrobial properties without altering its surface chemistry and topography. These findings, along with the characteristic biocompatibility and elasticity of PDMS, make our approach suitable for future tests within wound dressings and urinary catheters applications. This approach could also be translated to existing medical devices and be used to prevent surface colonisation by Gram-positive and Gram-negative bacteria.

3.5 Annex





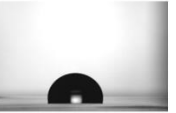







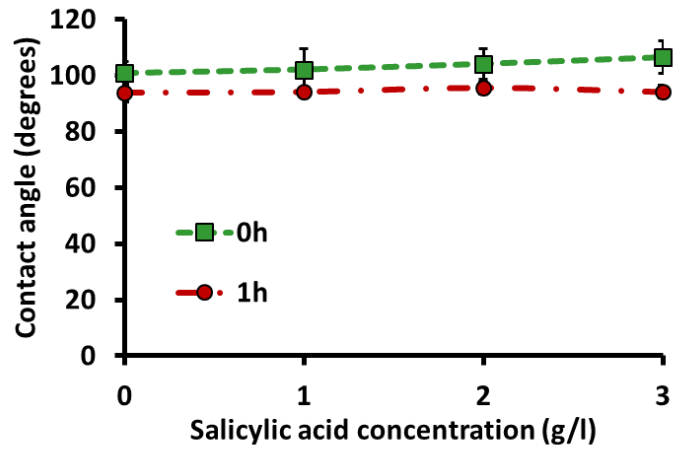
Time (hours)	0	0.5	1	1.5	2
PDMS	 101.5 ± 2.3°	 105 ± 0.1°	 101.9 ± 0.4°	 96.6 ± 0.8°	 95.6 ± 2.3°
PDMS-SA	 101.7 ± 4.3°	 83.2 ± 7.4°	 63.3 ± 1.7°	 63.5 ± 2.4°	 58.8 ± 1.9°

Fig. 3.5.1 Time-dependent static contact angle of pristine PDMS and PDMS-SA measured over 2 hrs. Measurements were taken using model buffer. The decrease in size of the drop is likely due to evaporation.




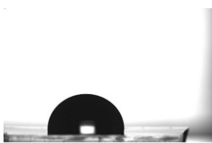

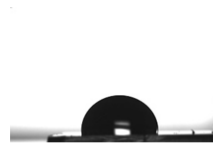


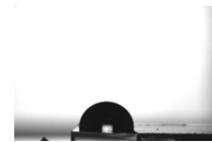

SA concentration	0 g/l	1 g/l	2 g/l	3 g/l
0 h	 100.7 ± 4.3°	 102 ± 7.4°	 104.1 ± 5.5°	 106.5 ± 5.8°
1 h	 93.9 ± 2.9°	 94.1 ± 1.3°	 95.5 ± 1.7°	 94.1 ± 1.7°

Fig. 3.5.2 Contact angle of PDMS measured using model buffer with different concentrations of Salicylic acid. Measurements were repeated after 1h.

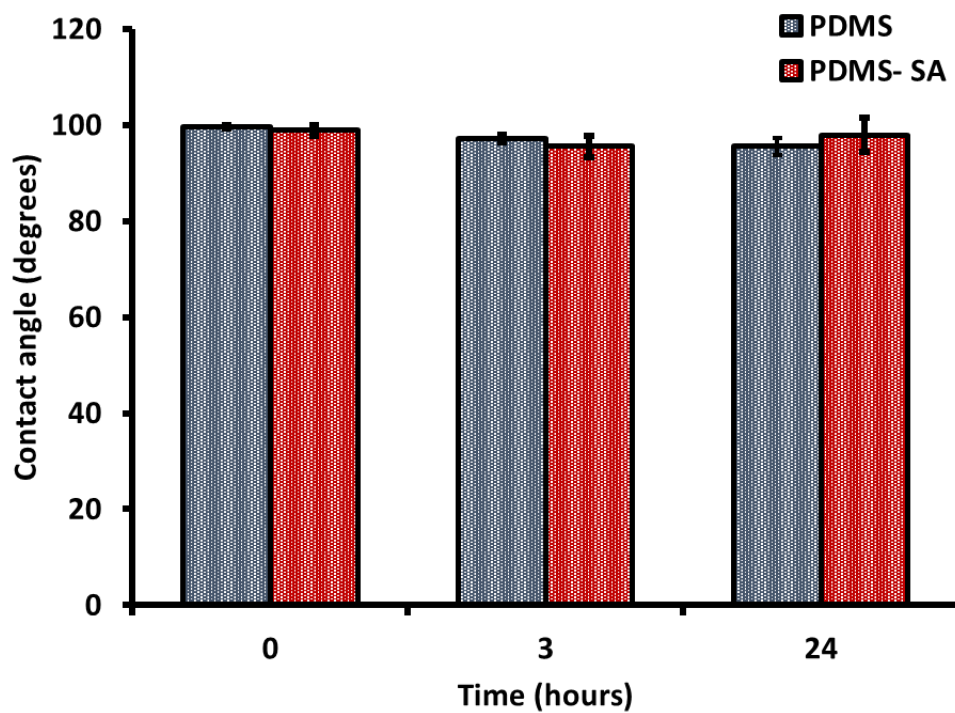


Fig. 3.5.3 Static contact angle of pristine PDMS and PDMS-SA measured on dry samples (0 hrs) and on samples left for 3 and 24 hrs in model buffer. Measurements were taken using model buffer.

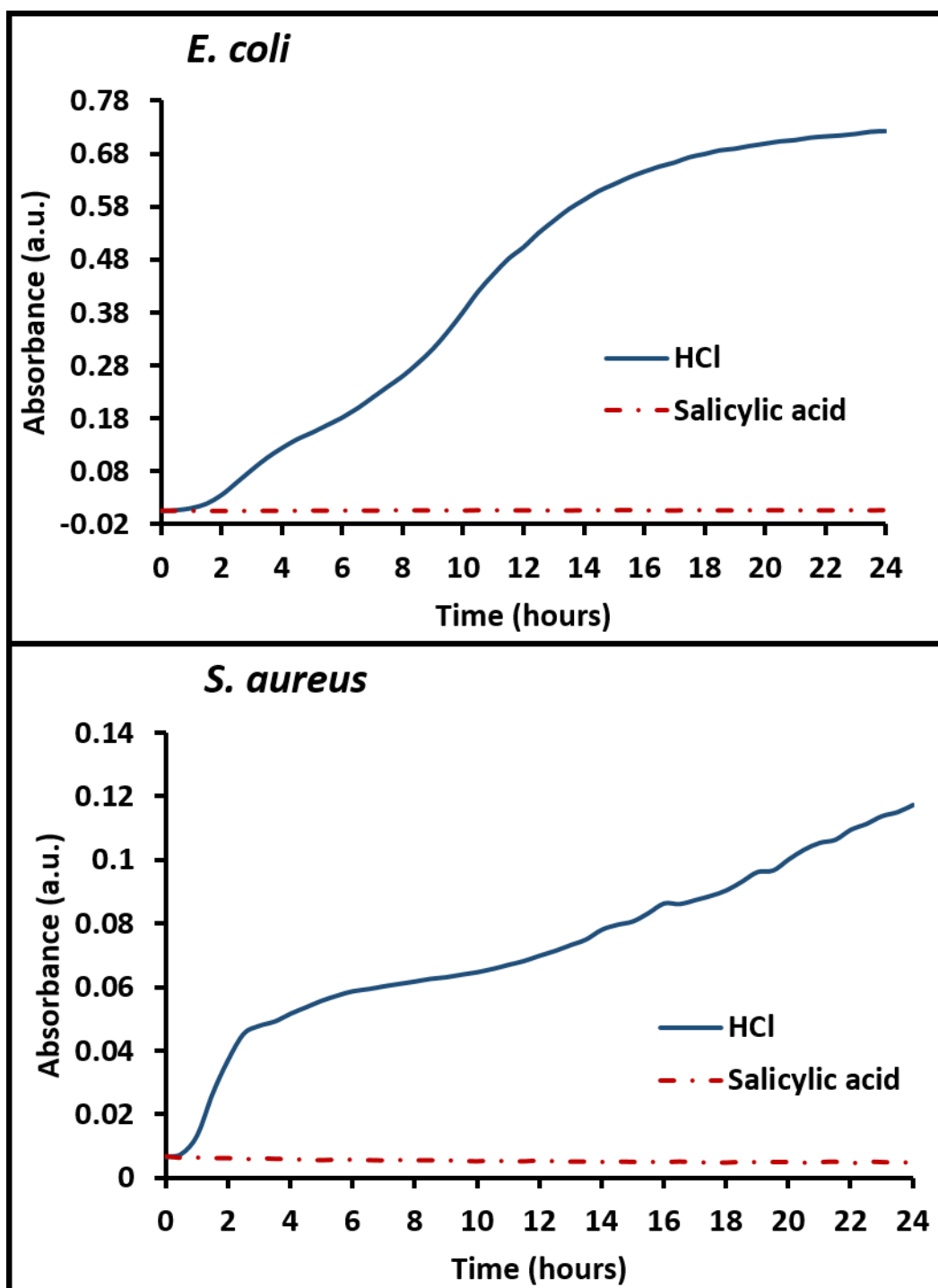


Fig. 3.5.4 Absorbance of bacterial suspensions measured over 24 hours. *E. coli* J96 (above) and *S. aureus* SH1000 (below) were grown in LB medium at the MBC of SA for each species (red) and at the same pH in the presence of HCl (blue)

3.6 References

[1] PDMS (Polydimethylsiloxane): a review

Casquillas GV, Houssin T

<https://www.elveflow.com/microfluidic-reviews/general-microfluidics/the-poly-di-methyl-siloxane-pdms-and-microfluidics-2/> (accessed 13th of September 2020)

[2] Characterization of polydimethylsiloxane (PDMS) properties for biomedical micro/nanosystems

Mata A, Fleischman AJ, Roy S

Biomed Microdevices 7(4) (2005) 281-293

[3] Inorganic Polymers

Mark JE, Allcock HR, West R

Oxford University Press, 2nd Edition, 2005

[4] Effects of strain rate, mixing ratio, and stress-strain definition on the mechanical behavior of the polydimethylsiloxane (PDMS) material as related to its biological applications

Khanafer K, Duprey A, Schlicht M, Berguer R

Biomed Microdevices 11(2) (2009) 503-508

[5] Improved biocompatibility of silicone rubber by removal of surface entrapped air nuclei

Kalman PG, Ward CA, McKeown NB, McCullough D and Romaschin AD

J Biomed Mater Res 25 (1991) 199-211

[6] Absorptive supramolecular elastomer wound dressing based on polydimethylsiloxane

Deng W, Lei Y, Zhou S, Zhang A, Lin Y

RSC Adv. 6, (2016) 51694–51702

[7] Preventing biofilm formation and associated occlusion by biomimetic glycolyxlike polymer in central venous catheters

Chauhan A, Bernardin A, Mussard W, et al.

J. Infect. Dis 210(9) (2014) 1347–1356

[8] Urinary Tract Infections: Molecular Pathogenesis and Clinical Management

Mulvey MA, Klumpp DJ, Stapleton AE

John Wiley & Sons, 2nd edition, 2020.

[9] Silicone elastomers for reduced protein adsorption

Chen H, Brook MA, Sheardown H

Biomaterials 25(12) (2004) 2273-2282

[10] Adaptive evolution in single species bacterial biofilms

Kraigsley AM, Finkel SE

FEMS Microbiol Lett. 293(1) (2009) 135-140

- [11] **Biofilms: an emergent form of bacterial life**
Flemming HC, Wingender J, Szewzyk U, Steinberg P, Rice SA, Kjelleberg S.
Nat Rev Microbiol. 14(9) (2016) 563-575
- [12] **Hemocompatibility Assessment of 3C-SiC for Cardiovascular Applications**
Schettini N
Silicon Carbide Biotechnology, 1st Edition, 2012, 153-208
- [13] **Suppressing Surface Reconstruction of Superhydrophobic PDMS Using a Superhydrophilic Zwitterionic Polymer**
Keefe AJ, Brault ND, Jiang S
Biomacromolecules 13(5) (2012) 1683–1687
- [14] **Formation of more stable hydrophilic surfaces of PDMS by plasma and chemical treatments**
Dhananjay B, Malek K
Microelectronic Engineering 83 (2006) 1277-1279
- [15] **Biofunctionalization of silicone polymers using poly(amidoamine) dendrimers and a mannose derivative for prolonged interference against pathogen colonization**
Lopez AI, Kumar A, Planas MR, Li Y, Nguyen TV, Cai C
Biomaterials 32(19) (2011) 4336-4346
- [16] **Polyacrylamide brush coatings preventing microbial adhesion to silicone rubber**
Fundeanu I, Van Der Mei HC, Schouten AJ, Busscher HJ
Colloids and Surfaces B: Biointerfaces 64(2) (2008) 297-301
- [17] **Does metal coating improve the durability of silicone voice prostheses?**
Arweiler-Harbeck D, Sanders A, Held M, Jerman M, Ehrich H, Jahnke K
Acta Otolaryngol. 121(5) (2001) 643-646
- [18] **Surface modification of poly(dimethylsiloxane) through oxygen and nitrogen plasma treatment to improve its characteristics towards biomedical applications**
Gomathi N, Mishra I, Varma S, Neogi S
Surface Topography: Metrology and Properties (3) (2015) 035005
- [19] **Surface grafting of a thermoplastic polyurethane with methacrylic acid by previous plasma surface activation and by ultraviolet irradiation to reduce cell adhesion**
Alves P, Pinto S, Kaiser JP, Bruinink A, De Sousa HC, Gil MH
Colloids Surf B Biointerface 82(2) (2011) 371-377
- [20] **On the Aging of Oxygen Plasma-Treated Polydimethylsiloxane Surfaces**
Morra M, Occhiello E, Marola R, Garbassi F, Humphrey P, Johnson D
J. Colloid Interface Sci. 137(1) (1990) 11-24
- [21] **Modification of polysiloxane polymers for biomedical applications: a review**
Abbasi F, Mirzadeh H, Katbab AA
Polym Int 50 (2001) 1279-1287

- [22] **Silicone rubber-hydrogel composites as polymeric biomaterials**
Hron P, Slechtová J, Smetana K, Dvoránková B, Lopour P
Biomaterials 18(15) (1997) 1069-1073
- [23] **Development of antibacterial and high light transmittance bulk materials: Incorporation and sustained release of hydrophobic or hydrophilic antibiotics**
Wang B, Liu H, Zhang B, Han Y, Shen C, Lin Q, Chen H
Colloids and Surfaces B: Biointerfaces 141 (2016) 483-490
- [24] **PDMS tri-block copolymers bearing quaternary ammonium salts for epidermal antimicrobial agents: Synthesis, surface adsorption and non-skin- penetration**
Lei Y, Zhou S, Dong C, Zhang A, Lin Y
Reactive and Functional Polymers 124 (2018) 20-28
- [25] **Recent advances on topical antimicrobials for skin and soft tissue infections and their safety concerns**
Lam PL, Lee KKH, Wong RSM, et al.
Crit Rev Microbiol. 44(1) (2018) 40-78
- [26] **Wound-related allergic/irritant contact dermatitis**
Alavi A, Sibbald RG, Ladizinski B, et al.
Adv. Skin Wound Care 29 (2016) 278–286
- [27] **Adverse drug reactions and organ damage: the liver**
Licata A
Eur. J. Intern. Med. 28 (2016) 9–16
- [28] **Solvent Compatibility of Poly(dimethylsiloxane)-Based Microfluidic Devices**
Lee JN, Park C, Whitesides GM
Anal. Chem. 75(23) (2003) 6544–655
- [29] **Swelling of PDMS networks in solvent vapours; applications for passive RFID wireless sensors**
Rumens CV, Ziai MA, Belsey KE, Batchelor JC, Holder SJ
J. Mater. Chem. C 3 (2015) 10091-10098
- [30] **Physical Techniques**
Collins AM
Nanotechnology Cookbook, 1st Edition, (2012) 205-253
- [31] **Winter swelling behavior of partially cross-linked polymers: a ternary system**
Souvik N, Henning H
Macromolecules 38 (2005) 4447-4455
- [32] **Biomaterial modification of urinary catheters with antimicrobials to give long-term broad spectrum antibiofilm activity**
Fisher LE, Hook AL, Ashraf W, et al.
Journal of Controlled Release 202 (2015) 57–64

- [33] **Salicylic acid beyond defence: its role in plant growth and development**
Rivas-San Vicente M, Plasencia J
Journal of Experimental Botany 62(10) (2011) 3321–3338
- [34] **Salicylic Acid and Some of Its Derivatives as Antibacterial Agents for Viscose Fabric**
Kantouch, A, El-Sayed AA, Salama M, El-Kheir AA, Mowafi S
Int. J. Biol. Macromol. 62 (2013) 603–607
- [35] **Excellent Clinical Results With a New Preparation for Chemical Peeling in Acne: 30% Salicylic Acid in Polyethylene Glycol Vehicle**
Dainichi T, Ueda S, Imayama S, Furue M
Dermatologic Surg. 34(7) (2008) 891–899
- [36] **Salicylic Acid Peels for the Treatment of Acne Vulgaris in Asian Patients**
Lee HS, Kim IH
Dermatol. Surg. 29 (12) (2003) 1196–1199
- [37] **Infrared and Raman spectroscopical studies of salicylic and salicylate derivatives in aqueous solution**
Humbert B, Alnot M, Quile`s F
Spectrochimica Acta Part A 54 (1998) 465–476
- [38] **The effects of salicylate on bacteria**
Price CTD, Lee IR, Gustafson JE
The International Journal of Biochemistry & Cell Biology 32 (2000) 1029 –1043
- [39] **Effect of Salicylic Acid on the Membrane Proteome and Virulence of Pseudomonas aeruginosa**
Bandara MS, Zhu P, Hume H, Willcox E
Invest Ophthalmol Vis Sci. 57 (2016) 1213–1220
- [40] **Biodegradation of poly(anhydride-esters) into non-steroidal anti-inflammatory drugs and their effect on Pseudomonas aeruginosa biofilms in vitro and on the foreign-body response in vivo**
Bryers JD, Jarvis RA, Lebo J, Prudencio A, Kyriakides TR, Uhrich K
Biomaterials 27 (2006) 5039–5048
- [41] **Salicylic Acid Decreases Extracellular Biofilm Production by Staphylococcus epidermidis: Electron Microscopic Analysis**
Teichberg S, Farber B F, Wolff A G, Roberts B
J. Infect. Dis. 167(6) (1993) 1501–1503
- [42] **A degradation product of the salicylic acid pathway triggers oxidative stress resulting in down-regulation of Bacillus subtilis biofilm formation on Arabidopsis thaliana roots**
Rudrappa T, Quinn WJ, Stanley-Wall NR, Bais HP
Planta 226(2) (2007) 283–297
- [43] **Salicylic acid-releasing polyurethane acrylate polymers as anti-biofilm urological catheter coatings**
Nowatzki PJ, Koepsel RR, Stoodley P, et al.
Acta Biomater. 8(5) (2012) 1869–1880

- [44] **Effect of Salicylate on Expression of Flagella by Escherichia coli and Proteus, Providencia, and Pseudomonas spp.**
Kunin CM, Hua TH, Bakaletz LO
Infect Immun. 63(5) (1995) 1796-1799
- [45] **Salicylic Acid Affects Swimming, Twitching and Swarming Motility in Pseudomonas aeruginosa, resulting in Decreased Biofilm Formation**
Chow, Samuel M W et al.
Journal of Experimental Microbiology and Immunology (JEMI) 15 (2011) 22-29
- [46] **Salicylic acid-based poly(anhydride esters) for control of biofilm formation in Salmonella enterica serovar Typhimurium**
Rosenberg LE, Carbone AL, Römling U, Uhrich KE, Chikindas ML
Let. Appl. Microbiol 46(5) (2008) 593–599
- [47] **Raman, mid-infrared, near-infrared and ultraviolet–visible spectroscopy of PDMS silicone rubber for characterization of polymer optical waveguide materials**
Cai D, Neyer A, Kuckuk R, Heise HM
Journal of Molecular Structure 976 (2010) 274–281
- [48] **Light at the interface: the potential of attenuated total reflection infrared spectroscopy for understanding heterogeneous catalysis in water**
Mojet BL, Ebbesen SD, Lefferts L
Chem. Soc. Rev. 39 (2010) 4643–4655
- [49] **Urinary tract infections: epidemiology, mechanisms of infection and treatment options**
Flores-Mireles AL, Walker JN, Caparon M, Hultgren SJ
Nat Rev Microbiol. 13(5) (2015) 269–284
- [50] **Construction and Expression of Recombinant Plasmids Encoding Type 1 or D-Mannose-Resistant Pili from a Urinary Tract Infection Escherichia coli Isolate**
Hull RA, Gill RE, Hsu P, Minshew BH, Falkow S
Infect Immun. 33(3) (1981) 933-938
- [51] **Staphylococcus aureus SH1000 and 8325-4: comparative genome sequences of key laboratory strains in staphylococcal research**
O’Neill AJ
Letters in Applied Microbiology 51 (2010) 358–361
- [52] **Agents that increase the permeability of the outer membrane**
Vaara, M
Microbiol. Rev. 56 (1992) 395–411
- [53] **Enhancement of Escherichia coli and Staphylococcus aureus antibiotic susceptibility using sesquiterpenoids.**
Simões M, Rocha S, Coimbra MA, Vieira MJ
Med. Chem. 4 (2008) 616–623

- [54] **Antimicrobial activity of selected phytochemicals against Escherichia coli and Staphylococcus aureus and their biofilms**
Monte J, Abreu AC, Borges A, Simões LC, Simões M
Pathogens 3 (2014) 473-498
- [55] **Synergistic effects of anacardic acids and methicillin against methicillin resistant Staphylococcus aureus**
Muroi H, Nihei K, Tsujimoto K, Kubo I
Bioorg. Med. Chem. 1(2) (2004) 583–587
- [56] **Accuracy of Plate Counts**
Sutton S
Journal Of Validation Technology 17(3) (2011) 42-46
- [57] **Biofilms on Indwelling Vascular Catheters**
Passerini L, Lam K, Costerton JW, King EG
Crit. Care Med. 20(5) (1992) 665–673
- [58] **Development of a Standard Test To Assess the Resistance of Staphylococcus Aureus Biofilm Cells to Disinfectants**
Luppens SB, Reij MW, van der Heijden RW, Rombouts FM, Abee T.
Appl. Environ. Microbiol. 68 (9) (2002) 4194–4200
- [59] **Propidium Iodide Nucleic Acid Stain**
<https://www.thermofisher.com/order/catalog/product/P1304MP?SID=srch-srp-P1304MP#/P1304MP?SID=srch-srp-P1304MP> (accessed on the 10th of September 2020)
- [60] **A review of the toxicological and environmental hazards and risks of tetrahydrofuran**
Fowles J, Boatman R, Bootman J, et al.
Crit. Rev. Toxicol. 43(10) (2013) 811–828
- [61] **The Effects of Surface Topography on the Accumulation of Biofouling**
Kerr A, Cowling MJ
Philos. Mag. 83 (2003) 2779–2795
- [60] **Promising Future Processing Technology**
Doi T, Marinescu ID, Kurokawa S
Advances in CMP Polishing Technologies, 1st Edition, 2012, 229-295
- [62] **Atomic force microscopy in biofilm study**
Chatterjee S, Biswas N, Datta A, Dey R, Maiti P.
Microscopy (Oxf). 63(4) (2014) 269-278
- [63] **Surface characterization techniques for determining the root-mean-square roughness and power spectral densities of optical components**
A. Duparré, J. Ferre-Borrull, S. Gliech, G. Notni, J. Steinert, and J. Bennett
Appl. Opt. 41 (2002)154-171

[64] Quantitative Characterization of the Influence of the Nanoscale Morphology of Nanostructured Surfaces on Bacterial Adhesion and Biofilm Formation

Singh AV, Vyas V, Patil R, Sharma V, Scopelliti PE, Bongiorno G, Podesta A, Lenardi C, Namdev Gade W, Milani P

PLoS One 6(9) (2011) e25029

[65] Enhancement of Protein Adsorption Induced by Surface Roughness

Rechendorff K, Hovgaard MB, Foss M, Zhdanov VP, Besenbacher F

Langmuir 22 (2006) 10885-10888

[66] The Effects of Surface Topography on the Accumulation of Biofouling

Kerr A, Cowling MJ

Philos. Mag. 83 (2003) 2779–2795

[67] Physico-chemistry of initial microbial adhesive interactions: its mechanisms and methods for study

Bos R, Van Der Mei HC, Busscher HJ

FEMS Microbiol Rev 23 (1999) 179–230

[68] Escherichia coli, Pseudomonas aeruginosa, and Staphylococcus aureus Attachment Patterns on Glass Surfaces with Nanoscale Roughness

Mitik-Dineva N, Wang J, Truong VK, Stoddart P, Malherbe F, Crawford RJ, Ivanova EP

Curr Microbiol 58 (2009) 268–273

[69] Surface characteristics influencing bacterial adhesion to polymeric substrates

Yuan Y, Hays MP, Hardwidge PR, Kim J

RSC Adv. 7 (2017) 14254-14261

[70] Effect Of Intramolecular Hydrogen Bonding On Ionization Constants Of Substituted Salicylic Acids

Dunn GE, Kung FL

Canadian Journal of Chemistry 44 (2011) 1261-1269

[71] Dissipative Particle Dynamics Investigation of the Transport of Salicylic Acid through a Simulated In Vitro Skin Permeation Model

Otto DP, Combrinck J, Otto A, Tiedt LR, De Villiers MM

Pharmaceuticals 11 (2018) 134

[72] A review of surface roughness in antifouling coatings illustrating the importance of cut off length

Howell D, Behrends B

Biofouling 22 (2006) 401–410

Chapter 4

Insights on the first stages of biofilm formation of staphylococcal cells on nanostructured Silicon surfaces

4.1 Introduction

4.1.1 The first stages of biofilm formation on surfaces

Bacterial biofilms are one of the most widely distributed and successful lifestyles on earth, due to their adaptability and persistency. The most effective course of action to limit the spreading of biofilms, rather than remediation, is preventing initial colonisation of bacteria [1].

Biofilms are defined as aggregates of microorganisms in which cells are frequently embedded in self-produced matrices of extracellular polymeric substances (EPS) that are adherent to each other and/or a surface [2]. Biofilms allow bacterial cells to live in a multicellular community surrounded by this protective matrix that consists of polysaccharides, extracellular DNA, proteins and water. The term 'aggregate' accounts for cell-to-cell contact points that take place amongst most cells in a multi-layered system, either in surface-attached biofilms, in which only the first bacterial layer is in direct contact with the substrate, or in flocs, defined as mobile biofilms that form in the absence of a solid substrate [2].

The solid-liquid interface between a solid surface and an aqueous medium (e.g., water, blood) provides an ideal environment for bacterial attachment and growth, due to numerous advantages compared to the planktonic state, including increased

nutrient availability and protection from disinfectants, phagocytes and xenobiotic stress [3]. Surface colonisation by bacteria leading to biofilm development is a phenomenon increasingly recognised for its socio-economic impact on several aspects of society, from bio-induced corrosion of industrial piping to serious implications on human health [1]. As an example, infections in orthopaedic implants have been observed to occur in 1.5-2.5 % in primary hip and knee arthroplasties and 3.2-5.6 % during the revision surgery [4], as biomaterial-associated infections in orthopaedic implants lead ultimately to osteomyelitis with devastating effects on the bone and the surrounding soft tissues [5, 6]. These infections become chronic when they do not respond any longer to debridement and antibiotic therapy, leading to the mobilisation of the implant and device failure [6]. In these cases the only solution is removal and substitution of the implant, although the risk of relapse remains high.

Staphylococcus aureus and *Staphylococcus epidermidis* are considered the main pathogens causing prosthetic infections (**Fig. 4.1.1**), and responsible for the majority of hospital acquired bacteremias [7, 8], probably due to the fact that they are permanent and ubiquitous colonisers of the human skin and of mucous membranes, with a high probability of device contamination during insertion [9].

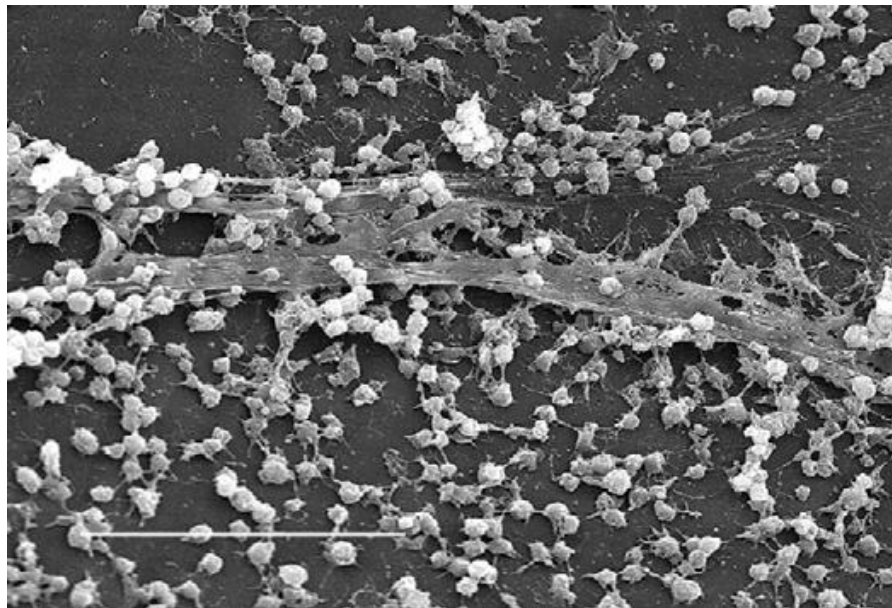


Fig. 4.1.1 Scanning electron microscopy image of a staphylococcal biofilm on the surface of a medical device. Scale bar: 20 μm . Image adapted from [10].

Over the last decades, these bacterial species have developed resistance to multiple antibiotics [11] enhanced by the formation of biofilms that resist the action of most of the available antibiotic therapies [12].

Bacterial adhesion, which is the first biological process leading to biofilm formation, can be divided in two main stages: the primary or docking stage, related to the reversible attachment of bacteria, and the secondary or locking phase, when bacterial attachment becomes irreversible [13, 14]. These processes will be discussed in the following sections.

Reversible attachment (docking stage)

Primary adhesion constitutes the first contact between a surface and a planktonic microorganism. At this stage the adhesion is reversible and maybe influenced by a number of physio-chemical variables that mediate the interactions between prokaryotic cells and surfaces [13, 14]. The organisms are brought in proximity to the surface either passively (e.g. due to the flow of a fluid over a surface) or more actively via chemotaxis and motility [2]. Once the planktonic cells are within ~1 nm from the substrate, the balance of attractive and repulsive forces generated at the interface between the cell wall and the surface dictates the success or failure of the initial adhesion. Some of these forces include electrostatic and hydrophobic interactions, Van Der Waals forces, steric hindrance, acid-base interactions, and hydrodynamic [14, 15, 2]. Electrostatic interactions tend to oppose attachment, as most bacteria and inert surfaces are negatively charged [15, 2]. In staphylococcal cells the degree of hydrophobicity of the cell wall and of the biomaterial surface are essential for the fate of primary adhesion events [16]. Currently, it is mostly accepted that hydrophilic surfaces facilitate the attachment of hydrophilic bacteria while hydrophobic surfaces facilitate the attachment of hydrophobic bacteria [17], which may lead to the conclusion that *S. aureus* and *S. epidermidis* are less likely to adhere to hydrophilic surfaces, as their cell surface has been shown to be hydrophobic [18]. However, the complexity of surface-bacteria interactions cannot

be rationalised only on the basis of physical forces, as bacterial cell envelope is dynamic and responsive to environmental and surface cues.

Irreversible attachment (locking stage)

The second stage of bacterial adhesion is related to irreversible attachment and referred to as the anchoring or locking phase. This stage employs molecularly mediated binding between specific adhesins on the cell wall and the surface [13, 14]. During this phase loosely bound bacteria consolidate their surface adhesion by secreting exopolysaccharides able to bind surface materials and/or by producing receptor-specific ligands located on pili, fimbriae, and fibrillae, or both [15]. After the locking process, adhesion is irreversible in the absence of external physical or chemical forces and the organism is attached firmly to the surface [15]. Some bacteria use several distinct adhesins to attach to surfaces depending on the environment. For example, the microorganism *Vibrio cholerae El Tor*, uses a toxin-co-regulated pilus to attach to and to colonize intestinal epithelium, while it secretes a mannose-sensitive hemagglutinin as the primary adhesin used to anchor to abiotic surfaces in aquatic environments [19]. During this stage of biofilm formation, planktonic microorganisms can form aggregates by sticking to each other or to different surface-bound organisms. All species of bacteria produce multiple adhesins, some regulated at the transcriptional level, enabling organisms to switch and adapt from sessile to planktonic state under different environmental conditions [13, 14]. In staphylococcal cells, active adhesion is related to the production of specific proteins, referred to as autolysins, that mediate the binding to abiotic surfaces. Autolysins bind to the surface via ionic or hydrophobic interactions and possess a double function: enzymatic (hydrolysing the peptidoglycan in the cell wall) and adhesive [20]. *S. aureus* recognises the contact with the surface due to cell wall deformations [21], which leads the bacterium to express adhesins at the cell wall, strengthening the adhesion forces [22].

Two specific proteins that contribute to *S. epidermidis* attachment to abiotic surfaces are the abundant surface protein AtlE [23], which has both the function of adhesin and autolysin, and the Bap protein (also known as Bhp) [24]. These two proteins are likely to contribute to the hydrophobicity of the cell surface [9].

Biofilm maturation

Once bacteria adhere irreversibly onto a surface, the biofilm maturation phase begins. This stage involves replication of surface-bound organisms while secreting extracellular components that interact with organic and inorganic molecules in the close environment, increasing the overall density and complexity of the biofilm [14]. In the case of infected biomedical implants, bacteria might take advantage of host-produced inflammatory response proteins or matrix proteins such as fibrinogen, fibronectin, and glycosaminoglycans to improve the conditioning of the colonized surface (**Fig 4.1.2**) [14]. Proteins like exopolysaccharides are predominantly secreted by bacteria in order to form the extracellular biofilm matrix [9] while teichoic acids [25] and extracellular DNA originated from lysed cells [26] may contribute to aggregation, due to the polyanionic nature of DNA [9]. Many *S. epidermidis* strains also produce a homopolymer named poly-*N*-acetylglucosamine (PNAG) that surrounds and connects *S. epidermidis* cells within the biofilm [9].

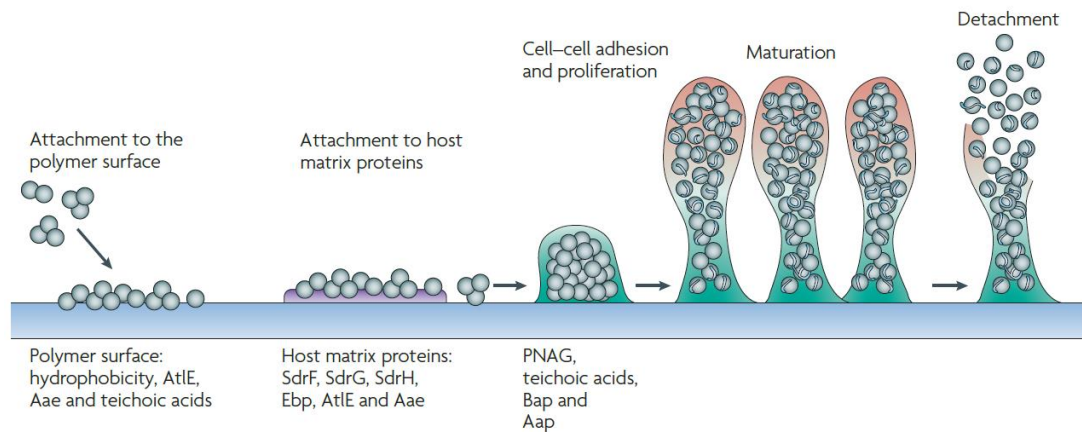


Fig. 4.1.2 Schematisation of biofilm development in *Staphylococcus epidermidis*. Attachment to an abiotic substrate is mainly dependent on hydrophobicity of the cell membrane and of the surface. After initial adhesion, exopolysaccharide (for example, poly-*N*-acetylglucosamine (PNAG), specific proteins (Bap and Aap) and macromolecules like teichoic acids drive intercellular aggregation. Mechanisms for biofilm maturation and detachment are not fully understood, but most likely involve quorum sensing-controlled expression of detergent-like peptides and proteolytic activity in exposed layers of the biofilm [9]. Image adapted from [9].

4.1.2 Bacterial division

Bacteria appear in a variety of shapes and sizes, from round and rod-shaped cells to curved, spiral and even square shapes [27]. This diversity in shape implies that prokaryotic cells rely on different mechanisms to guide their growth and division. The cell shape of most bacterial species is maintained by the cell wall, the main component of the cell wall is peptidoglycan, a macromolecule formed by glycan chains crosslinked by short peptides [27]. The role of the cell wall is to provide stability against differential intracellular–extracellular osmotic pressure, preventing cell lysis. It also needs, however, to be flexible enough to allow for changes in cell shape during growth and division [27].

Within the cell wall, the location of proteins is highly regulated in terms of spatial organization and control that during cell division, or cytokinesis, ensures the equal partition of DNA between the two new-born cells [28]. The important question that still needs to be fully resolved is how bacterial cells identify the site of division.

Peptidoglycan synthesis during cell division in *Staphylococci*

In order to grow and divide, bacteria must synthesise new cell wall, the main structural component of which is peptidoglycan [29]. Bacteria generally have two groups of proteins that coordinate peptidoglycan insertion: The *elongasome*, responsible for elongation, and the *divisome*, involved with division. Despite *Staphylococci* lacking an apparent *elongasome* machinery, throughout their cell cycle new peptidoglycan is constantly added all over the cell envelope. This process, along with peptidoglycan hydrolysis, causes *Staphylococci* cells to increase in size at a constant rate [29] (**Fig. 4.1.3**).

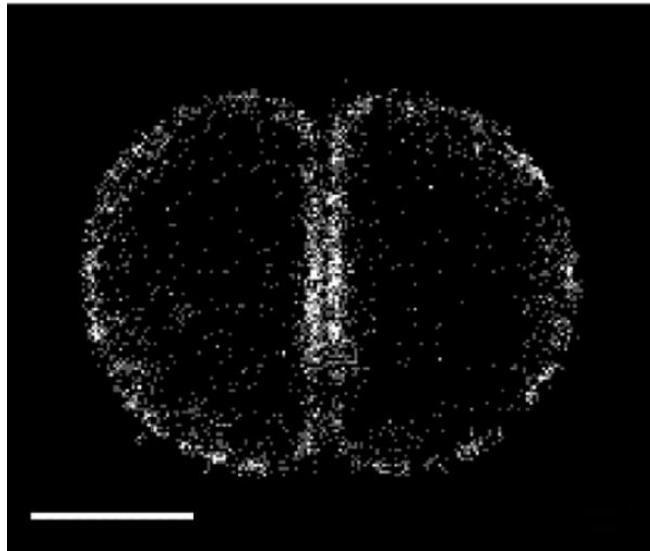


Fig. 4.1.3 Localisation microscopy image of a *S. aureus* cell labelled with ADA (azido D-alanine) clicked to Alexa Fluor 647, highlighting the sites of peptidoglycan insertion during cell division. Scale bar: 0.5 μm . Image adapted from [29].

The Staphylococcal *divisome* contains enzymes like penicillin-binding proteins (PBPs), the role of which is to catalyse the addition of new monomers to the peptidoglycan matrix; this protein complex not only catalyses the synthesis of peptidoglycan, but it may also include autolysins, able to hydrolyse peptidoglycan [30, 27].

S. aureus, the most common bacterium in the *Staphylococci* family, is an invasive pathogen and one of the most common species causing antibiotic-resistant

infections. It has been used as a minimalist model to investigate cell wall synthesis and growing mode. *S. aureus* cells contain four native PBPs, namely: the HMM class B proteins PBP1 and PBP3, which with the low-molecular-mass (LMM) protein PBP4, possess transpeptidase activity, and the high-molecular-mass (HMM) class A protein PBP2 which is bifunctional, having both transglycosylase and transpeptidase activity. PBP1, PBP2 and PBP4 are localised at the division septum, while PBP3 is believed to be part of the *divisome* (Fig 4.1.4). PBP2 is recruited to the septum by its substrate, lipid II, while PBP4, responsible of the generation of highly crosslinked peptidoglycan, is recruited to the septum by an unidentified intermediate of wall teichoic acid synthesis [30]. Due to the fact that wall teichoic acids are attached to peptidoglycan, this process is likely to occur only after septal peptidoglycan synthesis has been initiated. This delay could favour the incorporation of polysaccharides and proteins into the cell wall, which might be hindered if the peptidoglycan matrix was highly crosslinked at an earlier stage of the process [27]. After the septal peptidoglycan is synthesised by the PBPs, autolysins are required to degrade the cell wall in order to split the septum generating two daughter cells. Cryo-electron microscopy images of thin sections of *S. aureus* cells have shown the presence of a low-density zone separating two highly dense areas within the septum. These high density zones correspond to the two adjacent cell walls [32, 27]. It has been hypothesised that the action of the autolysins takes place only at the periphery of the septum and not along the entire length of the septum, due to the presence of low-density zone in the septum not extending into the surface cell wall [27].

Amongst the proteins involved in the septum formation, the most important role is played by FtsZ, an essential protein in the coordination of cell division in almost all bacterial species [29]. FtsZ assembles into the Z-ring, a cytoskeletal scaffold for the formation of the division septum [33]; the Z-ring assembly is regulated by several enzymes, including EzrA, a membrane protein which acts as an interface between FtsZ and PBPs forming a matrix to encapsule other cell division components [29].

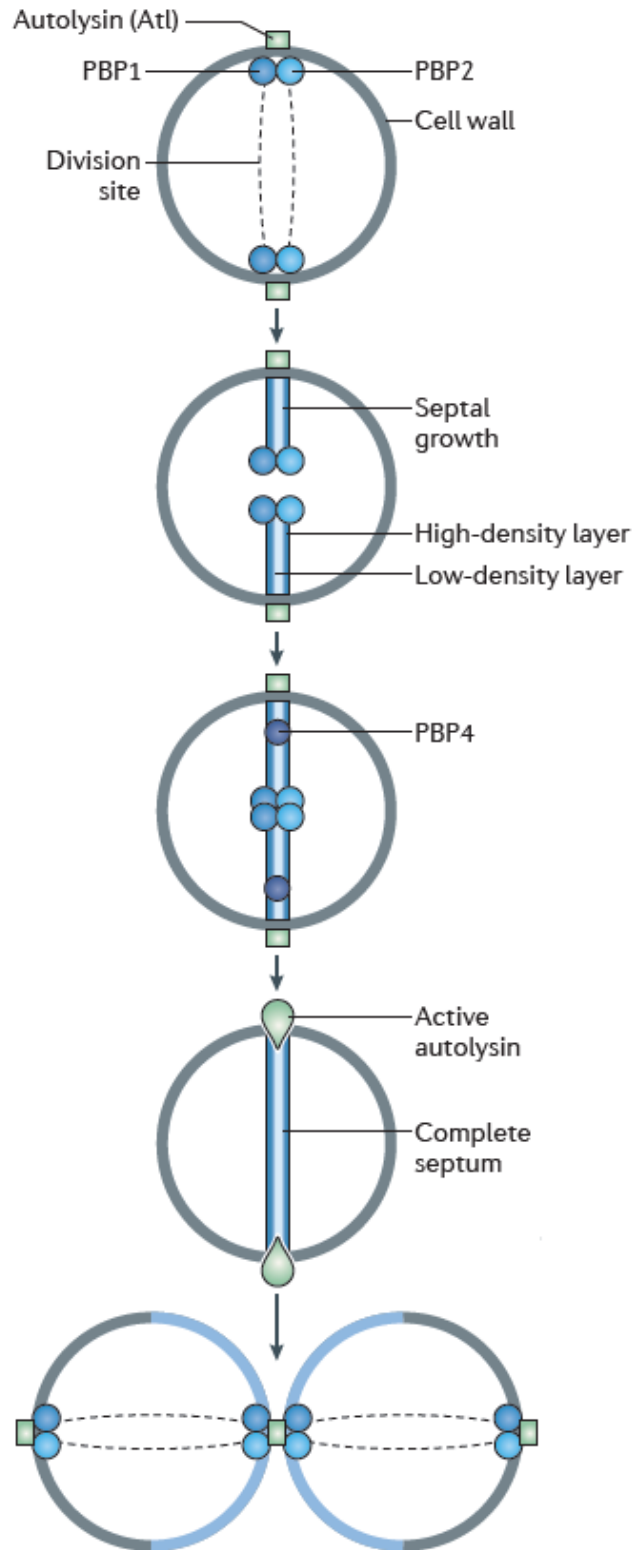


Fig 4.1.4 Cell wall synthesis in spherical cocci: the peptidoglycan synthesis takes place at the septum only, involving at least penicillin-binding proteins, PBP1 and PBP2. At a later stage of the division stage, PBP4 is recruited to the septum to increase peptidoglycan crosslinking. The role of PBP3 is currently unknown. The septum is composed of a low-density middle layer separating two high-density layers, set to become the new cell wall of the two daughter cells. Image adapted from [27].

After splitting, the septum is immediately exposed to the surrounding milieu, and the higher internal osmotic pressure pushes the flat septum outwards, forcing the new daughter cell to adopt a spherical shape (**Fig 4.1.4**). The cell re-shaping is so fast that intermediates are rarely observed by electron or fluorescence microscopy. This suggests that osmotic pressure alone (and not enzyme-mediated remodelling) is responsible for inducing the morphological transition, possibly by inducing stretching in the glycan and peptide chains, which might provide an increased surface area without the need for the cell to synthesise new cell wall [34, 27]. However, this hypothesis has not yet been confirmed.

Successive division cycles in *Staphylococci*: planktonic growing mode

Staphylococci organisms divide sequentially in three orthogonal planes over three consecutive division cycles [27]. In order to replicate with fidelity, the daughter cell needs to carry information about the previous division plane. When a spherical cell divides, it generates two daughter cells with an approximate hemispherical shape with a longer axis (parallel to the division septum) and a shorter one (perpendicular to the division septum) (**Fig 4.1.5**). Entropic forces are thought to play an important role in chromosome segregation [35, 36] as they could explain the successive division of the cell in two perpendicular planes: on division of spherical cells, the axis that will be less constrained in terms of space and therefore more entropically favourable to chromosome segregation will necessarily be the parallel to the complete septum, as the axis perpendicular to the division septum would be more constrained in terms of space (**Fig 4.1.5**).

When the chromosome segregates parallel to the equatorial division septum, the only plane lacking Noc is inevitably the one perpendicular to the previous division plane, leading the division to take place in two orthogonal planes over two division cycles (**Fig. 4.1.5**) [35, 36].

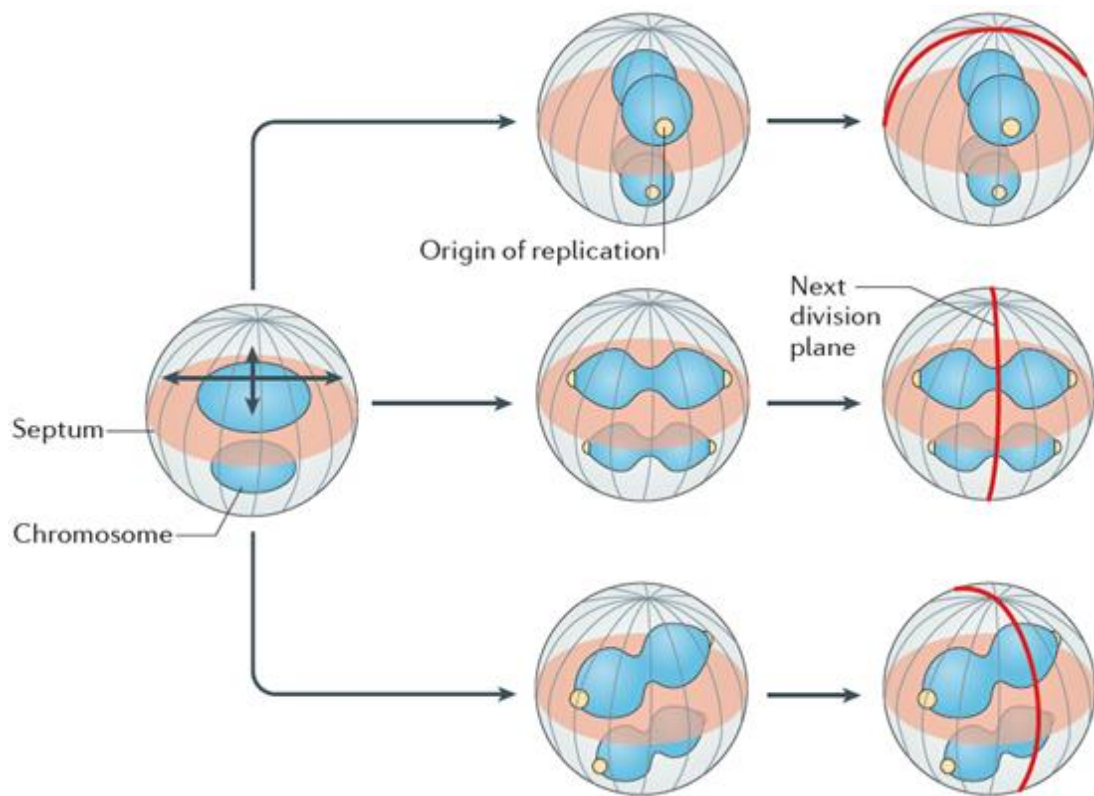


Fig. 4.1.5 *Staphylococci* growing mode: the schematic shows a cell forming the septum at the equatorial plane of division. The long black arrow represents the axis of chromosome segregation in each half of the original cell, parallel to the septum; this axis is favoured by entropy being less constrained than the others in terms of space. The red median represents the plane perpendicular to the previous division plane, free from DNA and also therefore free from the nucleoid occlusion protein (Noc)-mediated inhibition of FtsZ polymerization [37]. Image taken from [27].

4.1.3 *Staphylococci* response to nanostructured surfaces

The chemistry and topography of the surface have a strong impact on bacterial attachment and proliferation. Roberts *et al.* [38] found that, on mineral surfaces such as the iron and aluminum oxides, bacterial attachment is driven by the electrostatic interactions between the positively charged mineral surfaces and negatively charged microorganisms. The solid-phase composition of alumina silicates and localized charge heterogeneity have also been shown to influence attachment to these minerals.

Fadeeva *et al.* [39] used a femtosecond laser to fabricate micro- and nanostructured superhydrophobic titanium surfaces mimicking the topography of the lotus leaf. The resulting substrates were highly effective against the attachment of *P. aeruginosa*, while showing an enhancement in the case of *S. aureus*. The differences in morphology and size between the two bacterial species, with *P. aeruginosa* being a larger rod-shaped and *S. aureus* being a smaller spherical coccus cell, were reflected in the available contact area between the bacterium and the substrate, resulting in vastly distinct attachment preferences between the two pathogens. This study highlighted the possibility of engineering topographic substrates to selectively inhibit the attachment and growth of bacterial species while encouraging another.

A 2020 study by Jenkins *et al.* [40] focused on the bacterial response to nanopillared titanium alloy surfaces (NW-850-5) produced via thermal oxidation. As the pristine material is often used for orthopaedic implants, its antimicrobial effect was evaluated on *S. aureus*, amongst other species. The metabolic activity of the bacteria was evaluated over 10 h via the indicator assay RealTime-Glo, noticeably lower values were recorded for *S. aureus* cells incubated on NW-850-5, plateauing after 6 h, while on flat Ti alloy plates, the signal increased over the entire 10-h incubation period. Scanning electron microscopy (SEM) images (**Fig. 4.1.6**) of *S. aureus* incubated on NW-850-5 showed the cells dividing, as evident from the bacterial septum at the mid-cell, with a wide range of orientations, while adhering to the tips of the pillars. The images also showed deformation of the cell envelope, with the nanopillars indenting and changing the morphology of the cells in a contact-dependent manner; *S. aureus* showed to be less susceptible to nanopillar deformation compared to Gram-negative species, this could be partly explained by its increased peptidoglycan thickness (30–100 nm), which provides higher rigidity and turgor pressure. An in-depth analysis via transmission electron microscopy (TEM) assessed a low frequency of cell membrane penetration by the nanopillars, rarely resulting in mechanical rupture and cell lysis. As these sporadic ruptures could not solely cause the assessed reduction in cell viability, proteomic analyses was performed and identified a number of *S. aureus* differentially expressed proteins (DEPs) associated with oxidative stress, suggesting that *S. aureus* cells

incubated on NW-850-5 display higher levels of H₂O₂ levels compared to the ones on flat Ti alloy plates, a conditions frequently observed in bacteria exposed to antibiotics. Another notable mechanism observed by Jenkins *et al.* was nanopillar-induced cell impedance, which is expected to reduce the capacity of bacteria to replicate on the nanostructured Ti surfaces, causing a decrease in biofilm formation.

The attachment of *S. aureus* on nanopillared aluminium surfaces was recently

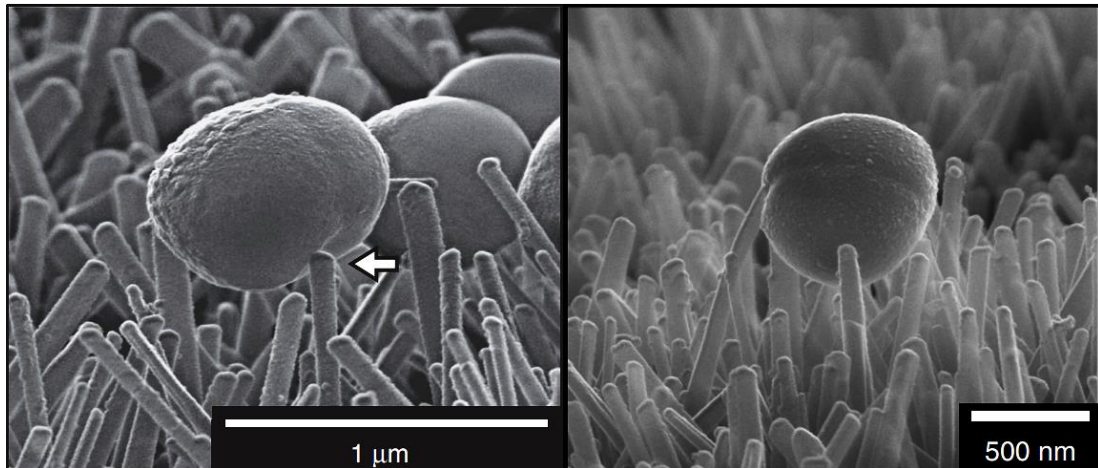


Fig. 4.1.6 SEM image showing *S. aureus* morphology on nanopillar Ti surface NW-850-5 following 3 h incubation. The white arrow highlights the region of nanopillar-induced envelope deformation. Image adapted from [40].

investigated by Hizal *et al.* [41]. The hydrophobicity was regulated by spin-coating of a nanoscopically thin layer of Teflon. SEM images (**Fig. 4.1.7**) allowed to investigate the morphology of the bacteria adhering to the nanostructured surfaces. *S. aureus* appeared to adhere both to the tips as well as in the valleys of the conically aggregated nanopillar structures. The morphology of the surface showed a periodicity similar to the dimension of the investigated bacteria and the hydrophilicity of the surface allowed the structured surface to be completely wet by the bacterial suspension, increasing adhesion configurations. Regarding bacterial surface coverage, the nanopillared surfaces showed a large reduction in *S. aureus* adhesion, compared to electropolished flat substrates.

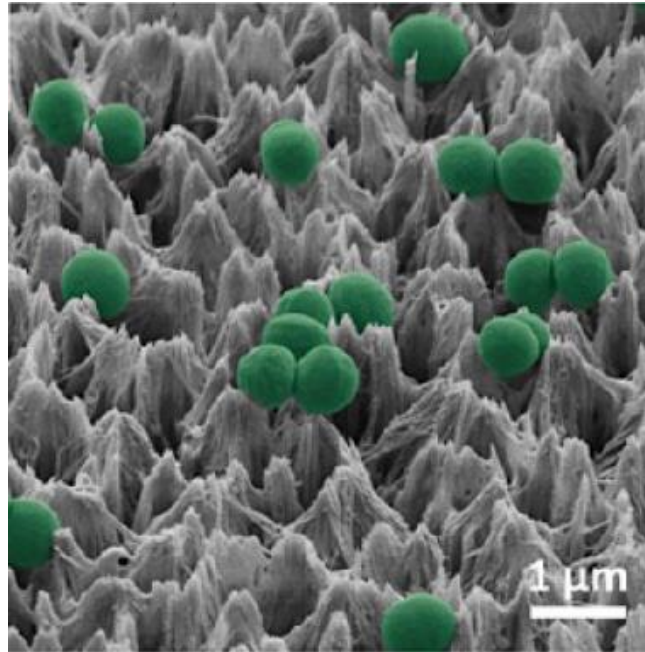


Fig. 4.1.7 SEM image showing *S. aureus* adhesion on hydrophilic nanostructured surfaces. Bacterial cells are represented in artificially added green colour. Image adapted from [41].

4.1.4 Silicon

Silicon (Si) is the second most abundant element in the earth's crust after oxygen [42, 43]. It is a tetravalent metalloid, in the same group as carbon in the periodic table, but, in comparison, less reactive. Due to its biocompatibility, in the last century flat Si semiconductors were widely used in medical devices and implants, including pacemakers [44]. Several *in vitro* and *in vivo* studies demonstrated that Si is beneficial for bone tissue structure and function [45, 43]. Recently animal studies confirmed an increase in bone density and bone turnover in osteopenic rats associated to Si application, especially in animals that were fed Calcium-reduced food [46]. In 2007 Müller *et al.* [47] demonstrated that MG-63 osteoblasts and 3T3 fibroblasts appeared to spread on plasma oxidised flat Si surfaces, indicating high adhesion and biocompatibility.

Padial-Molina *et al.* [48] were able to produce different degrees of nanoroughness on oxidized Si wafers that were etched with caustic solutions for increasing time periods. The evaluation of the interaction of MG-63 osteoblast-like cells with these surfaces showed that the nanoroughness improved MG-63 cell behaviour in terms of cell morphology, proliferation and immunophenotype (**Fig 4.1.8**).

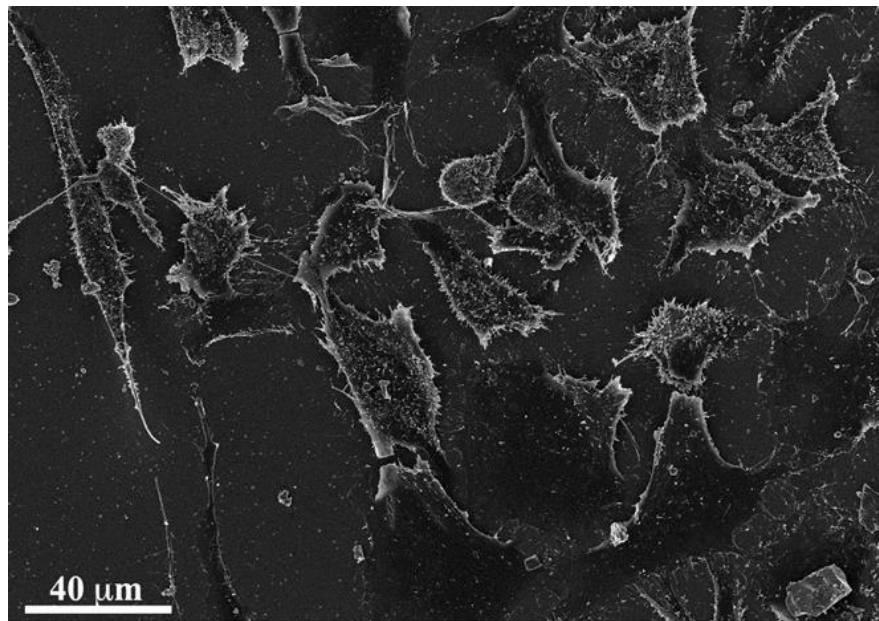


Fig. 4.1.8 MG-63 osteoblast culture on a silica rough surface ($R_a = 16.6$ nm) showing a highly spread, random distribution and dispersion (SEM, 1440x). Image adapted from [48].

Nanostructured Si surfaces

The surface properties of Si can be controlled via several fabrication methods that modify the topography at the nanoscale. Nanoporous Si materials have been tested for biomedical application after different types of treatment [49], biocompatibility experiments with human ocular cells showed that this type of material was able to support attachment and growth of the cells. The nanostructured porous Si was demonstrated to be non-toxic, non-inflammatory and biodegradable [40], Nanostructured porous Si has found also applications as scaffold for orthopaedic implants [50], and appropriately-derivatised porous Si have shown to support the attachment and growth of a variety of mammalian cells [51, 52, 44].

A different kind of nanostructured Si surface is based on Si nanowire (SiNW) arrays, which are Si surfaces functionalised with highly oriented filamentary Si crystals with ~ 100 nm diameter and up to several micrometres height [53]. SiNWs arrays show a high *in vitro* biocompatibility [54, 55] and the adhesion and growth of mammalian cells on nanostructured topographies has been investigated with the use of SiNWs substrates [56, 57]. However, the adhesion and division of bacteria on SiNWs remains relatively unexplored [58].

A number of studies have shown how surface structural cues such as size, spacing, aspect ratio and roughness can either promote or hinder the irreversible adhesion of bacteria [59, 60, 61]. Even subtle differences in surface roughness can affect the number of attached cells and the number of exopolysaccharides (EPS) secreted [61, 62, 63].

In a recent study by Susarrey-Arce *et al.* [58], SiNWs were functionalised with (3-aminopropyl)triethoxysilane for incorporation of chlorhexidine digluconate, an approved biocide. This system showed an antimicrobial effect on planktonic and surface-attached *Escherichia coli* and *S. aureus* cells. SEM imaging showed bacterial proliferation on unfunctionalised SiNWs (**Fig. 4.1.9**).

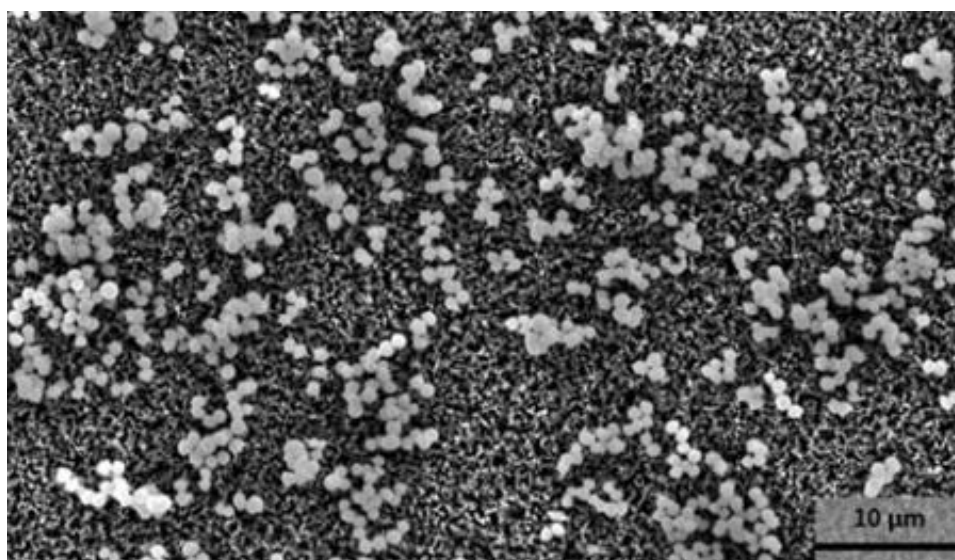


Fig. 4.1.9 Top-view SEM image of *S. aureus* cells after 8 h of culture on unfunctionalised SiNWs. Image adapted from [58].

The present chapter will focus on the investigation of adhesion and division of *S. aureus* and *S. epidermidis*, the two bacterial species mainly responsible for prosthetic infections, on Si, one of the materials currently used in medical implants. The bacterial morphology and division modes for these species will be investigated on flat surfaces and SiNW arrays: nanostructured substrates that mimic the rough topography currently in use in orthopaedic implants to stimulate osteogenesis. The SEM images in this work allow the identification of the points of contact of microcolonies with the surface, to describe in detail the morphology of the single cells and the effect that the topography-induced direction of division has on the final colony morphology.

4.2 Experimental Details

4.2.1 Fabrication and characterisation of Silicon NanoWire (SiNW) arrays

SiNW wafers were provided by J. G. E. Gardeniers, and R. M. Tiggelaar (MESA+ Institute for Nanotechnology, University of Twente, The Netherlands).

Fabrication of SiNWs

SiNW were fabricated on flat Si wafers (p-type boron doped, (100)-orientation, resistivity 5– 10 Ω cm, 100 mm diameter, thickness 525 mm, single side polished; Okmetic, Finland). Si wafers were cleaned by immersion in 100% nitric acid (UN2031; OM Group) for 10 min and then in boiling 69% nitric acid (BASF, 51153574) for 15 min. The following step consisted in the substrates being rinsed with deionised water and spin dried. UV-lithography was used to define a regular pattern of 10 mm x 10 mm, which was used to form the SiNWs in an 8 mm x 8 mm area. The patterned surfaces were then post-baked for at least 10 min at 120 °C in air. SiNWs were formed in the lithographically patterned areas using a two-step metal assisted chemical etching (MACE) process [64]. The nanopatterned surfaces were subsequently submerged in a 5 mM solution of AgNO_3 (Sigma-Aldrich, 99%) in 10% aqueous HF (BASF-51151083) for 1 min in the dark. The substrates were then directly immersed in a solution of DI water, 50%-HF and H_2O_2 (BASF, 55316830) (volumetric ratio DI:HF: H_2O_2 = 77.5:20:2.5), and etched for 20 min (in the dark– etch rate ca. 0.6 mm min⁻¹). After this process, the samples were rinsed using deionised water. The AgNPs were removed from the substrates by immersing them in 69% nitric acid (HNO_3 ; BASF, 51153574) at room temperature for 65 h and subsequent rinsing with DI water. SiNW samples were then cleaned using Piranha-solution (a 3:1 volumetric mixture of sulphuric acid (H_2SO_4 ; BASF, UN 1830) and H_2O_2 ; temperature 95 °C, cleaning time 15 min) in order to remove all traces of photoresist, after this process they were rinsed with DI water and dried under

nitrogen flow. Finally, individual samples of 1 cm x 1 cm size were cut using a dicing machine (Disco DAD-321).

Imaging of sessile bacteria on flat Si and SiNWs

S. aureus (DSM 346) and *S. epidermidis* (ATCC 12228) were transferred from frozen stock to a fresh agar plate and incubated overnight at 37 °C. Three colonies of each bacterial species were taken from the agar plate with a sterile plastic loop, transferred to fresh nutrient broth (NB) medium (Oxoid, Thermofisher) and grown overnight in a shaking incubator (200 rpm, at 37 °C). SiNW surfaces and flat Si wafers underwent sterilisation under UV light for 20 min and were then placed in a sterile 24- well plate. 1 mL of 10^5 CFUs/mL bacterial suspension in NB was subsequently added to each of the wells and the samples were incubated for 8 h at 37°C. Viability and imaging assays using bacteria were performed in triplicate.

Viability of sessile bacteria

The viability of bacteria adhering to surfaces was studied via confocal laser scanning microscopy (CLSM). At the end of the incubation period, flat Si and SiNW surfaces were washed 3 times with sterile 0.85% (w/w) NaCl solution and stained with Live/Dead BacLight bacterial viability kit (Molecular Probes, L7012). In this test, each sample was incubated in a 24-well plate for 15 min in the dark at room temperature in 1 mL of a sterile 0.85% solution containing a mixture of SYTO 9 and propidium iodide (PI). These nucleic acid stains differ in their absorption and emission wavelengths and their capacity to penetrate bacterial cell walls. SYTO 9 (green stain) is capable to penetrate all live and dead Gram-positive and Gram-negative bacteria in a population (i.e. bacteria with both intact and disrupted membranes) [65]. In contrast, PI is only capable of penetrating bacteria with damaged cell walls and binds strongly between the bases in the DNA with little or no sequence preference [66]. Consequently, when both stains are present in a bacterial cell with

a damaged membrane, PI displaces SYTO 9 from the nucleic acid chains, leading to emit a red fluorescent emission [66]. Despite this staining method to identify live and dead bacterial cells has been used for decades, the exact mechanism of interaction of SYTO 9 with nucleic acids is not fully understood [66]. After staining, the samples were immediately imaged using a confocal upright Zeiss LSM 880 Multiphoton microscope. Collected confocal fluorescence images were processed using Fiji software.

Scanning Electron Microscope (SEM) imaging

At the end of the incubation period, samples for SEM imaging were fixed overnight at 4°C in a 4% paraformaldehyde and 2.5% glutaraldehyde in 0.1 M phosphate buffer. Sample fixation required three sequential steps involving aqueous solutions of 2% osmium tetroxide for 1 h, 1% tannic acid for 30 min and 2% osmium tetroxide for 1 h. In between each staining step, DI water was used to rinse the surfaces. The final staining step involved the samples to be immersed overnight in 1% uranyl acetate solution in water. For the final staining step, the samples were rinsed with DI-water, and progressively dehydrated using different volumetric ratios of ethanol (i.e. 30%, 50%, 70%, 90% and 100%). After the dehydration procedure, samples were critical-point dried using CO₂ (Quorum Technologies K850) and subsequently sputter coated with 10 nm of Au/Pd (Quorum Technologies Q150T) for SEM imaging at 10 kV using a JEOL7001F FE-SEM system.

Characterisation of SiNW arrays by EDS mapping

EDS mapping was used to map the chemical composition of the SiNW substrates before contact with bacterial suspension. The sample preparation for EDS mapping consisted in the sputter coating with 10 nm of Au (Quorum Technologies Q150T) for SEM imaging at 10 kV using a JEOL7001F FE-SEM system.

EDS mapping was carried out at 20 keV using a JEOL 2100F S/TEM, with EDAX Octane T Optima windowless 60 mm² SDD EDS detector. Despite not being possible to measure with high accuracy, these experimental conditions guarantee a probing depth of the order of micrometres [76].

4.3 Results and discussion

4.3.1 Characterisation of SiNWs surfaces

The SiNWs surfaces were characterised via high resolution SEM imaging (**Fig. 4.3.1**) and EDS mapping (**Fig. 4.3.2**). SEM images showed that the average diameter between neighbouring SiNWs was 143 ± 24 nm and the spacing was 77 ± 16 nm [67]. Higher magnifications show the top of the nanowires to be tapered at the end and slightly bent towards adjacent wires, giving the surface a nanocoral-like pattern (**Fig. 4.3.1**, left).

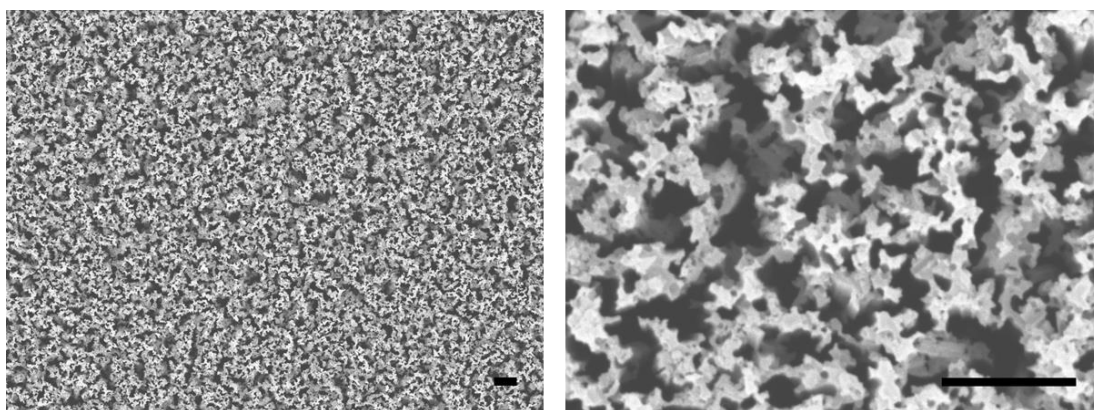


Fig. 4.3.1 Scanning electron microscopy images of a silicon nanowire arrays. Scale bars are $1\mu\text{m}$.

The chemical composition of SiNWs was investigated using EDS. Measurements taken on multiple sites of the nanostructured surface showed that the material is composed by 81.7 ± 0.6 % Si, 17.7 ± 0.6 % oxygen, with low traces of Au due to the SEM coating process. The EDS spectrum of a SiNWs array (**Fig. 4.3.2**) with a penetration depth of $> 1 \mu\text{m}$ within the surface, displays an intense peak at 0 KeV due to the electronics of EDX detector. No traces of Au are visible, while the signal related to Si was detected at 1.75 KeV and a peak related to Oxygen, present in low traces at the depth probed, is visible at 0.53 KeV.

These results indicate the presence of a thin SiO₂ layer at the surface of the SiNW arrays, thinner than the penetration length of the probing electron beam, coating the pure Si of the material's bulk.

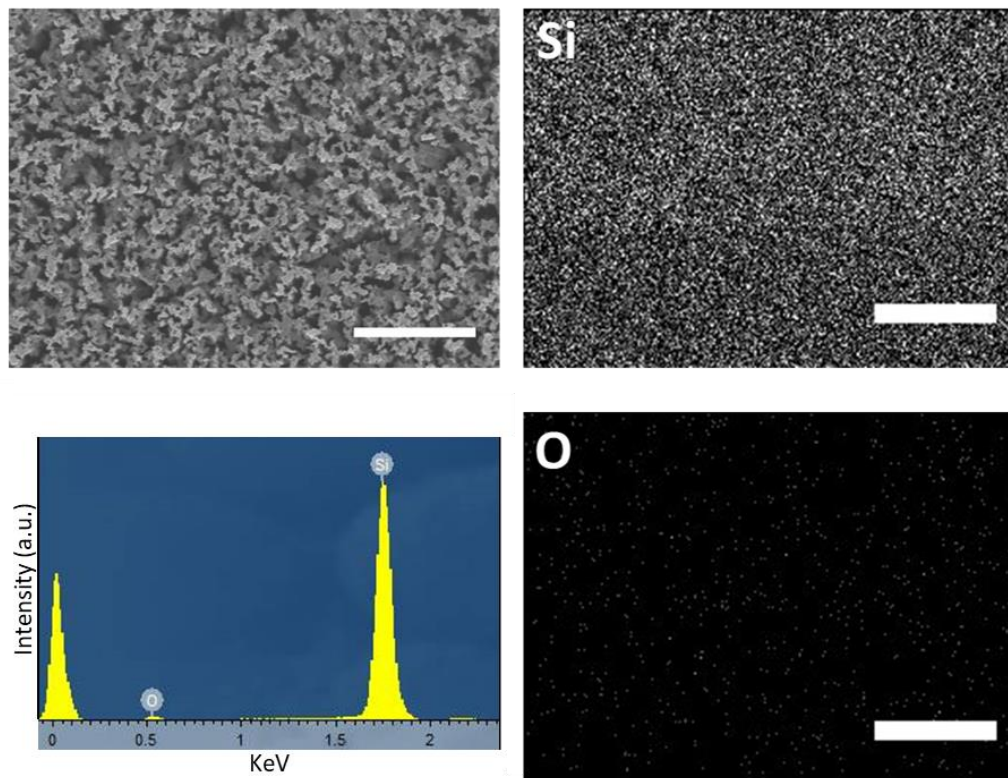


Fig. 4.3.2 Representative high-resolution SEM images (above, left) with relative EDS mapping (scale bars are 3 μm) of the SiNWs surfaces. **Above:** Silicon EDS map **Below:** EDS spectrum of SiNW surface (left), Oxygen EDS map (right).

4.3.2 Viability of sessile bacteria on flat Si and SiNWs

Confocal laser scanning microscopy (CLSM) images of bacteria stained with Live/dead viability kit allowed the investigation of the viability of *S. aureus* and *S. epidermidis* cells attached to flat Si and SiNWs surfaces. The assay was carried out with the use of SYTO 9, a cell-permeant dye that provides a fluorescence enhancement when binding nucleic acids, and Propidium Iodide, a nucleic acid binding dye capable of permeating disrupted bacterial membranes, commonly used to detect dead cells in a population [68]. Live/dead viability assays consequently shows dead cells as red or yellow and alive cells in green.

The CLSM images (**Fig. 4.3.3**) show a high coverage of bacterial cells on both the flat and nanostructured surfaces, the tendency of *S. aureus* colonies to grow in 3D is confirmed by the variance in intensity and dimensions amongst the cells, while a more homogenous pattern is noticeable for *S. epidermidis*.

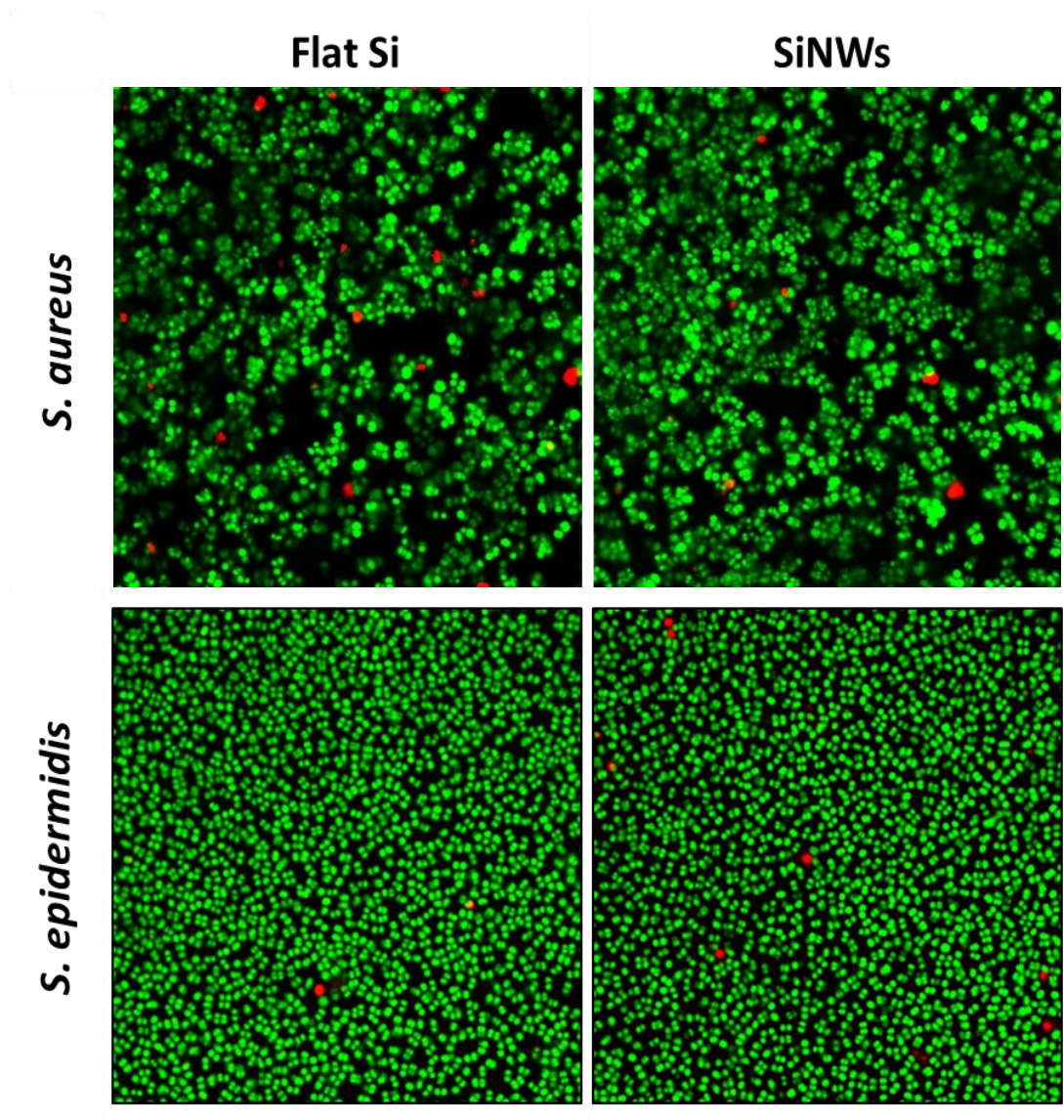


Fig. 4.3.3 Representative merged confocal laser scanning microscopy images for live (green) and dead (red) *S. aureus* and *S. epidermidis* cells attached to flat Si and SiNWs after 8 h of culture. Images size: 71.8 x 71.8 μm^2 .

Bacteria displayed high viability on both surfaces, with 98.1 (\pm 3.5) % live cells on flat Si for *S. aureus* and 98.9 (\pm 4.9) % in the case of *S. epidermidis*. The viability of both strains was not affected by the nanostructured surface, as 97.7 (\pm 9.3) % live sessile *S. aureus* cells and 98.5 (\pm 7.9) % of *S. epidermidis* were imaged on SiNWs assays (**Table 4.3.1**). These data highlight that SiNWs surfaces do not have an antimicrobial effect on the tested strains, in contrast to what was assessed by Jenkins *et al.* [40] on Ti nanopillar surface, which caused a 1-fold decrease in bacterial concentration after 10 h culture.

Table 4.3.1 Percentage (%) alive *S. aureus* and *S. epidermidis* sessile bacteria on flat Si and SiNWs surfaces.

	Flat Si	SiNWs
<i>S. aureus</i>	98.1 \pm 3.5	97.7 \pm 9.3
<i>S. epidermidis</i>	98.9 \pm 4.9	98.5 \pm 7.9

The concentration of attached cells in this work does not seem to be affected by the nanostructured topography of the SiNWs, in accordance with the studies by Susarrey-Arce *et al.* [58], which assessed high concentrations of *S. aureus* cells on SiNWs, and Campoccia *et al.* [69], which focused on the bacterial adhesion onto polyethylene terephthalate nanostructured surfaces. The topographic substrates displayed nanocylinders of 160 nm height and 110 nm diameter, with a spacing of 220 nm between each other. Control surfaces were considered flat with a Ra of 1.0 \pm 0.2 nm. After static culture, no difference in the concentration of sessile *S. aureus* was observed comparing the nanostructured surfaces with the flat ones.

A contrasting result was found by Puckett *et al.* [70] examining the adhesion of *S. aureus* and *S. epidermidis* on flat Ti, nanorough Ti produced by electron beam evaporation, and nanotubular and nanotextured Ti produced by two different anodization processes. *In vitro* viability tests showed a decrease in the adhesion of *S. aureus* and *S. epidermidis* on nanorough Ti surfaces created through electron beam evaporation while nanotubular and nanorough Ti produced an increase in

sessile bacteria. In this case is likely that the surface chemistry played a role, as a layer of TiO₂ was present on flat and nanorough Ti surfaces while the nanotubular and nanotextured Ti substrates were found to be amorphous.

4.3.3 Scanning electron microscope configurations

Scanning electron microscopy (SEM) is a powerful imaging technique that allows investigation of the morphology of inorganic samples and the topography of a wide range of surfaces [71]. In SEM a topographic image is formed by scanning across the surface an electron beam finely focused onto a small spot on the sample by the objective lens.

The resolution of the measurement can potentially reach the nanoscale and it is related to the size and the shape of the electron beam interacting with the sample, which is determined by an objective lens tuning the maximum angle of illumination [71]. When the electron beam irradiates the sample, different signals can be emitted: Auger electrons, secondary electrons, backscattered electrons, characteristic x-rays and photons of various energies [71]. The most common signal for SEM topographic imaging is related to the emission of secondary electrons, since these particles are confined to a very small volume near the beam impact area. Secondary electrons arise when the outer shell electrons of an atom and are ejected out by receiving sufficient kinetic energy from inelastic scattering collisions. Secondary electrons can then propagate through the material, escaping from the sample's surface and reaching the secondary electron detector to form a topographic image [71].

A change in tilt angle of sample in SEM systems (**Fig. 4.4.4**, right), like the one used in this work, may change the secondary electron (SE) to backscattered electron (BSE) ratio, resulting in contrast changes [71]. This is due to the fact that the emission of SEs depends largely on the incident angle of the probe: and the higher the angle, the stronger the emission of SEs [71]. An SEM in upright configuration

(Fig. 4.4.4, left) can on the other hand be used to image large surface areas, allowing for example to assess the concentration of bacteria attached to a sample, but provides limited information regarding the morphology of the cells or the topography of features protruding perpendicularly from the surface. Using a tilt angle allows to access this information, enabling the characterisation of the 3D structure and of the topographic properties of the sample to the nanometer scale.

On the other hand, when the sample is tilted, the length of the observed features may differ from the actual objects. Therefore, when measuring features within the sample is preferred to use an upright configuration or to correct the values obtained from the tilted state [71].

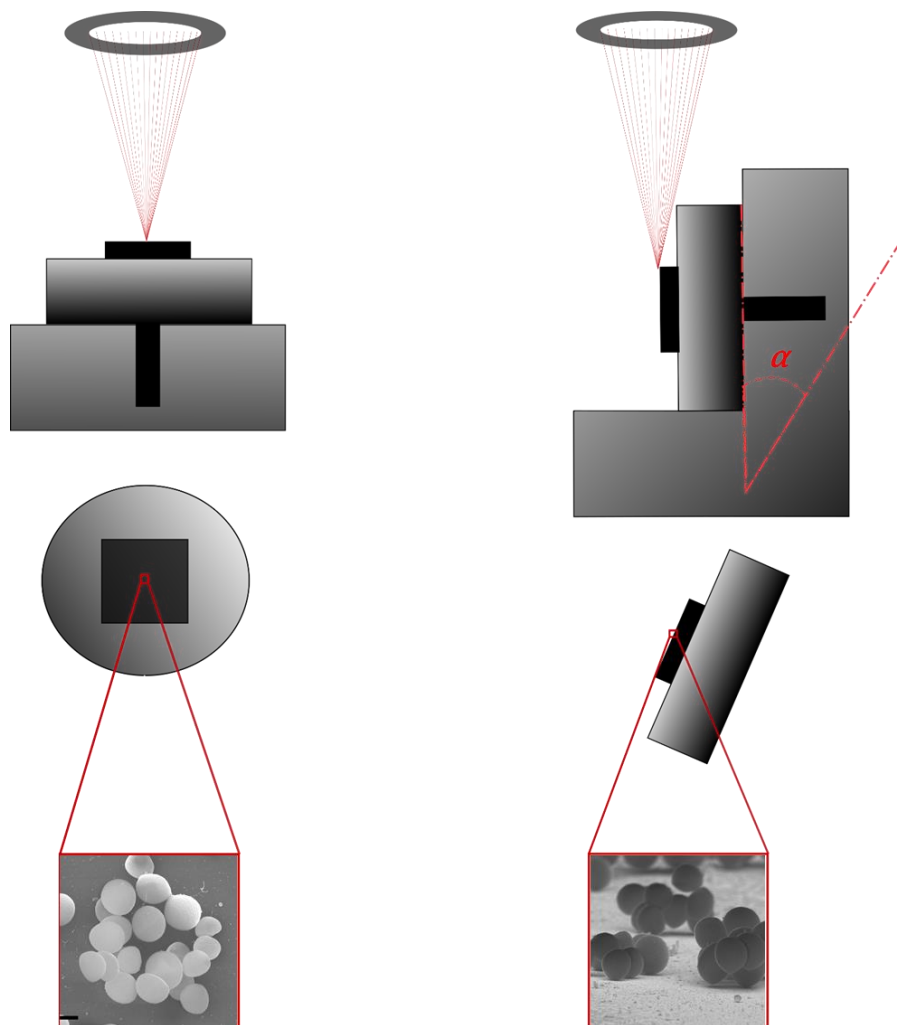


Fig. 4.3.4 Schematic representation of the two configurations used to acquire SEM images for this work, with representative SEM images. **Left:** upright configuration. **Right:** tilted, in which the tilting of sample stage can range over an angle α .

4.3.4 Biofilm formation of *S. aureus* cells on flat Si and SiNWs

We investigated *S. aureus* biofilms using high resolution SEM imaging in tilted configuration, this technique allowed us to probe the morphology of the bacterial colonies, the attachment points and the division modes of *S. aureus* cells attached to flat Si and SiNWs substrates. The sample preparation protocol used for these assays preserved the bacterial membrane and the extracellular appendices of the sessile bacteria, allowing to obtain high resolution images of microcolonies and single cells. High-magnification SEM images of multilayers of *S. aureus* cells attached to flat Si (**Fig. 4.3.5 A, B, C** and **Fig. 4.3.6 A, B, C**) and SiNWs substrates (**Fig. 4.3.5 D, E, F** and **Fig. 4.3.6 D, E, F**) showed that in both cases a first monolayer of cells in immediate contact with the surface provided a foundation for the three dimensional growth of the biofilm. Few anchoring points can be observed between this layer of cells and the surfaces, as cells retain their spherical shape after attachment and division. Interestingly, we did not observe significant disruption of the cell morphology by the topography, in agreement with the Live/Dead data discussed above.

Small colonies formed by less than 2-5 cells can be occasionally observed attached to flat Si (**Fig. 4.3.5 A, B** and **Fig. 4.3.6 A, C**) while they are rarely visible on SiNW arrays (**Fig. 4.3.5 D** and **Fig. 4.3.6 D**) where cells seem to organise in bigger clusters, a phenomenon that could be due to the fact that planktonic bacteria approaching the samples find more anchoring points on flat Si rather than SiNWs, where they more easily attach to other sessile cells than to the substrate.

As the number of cells increases and the biofilm develops perpendicularly to the surface, we observed a higher degree of disorder that is apparent on SiNW arrays (**Fig 4.3.6** from **D** to **F**) as well as on flat Si (**Fig 4.3.6** from **A** to **C**). This phenomenon could be due to the fewer anchoring points between the colonies and the nanostructured substrate compared to the flat one, which leads the colony to develop mostly out of plane.

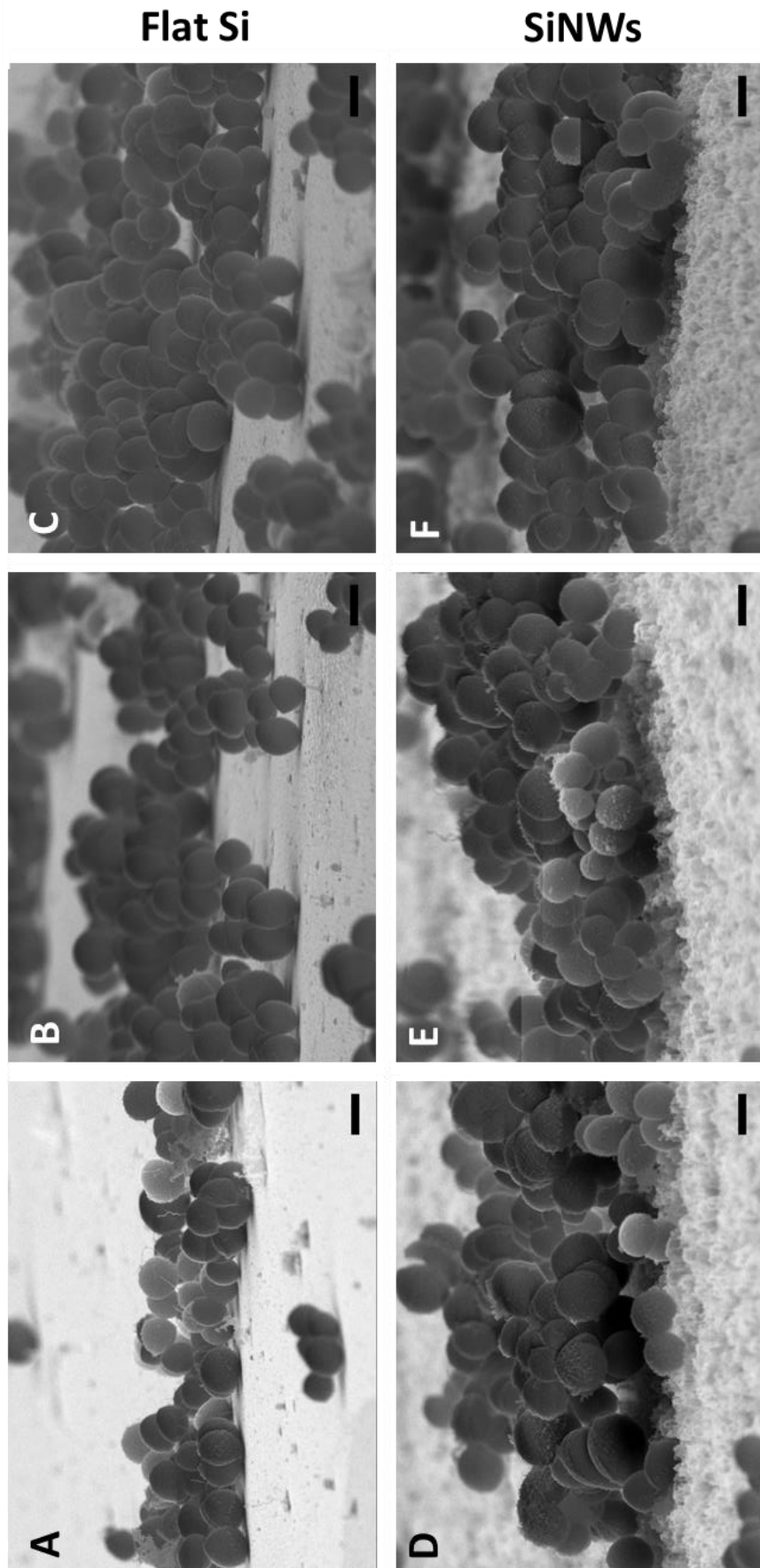


Fig. 4.3.5 Representative SEM images of *S. aureus* biofilm formation on flat Si (A, B, C) and SiNWs (D, E, F). Scale bars are 1 μm. image C is also present in [77].

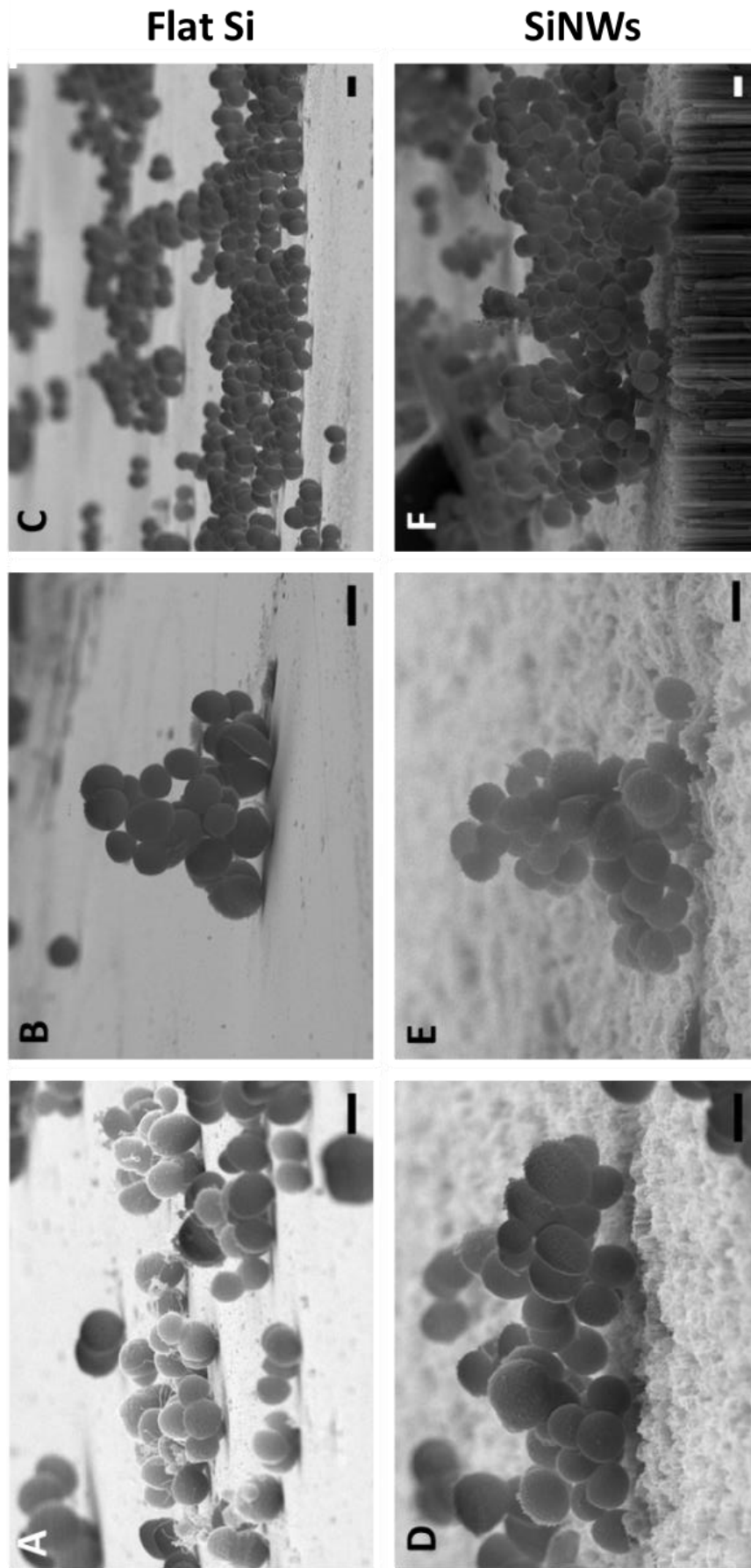


Fig. 4.3.6 Representative SEM images of *S. aureus* colonies on flat Si (A, B, C) and SiNWs (D, E, F). Scale bars are 1 μm . Image F is also present in [58].

Focusing on small *S. aureus* colonies forming on flat Si (**Fig. 4.3.7 A, B, C** and **Fig. 4.3.8 A, B, C**) and on SiNWs substrates (**Fig. 4.3.7 D, E, F** and **Fig. 4.3.8 D, E, F**), it can be observed in both cases a preferential out-of-plane growth resulting in 3D morphologies. *S. aureus* cells tend to divide out of plane and to maximize cell-to-cell contact rather than attachment to the substrate. The colonies adhering to flat Si displayed more cell–surface attachment points between adjacent cells than on SiNWs substrates, suggesting a potential effect of the surface topography on the attachment behaviour of *S. aureus*. The lower amount of anchoring points available for the cells to attach on SiNWs surfaces compared to flat Si led to extreme cases in which a colony formed by several bacteria made contact with the surface only with one or two cells (**Fig. 4.3.7 D, E, F**).

A second factor that leads to the formation of bacterial clusters is associated with intercellular interactions between planktonic bacteria approaching the surface and the sessile ones, this phenomenon becomes more predominant as the colony grows vertically and planktonic bacteria can recognize and attach to the sessile cells. The balance between the cell division (out of plane or parallel to the surface) and the attachment of planktonic cells will determine the predominant morphology of the colony at the surface.

S. aureus cells are known to secrete adhesins from the cellular membrane to facilitate both cell–cell, and cell–surface attachment (**Fig. 4.3.8 C**) [22]. **Fig 4.3.7 A** shows extracellular polymeric substance secreted from the colony, beginning the formation of the polysaccharide matrix that is an integral component in the formation of *S. aureus* biofilms.

A bacterial division event in which two cells are almost completely separated is visible in **Fig. 4.3.7 D**, where two hemispherical cells can be observed facing each other. For *S. aureus*, once the autolysins complete divide the two cell walls, the osmotic pressure quickly pushes the flat septum outwards, forcing the daughter cells to adopt a spherical shape, in this case the newly formed cell wall is still in a flat configuration, indicating that a full separation between the daughter cells is imminent

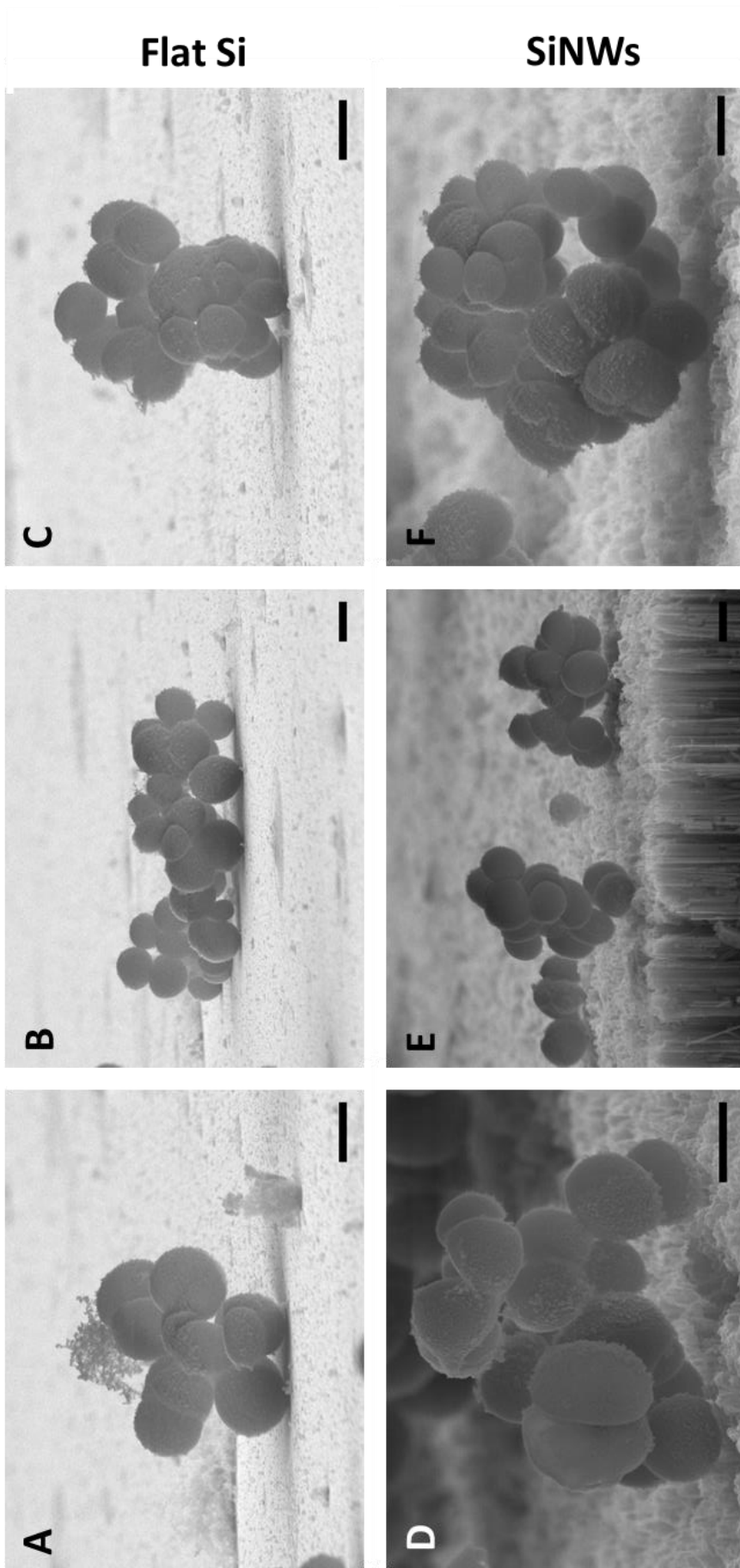


Fig. 4.3.7 Representative SEM images of *S. aureus* microcolonies on flat Si (A, B, C) and SiNWs (D, E, F). Scale bars are 1 μm

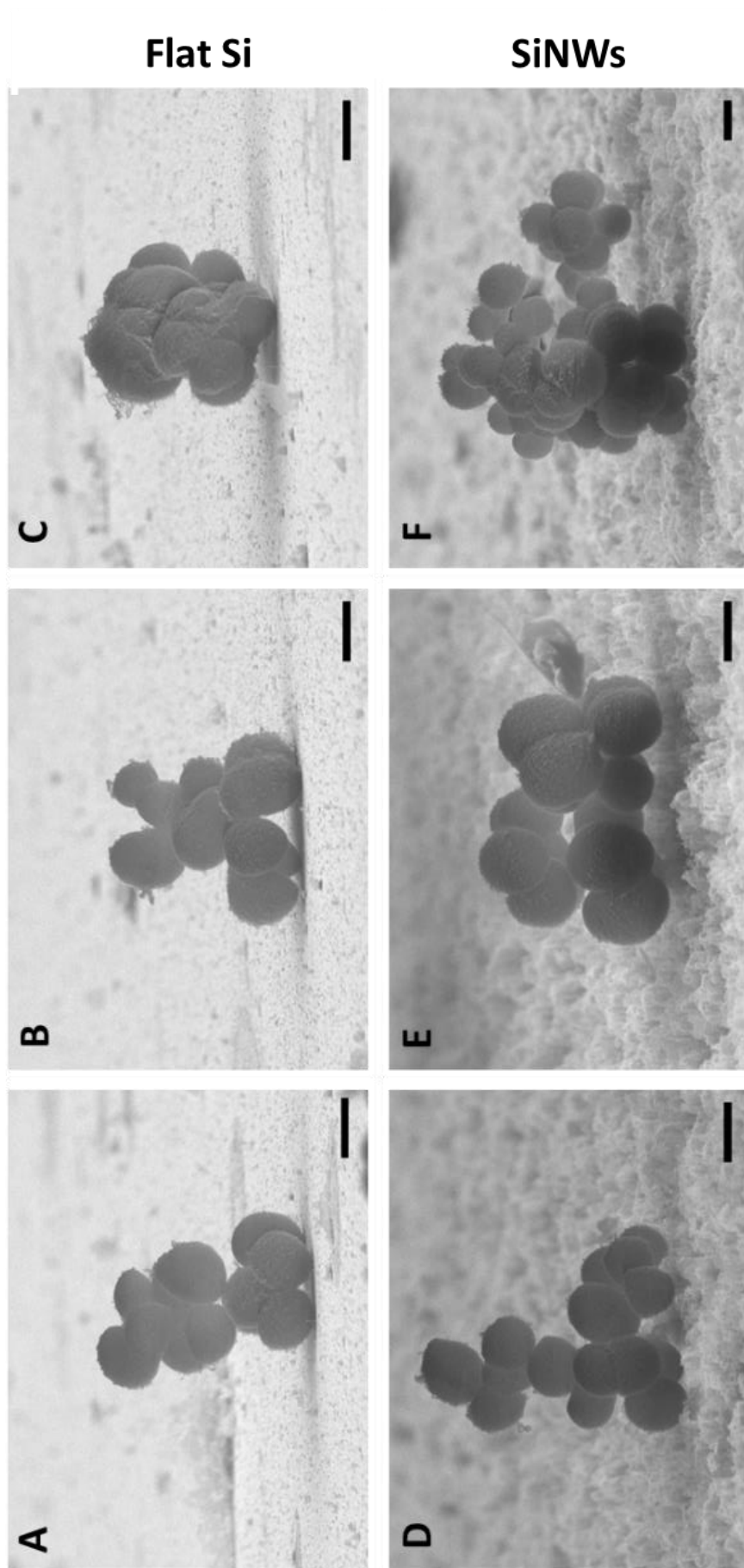


Fig. 4.3.8 Representative SEM images of *S. aureus* colonies on flat Si (A, B, C) and SiNWs (D, E, F). Scale bars are 1 μm

Focusing on single cells and division events taking place on flat Si (**Fig. 4.3.9 A, B, C** and **Fig. 4.3.10 A, B, C**) and SiNWs substrates (**Fig. 4.3.9 D, E, F** and **Fig. 4.3.10 D, E, F**), we observed that *S. aureus* cells, after attaching to a substrate can divide both parallel to the surface (**Fig. 4.3.9 A, D** and **Fig. 4.3.10 A, C, D**) and out of plane (**Fig. 4.3.9 C, F** and **Fig. 4.3.10 B, E, F**). **Fig 4.3.9 B** shows two *S. aureus* cells that previously divided parallel to the surface in the act of sequentially dividing in the orthogonal plane, adopting a tetrad conformation; the horizontal “scar” in the middle of the cell corresponds to the division site [72]. The same configuration can be seen on SiNWs in **Fig. 4.3.9 E**, although in this case the cells attached to the surface, forced to adapt to the uneven topography, display a tilted orientation of the final structure. There seems to be a tendency on SiNW substrates to observe *S. aureus* cells prevented from dividing parallel to the surface (**Fig 4.3.9 D** and **Fig 4.3.9 E**), unlike what we can observe on flat Si (**Fig. 4.3.10 A**). It is interesting to notice that *S. aureus* cells attached to both types of substrates are able to divide in a upright position in respect to the surface (**Fig. 4.3.9 C** and **Fig 4.3.10 E**), this can be explained by the fact that the orientation of the division plane in *Staphylococci* is dependent on the previous division event, as the nucleoid occlusion proteins prevent the elongation of the chromosome along the same axis as the previous division, therefore only allowing the new septum to form perpendicularly to the previous one [37].

Staphylococci, due to their spherical shape, unlike rod-shaped bacteria do not have a preferential direction of attachment to the surface, therefore the orientation of the post-attachment division plane only depended on the previous division event and can span from upright to horizontal in the case of flat Si. When *S. aureus* cells divide on SiNWs the uneven topography restricts the available angle at which the division plane can orientate, directly affecting the morphology of the bigger clusters (**Fig. 4.3.7 F**). As more division events take place and the colony grows, it is possible to observe a higher degree of disorder and irregularity in the bacterial clusters, this could be due to a post-fissional movement of the cells caused by the lytic enzymes responsible for splitting the division septum [73].

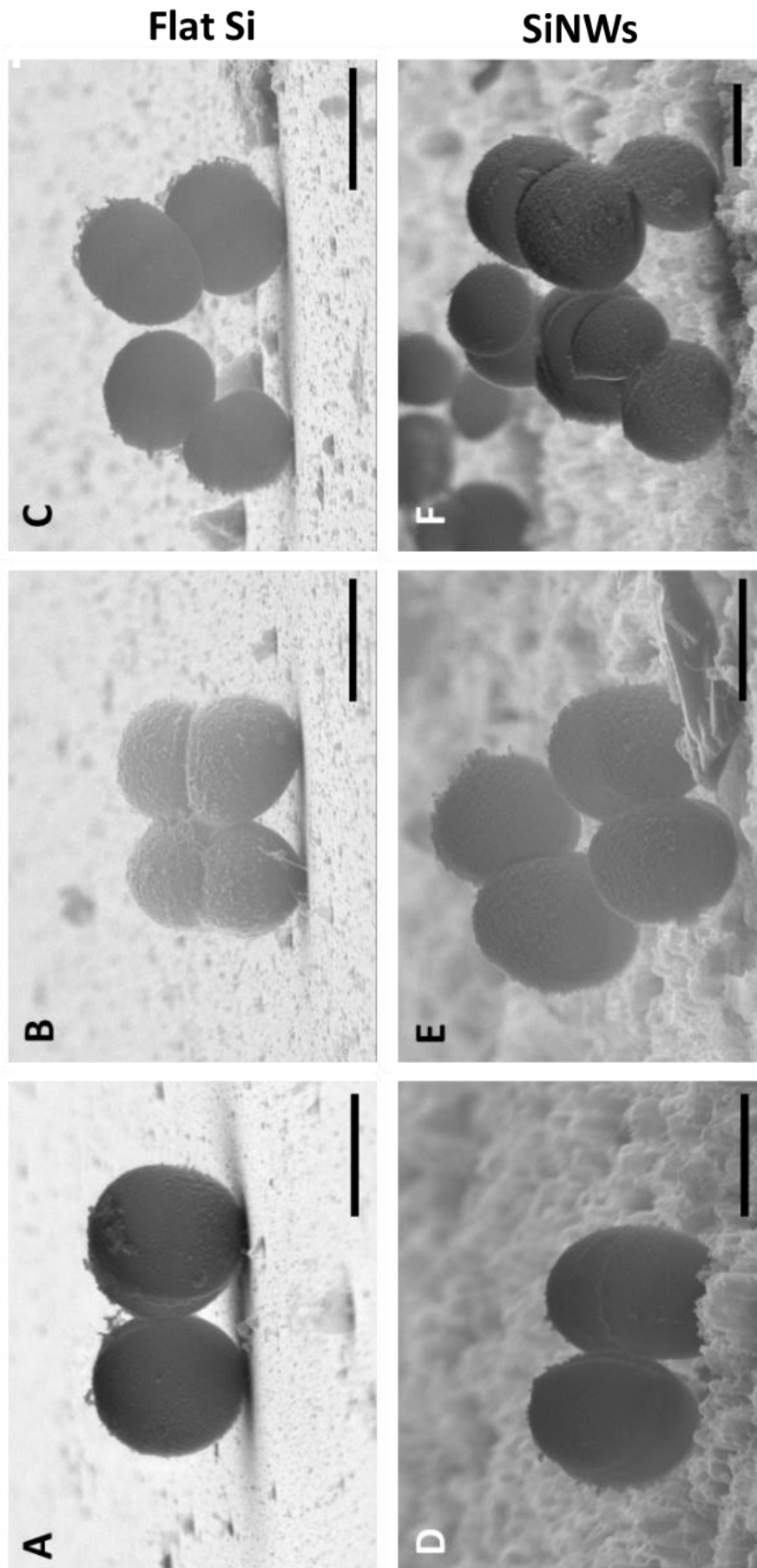


Fig. 4.3.9 Representative SEM images of *S. aureus* single cells and division events on flat Si (A, B, C) and SiNWs (D, E, F). Scale bars are 1 μm . Image F is also present in [77] and [58], supplementary.

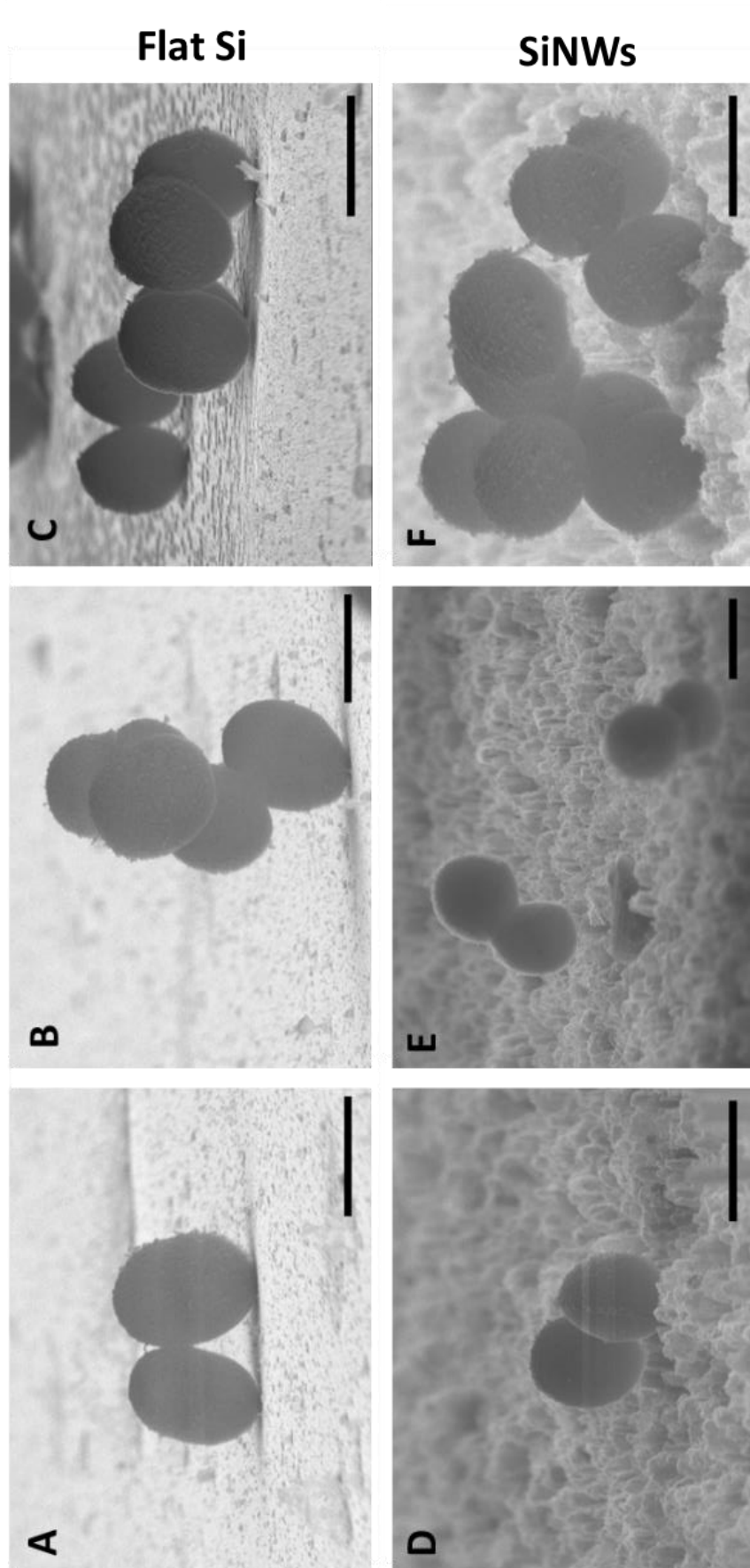


Fig. 4.3.10 Representative SEM images of *S. aureus* single cells and division events on flat Si (A, B, C) and SiNWs (D, E, F). Scale bars are 1 μm

4.3.5 Biofilm formation of *S. epidermidis* cells on flat Si and SiNWs

We also investigated *S. epidermidis* biofilms on flat and topographic surfaces. SEM images of colonies and multilayers of *S. epidermidis* cells on flat Si (**Fig. 4.3.11 A, B, C**) and SiNWs substrates (**Fig. 4.3.11 D, E, F**) showed the initial stages of biofilm formation, with cells multiplying and adhering to the surface. On both surfaces the first monolayer of cells displayed few anchoring points with the surface as the cells retain their spherical shape after attachment and division. Like for *S. aureus*, the biofilm developed in 3D, with cells dividing and adhering to each other rather than to the substrate.

In our study, after 8 h of growth on flat Si and SiNWs, minimal traces of extracellular polymeric substance (EPS) are visible. The production of EPS, covering the surface of the cells, is essential for the evolution of the biofilm and has been observed by Takahashi *et al.* [74] on *S. epidermidis* grown on plastic well plates for 12 h or more.

Comparing **Fig. 4.3.11 A** and **Fig. 4.3.11 D**, with few cells adhering to the substrates, we can notice that singular or paired cells adhere to flat Si, while on SiNWs bacteria seem to arrange preferentially in bigger clusters. This could be attributed to fewer adhesion points available on the nanostructured surface, which facilitates the detachment of cells from the surface.

Division events can be observed taking place on both types of surfaces, in cells adhering to the substrate and to each other. Similarly to *S. aureus*, cells on the flat surface are able to divide horizontally while on SiNWs we observe a tendency of the bacteria to adapt to the uneven topography, leading to division in an upright position.

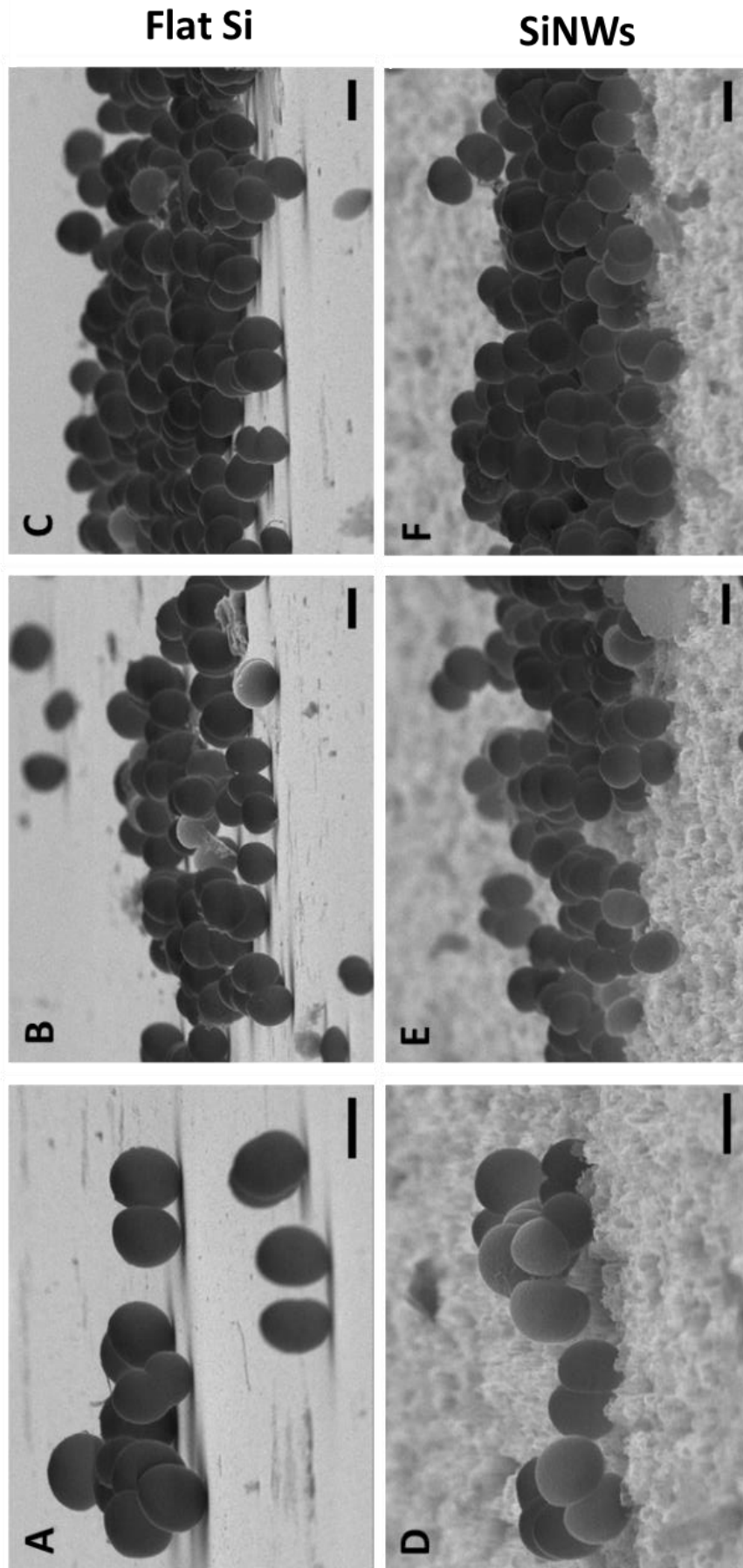


Fig. 4.3.11 Representative SEM images of *S. epidermidis* aggregates on flat Si (A, B, C) and SiNWs (D, E, F). Scale bars are 1 μm

Observing the morphology of single cells and small bacterial clusters on flat Si (**Fig. 4.3.12 A, B, C** and **Fig. 4.3.13 A, B, C**) and SiNWs (**Fig. 4.3.12 D, E, F** and **Fig. 4.3.13 D, E, F**), several division events can be individuated on both substrates. Cells appear to be at different stages of the division process, which is consistent with the fact that after 8 h of incubation *S. epidermidis* is in the exponential growth phase. Cells at the earliest visible stage of division are visible on the right side of **Fig. 4.3.13 E**, still maintaining an approximately spherical shape and displaying a light horizontal “scar” at the centre, related to the septum under development. Two bacteria on the right side of **Fig. 4.3.10 C** are seen at the last stage of division, with the two daughter cells appearing completely divided and in the process of acquiring their spherical shape.

We can notice a difference between *S. epidermidis* and *S. aureus* related to the roughness of the cell wall. While the cell wall of some *S. aureus* appears “wrinkled”, secreting EPS (**Fig. 4.3.9 C** and **E**), the cell wall of *S. epidermidis* displayed a smoother appearance, with only few cells (**Fig. 4.3.12 C** and **Fig. 4.3.13 E**) secreting short appendices.

Fig. 4.3.12 D shows a small cluster of *S. epidermidis* cells dividing on SiNWs, with only few bacteria sustaining the whole colony in its out-of-plane growth. In contrast, in **Fig. 4.3.12 B** the bacteria seem to be able to spread and divide more easily on the flat Si surface.

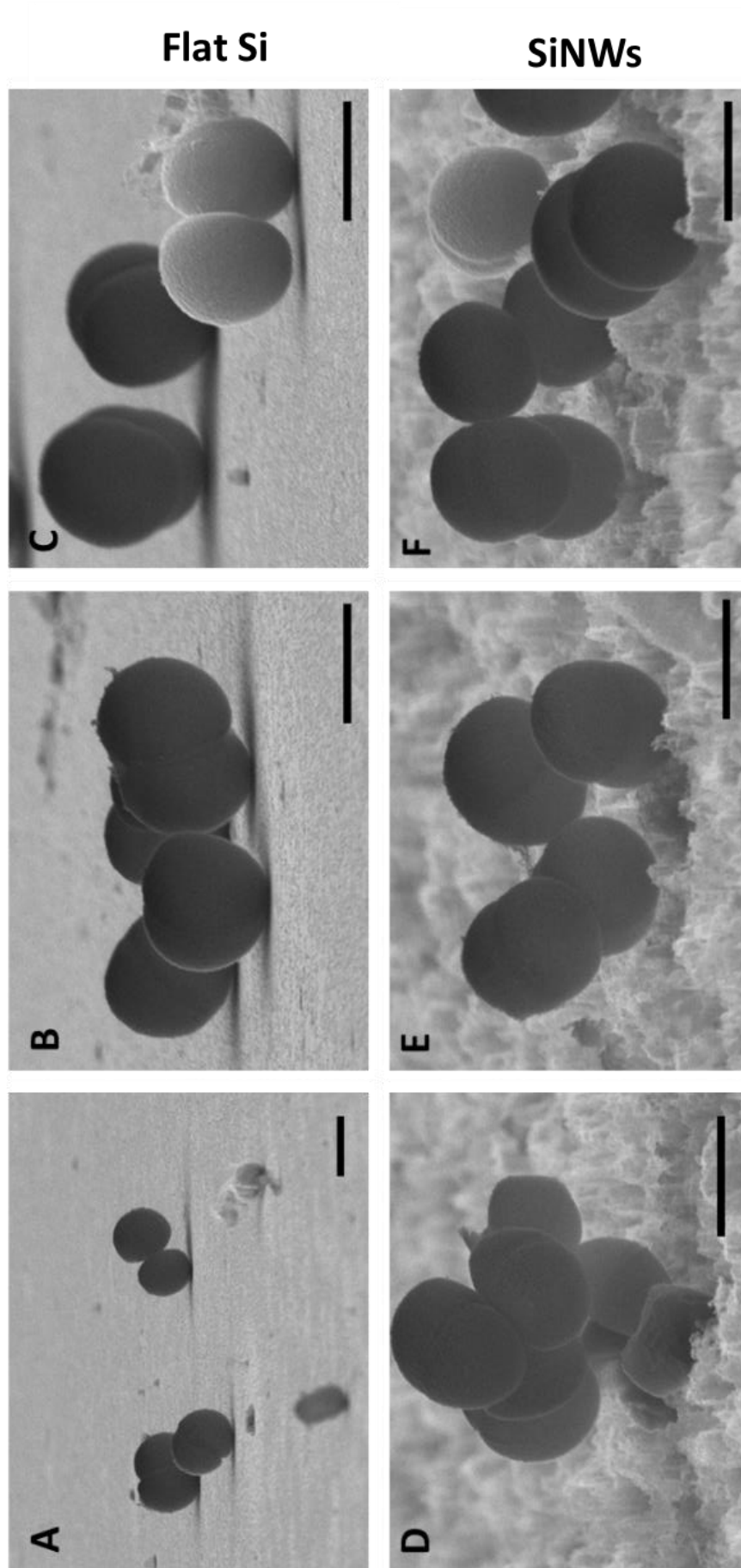


Fig. 4.3.12 Representative SEM images of *S. epidermidis* cells and small clusters on flat Si (A, B, C) and SiNWs (D, E, F). Scale bars are 1 μm

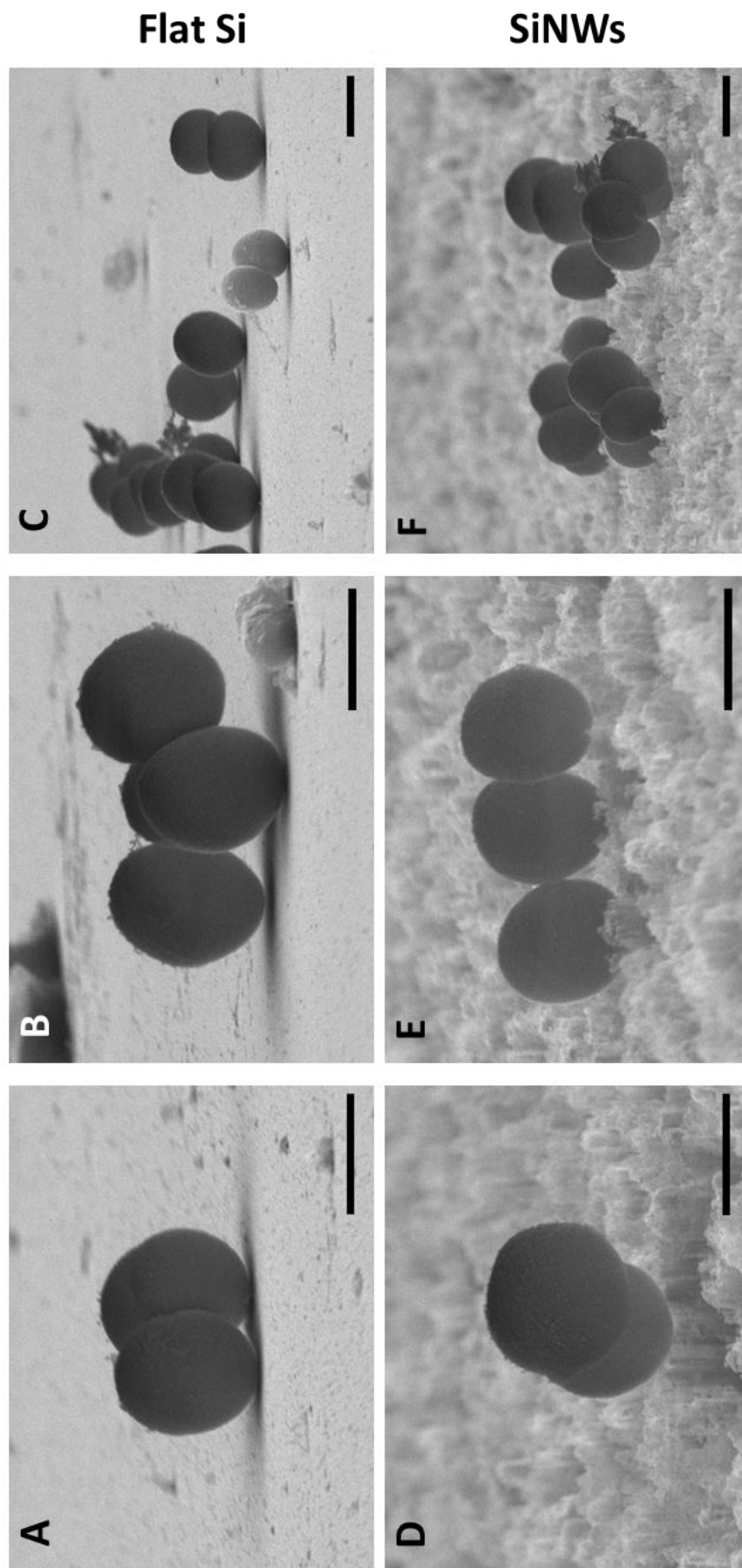


Fig. 4.3.13 Representative SEM images of *S. epidermidis* cells and microcolonies on flat Si (A, B, C) and SiNWs (D, E, F). Scale bars are 1 μm

4.4 Division modes of *Staphylococci* at the surface

The data discussed in the previous sections suggest strong similarities between the adhesion and growth of *S. aureus* and *S. epidermidis* on flat Si and SiNWs. When multilayers of *Staphylococci* populate the surface, it is possible to locate some colonies in which the degree of vertical growth and disorder seems to be affected by the cells in contact with the surface (comparing **Fig. 4.3.6 C** with **Fig. 4.3.6 F** and **Fig. 4.3.11 C** with **Fig. 4.3.11 F**). On SiNWs substrates the lower number of available attachment points and the uneven topography led to a relatively lower number of cells dividing parallel to the surface.

High magnification SEM images of Staphylococcal cells dividing on Flat Si and SiNWs surfaces allowed us to observe directly the effect of the surface on the common growing modes assessed for these bacteria in the planktonic state. **Fig. 4.4.1** shows a scheme of the available orientation range of Staphylococcal cells on flat Si surfaces. *Staphylococci* have a spherical shape which does not lead to a preferential direction of attachment at the surface, unlike rod-shaped bacteria which may align and orientate with a parallel orientation due to higher number of bacteria-surface anchoring points available in this configuration [58]. Consequently, after the attachment of the Staphylococcal cells becomes irreversible, the orientation of the new division plane will only be dependent on the previous division event, due to the nucleoid occlusion proteins preventing chromosome elongation along the same axis as the previous division. These mechanisms only allow the new septum to form perpendicularly to the previous division septum [37]. The orientation of the division axis can span from upright to horizontal (**Fig. 4.4.1**) on flat Si, leading therefore to the formation of small colonies with daughter cells orientated parallel to the surface. **Fig 4.4.2** shows representative SEM images of *S. aureus* and *S. epidermidis* dividing on flat Si with different orientations in respect to the surface. These images show bacteria dividing both parallel and perpendicularly to the substrate.

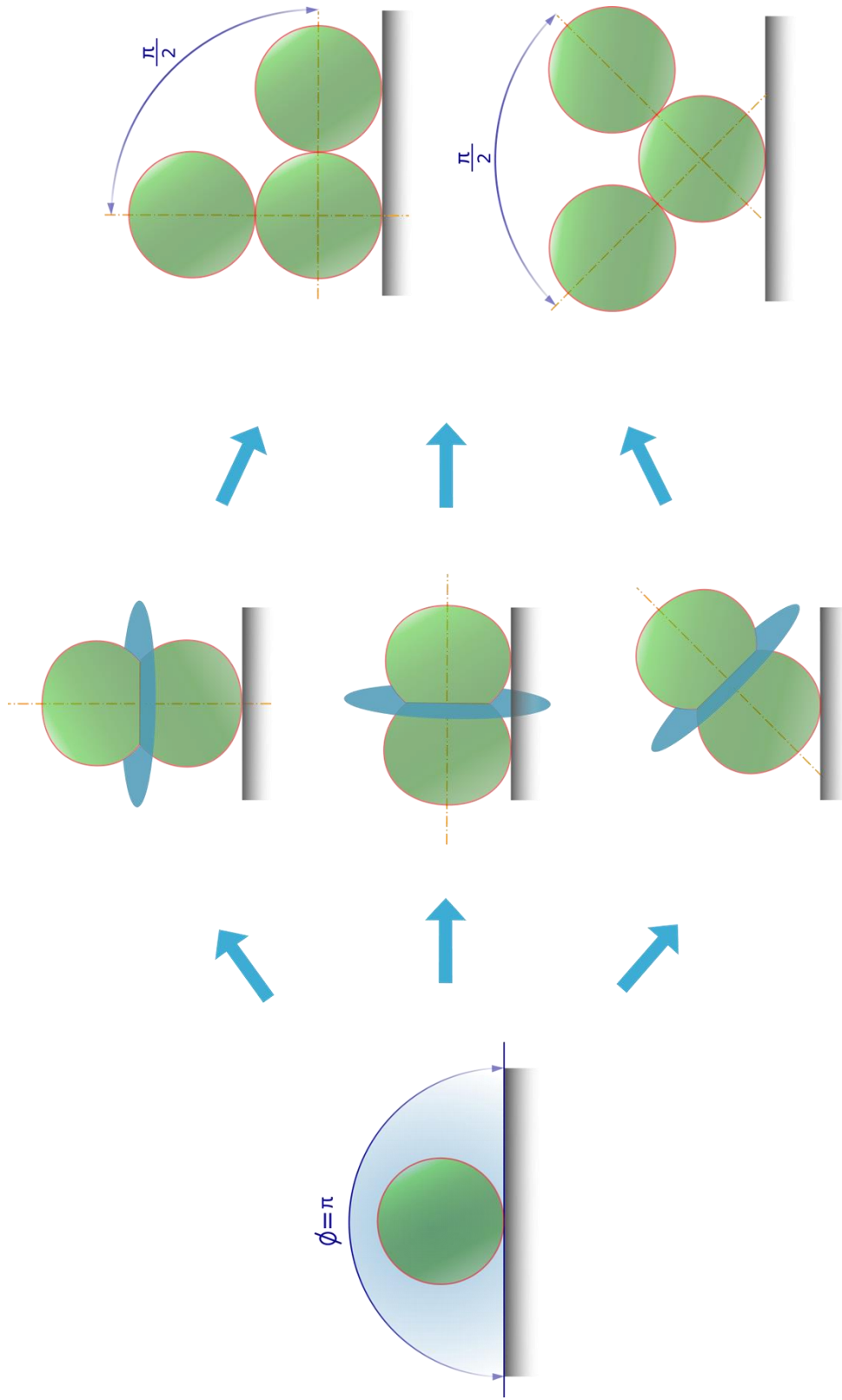


Fig. 4.4.1 Schematic representation of *Staphylococci* dividing on flat Si, showing the available orientations for the daughter cells.

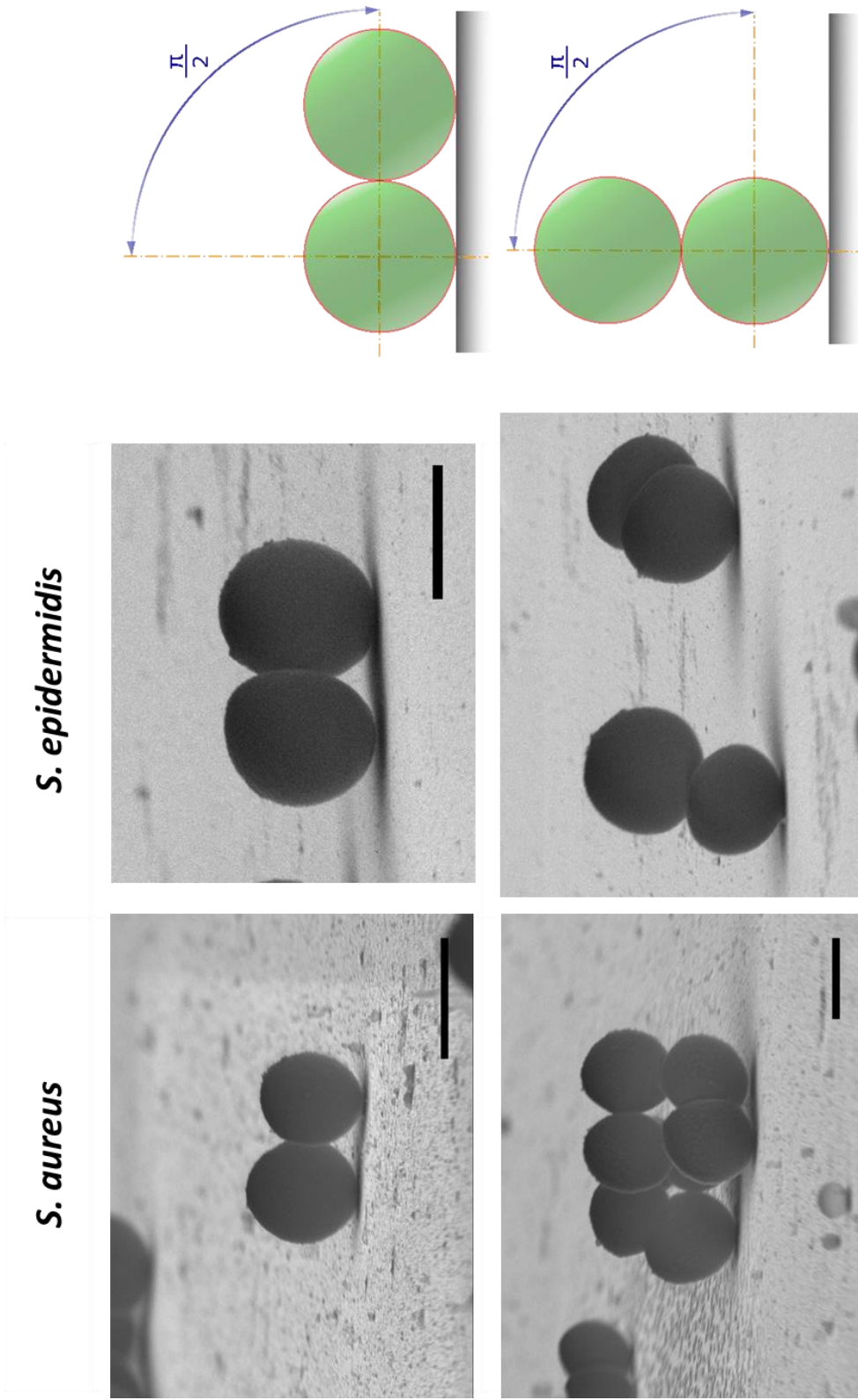


Fig. 4.4.2 SEM images and relative schematic representation of *Staphylococci* attached to flat Si dividing parallel to the surface (above) and out of plane (below). Image below, left, also present in [77]. Scale bars are 1 μm .

High magnification SEM images of *S. aureus* and *S. epidermidis* cultured for 8 h on SiNWs show that occasionally their division and growth are affected by the uneven topography of the nanostructured surface. The cell membrane of Gram-positive bacteria like *S. aureus* and *S. epidermidis* is composed of a 30–100 nm thick peptidoglycan layer that provides high rigidity [75], preventing the cells from adapting to the topography. **Fig. 4.4.3** shows a scheme of the restricted available orientation range of *Staphylococci* on SiNWs: observing the uneven topography of the nanostructured substrates, we can hypothesise that in some cases a bacterium can attach to the surface in the proximity of surface features that restrict the available angle at which the division plane can orientate. Examples are shown in **Fig. 4.3.10 E** for *S. aureus* and in **Fig. 4.3.12 E** for *S. epidermidis*, in which the bacterial cells and the valleys of the nanostructured surface are comparable in size, causing the *Staphylococci* to accommodate within the nanostructured features. The orientation of the division axis in some cases may be restricted by the surface topography, as previously observed in the SEM images in study of Jenkins *et al.* [40] (**Fig. 4.1.6**), preventing Staphylococcal cells to divide parallel to the sample and leading to the formation of small clusters that displays few attachment points to the surface (**Fig 4.4.4**). These configurations affect directly the morphology of the bigger clusters and the multilayers of cells, which tend to grow out of plane (**Fig. 4.3.7 D, E** and **F**, **Fig. 4.3.9 F**, **Fig. 4.3.10 F** for *S. aureus* and **Fig. 4.3.12 D**, **Fig. 4.3.13 F** for *S. epidermidis*).

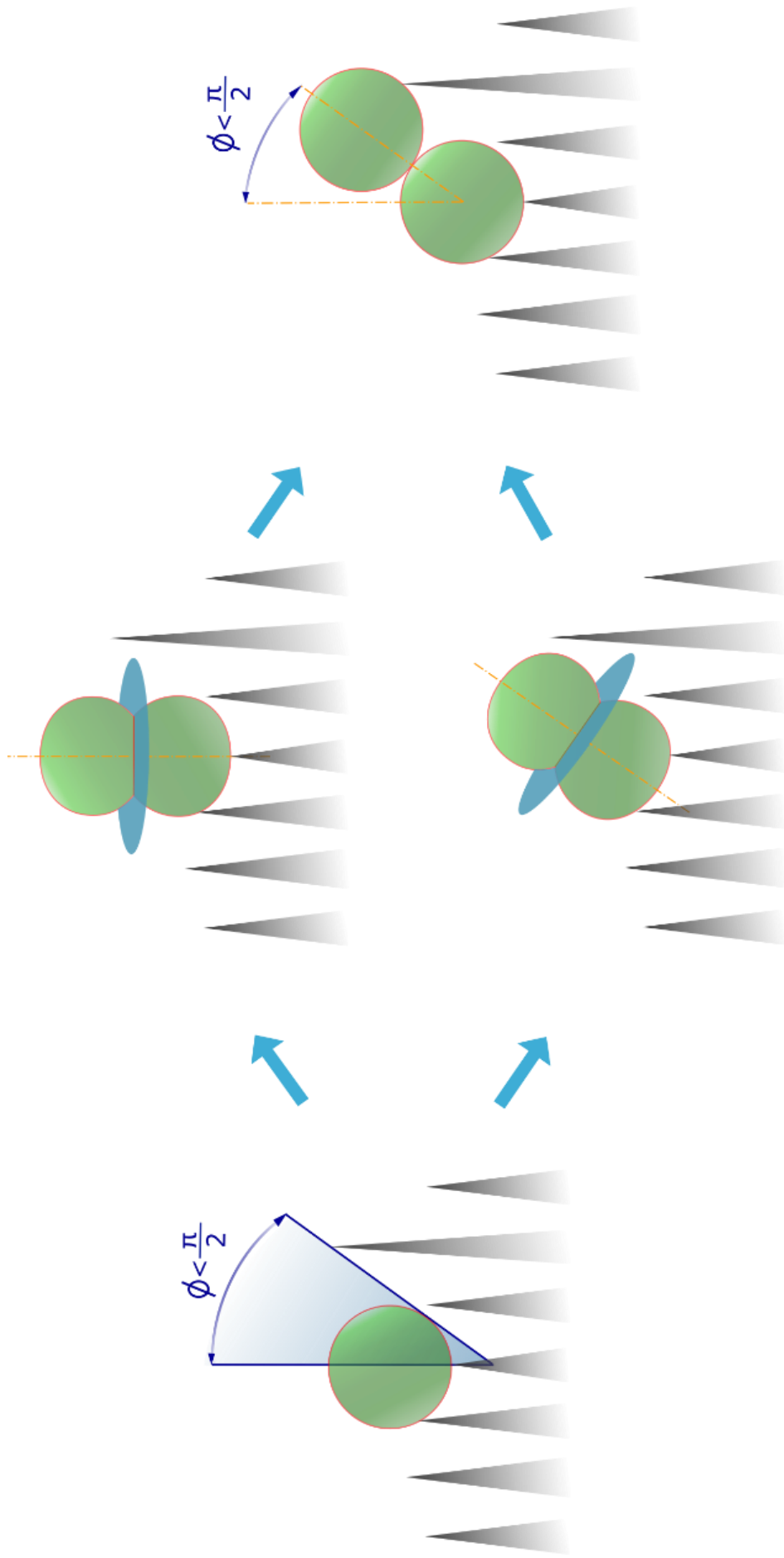
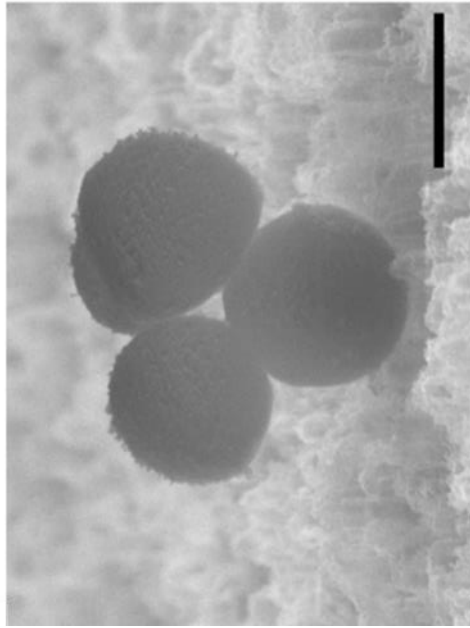
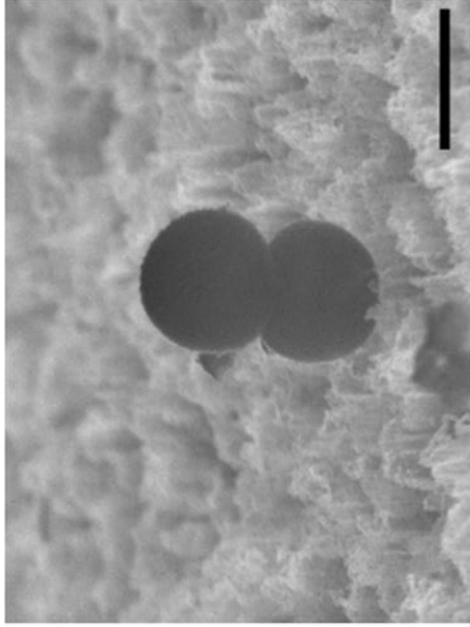


Fig. 4.4.3 Schematic representation of *Staphylococci* dividing on SiNWs, with focus on the available orientations range for the daughter cells to assume.

S. aureus



S. epidermidis



$$\phi < \frac{\pi}{2}$$

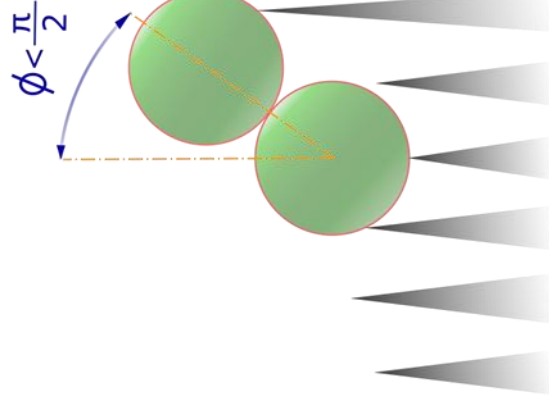


Fig. 4.4.4 SEM images and relative schematic representation of *Staphylococci* attached to SiNWs surfaces and their division effected by the uneven topography. Scale bars are 1 μm .

4.5 Conclusion

In this work we investigated bacterial colony morphology and division modes at the surface of the two main pathogens causing prosthetic infections [7, 8]: *Staphylococcus aureus* and *Staphylococcus epidermidis*. We compared cells incubated for 8 h on flat Si and SiNWs, which are Si surfaces functionalised with highly oriented filamentary Si crystals with ~ 100 nm diameter or less [53], that have shown to be biocompatible [54, 55]. Several in vitro and in vivo studies have demonstrated that Si is beneficial for bone tissue structure and function [42, 43] while SiNW arrays mimic the rough topography currently in use in orthopaedic implants to stimulate osteogenesis.

The high resolution SEM images presented in this work were acquired in tilted configuration to investigate at the nanometer scale the morphology of the cells and their attachment points to the substrates.

The SEM images show *S. aureus* and *S. epidermidis* attaching and growing on both types of surfaces, however the high rigidity of their cell wall seems to prevent them from adapting to the uneven surface topography of SiNWs, leading colonies with less attachment points to these nanostructured surfaces. Multilayers of cells can be observed developing vertically in respect to the sample surface, while small clusters of bacteria showed flat or out-of-plane morphologies depending on the number of attachment points to the surface and on the local morphology. High resolution SEM images also showed cells dividing with their division plane tilted in respect to the substrate, in some cases appearing to divide a second time, orthogonally in respect to their first division plane, generating tetrad morphologies, as expected due to the *Staphylococci* growing mode.

When *Staphylococci* are attached to flat Si surfaces the orientation of their division plane can span from upright to horizontal, which leads to formation of small colonies that display daughter cells orientated parallel to the substrate. On the other hand the uneven topography of the SiNWs surfaces in some cases appears to

prevent Staphylococcal cells from dividing parallel to the surface, leading to the formation of small clusters of cells displaying few attachment points to the surface and growing out of plane with respect to the sample surface. These data suggested that the nanostructured topography of SiNWs has an impact on the biofilm formation of Staphylococcal cells, a finding that could enable the engineering of materials able to effectively control and prevent bacterial adhesion and proliferation, with potential biomedical and industrial applications.

4.6 References

- [1] **Surface topographical factors influencing bacterial attachment**
Crawford RJ, Webb HK, Truong VK, Hasan J, Ivanova HP
Advances in Colloid and Interface Science 179–182 (2012) 142–149
- [2] **Biofilms: an emergent form of bacterial life**
Flemming HC, Wingender J, Szewzyk U, Steinberg P, Rice SA, Kjelleberg S
Nat Rev Microbiol 14 (2016) 563–575
- [3] **Bacterial adhesion at the single- cell level**
Berne C, Ellison CK, Ducret A, Brun YV
Nat Rev Microbiol 16 (2016) 616–627
- [4] **Scenery of Staphylococcus implant infections in orthopedics**
Montanaro L, Speziale P, Campoccia D, Ravaioli S, Cangini I, Pietrocola G, et al.
Future Microbiol. 6 (2011) 1329-1349
- [5] **Advancements in molecular epidemiology of implant infections and future perspectives**
Montanaro L, Campoccia D, Arciola CR
Biomaterials 28(34) (2007) 5155-5168
- [6] **Biofilm formation in Staphylococcus implant infections. A review of molecular mechanisms and implications for biofilm-resistant materials**
Arciola CR, Campoccia D, Speziale P, Montanaro L, Costerton JW
Biomaterials 33 (2012) 5967-5982
- [7] **Pathogens old, new and revived**
Frere JM, Dubus A, Fonzé E
Nat Biotechnol 17 (1999) BV17–BV18
- [8] **Coagulase-negative Staphylococci: role as pathogens.**
Huebner J, Goldmann DA
Annu. Rev. Med. 50 (1999) 223–236.
- [9] **Staphylococcus epidermidis — the ‘accidental’ pathogen**
Otto M
Nat Rev Microbiol. 7(8) (2009) 555–567
- [10] **Biofilms: Microbial Life on Surfaces**
Donlan RM
Emerg. Infect. Dis. 8(9) (2002) 881-90
- [11] **Effects on antibiotic resistance of Staphylococcus epidermidis following adhesion to polymethylmethacrylate and to silicone surfaces**
Arciola CR, Campoccia D, Montanaro L
Biomaterials 23 (2002) 1495–1502

- [12] **Emerging pathogenetic mechanisms of the implant-related osteomyelitis by *Staphylococcus aureus***
Montanaro L, Testoni F, Poggi A, Visai L, Speziale P, Arciola CR
Int J Artif Organs 34(9) (2011) 781-788
- [13] **Mechanisms of bacterial adhesion and pathogenesis of implant and tissue infections**
An YH, Dickinson RB, Doyle RJ
Handbook of bacterial adhesion: principles, methods, and applications, Humana Press, 1st Edition (2000) 1–27
- [14] **Bacterial adhesion: seen any good biofilms lately?**
Dunne WMJ
Clin Microbiol Rev. 15 (2002) 155–166
- [15] **Biofilms and their consequences, with particular reference to hygiene in the food industry**
Carpentier B, Cerf O
J. Appl. Bacteriol. 75 (1993) 499–511
- [16] **New surfaces with hydrophilic/hydrophobic characteristics in relation to (no)bioadhesion**
Legeay G, Poncin-Epaillard F, Arciola CR
Int J Artif Organs 29(4) (2006) 453-461
- [17] **Concise review of mechanisms of bacterial adhesion to biomaterial surfaces.**
An YH, Friedman RJ
J Biomed Mater Res 43 (1998) 338–348
- [18] **Slime-producing *Staphylococcus epidermidis* and *S. aureus* in acute bacterial conjunctivitis in soft contact lens wearers.**
Catalanotti P, Lanza M, Del Prete A, Lucido M, Catania MR, Galle F, Boggia D, Perfetto B, Rossano F
New Microbiol 28 (2005) 345–354
- [19] **A role for the mannose- sensitive hemagglutinin in biofilm formation by *Vibrio cholerae* El Tor**
Watnick PI, Fullner KJ, Kolter R
J. Bacteriol. 181 (1999) 3606–3609
- [20] **Evidence for autolysin-mediated primary attachment of *Staphylococcus epidermidis* to a polystyrene surface**
Heilmann C, Hussain M, Peters G, Götz F
Mol Microbiol 24 (1997) 1013-1024
- [21] **Residence- time dependent cell wall deformation of different *Staphylococcus aureus* strains on gold measured using surface-enhanced fluorescence**
Li J, et al.
Soft Matter 10 (2014) 7638–7646

- [22] **Chemical signals and mechano-sensing in bacterial responses to their environment**
Harapanahalli AK, Younes JA, Allan E, van der Mei HC, Busscher HJ
PLoS Pathog. 11 (2015) e1005057
- [23] **Evidence for autolysin-mediated primary attachment of *Staphylococcus epidermidis* to a polystyrene surface**
Heilmann C, Hussain M, Peters G, Gotz F
Mol. Microbiol. 24 (1997) 1013–1024
- [24] **Bap-dependent biofilm formation by pathogenic species of *Staphylococcus*: evidence of horizontal gene transfer?**
Tormo MA, Knecht E, Gotz F, Lasa I, Penades JR
Microbiology 151 (2005) 2465–2475
- [25] **Key role of teichoic acid net charge in *Staphylococcus aureus* colonization of artificial surfaces.**
Gross M, Cramton SE, Gotz F, Peschel A
Infect. Immun. 69 (2001) 3423–3426
- [26] **The CidA murein hydrolase regulator contributes to DNA release and biofilm development in *Staphylococcus aureus***
Rice KC et al.
Proc. Natl Acad. Sci. 104 (2007) 8113–8118
- [27] **How to get (a)round: mechanisms controlling growth and division of coccoid bacteria**
Pinho MG, Kjos M, Veening JW
Nat Rev Microbiol 11(9) (2013) 601-614
- [28] **Spatial regulation in *Caulobacter crescentus***
Thanbichler M
Curr. Opin. Microbiol. 12 (2009) 715–721
- [29] **Molecular coordination of *Staphylococcus aureus* cell division**
Lund VA, Wacnik K, Turner RD, Cotterell BE, Walther CG, Fenn SJ, Grein F, Wollman AJ, Leake MC, Olivier N, Cadby A, Mesnage S, Jones S, Foster SJ
Elife 21(7) (2018) e32057
- [30] **Dispersed mode of *Staphylococcus aureus* cell wall synthesis in the absence of the division machinery**
Pinho MG, Errington J
Mol. Microbiol. 50 (2003) 871–881
- [31] **Teichoic acids are temporal and spatial regulators of peptidoglycan cross-linking in *Staphylococcus aureus***
Atilano ML et al.
Proceedings of the National Academy of Sciences 107(44) (2010) 18991-18996
- [32] **Cryo-electron microscopy of cell division in *Staphylococcus aureus* reveals a mid-zone between nascent cross walls**
Matias VR, Beveridge TJ
Mol. Microbiol. 64 (2007)195–206

- [33] **Division site selection in rod-shaped bacteria**
Bramkamp M, Van Baarle S
Current Opinion in Microbiology 12 (2009) 683–688
- [34] **A model for the three-dimensional structure of peptidoglycan in *Staphylococci***
Seligman SJ, Pincus MRJ
Theor. Biol. 124 (1987) 275–292
- [35] **Entropy-driven spatial organization of highly confined polymers: lessons for the bacterial chromosome**
Jun S, Mulder B
Proc. Natl Acad. Sci. 103 (2006) 12388–12393
- [36] **Entropy as the driver of chromosome segregation**
Jun S, Wright A
Nature Rev. Microbiol. 8 (2010) 600–607
- [37] **Absence of nucleoid occlusion effector Noc impairs formation of orthogonal FtsZ rings during *Staphylococcus aureus* cell division**
Veiga H, Jorge AM, Pinho MG
Mol. Microbiol. 80 (2011) 1366–1380
- [38] **Inhibition and enhancement of microbial surface colonization: the role of silicate composition**
Roberts JA, et al.
Chem. Geol. 212 (2004) 313–327
- [39] **Bacterial retention on superhydrophobic titanium surfaces fabricated by femtosecond laser ablation**
Fadeeva E, Truong VK, Stiesch M, Chichkov BN, Crawford RJ, Wang J, Ivanova EP
Langmuir 27 (2011) 3012–3019
- [40] **Antibacterial effects of nanopillar surfaces are mediated by cell impedance, penetration and induction of oxidative stress**
Jenkins J, Mantell J, Neal C, Gholinia A, Verkade P, Nobbs AH, Su B
Nat Commun. 2(11) (2020) 1626
- [41] **Nanoengineered superhydrophobic surfaces of Aluminium with extremely low bacterial adhesivity**
Hizal F, Rungraeng N, Lee J, Jun S, Busscher HJ, Van der Mei HC, Choi CH
ACS Appl. Mater. Interfaces 9 (2017) 12118–12129
- [42] **Silicone and bone health**
Jugdaohsingh R
J. Nutr. Health Aging 11 (2007) 99–110
- [43] **Effects of Silicon Compounds on Biomineralization, Osteogenesis, and Hard Tissue Formation**
Götz W, Tobiasch E, Witzleben S, Schulze M
Pharmaceutics 11 (2019) 117

- [44] **The biocompatibility of porous Silicon in tissues of the eye**
Low SP, Voelcker NH, Canham LT, Williams KA
Biomaterials 30 (2009) 2873–2880
- [45] **Silicone and bone health**
Jugdaohsingh R
J. Nutr. Health Aging 11 (2007) 99–110.
- [46] **Update on the possible nutritional importance of Silicon**
Nielsen FH
J. Trace Elem. Med. Biol. 28 (2014) 379–382
- [47] **Adhesion of eukaryotic cells and Staphylococcus aureus to Silicon model surfaces**
Müller R, Ruhl S, Hiller KA, Schmalz G, Schweikl H
J. Biomed. Mater. Res. 84(3) (2008) 817-827
- [48] **Role of wettability and nanoroughness on interactions between osteoblast and modified silicon surfaces**
Padial-Molina M, Galindo-Moreno P, Fernández-Barbero JE, O'Valle F, Jódar-Reyes AB, Ortega-Vinuesa JL, Ramón-Torregrosa PJ
Acta Biomaterialia 7 (2011) 771–778
- [49] **Porous Silicon for Biomedical Applications**
Santos HA
Woodhead Publishing, 1st edition, 2014
- [50] **High-porosity poly(3-caprolactone)/mesoporous Silicon scaffolds: calcium phosphate deposition and biological response to bone precursor cells**
Whitehead MA, Fan D, Mukherjee P, Akkaraju GR, Canham LT, Coffey JL
Tissue Eng Part A 14 (2008) 195–206
- [51] **Bioactive properties of nanostructured porous Silicon for enhancing electrode to neuron**
Moxon KA, Hallman S, Aslani A, Kalkhoran NM, Lelkes PI
interfaces.J Biomater Sci Polym 18 (2007) 1263–81
- [52] **Interaction of B50 rathippocampal cells with stain-etched porous Silicon**
Sapelkin AV, Bayliss SC, Unal B, Charalambou A
Biomaterials 27 (2006) 842–846
- [53] **Silicon Nanowires: A Review on Aspects of Their Growth and Their Electrical Properties**
Schmidt V, Wittemann JV, Senz S, Gósele U
Adv. Mater. 21 (2009) 2681–2702
- [54] **Highly Efficient Biocompatible Single Silicon Nanowire Electrodes with Functional Biological**
Martinez JA, Misra N, Wang Y, Stroeve P, Grigoropoulos CP, Noy A
Pore Channels. Nano Lett. 9 (3) (2009) 1121–1126

- [55] **In Vitro Biocompatibility of N-Type and Undoped Silicon Nanowires**
Garipcan B, Odabas S, Demirel G, Burger J, Nonnenmann SS, Coster MT, Gallo EM, Nabet B, Spanier JE, Piskin E
Adv. Eng. Mater. 13 (2011) B3–B9.
- [56] **Cell Adhesion and Spreading Behavior on Vertically Aligned Silicon Nanowire Arrays**
Qi S, Yi C, Ji S, Fong CC, Yang M
ACS Appl. Mater. Interfaces 1 (1) (2009) 30–34.
- [57] **Effects of Silicon Nanowires on HepG2 Cell Adhesion and Spreading**
Qi S, Yi C, Chen W, Fong CC, Lee ST, Yang M
Chem Bio Chem 8 (10) (2007) 1115–1118
- [58] **Bacterial viability on chemically modified Silicon nanowire arrays**
Susarrey-Arce A, Sorzabal-Bellido I, Oknianska A, McBride A, Beckett A, Gardeniers JGE, Raval R, Tiggelaar RM, Diaz Fernandez YA
J. Mater. Chem. B 4 (2016) 3104
- [59] **Nano and Microscale Topographies for the Prevention of Bacterial Surface Fouling**
Graham M, Cady N
Coatings 4 (2014) 37–59
- [60] **The Effect of Surface Topography on the Retention of Microorganisms**
Whitehead KA, Verran J
Trans. Inst. Chem. Eng., Part C, 84 (2006) 253–259
- [61] **The impact of structure dimensions on initial bacterial adhesion**
Helbig R, Günther D, Friedrichs J, Rößler F, Lasagni A, Werner C
Biomater. Sci. 4 (2016) 1074
- [62] **The Effects of Surface Topography on the Accumulation of Biofouling**
Kerr A, Cowling MJ
Philos. Mag. 83 (2003) 2779–2795
- [63] **Influence of Nanophase Titania Topography on Bacterial Attachment and Metabolism**
Park MR, Banks MK, Applegate B Webster TJ
Int. J. Nanomed. 3 (2008) 497–504
- [64] **Metal-Particle-Induced, Highly Localized Site-Specific Etching of Si and Formation of Single-Crystalline Si Nanowires in Aqueous Fluoride Solution.**
Peng K, Fang H, Hu J, Wu Y, Zhu J, Yan Y, Lee ST
Chem. - A Eur. J. 12 (30) (2006) 7942–7947
- [65] **SYTO™ 9 Green Fluorescent Nucleic Acid Stain**
<https://www.thermofisher.com/order/catalog/product/S34854> (accessed 5 September 2020)

- [66] **Mechanism and Use of the Commercially Available Viability stain, BacLight**
Stocks SM
Cytometry 61A (2) (2004) 189–195
- [67] Data courtesy of Dr. Ioritz Sorzabal Bellido
- [68] **Propidium Iodide Nucleic Acid Stain**
<https://www.thermofisher.com/order/catalog/product/P1304MP?SID=srch-srp-P1304MP#/P1304MP?SID=srch-srp-P1304MP> (accessed on the 10th of September 2020)
- [69] **Study of Staphylococcus aureus adhesion on a novel nanostructured surface by chemiluminometry**
Campoccia D, Montanaro L, Agheli H, Sutherland DS, Pirini V, Donati ME
Int J Artif Organs 29 (2006) 622–629
- [70] **The relationship between the nanostructure of titanium surfaces and bacterial attachment**
Puckett SD, Taylor E, Raimondo T, Webster TJ
Biomaterials 31 (2010) 706–713
- [71] **Scanning Electron Microscopy and X-Ray Microanalysis**
Goldstein J, Newbury DE, Joy DC, Lyman CE, Echlin P, Lifshin E, Sawyer L, Michael JR
Kluwer Academic/Plenum Publishers, 3rd edition, 2003
- [72] **Cell shape dynamics during the staphylococcal cell cycle**
Monteiro J, Fernandes P, Vaz F, *et al.*
Nat Commun 6 (2015) 8055
- [73] **Formation of regular packets of Staphylococcus aureus cells**
Koyama T, Yamada M & Matsuhashi M
J Bacteriol 129 (1977) 1518–1523
- [74] **Electron microscopy of Staphylococcus epidermidis fibril and biofilm formation using image-enhancing ionic liquid**
Takahashi C, Kalita G, Ogawa N, Moriguchi K, Tanemura M, Kawashima Y, Yamamoto H
Anal Bioanal Chem 407(2015) 1607–1613
- [75] **The bacterial cell envelope**
Silhavy TJ, Kahne D, Walker S
Cold Spring Harb Perspect Biol 2(5) (2010) a000414
- [76] **Achieving Nanometer Resolution EDS Analysis in an SEM – Zeiss**
<https://blogs.zeiss.com/microscopy/en/nanometer-resolution-eds/> (accessed on the 11th of November 2020)
- [77] **Fabrication and Characterisation of Antimicrobial Surfaces**
Sorazabal-Bellido I
PhD thesis (2018) University of Liverpool, DOI:10.17638/03022760

Chapter 5

Insights on the effect of nanostructured Silicon on the first stages of biofilm formation of rod-shaped bacteria

5.1. Introduction

5.1.1 Why do bacteria form biofilms?

Several advantages drive bacteria to attach to surfaces and grow into biofilms: surfaces provide a degree of stability and a growth environment as, regardless of its chemical or physical properties, any surface tends to adsorb (macro)molecules [1, 2]. The layer of molecules at the solid–liquid interface on surfaces is commonly referred to as conditioning film and brings a higher concentration of proteins, polysaccharides, and other nutrients at the surface in comparison to the liquid phase, providing a metabolically favourable environment for bacterial cells and serving as nutritional trigger to biofilm formation [1, 2].

Biofilms offer protection to prokaryotic cells from a wide range of environmental threats, such as exposure to UV light [3], dehydration and salinity [4], exposure to acids [5], phagocytosis [6] and antimicrobial agents [7, 8, 9].

The tendency of bacteria to form biofilms is directly related to the abundance of nutrients in the surrounding environment. Cells in high-nutrient conditions tend not

to form biofilms or form loose structures at the substratum which can be easily disrupted by a fluid shear [10, 11, 12, 2], bacteria are more likely to form biofilms under starvation or low-nutrient conditions [13, 14, 15]. Dewanti and Wong [16] assessed that *Escherichia coli* O157:H7 biofilms developed on stainless steel were formed by a higher number of adherent cells when grown in low-nutrient conditions than when grown in tryptic soy broth. This phenomenon, called attachment-upon-starvation response, is common for a vast range of pathogenic bacteria, and microorganisms found in soil and the marine environment [17, 18, 19].

Surface attachment of rod-shaped bacteria and the role of adhesins

The initial surface attachment phase of most bacteria can be separated in two different stages, commonly referred to as reversible and irreversible attachment [20, 21, 2]. Reversible attachment refers to the phase in which bacteria are loosely attached to the surface and may detach returning to the planktonic phase. Adhesins located on pili and flagella have a central role in making the first physical contact with the surface, allowing bacteria to overcome the physicochemical forces that influence the fate of the first contact: van der Waals interactions are generally attractive; electrostatic interactions are influenced by the polarity and the pH of the liquid medium; acid–base hydrophobic interactions can be attractive or repulsive depending on the environment, membrane and substrate chemistries (**Fig. 5.1.1**) [22, 23, 2]. In aqueous media, various organic and inorganic molecules adsorb onto the surface to form a layer known as conditioning film, which modifies the physicochemical properties of the substrate by altering charge, potential and surface energy, favouring bacterial attachment [23, 24]. During the reversible attachment phase, prokaryotic cells can be observed rotating around their axis, indicating attachment of the flagella to the surface [22, 2] while some bacteria also display a type of jerky motion named twitching motility, which requires the attachment of pili (or fimbriae) to the surface [2]. Since the nomenclature regarding these appendages is still source of confusion, this work will refer to the review

published in 2004 on Nature by Kaper *et al.* [25] for the terminology, noting that fimbriae and pili originated as synonyms and the terms are still used indistinctly to this day [26, 27, 25].

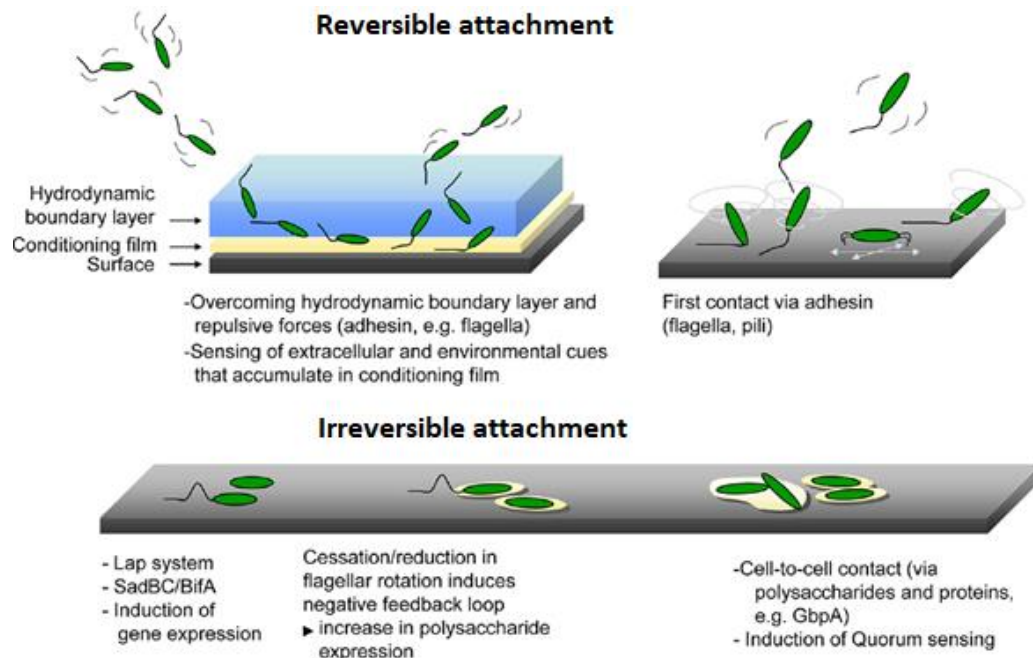


Fig. 5.1.1. Representation of events and factors enabling bacteria to transition from a planktonic to a sessile state. Cell first need to overcome the hydrodynamic boundary layer and repulsive electrostatic forces they encounter when approaching the surface. Reversible attachment is characterized by bacteria loosely attached to the surface via a single adhesin, resulting in cells displaying a spinning or twitching motion. Irreversible attachment results in bacteria attached to the surface along their axis, with the resulting reduction in flagellar rotation triggering an increase in polysaccharide production, leading to biofilm formation. Image adapted from [2].

Many strains of prokaryotic cells display proteinaceous membrane appendages that have a direct or indirect role in the attachment process. For example, in *E. Coli* the flagellum has both the role of actively propelling bacteria to the surface and, during the adhesion process, it provides a physical contact with the substrate [28, 23]. Upon contact with the surface, bacteria use their flagella to probe the substrate or, in the presence of nanofeatures of the topography, to access microenvironments and attachment points that would be inaccessible to the relatively large cell body, increasing adhesion efficiency [23]. A recent work by Friedlander *et al.* [29] demonstrated how, on micro-structured surfaces, the adhesion of *E. coli* strains

harbouring flagella was improved compared with flat substrates, probably due to the capacity of these appendages to access crevices and initiate adhesion. Other bacterial filamentous protein extensions involved in the initial adhesion to abiotic surfaces include type IV pili, curli and in the case of *E. coli*, type I pili [30, 23] (Fig. 5.1.2). These cell wall features, often featuring adhesins or carbohydrate molecules at their probing end, play an important role in bacterial attachment, reinforcing adhesion and initiating biofilm formation.

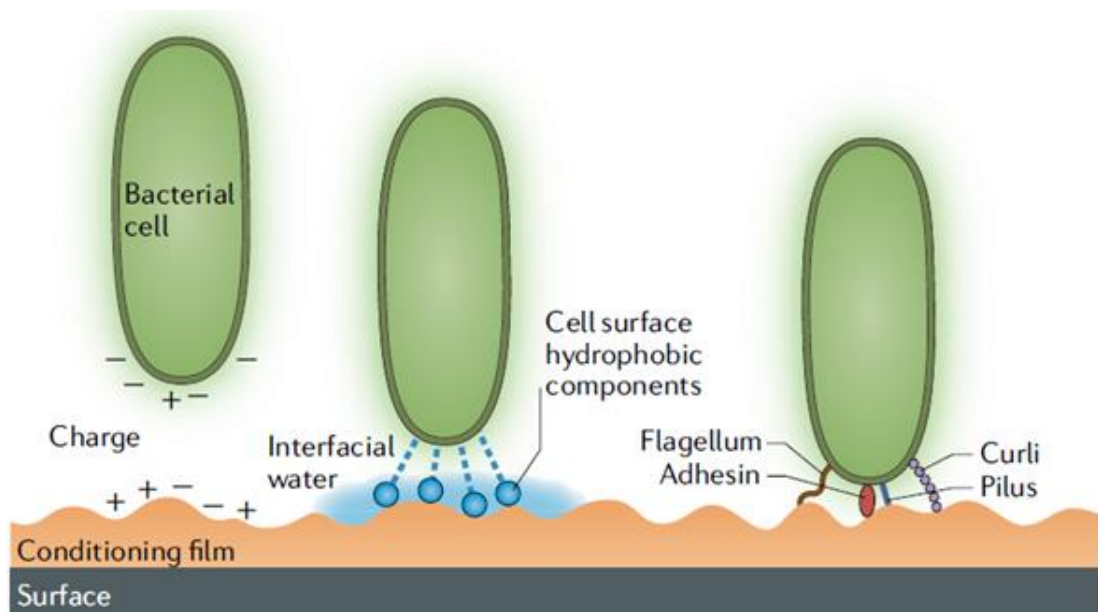


Fig. 5.1.2 Schematisation of the process and the components involved in the interaction between the surface and the bacterium: The cell membrane of most bacteria is negatively charged but the cell surface is heterogeneous and exhibits different charges around the cell body. In addition, the conditioning film (orange) alters the physicochemical properties of the substrate by altering its charge, potential and surface tension, thus affecting local adhesion. A thin layer of water (interfacial water, light blue) deposited on the surface can potentially inhibit bacterial adhesion due to the hydrophobic components on the cell membrane (dark blue), such as proteins and extracellular polysaccharides. Once the bacterium is <1 nm from the surface, adhesins (red), flagella (brown), pili (blue) and curli (purple) probe the surface and actively initiate the adhesion process. Image adapted from [23].

A recent work by Ellison *et al.* on *Caulobacter crescentus* [31] highlighted the importance of pili in the attachment process. The tracking of labelled Tad pili of single *C. crescentus* cells by live microscopy showed that these appendices undergo multiple retraction and extension cycles, probing the surface and searching for

adhesion sites. The dynamic activity of pili ceases concomitantly with irreversible attachment, leading to adhesin synthesis to further increase surface contact.

Surface sensing and stimulation of adhesin production

The attachment of a bacterium to a substrate results in adhesion forces triggering mechanical stress and slightly deforming the cell envelope. The deformation of the membrane upon attachment to a surface can in some cases stimulate production of adhesins. In the case of *E. coli*, the stress in the cell membrane upon contact with hydrophobic surfaces triggers the regulation of curli transcription which facilitate the adhesion process [32, 23].

The flagellum acts as a surface sensor in many bacterial species, although its exact role in this process remains unclear. In the case of *Bacillus subtilis*, inhibition of flagellar rotation acts as a mechanical trigger to activate the signal transduction system that activates the productions of proteins necessary for biofilm formation [33].

Planktonic *C. crescentus* cells probe the substrate and attach via the polar flagellum, triggering the production of the adhesin holdfast that allows the bacterium to be irreversibly attached within seconds from the first contact [34]. These adhesins undergo an intramolecular rearrangement upon contact with the substrate, increasing the number of bonds and strengthening the adhesion force between the adhesins and the substrate [35, 23].

In most cases the transition from reversible to irreversible attachment involves the repositioning of the cell body from a polar to a longitudinal position in respect to the surface, maximising the contact area and the bonds between the cell and the substrate [2] (**Fig. 5.1.3**)

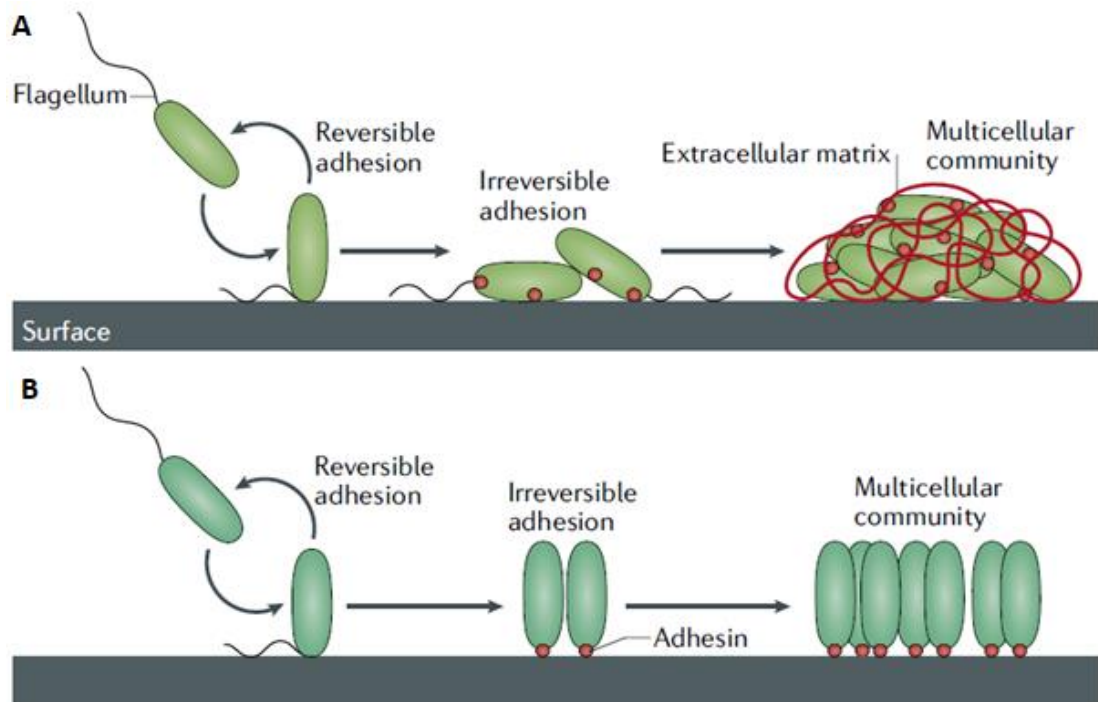


Fig 5.1.3 **A** In *E. coli* and other rod-shaped bacteria, initial surface contact is mediated by flagella and pili, which leads to the cell adhering to one of its poles. The transition from reversible to irreversible attachment involves the repositioning of the cell parallel to the substrate. Upon attachment, *E. coli* cells enhanced the strength of the adhesion by synthesising polysaccharide adhesins. The formation of a multicellular biofilm is initiated by the production of an extracellular matrix composed of polysaccharides, proteins and DNA. **B** *C. crescentus* attaches to the surface via the polar flagellum. Cells remain perpendicular to the surface and achieve irreversible attachment through the secretion of holdfast adhesin (red dots). Consequently, a *C. crescentus* multicellular community displays cells mainly oriented polarly and does not involve the production of an extracellular matrix. Image adapted from [23].

When surface attachment is consolidated and conditions are favourable and suitable for growth, sessile bacteria divide to form multicellular colonies, ultimately leading to growth and development of a mature biofilm [23].

5.1.2 Cell division in rod-shaped bacteria

To initiate bacterial division, the central cell division protein FtsZ assembles into a cytoskeletal scaffold known as the Z-ring. Subsequently, other proteins are recruited to the division site, causing the ingrowth of the cell membrane and synthesis of new cell wall [36, 37]. Rod-shaped bacteria divide with high precision in the middle of the cell generating two equally sized daughter cells. The positioning of the division plane in *E. coli*, *Acinetobacter baumannii* and *B. subtilis* is regulated by two inhibitory systems: the Min system prevents aberrant division at the cell poles, while nucleoid occlusion (NO) prevents the division plane from occurring over the nucleoids [36, 38].

The Min system

As shown in **Fig. 5.1.4**, the Min system of *E. coli* is initiated by MinE molecules forming a ring-like structure known as the E ring. This complex gradually secretes the ATPase protein MinD which, in complex with ATP, binds to the cell membrane and recruits MinC, which inhibits the polymerization of FtsZ, preventing the assembling of the Z-ring. In the cytoplasm of the bacterium, the released complex MinD–ADP undergoes nucleotide exchange and re-generates MinD–ATP, which assembles where the concentration of MinE is lowest: at the membrane of the opposite cell pole [38]. As this process repeats, the concentration of the MinCD complex increases at the poles of the bacteria, directing the polymerisation of FtsZ to the middle of the cell [36].

In *B. subtilis*, MinCD does not oscillate but binds to the proteic complex MinJ–DivIVA at the cell poles. During the late stages of the cell cycle, DivIVA is recruited to mid-cell, at the septum formation site, and is retained at the poles of the daughter cells after division [38, 39]. A peculiarity of *B. subtilis* is its stress response mechanism: in adverse environmental conditions this species differentiates into two cell types, the endospore and the mother cell. The endospore forms within the

mother cell and is enclosed in a multilayer of proteins that shelters the bacterial genome. When conditions are suitable the mother cell lyses and the spore is released into the environment where it quickly germinates and returns to the vegetative state [40].

Homologs of Min system proteins can be traced in the *A. baumannii* genome; although some have substantially different sequences compared to their *E. coli* counterparts, the sequences related to FtsZ are relatively similar within the core domain, essential for the polymerization of FtsZ into the Z-ring [41].

The nucleoid occlusion system

The molecular mechanism of nucleoid occlusion is regulated in *B. subtilis* by the nucleoid occlusion protein (Noc) [42] and in *E. coli* by the protein SlmA [43]. These proteins form a complex with DNA sequences scattered throughout the bacterial chromosome that are missing the terminus region (*ter*) [44]. Before the start of the DNA replication process, the region of the chromosome close to the origin of replication (*oriC*) occupies the middle part of the bacterium protected by the nucleoid effector protein, which prevents the formation of the the Z-ring at this site [38]. As the cell prepares for division, the *oriC* region of the chromosome and the associated nucleoid effector protein move towards the cell poles. Gradually in the middle of the cell is formed a region free of nucleoid effector, allowing the polymerization of FtsZ and the formation of the Z-ring. Nucleoid occlusion thus has a crucial role in coordinating chromosome segregation and cell division [44].

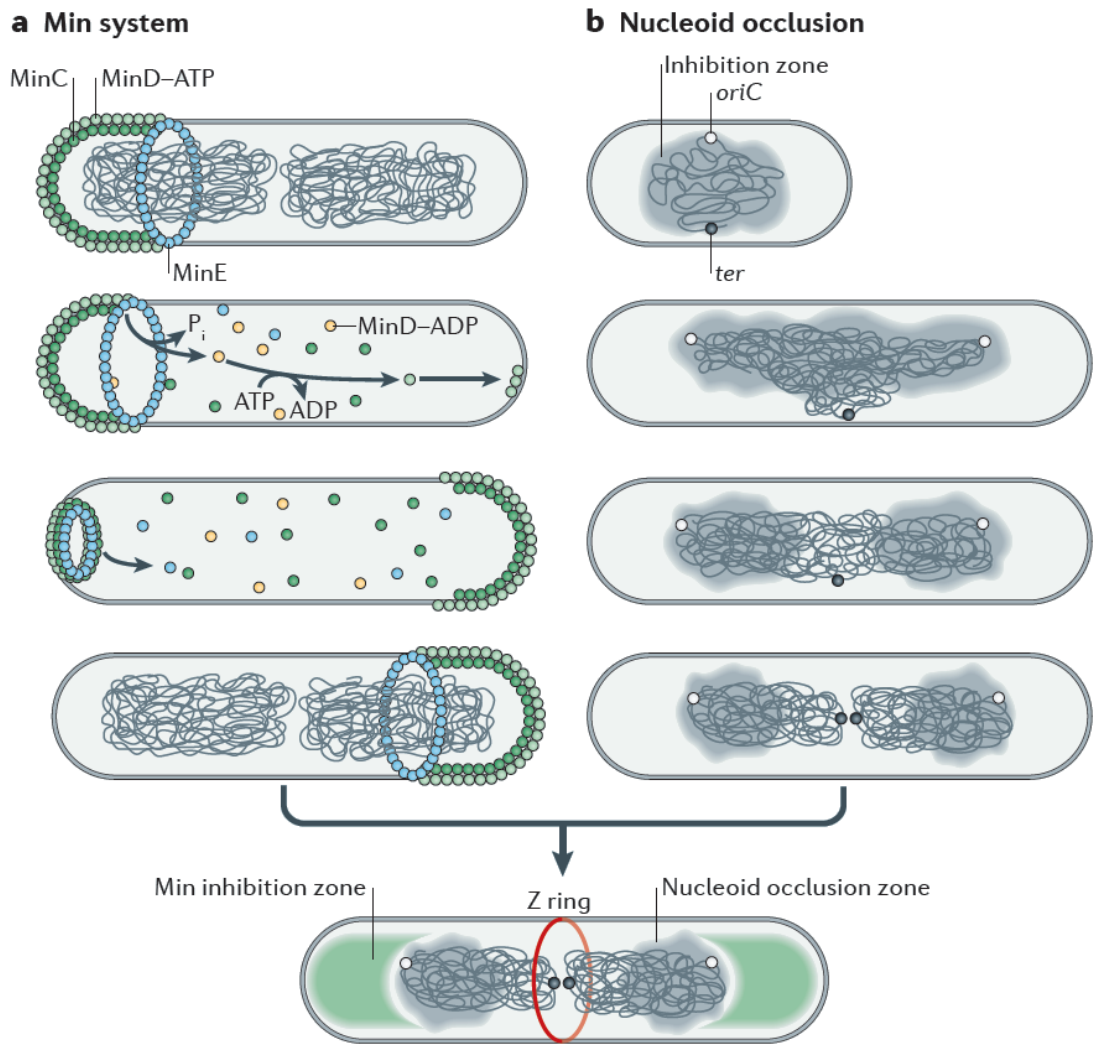


Fig 5.1.4 Schematisation of the role of the Min system (left) and the Nucleoid occlusion (right) in driving the division at the middle of the cell. Image adapted from [38].

***Caulobacter crescentus* cell cycle**

The division of *C. crescentus* involves the coordination of morphological, metabolic and cell-cycle events (**Fig 5.1.5**). At the beginning of its cell cycle *C. crescentus* is in planktonic state, using a single polar flagellum for motility and polar type IV pili to mediate adhesion to biotic and abiotic surfaces. In its planktonic form (labelled as **G1** phase in **Fig. 5.1.5**) *C. crescentus* cannot initiate chromosome division, the passage from planktonic to sessile involves the release of the polar flagellum and the retraction of the polar pili, while a narrow elongation of the cell wall, named stalk, protrudes from the same pole as the discarded flagellum. The stalk possesses an adhesin holdfast at its end, which allows *C. crescentus* to irreversibly attach to the surface within seconds from the first contact [34], this stage indicates the transition to the **S** phase represented in **Fig. 5.1.5**. Upon transition to irreversible attachment the cell begins chromosome duplication; the peptidoglycan synthesis of *C. crescentus* follows a distinct pattern throughout cell growth: in the early stages of cell life, the synthesis of peptidoglycan occurs laterally along the sidewall of the cell, it bursts at the cell pole, however, in order to synthesise the stalk [45]. The formation of the FtsZ ring at the mid-cell shifts the cell elongation mode from lateral to mid-cell peptidoglycan insertion [46]; interestingly FtsZ has been shown to be also involved in peptidoglycan synthesis at the cell pole during the formation of the stalk [47].

Caulobacter cells duplicate their chromosome only once before cell division while rapidly growing bacteria like *E. coli* cells can replicate their DNA replication up to four times before dividing. The chromosome replication and its segregation at the poles of the growing pre-divisional cell occurs during **S** phase and the brief **G2** phase. Before dividing, a new flagellum and new pili are grown at the pole opposite the stalk. Once the formation of the flagellum is complete, the cell divides in two physiologically and morphologically different daughter cells, one stalked cell attached to the substrate and one planktonic [48].

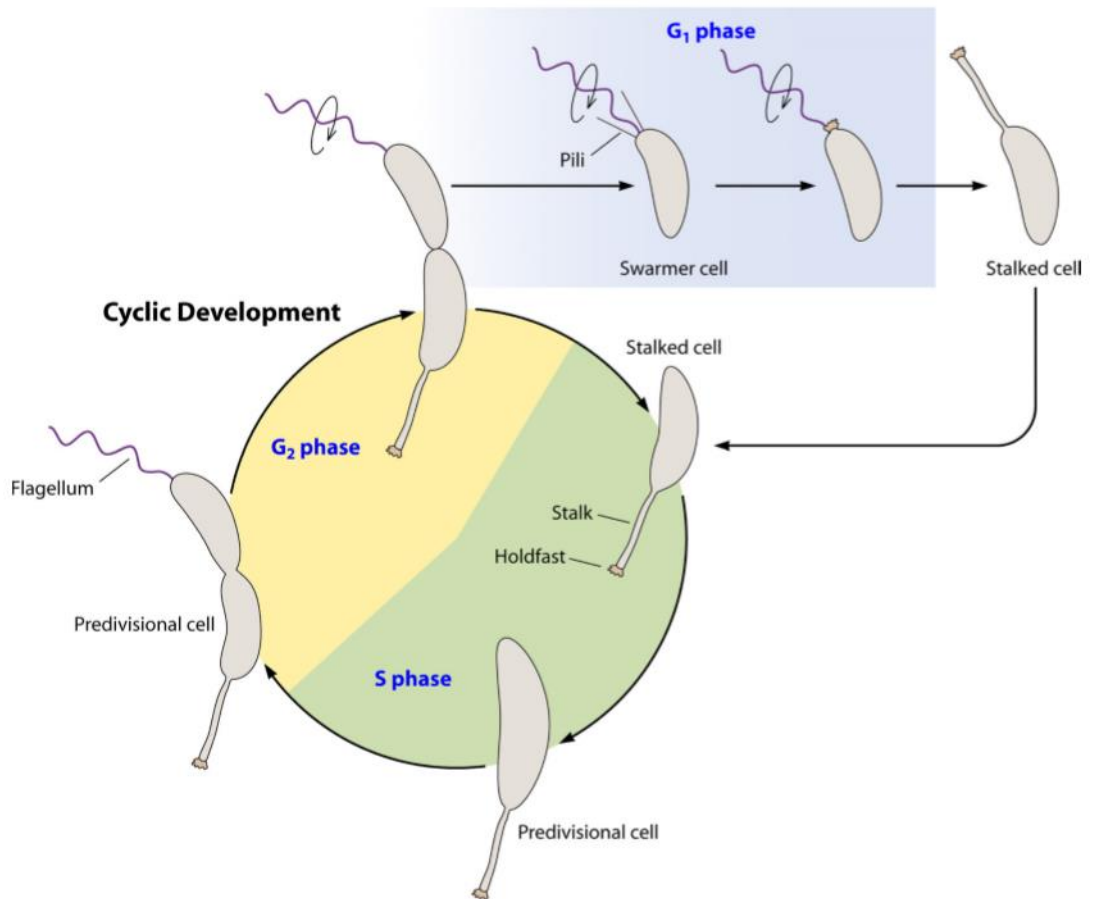


Fig 5.1.5 The life cycle of *C. crescentus* begins with the stalked cell with an adhesive holdfast at the tip of the stalk. Once the bacterium is attached to the substrate it enters the **S** phase, a cell state in which the cell grows and duplicates its chromosome, becoming a pre-divisional cell. Once the DNA has been replicated *C. crescentus* enters the **G₂** phase, in which flagellum and pili are formed at the swarmer cell pole. Two different cell types are generated: the stalked cell which re-enters the **S** phase, and the swarmer cell with the newly formed flagellum. The swarmer cell in a separate phase in respect to the stalked one, referred to as **G₁** phase, and cannot duplicate its chromosome. During this phase the adhesin holdfast is formed. Image adapted from [49].

5.1.3 The effect of nanostructured topography on the attachment of rod-shaped bacteria

As described above, bacterial adhesion to abiotic surfaces is strongly affected by the physio-chemical properties of both the substrate and the bacterial membrane, the latter including structural features such as flagella, pili and lipopolysaccharides [50, 51]. The interactions between bacteria and biological tissues (or abiotic surfaces functionalized with biomolecules) rely on ligand/receptor-like bonding.

Rod-shaped bacteria are bigger than *Staphylococci*, reaching 1-2 μm in length, and less deformable than eukaryotic cells, tending to maintain their shape upon attachment to a topographic surface [50]. Their cell membrane features allow them to react and attach to nanometre topographical substrates: the previously described *pili* are protrusions present on rod-shaped bacterial membranes in hundreds, have diameters less than 10 nm and length varying from a few hundred nanometres to a few micrometres [52]. *Flagella* are thicker, with a diameter reaching tens of nanometres, and also play a role in bacterial attachment [52]. Although evidence of this still has to be demonstrated, these membrane protrusions are capable of reaching surface features of nanometric scale, thus increasing the binding energy between the bacterium and the substrate [50].

The ability of prokaryotes to sense topographical nanofeatures has been studied by Bruinsma *et al.* [53], their study demonstrated that the initial attachment of *Pseudomonas aeruginosa* was statistically different on a topography with a roughness average (*Ra*) of 4 nm compared with a substrate with a *Ra* of 10 nm.

A recent work by Hizal *et al.* [54] focused on the attachment of *E. coli* on nanopillared aluminium surfaces. The substrates were hydrophilic due to their inherent oxide layer, but the effect of hydrophobicity was evaluated by spin-coating a nanoscopically thin layer of Teflon. The topography showed a periodicity similar to the length of the investigated bacteria and the hydrophilic surfaces allowed even the cavities of the substrate to be wet by the bacterial suspension, increasing the adhesion sites. Scanning Electron Microscope (FE-SEM) images allowed the

investigation of the morphology of the adhering bacteria: *E. coli* cells grown in static conditions (**Fig. 5.1.6 A**) appeared to adhere both to the tips as well as in the cavities of the conically aggregated nanopillar structures. In laminar flow growing conditions (fluid shear rate of 37 s^{-1}) *E. coli* cells appeared to be only adhering to the cavities of the uneven topography (**Fig. 5.1.6 B**), probably due to the fact that the anisotropic morphology of rod-shaped bacteria makes them more susceptible to fall down or roll over when subjected to a laminar flow. Regarding bacterial surface coverage, the nanopillared surfaces showed a significant reduction in *E. coli* adhesion, compared to electropolished flat substrates.

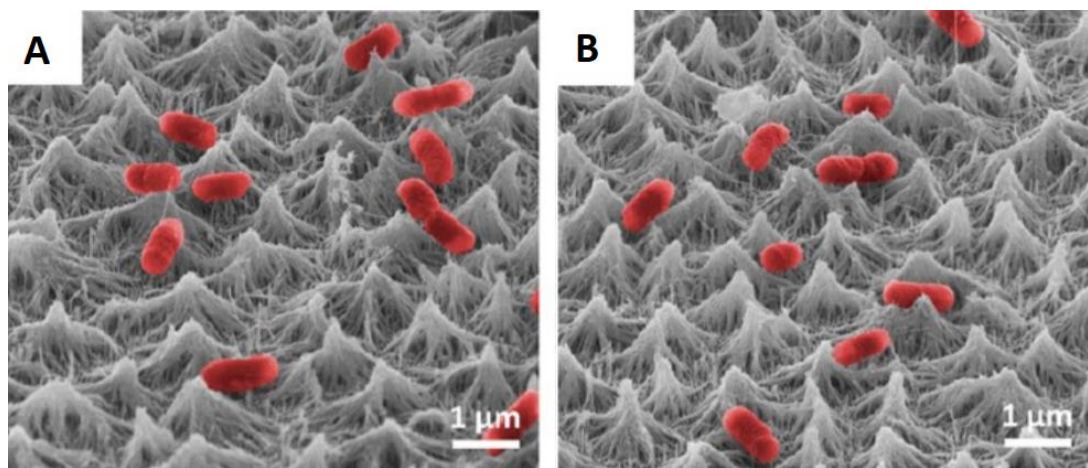


Fig. 5.1.6 False colour FE-SEM images of *E. coli* cells grown on static (A) and in steady flow (B) conditions on nanopillared aluminium surfaces. Image adapted from [54].

Several studies have highlighted how the optimal size for bacterial interaction with the surface may, be on the microscale level [55, 56, 57]. A possible explanation of these results is the shielding from shear forces and the higher number of adhesion sites due to the increase in surface area available for attachment, allowing an increase in binding energy.

A study by Edwards and Rutenberg [58] hypothesises that the shape of the topographic features influences the total binding adhesion energy more than their size. The studied also highlighted how the cost to the bacterial cell in terms of elastic energy due to its distortion may constitute an energetic barrier to bacterial

adhesion, highlighting once again how bacterial attachment relies on a complex balance of attractive and repulsive forces.

Serrano *et al.* [59] granted antibiofouling properties to commercial medical textiles used for surgical sutures; their method produced nanostructured topographies at the surface of the materials, using oxidative plasma treatment to control the degree of surface etching and features dimensions. The functionalised polymers included poly(ethylene terephthalate) (PET, Miralene®) and modified glycolic acid (Monosyn®). Bacterial attachment significantly decreased to the nanostructured substrates, with increasing plasma treatment time leading to an almost linear decrease in bacterial colonisation, up to a reduction by an order of magnitude in the samples plasma treated for 20 min. SEM images of *E. coli* cells adhering to the nanostructured polymers, acquired in tilted configuration (**Fig. 5.1.7**) showed the bacteria adopting a random orientation on the sample, not conforming to the nanopattern preferential direction; the cells were observed making contact only with the peaks of the topographical features, none were visible inside the valleys, not even where these were larger than the size of the cells. Bacteria were seen dividing via polar growth on the untreated substrates, adopting a configuration parallel to the substrate, with a last string of the septum maintaining the contact between the two daughter cells.

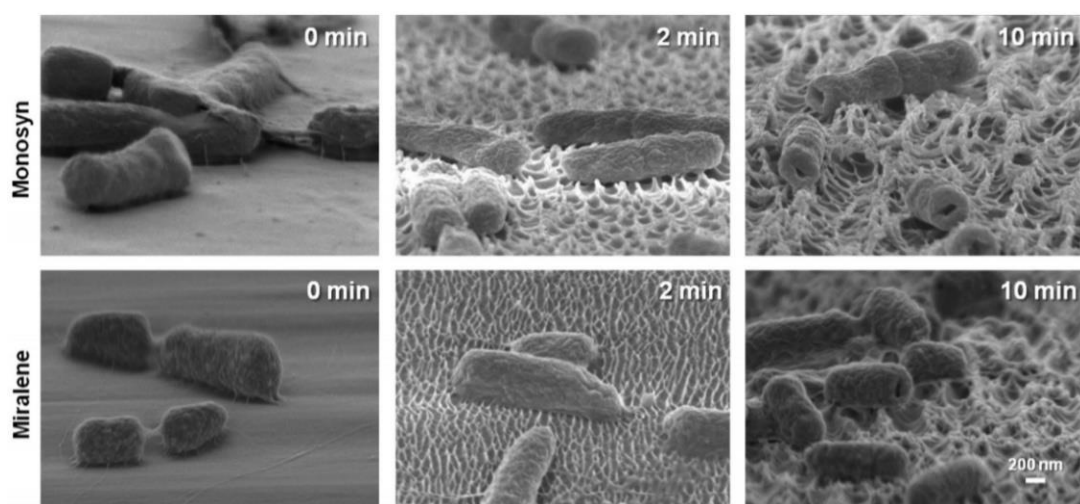


Fig. 5.1.7 SEM images of *E. coli* cells cultured for 2 h on untreated and plasma-treated (2 and 10 min) Monosyn and Miralene sutures. Image adapted from [59].

While Live/Dead assay did not highlight a bactericidal effect of the nanostructured surfaces, the cells on the samples that were plasma-treated for 10 min displayed a deformed morphology, an effect that might have been caused by the drying stage of sample preparation for SEM imaging.

In their 2020 work, Jenkins *et al.* [60] used thermal oxidation technique to generate nanopillars on the surface of grade 5 titanium alloy, a material widely used for orthopaedic implants. The antimicrobial effect of the substrates was evaluated on Gram-positive and Gram-negative species. In the case of *E. coli*, whose membrane is characterised by a thin peptidoglycan layers (≈ 5 nm), the nanopillar-induced envelope deformation and penetration was observable both in SEM (**Fig. 5.1.8**) and TEM monographs. Viability testing was performed via BacTiter-Glo assay, revealing significant decrease in the viability of *E. coli* cells when incubated for 3 and 10 h on Ti nanopillars (NW-850-5) relative to controls (flat titanium alloy plates). An in-depth analysis assessed some cases of membrane penetration by the nanopillars, rarely resulting in mechanical rupture and cell lysis. As these interactions could not solely account for the assessed reduction in cell viability, proteomic analysis was performed and identified a number of *E. coli* differentially expressed proteins (DEPs) associated with oxidative stress, indicating that H_2O_2 levels were higher in cells incubated on NW-850-5 than on controls, a conditions often observed in bacteria exposed to bactericidal antibiotics. Another condition observed in this work was nanopillar-induced cell impedance, which reduced the capacity of bacteria to replicate on NW-850-5 surfaces, contributing to the reduction in biofilm formation.

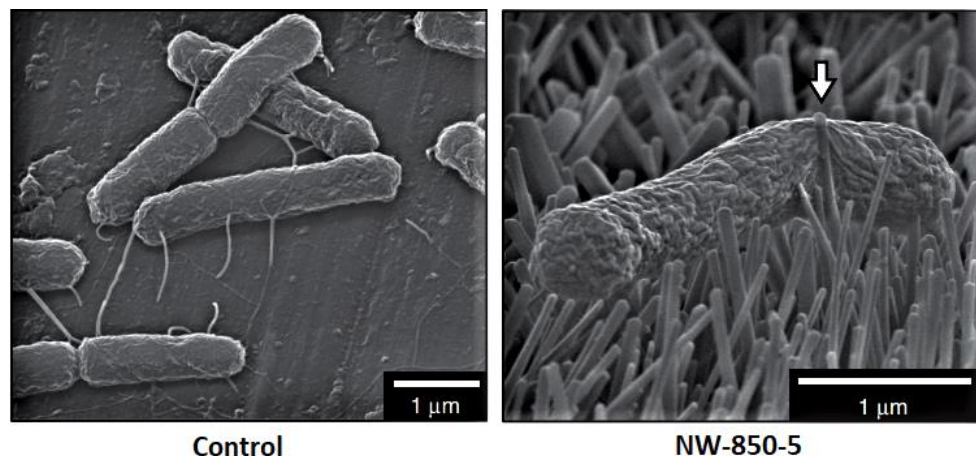


Fig. 5.1.8 SEM images of *E. coli* cells cultured for 3 h on flat titanium alloy (control) and TiO₂ nanopillar surface (NW-850-5). Image adapted from [60].

A recent study by Susarrey-Arce *et al.* [61] focused on the functionalization of silicon nanowire arrays (SiNWs), an example of nanostructured topography presented in the previous chapter, with (3-aminopropyl)triethoxysilane for the incorporation of chlorhexidine digluconate, an approved biocide. This system showed an antimicrobial effect on planktonic and surface-attached *E. coli* cells while SEM imaging showed bacterial proliferation on non-functionalised SiNWs. Single bacteria did not present membrane disruption due to the interaction with the sharp features of SiNWs arrays and *E. coli* cells appeared to be capable to take advantage of flagella and pili to generate multiple contact points with the irregular topography. Even on the nanoscale it may be possible for these features to increase binding energy with topographical and chemical surface features.

The works of Scheuerman *et al.* [56] and Medilanski *et al.* [62] demonstrated that motile bacterial strains were capable of colonising microstructured surfaces less than their correspondent mutant non-motile strain, suggesting that flagella play a role in recognising topographical features and finding attachment sites. However, the involvement of extracellular protrusions in attachment to nanotopographical surfaces has not been extensively studied in literature, although Bakker *et al.* [63] proposed that bacterial adhesion to nanometre-scaled surfaces is mediated by structures such as fimbriae.

Recently Hsu *et al.* [64] studied the effect of nanoscale topography on the adhesion of *E. coli* and *Pseudomonas fluorescens* using silicon wafers with nanoscale patterns of pores created in thermally grown Silicon dioxide. The results suggest that bacterial cells attach in orientations that allow them to maximize their contact area with the surface in order to achieve a stronger and more stable attachment. SEM images (**Fig. 5.1.9**) show the different morphologies that bacterial cells exhibit, including different number and size of cellular appendages, to adapt to the topographical features of the substrate.

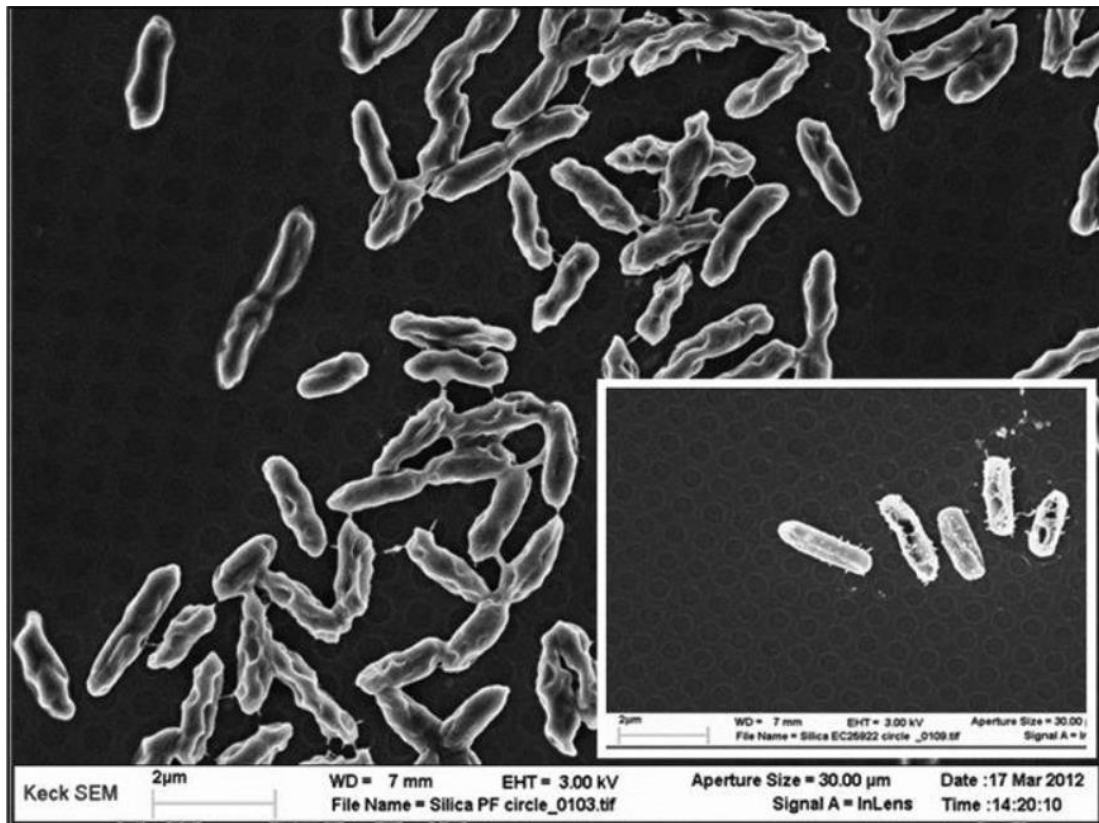


Fig. 5.1.9 SEM images of *E. coli* (large photos) and *P. fluorescens* (insets) cells attached to nanostructured silica substrates after 24 h culture. Image adapted from [64].

The biocidal effect of nanostructured Silicon surfaces on *E. coli* was investigated by Tripathy et al. [65]: the nanostructured silicon surfaces (NSS), inspired by dragonfly wing, displayed tall (8–9 μm high) structures with sharp tips (35–110 nm) and were fabricated using a single-step, maskless deep reactive ion etching technique. SEM cross section images allowed to measure the sharpness of the nanostructures with tip angles ranging from 32° to 45°. SEM images of sessile *E. coli* cells stretching and deformation on NSS (Fig. 5.1.10) with a projected surface area increased almost three times as compared to the projected surface area of *E. coli* adhering to flat Silicon surfaces.

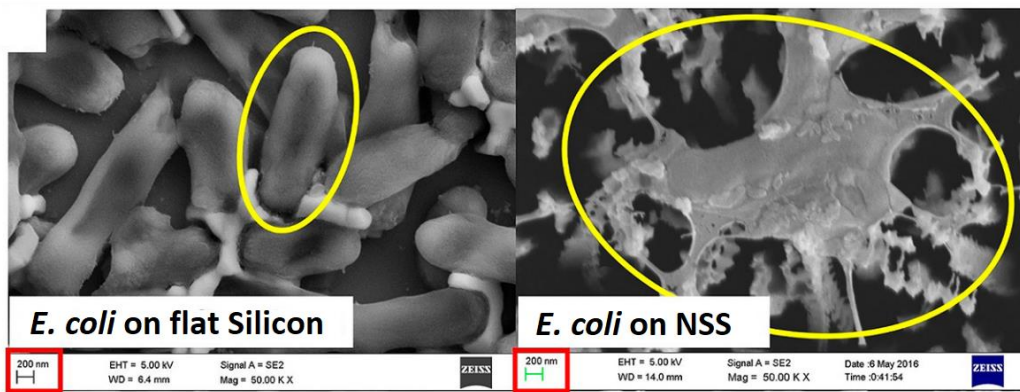


Fig 5.1.10 SEM images of *E. coli* adhering to flat Si (left) and NSS (right). The stretching of the cells on NSS increases their projected surface area compared to the on flat Si surfaces. Image adapted from [65].

Ivanova *et al.* [66] studied the adhesion of *B. subtilis* to black silicon: a synthetic Si substrate that displays high aspect ratio nanoprotusions on its surface, mimicking the topography of the wings of the dragonfly *Diplacodes bipunctata*. The samples were fabricated through a simple reactive-ion etching technique already used in photovoltaic applications. The results highlighted a mechanical bactericidal effect of these substrates, independent of chemical composition. SEM images (**Fig. 5.1.11**) showed the *B. subtilis* membrane integrity to be considerably disrupted by the nanopillars, with deformation and engulfment of the cells.

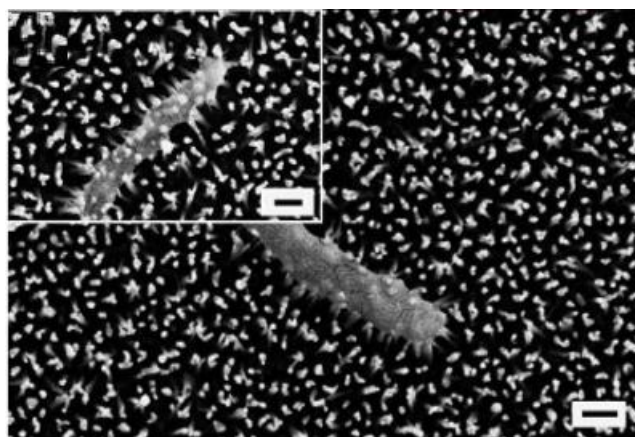


Fig 5.1.11 SEM images of *B. subtilis* adhering to black silicon. The cell membrane appears to be significantly disrupted through interaction with the nanostructured surface. Scale bars are 200 nm. Image adapted from [66].

The literature on the subject of adhesion of rod shaped bacteria on nanostructured surfaces is not comprehensive [50], probably due to the fact that description of the bacterial structures associated with attachment is relatively recent and their small size requires high resolution imaging with advanced sample preparation techniques. A closer study on the involvement of membrane structures during attachment to nanostructured substrates is needed to comprehend the mechanisms that enable bacteria to adapt and proliferate on topographic surfaces, this approach could lead to the engineering of antibiofouling substrates that discourage or completely prevent bacterial adhesion and colonisation. Moreover, the impact of nanostructured topographies on the orientation and division of bacteria, leading to their ability to form cell chains and biofilms was observed in previous studies [61, 50], which highlighted its variability amongst different species. This chapter focuses on the rod-shaped bacterial species: *E. coli*, *B. subtilis*, *Acinetobacter baumannii* and dedicates a section to the unique case of *C. crescentus*. The Live/Dead assay provides an insight on the concentration and viability of the adhering cells while SEM images in this work allow identification of the points of contact of microcolonies with the surface. The division modes of the listed bacteria will be furtherly described to analyse how the nanostructured topography impacts them and how bacteria adapt to it in the first stages of biofilm formation.

A closer focus on how the attachment and division of bacterial cells to surfaces with controlled nanotopography could enable the engineering and fabrication of materials able to effectively control bacterial adhesion, with considerable potential biomedical and industrial applications.

5.2 Experimental Details

5.2.1 Fabrication and Functionalisation of Silicon NanoWire (SiNW) arrays

SiNW wafers were provided by J. G. E. Gardeniers, and R. M. Tiggelaar (MESA + Institute for Nanotechnology, University of Twente, The Netherlands).

Fabrication of silicon nanowires (SiNW)

SiNW were fabricated on flat silicon wafers (p-type boron doped, (100)-orientation, resistivity 5–10 Ω cm, 100 mm diameter, thickness 525 μ m, single side polished; Okmetic, Finland). Silicon wafers were cleaned by immersion in 100% nitric acid (UN2031; OM Group) for 10 min and then in boiling 69% nitric acid (BASF, 51153574) for 15 min. The following step consisted in the substrates being rinsed with deionised water and spin dried. UV-lithography was used to define a regular pattern of 10 μ m x 10 μ m, which was used to form the SiNWs in an 8 mm x 8 mm area. The patterned surfaces were then post-baked for at least 10 min at 120 $^{\circ}$ C in air. SiNWs were formed in the lithographically patterned areas using a two-step metal assisted chemical etching (MACE) process [67]. The nanopatterned surfaces were subsequently submerged in a 5 mM solution of AgNO_3 (Sigma-Aldrich, 99%) in 10% aqueous HF (BASF-51151083) for 1 min in the dark. The substrates were then directly immersed in a solution of DI water, 50%-HF and H_2O_2 (BASF, 55316830) (volumetric ratio DI:HF: H_2O_2 = 77.5:20:2.5), and etched for 20 min (in the dark—etch rate ca. 0.6 μ m min⁻¹). After this process, the samples were rinsed using deionised water. The AgNPs were removed from the substrates by immersing them in 69% nitric acid (HNO_3 ; BASF, 51153574) at room temperature for 65 h and subsequent rinsing with DI water. SiNW samples were then cleaned using Piranha-solution (a 3:1 volumetric mixture of sulphuric acid (H_2SO_4 ; BASF, UN 1830) and H_2O_2 ; temperature 95 $^{\circ}$ C, cleaning time 15 min) in order to remove all traces of

photoresist, after this process they were rinsed with DI water and dried under nitrogen flow. Finally, individual samples of 1 cm x 1 cm size were cut using a dicing machine (Disco DAD-321).

Imaging of sessile bacteria on flat Si and SiNWs: *Escherichia coli* (ATCC 10798), *Bacillus subtilis* (ATCC 6051) and *Acinetobacter baumannii* (ATCC 19606) were transferred from frozen stock to a fresh agar plate and incubated overnight at 37 °C. Three colonies of each bacterial species were taken from the agar plate with a sterile plastic loop, transferred to fresh nutrient broth (NB) medium (Oxoid, Thermofisher) and grown overnight in a shaking incubator (200 rpm, at 37 °C).

Caulobacter crescentus (ATCC BAA-2331) was transferred from frozen stock to fresh agar prepared dissolving 2.0 g of Peptone (Sigma-Aldrich, 91249), 1.0 g of Yeast Extract (Sigma-Aldrich, Y1625), 0.2 g of Magnesium Sulphate Heptahydrate (Sigma-Aldrich, 63138) and 13.0 g of Agar (Sigma-Aldrich, A1296) in 1L of deionised water, following ATCC indications [69]. *C. crescentus* was incubated overnight at 30 °C, three colonies were taken from the agar plate with a sterile plastic loop, transferred to a growing medium containing 2 g/L of Peptone, 1 g/L of Yeast Extract and 0.2 g/L of Magnesium Sulphate Heptahydrate in deionised water. The culture was grown overnight in a shaking incubator (200 rpm, at 30 °C).

SiNW surfaces and flat Si wafers underwent sterilisation under UV light for 20 min and were then placed in a sterile 24- well plate. 1 mL of 10^5 CFUs/mL bacterial suspension in growing medium was subsequently added to each of the wells and the samples were incubated for 8 h at 37°C, 30 °C in the case of *C. crescentus*.

Viability and imaging assays using bacteria were performed in triplicate.

Viability of sessile bacteria

The viability of bacteria adhering to surfaces was studied via confocal laser scanning microscopy (CLSM).

At the end of the incubation period, flat Si and SiNW surfaces were washed 3 times with sterile 0.85% (w/w) NaCl solution and stained with Live/Dead BacLight bacterial viability kit (Molecular Probes, L7012). In this test, each sample was incubated in a 24-well plate for 15 min in the dark at room temperature in 1 mL of a sterile 0.85% solution containing a mixture of SYTO 9 and propidium iodide (PI). These nucleic acid stains differ in their absorption and emission wavelengths and on their capacity to penetrate bacterial cell walls. SYTO 9 (green stain) is capable to penetrate all live and dead Gram-positive and Gram-negative bacteria in a population (i.e. bacteria with both intact and disrupted membranes) [68]. In contrast, PI is only capable of penetrating bacteria with damaged cell walls and binds strongly between the bases in the DNA with little or no sequence preference. Consequently, when both stains are present in a bacterial cell with a damaged membrane, PI displaces SYTO 9 from the nucleic acid chains, leading to emit a red fluorescent emission [71]. Despite this staining method to identify live and dead bacterial cells has been used for decades, the exact mechanism of interaction of SYTO 9 with nucleic acids is not fully understood [70]. After staining, the samples were immediately imaged using a confocal upright Zeiss LSM 880 Multiphoton microscope. Collected confocal fluorescence images were processed using Fiji software.

Scanning Electron Microscope (SEM) imaging

At the end of the incubation period, samples for SEM imaging were fixed overnight at 4°C in a 4% paraformaldehyde and 2.5% glutaraldehyde in 0.1 M phosphate buffer. Sample fixation required three sequential steps involving aqueous solutions

of 2% osmium tetroxide for 1 h, 1% tannic acid for 30 min and 2% osmium tetroxide for 1 h. In between each staining step, DI water was used to rinse the surfaces. The final staining step involved the samples to be immersed overnight in 1% uranyl acetate solution in water. For the final staining step, the samples were rinsed with DI-water, and progressively dehydrated using different volumetric ratios of ethanol (i.e. 30%, 50%, 70%, 90% and 100%). After the dehydration procedure, samples were critical-point dried using CO₂ (Quorum Technologies K850) and subsequently sputter coated with 10 nm of Au/Pd (Quorum Technologies Q150T) for SEM imaging at 10 kV using a JEOL7001F FE-SEM system.

5.3 Results

5.3.1 Viability of sessile bacteria on flat Si and SiNWs

Confocal laser scanning microscopy (CLSM) images (**Fig. 5.3.1**) of bacteria stained with Live/Dead viability kit allowed the investigation of the effect of the nanostructured topography on the viability of *E. coli*, *A. baumannii*, *B. subtilis* and *C. crescentus* cells. The green cells in **Fig. 5.3.1** are stained by SYTO 9, a cell-permeant dye that enhances its fluorescence upon binding with nucleic acids and is capable of penetrating live as well as dead cells [69]. The red cells are stained with Propidium Iodide, a DNA binding dye capable of permeating cells whose membrane integrity is compromised, and consequently detects dead cells in a population [71]. Live/dead viability assays show dead cells as red or yellow and alive cells in green.

No significant difference was found in the viability of bacteria adhering to flat Si and SiNWs (**Table 5.3.1**), with 93.96 (± 1.10) % live *E. coli* cells on flat Si and 90.55 (± 1.68) % on SiNWs. Similar percentages were found in the case of *A. baumannii*, with 91.11 (± 1.19) % live cells on flat Si and 85.91 (± 4.90) % on SiNWs. *B. subtilis* and *C. crescentus* respectively displayed 66.87 (± 14.73) % and 78.91 (± 15.76) % live cells on flat Si while their viability on SiNWs was 74.23 (± 6.24) % and 93.57 (± 3.88) %. These data highlight that SiNWs surfaces don't have an antimicrobial effect on the tested bacterial species.

Table 5.3.1 Percentage (%) of alive *E. coli*, *A. baumannii*, *B. subtilis* and *C. crescentus* sessile bacteria on flat Si and SiNWs surfaces after 8 h of culture.

	<i>E. coli</i>	<i>A. baumannii</i>	<i>B. subtilis</i>	<i>C. crescentus</i>
Flat Si	93.96 \pm 1.10	91.11 \pm 1.19	66.87 \pm 14.73	78.91 \pm 15.76
SiNWs	90.55 \pm 1.68	85.91 \pm 4.90	74.23 \pm 6.24	93.57 \pm 3.88

The comparable viability between *E. coli* cells attached to the nanostructured surface and the flat Si finds confirmation in the study of Tripathy *et al.* [65], in which bacteria adhering to flat and nanostructured Si surfaces displayed similar viability after 3 and 18 h growth. The viability was sensibly reduced when the nanostructured surfaces were chemically functionalised with Ag and Cu.

An antibiofouling, but not bactericidal, effect of nanostructured surfaces was observed by Serrano *et al.* [59] via Live/Dead assay on *E. coli* cells. Unlike the polymers for medical sutures modified in said study, our SiNWs did not show a significant reduction in bacterial density at the liquid/solid interface. The antimicrobial effect of the nanostructured Ti surface engineered by Jenkins *et al.* [60] was attributed to an increased oxidative stress and a decreased capacity of the cells to replicated, in comparison to flat Ti. The high viability and concentration of *E. coli* cells visible in our CLSM images suggest that these effects are absent or reduced on SiNWs.

Our data related to *B. subtilis* does not reflect the high percentage of cells with disrupted membranes found by Ivanova *et al.* [66] in their investigation. The lower antibacterial activity of the SiNWs arrays with respect to Ivanova's "black silicon" could be attributed to differences in topography such as the height of the peaks, their diameter, and interspacing, all of which represent important factors in a surface bactericidal performance [72]. Another factor to take into consideration is the chemical composition of the substrates, with the SiNWs arrays displaying a thin SiO₂ layer at the surface (see EDS analysis in Chapter 4). These differences between the two nanostructured Si surfaces suggest that both topography and surface chemistry play a role in their antimicrobial activity.

The CLSM images (**Fig. 5.3.1**) show a comparable coverage of bacterial cells adhering to flat Si and SiNWs for all species after 8 h growth, in contrast with the work of Hsu *et al.* [64] in which the two *E. coli* strains tested consistently exhibited higher levels of attachment to the flat Si surfaces than to the nanopatterned ones.

The images also display a higher coverage of *E. coli* and *A. baumannii* cells compared to *B. subtilis* and *C. crescentus*, probably due to the slower growing rate of the two latter species in these experimental conditions [73, 74, 75, 76]. As expected, *B. subtilis* exhibits its characteristic chains of cells connected to each other by their poles [77] while the other populations are mostly formed by single bacteria, with some cells coupled at different stages of a division event.

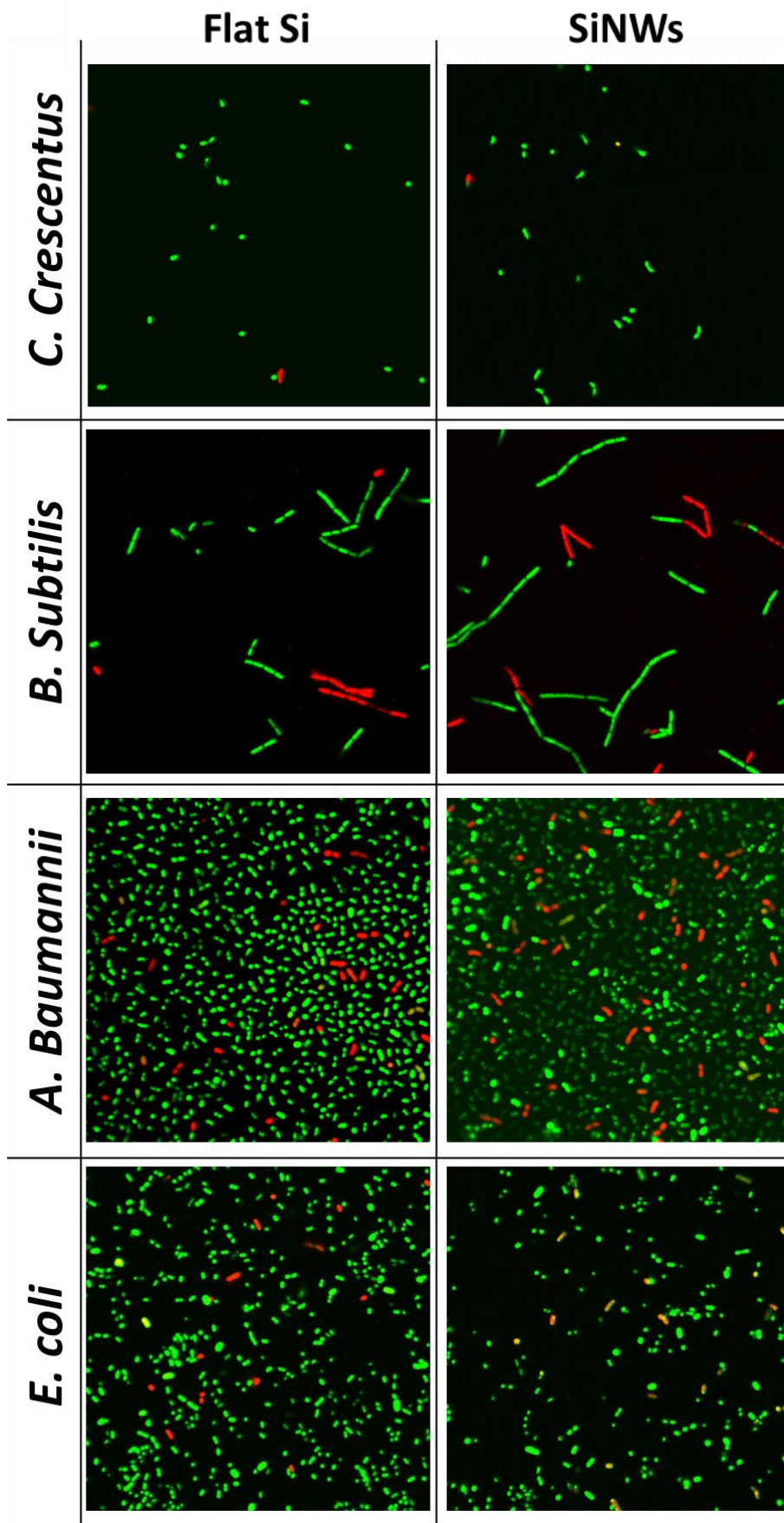


Fig 5.3.1 Representative merged confocal laser scanning microscopy images for live (green) and dead (red) bacterial cells adhering to flat Si and SiNWs after 8 h of culture. Images size: 71.8x71.8 μm^2 .

5.3.2 Attachment and division of *Escherichia coli* cells on flat Si and SiNWs

E. coli is a microorganism capable of colonising the gastrointestinal tract of children within a few hours after birth. Most *E. coli* strains coexist with their host with mutual benefit for decades, causing disease only in immunocompromised hosts or when breaching the normal gastrointestinal barriers, like in the case of peritonitis [25]. Highly adapted *E. coli* strains can cause disease even in healthy individuals, leading to infections that may be contained to the mucosal surfaces or spread across the body. Three clinical conditions are generally associated with infection due to pathogenic *E. coli* strains: urinary tract infection, sepsis/meningitis, and enteric/ diarrheal disease [78]. The strain studied in this work, ATCC 10798, isolated from the stool sample of a diphtheria patient in 1922 [79], is one of the most utilised of this species and will serve a model to investigate how *E. coli* interacts with nanostructured surfaces.

Like in the previous chapter, the biofilms and cells were investigated using high resolution SEM imaging in tilted and upright configurations. This technique allowed us to probe the morphology of the bacterial colonies, the attachment points and the division modes of bacterial cells attached to flat Si and SiNWs substrates. The sample preparation protocol used for these assays preserved the bacterial membrane and the extracellular appendices of the sessile bacteria, allowing to obtain high resolution images of microcolonies and single cells.

High-magnification SEM images of *E. coli* cells adhering to flat Si (**Fig. 5.3.2 A, B, C** and **Fig. 5.3.3 A, B, C**) show cells in immediate contact with the surface, producing in plane 'two-dimensional (2D)' bacterial colonies. The bacteria appear intact and morphologically unchanged, adopting multiple orientations to adhere to the Si substrate but preferentially aligning along the surface plane. **Fig. 5.3.2 B** shows long appendages protruding from the bacterial membrane, facilitating the attachment to surfaces and connecting the cells in the developing colony.

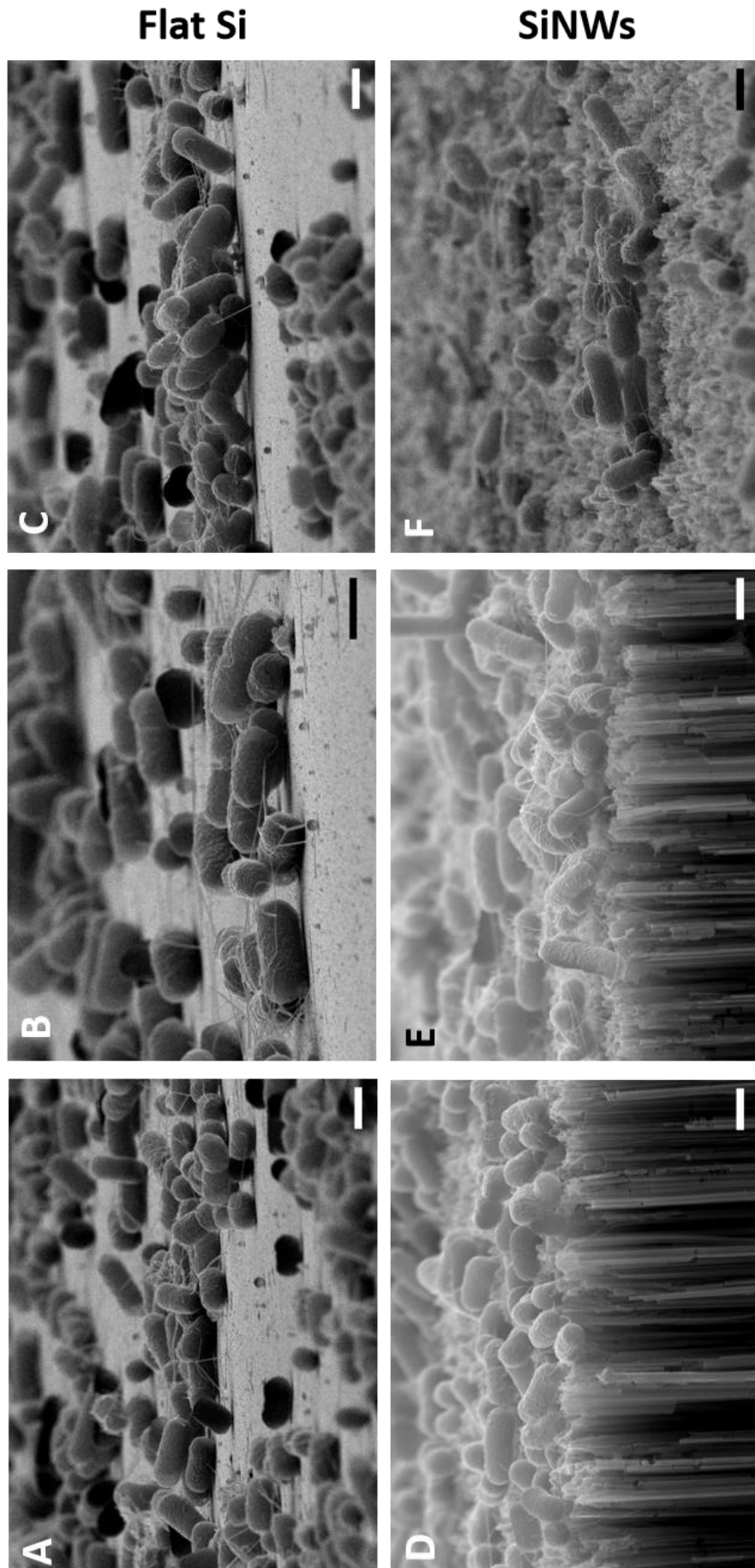


Fig. 5.3.2 Representative SEM images of colonies of *E. coli* cells adhering to flat Si (A, B, C) and SiNWs (D, E, F). Scale bars are 1 μm .

The SEM images of *E. coli* adhering to SiNWs surfaces (**Fig 5.3.2 D, E, F** and **Fig. 5.3.3 D, E, F**) shows bacterial cells taking advantage of flagella and pili to adhere to sharp tips and cavities of the nanostructures to colonise the substrate [45]. These extracellular protrusions and the characteristic rod shape of *E. coli* allow the cells to generate multiple contact points with the irregular nanostructured surface, as reported on other substrates [59, 80]. The SEM images do not show a dramatic cell wall disruption caused by the sharp features of the SiNWs, in accordance with our cell viability data obtained via Live/Dead assay.

In a previous study by Tripathy *et al.* [65], *E. coli* cells adhering to nanostructured substrates were observed stretching and deforming, increasing their projected surface area in order to adhere on nanostructured silicon surfaces. The SEM images in the study Serrano *et al.* [59] seemed to confirm these findings, with the cells adhering to the polymers that underwent plasma treatment for 10 min appearing deformed and not displaying their characteristic rod shape. This effect is even more evident in the work of Jenkins *et al.* [60], whose SEM images display *E. coli* cells sinking into the nanopillars, to an extent that in some cases caused membrane disruption and cell lysis.

The images in this work show bacteria with an unaltered morphology, retaining their rod shape while adhering to SiNWs arrays with the aid of extracellular protrusions. **Fig 5.3.2 F** shows a colony of *E. coli* cells adapting to the nanostructured topography with a few bacteria adhering to other sessile cells rather than to the substrate, a phenomenon that can be observed more closely in **Fig. 5.3.3 D**, which depicts what seems to be the beginning of a 3D bacterial formation. A similar cell cluster is observable on flat Si (**Fig. 5.3.3 A**), where a 3D bacterial formation develops vertically in respect to the surface, either generated by multiple cell divisions or by planktonic cells adhering to sessile ones. Another interesting aspect of the 3D colonies in **Fig 5.3.3 A, B** and **D** is the abundant presence of long appendages protruding from the membranes, connecting the cells and supporting the vertical growth of the colony.

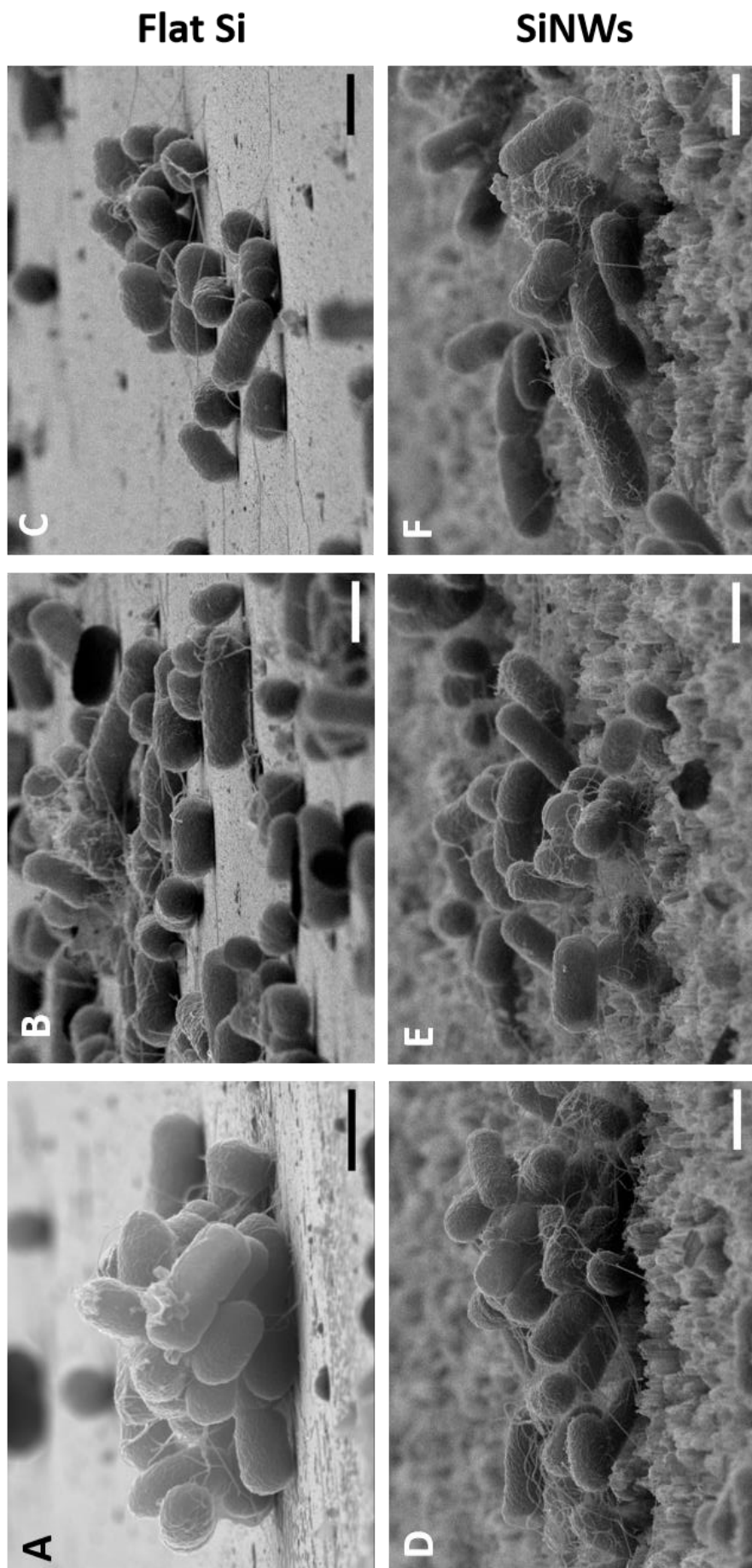


Fig. 5.3.3 Representative SEM images of small colonies of *E. coli* cells adhering to flat Si (A, B, C) and SiNWs (D, E, F). Scale bars are 1 μm .

Fig. 5.3.4 provides a closer look to *E. coli* cells adhering to flat Si (**A, B, C**) and SiNWs (**D, E, F**), allowing a deeper investigation on how the nanostructured topography effects growth and morphology of this specie. In the foreground of **Fig. 5.3.4 A** we can observe an *E. coli* cell at the very first stage of its division process, with a visible septum in formation at the mid-cell, locating the Z-ring within the membrane. In the same image we can see a bundle of extracellular structures protruding from the back of the dividing cell; **Fig 5.3.3 A** and **D** show similar filaments tethering cells to each other within the bacterial cluster, playing an essential role in the structural integrity of the newly formed colony.

On SiNW arrays, there seems to be a tendency for the cell division to take place in the plane parallel to the surface, as shown in **Fig. 5.3.4 D**. In **Fig. 5.3.3 D, E, F** the only cells dividing in upright positions appear to be adhering to other cells in the formation of a 3D colony. The cells in **Fig. 5.4.3 E** are at the late stage in their division process, their position at the edge of the SiNW array reveals the septum at the mid cell. In **Fig. 5.3.4 D**, short filaments can be observed protruding from the wrinkled membrane of the dividing bacteria; interestingly these protrusions seem to be present mostly on the surface of cells adhering to SiNWs, as if the nanoroughness stimulates *E. coli* to secrete additional appendages to increase the number of attachment points to the substrate.

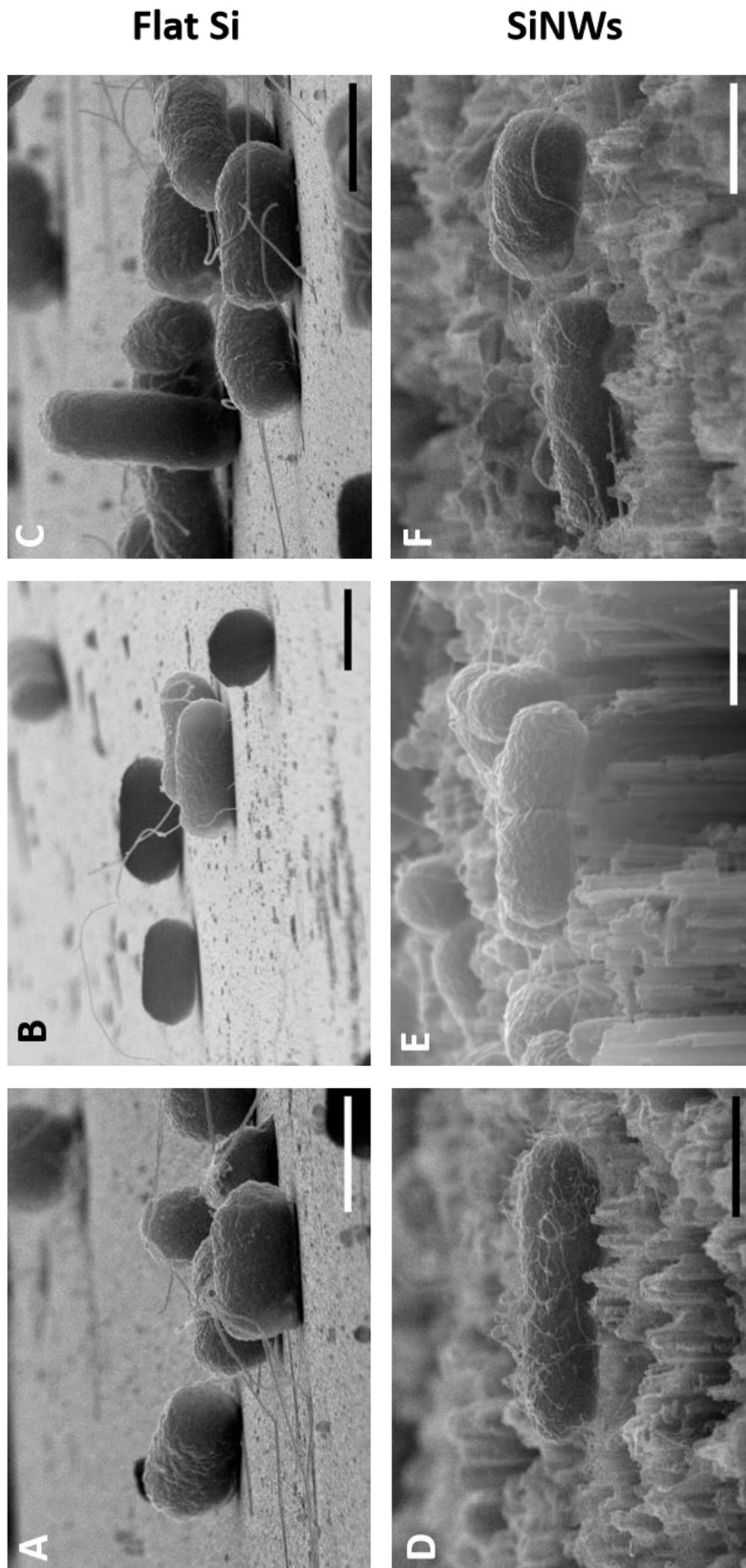


Fig. 5.3.4 Representative SEM images of *E. coli* cells adhering to flat Si (A, B, C) and SiNWs (D, E, F). Scale bars are 1 μm .

The SEM images in **Fig. 5.3.5** were taken using the electron microscope in upright configuration and reveal how far the extracellular protrusions of *E. coli* extend in order to anchor the cells to the surface. Long filaments can be seen interconnecting the cells on both flat Si (**C**) and SiNWs arrays (**F**), on flat Si they extend onto the surface for several micrometres, providing anchoring points and possibly searching other cells to form a network with. **Fig. 5.3.5 D** delivers a stunning visual of the filaments spreading in multiple directions to anchor the cell to SiNWs, while shorter protrusions form a web-like structure around the cell, which also could have the function to increase the number of contact points with the surface. An *E. coli* cell in **Fig. 5.3.5 F** appears to express the same type of protrusions, but we can observe the additional role they have in interconnecting nearby cells in the first stages of biofilm formation.

Interestingly, similar filaments were seen protruding from the *E. coli* cells cultured on flat Ti in the study of Jenkins *et al.* [60], but seemed to be absent on the cells cultured on nanostructured substrates (**Fig. 5.1.8**).

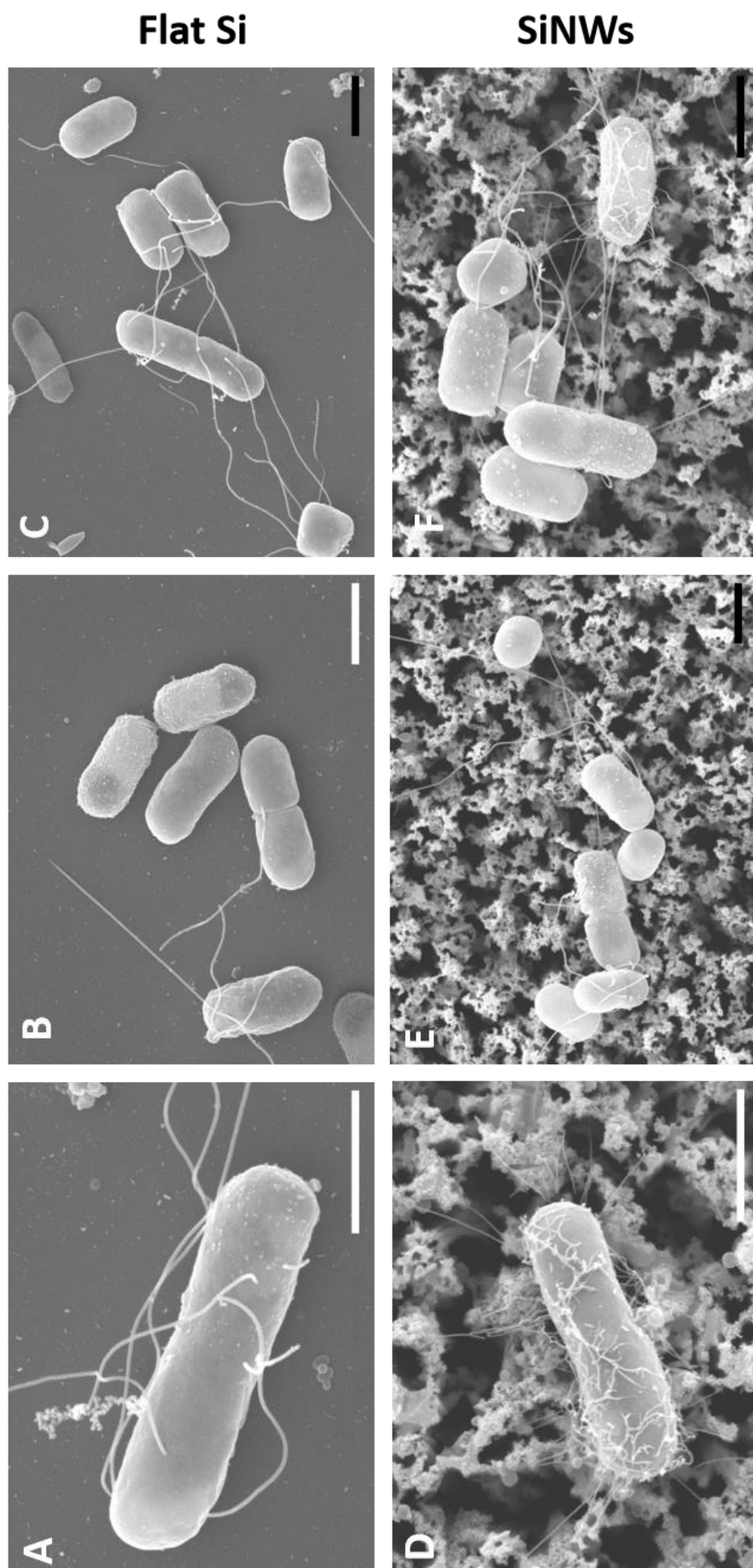


Fig. 5.3.5 Representative SEM images, taken in upright configuration, of *E. coli* cells adhering to flat Si (A, B, C) and SiNWs (D, E, F). Scale bars are 1 μm .

5.3.3 Attachment and division of *Acinetobacter baumannii* cells on flat Si and SiNWs

During the last 15 years, *A. baumannii* has globally emerged as one of the most dangerous pathogens: the World Health Organisation recently published a report that lists this bacterium amongst those for which the need of new antibiotics is most critical [81]. Its remarkable capacity to acquire and up-regulate resistance-related genes makes it one of the microorganisms threatening the current antibiotic era, as reports of *A. baumannii* strains resistant to all known antibiotics have recently been filed, raising awareness on the danger related to this pathogen [82]. This bacterium has been shown to infect human respiratory epithelial cells [83], a characteristic that combined with its ability to survive for prolonged periods in hospital environments makes hospital-acquired pneumonia the most common pathology it's associated with [84]. These findings highlight the necessity of engineering surfaces capable of preventing the attachment and growth of *A. baumannii*, and this paragraph will describe the effect of nanostructured topography on the attachment and division of the prototype strain ATCC 19606, which has shown a tendency to attach to and forms biofilms on glass surfaces and is particularly tolerant to changes in pH, osmotic pressure and antimicrobial agents [85, 86].

The SEM images in **Fig. 5.3.6** show the flat Si (**A, B, C**) and SiNWs surfaces (**D, E, F**) colonised by a monolayer of *A. baumannii* cells. Direct interaction of cells with the substrate appears to be favoured, in contrast with the *E. coli* images in the previous section, in which the cells occasionally tended to aggregate in clusters; this could be due a difference in growth rate between *A. baumannii* and *E. coli*, which would reduce the presence of aggregates generated by multiple cell divisions, or to the higher affinity of *A. baumannii* for the Si substrates, which would lead to the cells choosing to adhere to the substrate rather than to other cells.

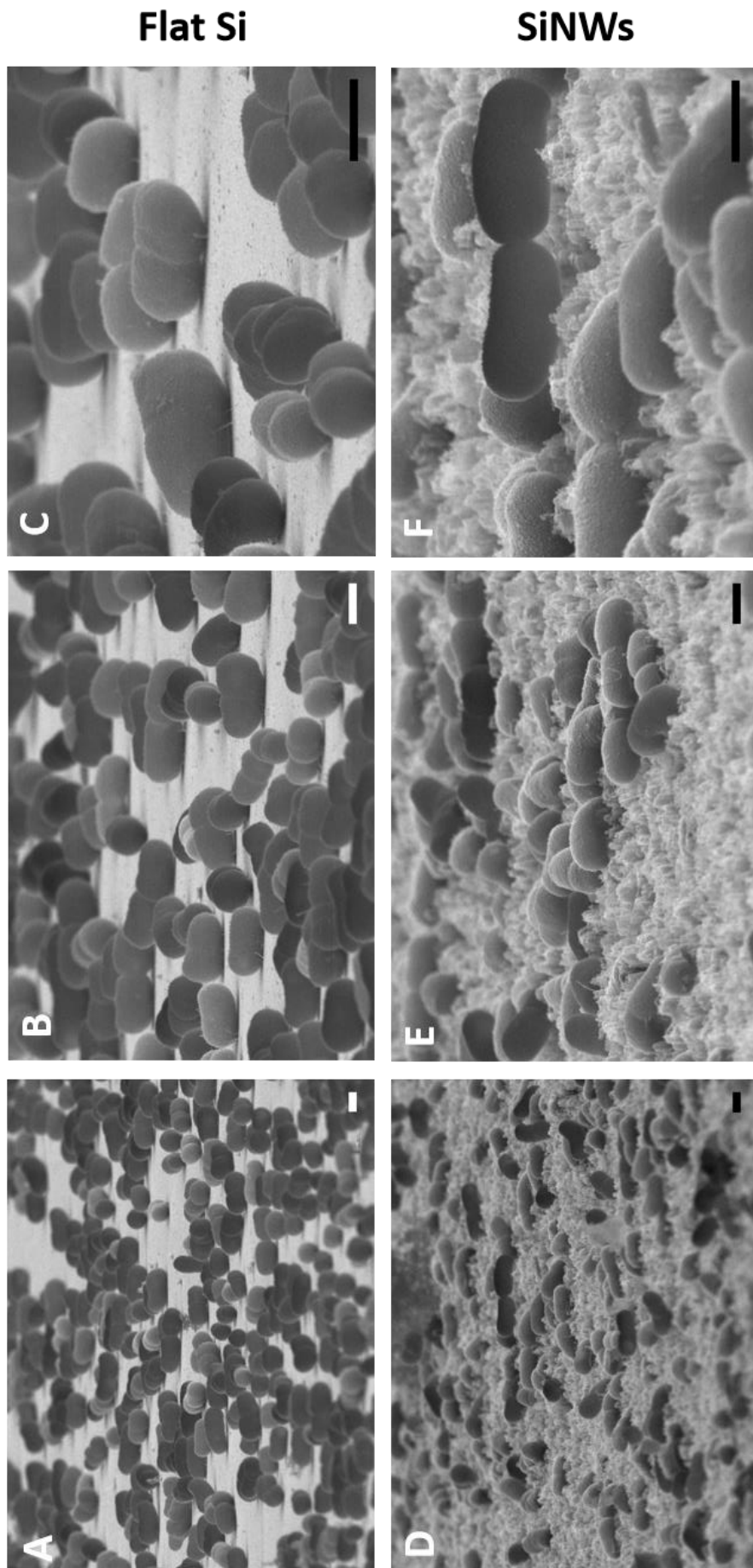


Fig. 5.3.6 Representative SEM images of colonies of *A. baumannii* cells adhering to flat Si (A, B, C) and SiNWs (D, E, F). Scale bars are 1 μm .

As for *E. coli*, the rods preferentially align along the surface plane, although comparing **Fig. 5.3.6 A** and **D** we can observe some cells adapting to the inhomogeneous SiNWs arrays, attempting to increase the number of contact points with the surface. As for *E. coli*, we did not observe significant disruption of the cell morphology caused by the nanotopography, in agreement with the Live/Dead data previously discussed.

Several cells can be observed at different stages of their division process, suggesting that *A. baumannii* is still in the exponential growth phase after 8 h incubation. On both substrates the dividing cells are oriented parallel to the surface, as the symmetric rod-shaped bacteria undergo division via polar growth [36], their original horizontal orientation directly leads to '2D structures'.

Higher magnification SEM images (**Fig. 5.3.7** and **Fig. 5.3.8**) allow closer investigation into the division process and the attachment of *A. baumannii* to flat Si (**A, B, C**) and SiNWs (**D, E, F**). **Fig. 5.3.7 A** and **D** display bacteria dividing on the tested substrates, "frozen" in the moment of the splitting, with the two daughter cells still connected by a thin portion of the septum, something we did not observe while investigating the division of the other bacterial species in this work. **Fig. 5.3.7 B** and **E** show a rare example of *A. baumannii* cells dividing in an upright position, displaying the strength of the bacterial adhesion that allows a small portion of one cell to hold the weight of two.

The extracellular protrusions on the membrane of *A. baumannii* cells are visible in **Fig. 5.3.7 B** and **E**, in accordance to the studies that show that pili and exopolysaccharides are essential for this specie in the early stages of biofilm formation on abiotic surfaces [86], in particular on the non-growing pole of the left cell in **Fig. 5.3.7 A** we can observe a bundle of long extracellular appendages, while hair-like short protrusions are visible on the membrane of all cells attached to both flat Si and SiNWs.

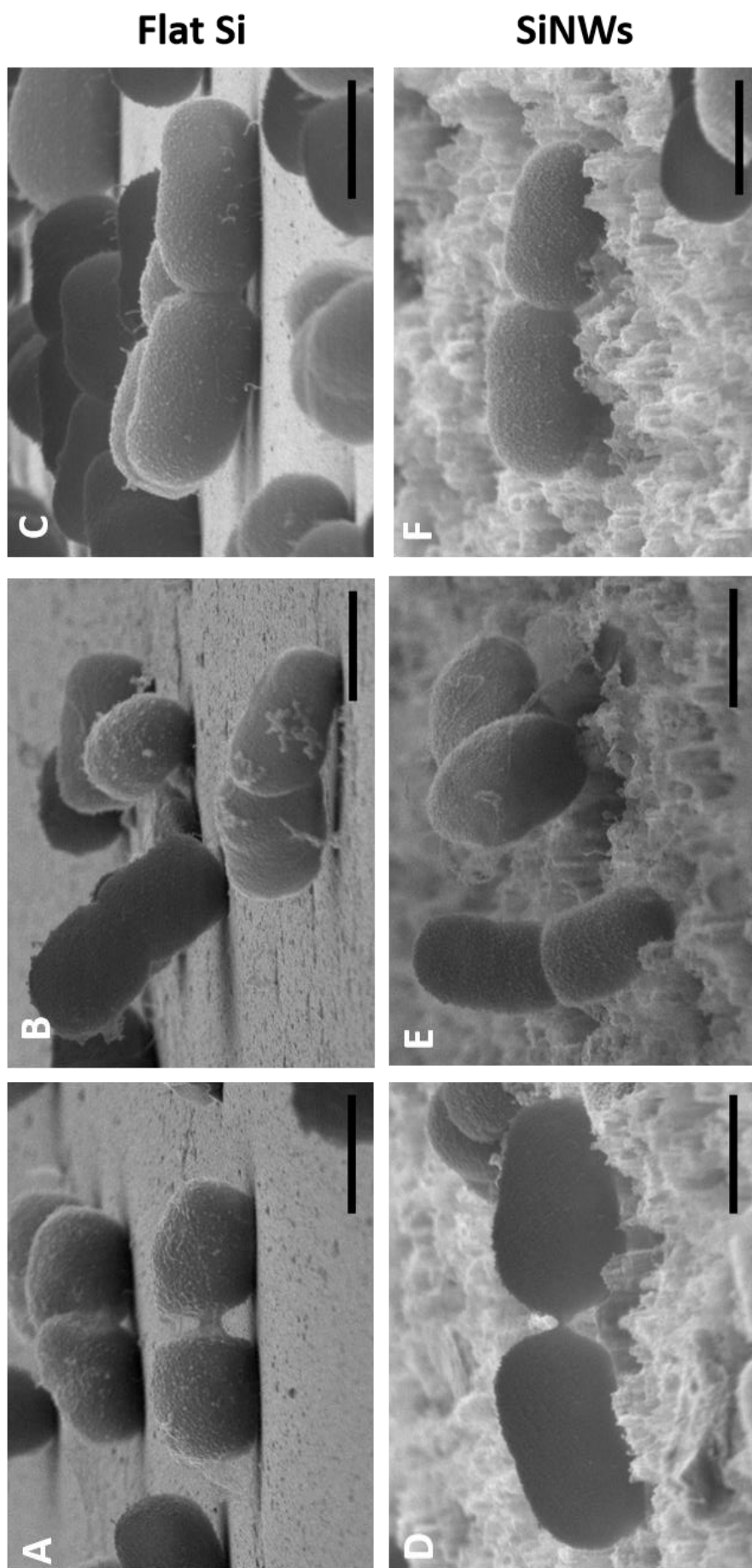


Fig. 5.3.7 Representative SEM images of *A. baumannii* cells adhering to flat Si (A, B, C) and SiNWs (D, E, F). Scale bars are 1 μm.

Bacterial extracellular protrusions are particularly visible on the membrane of cells in **Fig. 5.3.8**, attached to flat Si (**A, B, C**) and SiNWs (**D, E, F**). The two pairs of dividing cells in **Fig. 5.3.8 A** are connected at their poles by a long filament. Long protrusions seem to have a structural role in sustaining the small cell cluster in **Fig. 5.3.8 B**, appearing to provide anchoring points for the attachment to the Si surface while at the same time connecting the cells together, providing resistance to shear forces and possibly exchanging genetic material. The structural role of these protrusions is particularly evident in **Fig. 5.3.8 C**, in which the cell on the left appears to be held in an upright position by a “web” of extracellular protrusions. The images of *A. baumannii* adhering to SiNWs show filamentous protrusions connecting the cells to the nanostructured topography (**Fig. 5.3.8 D**), strengthening the attachment by providing additional anchoring points with the surface.

The bacteria in **Fig. 5.3.8** appear to be at different stages of their division process: cells at an early stage (**E**) display a light horizontal “scar” in the mid-cell, where the septum is forming. Bacteria at the final stage of division (**C, D**) display a more pronounced septum, with the two daughter cells acquiring the characteristic rod shape, appearing to be moments away from splitting.

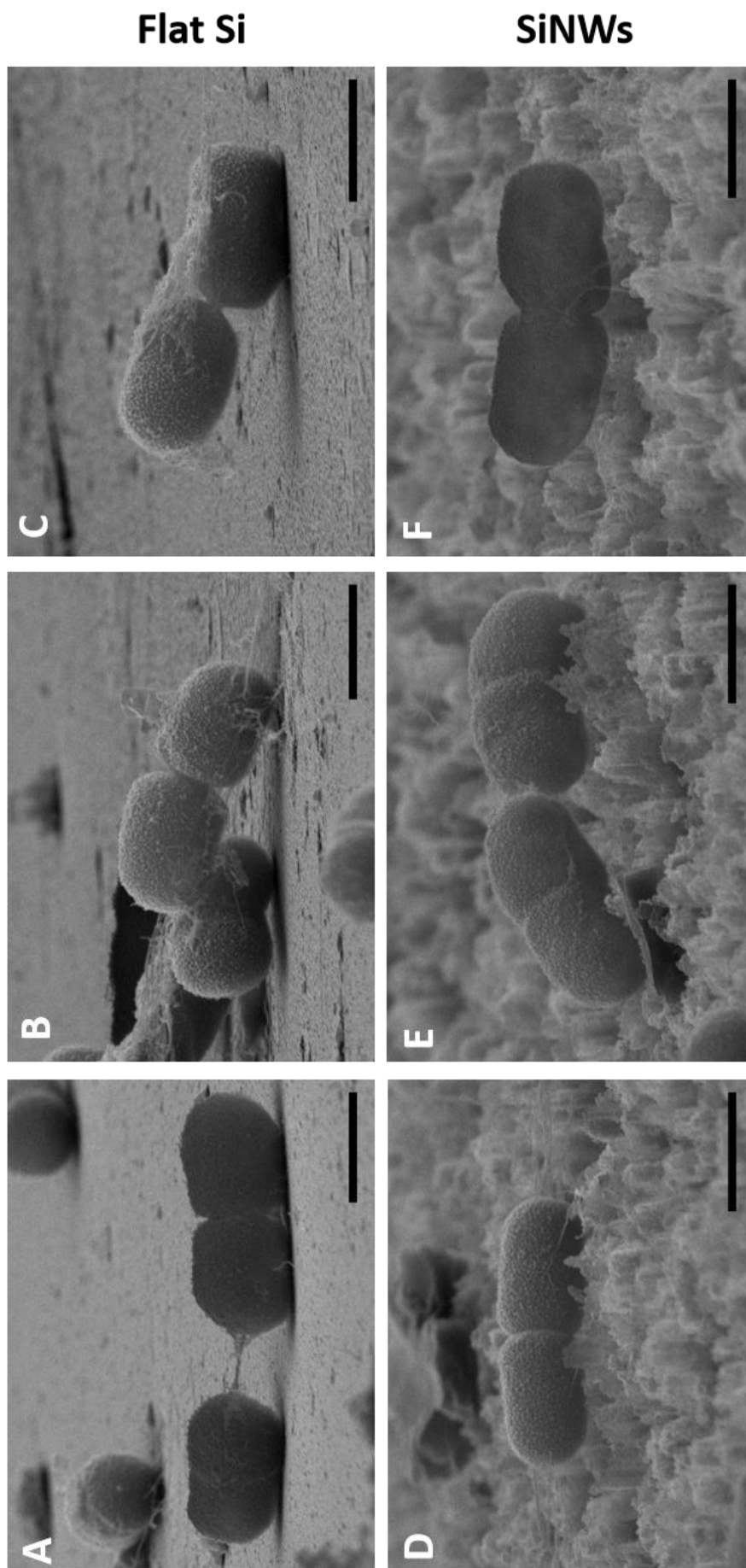


Fig. 5.3.8 Representative SEM images of *A. baumannii* cells adhering to flat Si (A, B, C) and SiNWs (D, E, F). Scale bars are 1 μm.

5.3.4 Attachment and division of *Bacillus subtilis* cells on flat Si and SiNWs

B. subtilis is a Gram-positive, non-pathogenic, spore-forming bacterium that is often utilised as a model for the study of biofilm formation [87]. Like most microorganisms it tends to attach to and form biofilms on surfaces due to the abundance of nutrients, but it can secrete proteins called hydrophobins to form highly hydrophobic biofilms capable of floating at the air–liquid interface [88]. When *B. subtilis* cells grow on a surface, they proliferate as long sessile chains, which is the predominant phenotype observed during the exponential growth phase [76].

The most common *B. subtilis* laboratory strain, 168, showed to differ excessively from a wild type, as it was created through random mutagenesis with X-rays and selected as an easy transformable organism which forms thin and relatively undifferentiated biofilms [89]. In this study, we utilised the undomesticated strain ATCC 6051, which has exhibited favourable attachment and growth properties on abiotic surfaces, compared to strain 168 [90].

Fig. 5.3.9 shows representative SEM images of *B. subtilis* cells adhering to flat Si (**A**, **B**, **C**) and SiNWs arrays (**D**, **E**, **F**). Their morphology appears elongated compared to the other rod-shaped bacteria analysed in this chapter; as observed in previous works [73, 76, 87], rather than organising in clusters like *E. coli*, *B. subtilis* forms long chains of cells attached by their poles, parallel to the surface plane. In contrast with the study of Ivanova *et al.* [66], in which *B. subtilis* cells appeared deformed and engulfed on nanopillared Si surfaces, the bacteria adhering to SiNWs appear intact and morphologically unchanged, consolidating the no-killing effect we assessed via fluorescence microscopy. **Fig. 5.3.9 A** gives us interesting insights on the role of the extracellular protrusions in the attachment of *B. subtilis* to abiotic surfaces: these filaments appear to anchor the cells to the substrate, increasing the number of contact points with the surface.

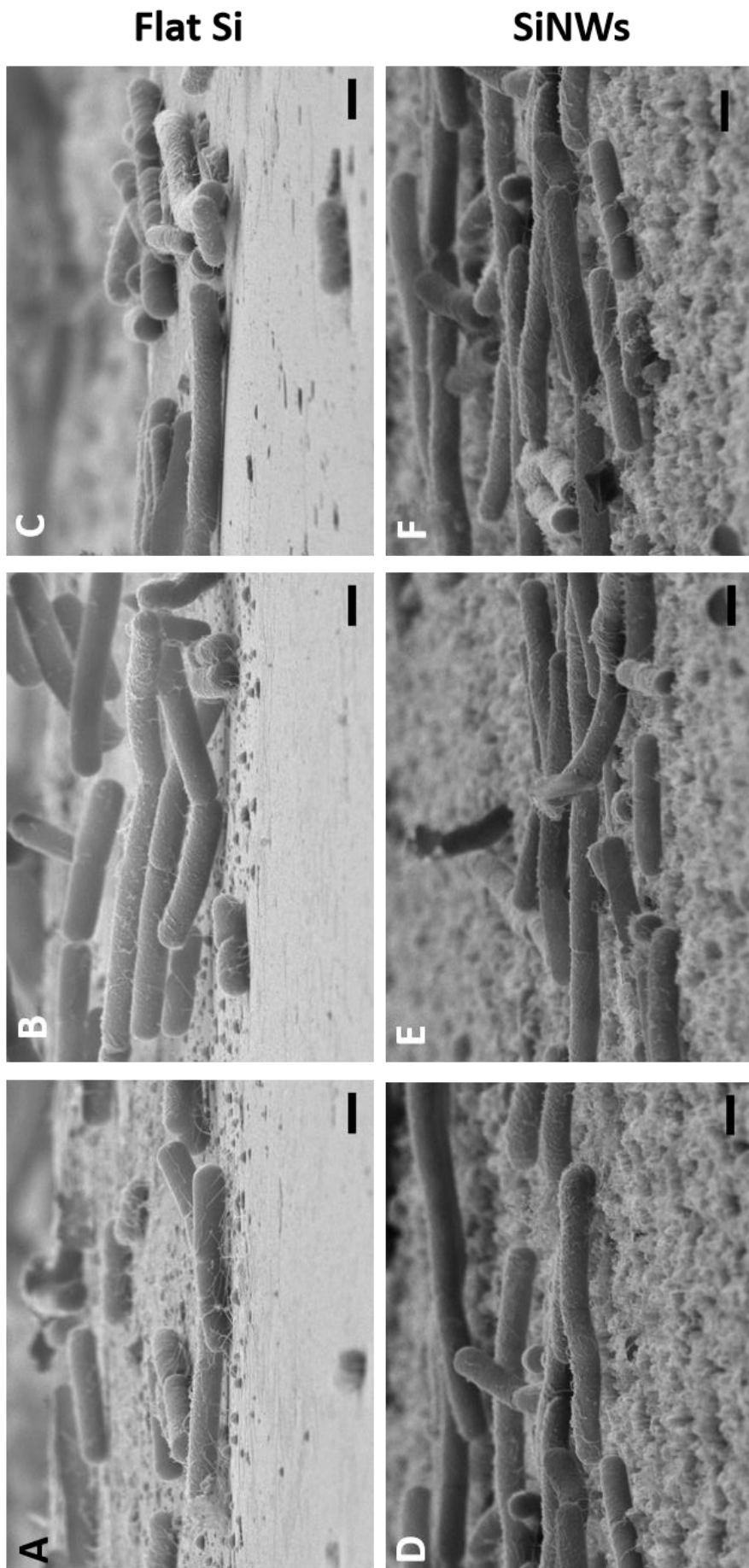


Fig. 5.3.9 Representative SEM images of colonies of *B. subtilis* adhering to flat Si (A, B, C) and SiNWs (D, E, F). Scale bars are 1 μm .

Fig. 5.3.10 provides insights on the different configurations and the division modes that *B. subtilis* can adopt on flat Si (**A, B, C**) and SiNWs arrays (**D, E, F**). A close up of bacteria dividing on flat Si (**A**) reveals the ingrowth of the septa in the late stage of division, with a chain of cells parallel to the substrate and a few extracellular protrusions anchoring them to the surface. Interestingly, a few bacteria in the chain seem to have minimum interaction with the flat Si, relying on the structural integrity of the cluster to maintain their sessile status. A similar configuration is adopted by the cells at the centre of **Fig. 5.3.9 D**, where their adhesion appears to be minimised to a few peaks of the nanostructured substrate but their sessile status is maintained due to the cohesive structure they form by connecting at their poles. **Fig. 5.3.10 C** and **E** provide examples of cells dividing in upright position and further clues on the adhesion strength of this specie, capable of sustaining the weight of multiple cells adhering only by the extremity of one.

Similar to *E. coli* (**Fig. 5.3.4 D**), the shortest filaments on the surface of *B. subtilis* seem to be secreted in higher concentration from bacteria adhering to SiNWs (**Fig. 5.3.10 D, E**) as if the nanoroughness requires the cells to spend additional energy to increase the number of attachment points to the substrate and strengthen the adhesion. **Fig. 5.3.10 A** and **B** give another example of the longer filaments we observed in **Fig. 5.3.9 A**, in this case almost forming a network to anchor the cells to the substrate.

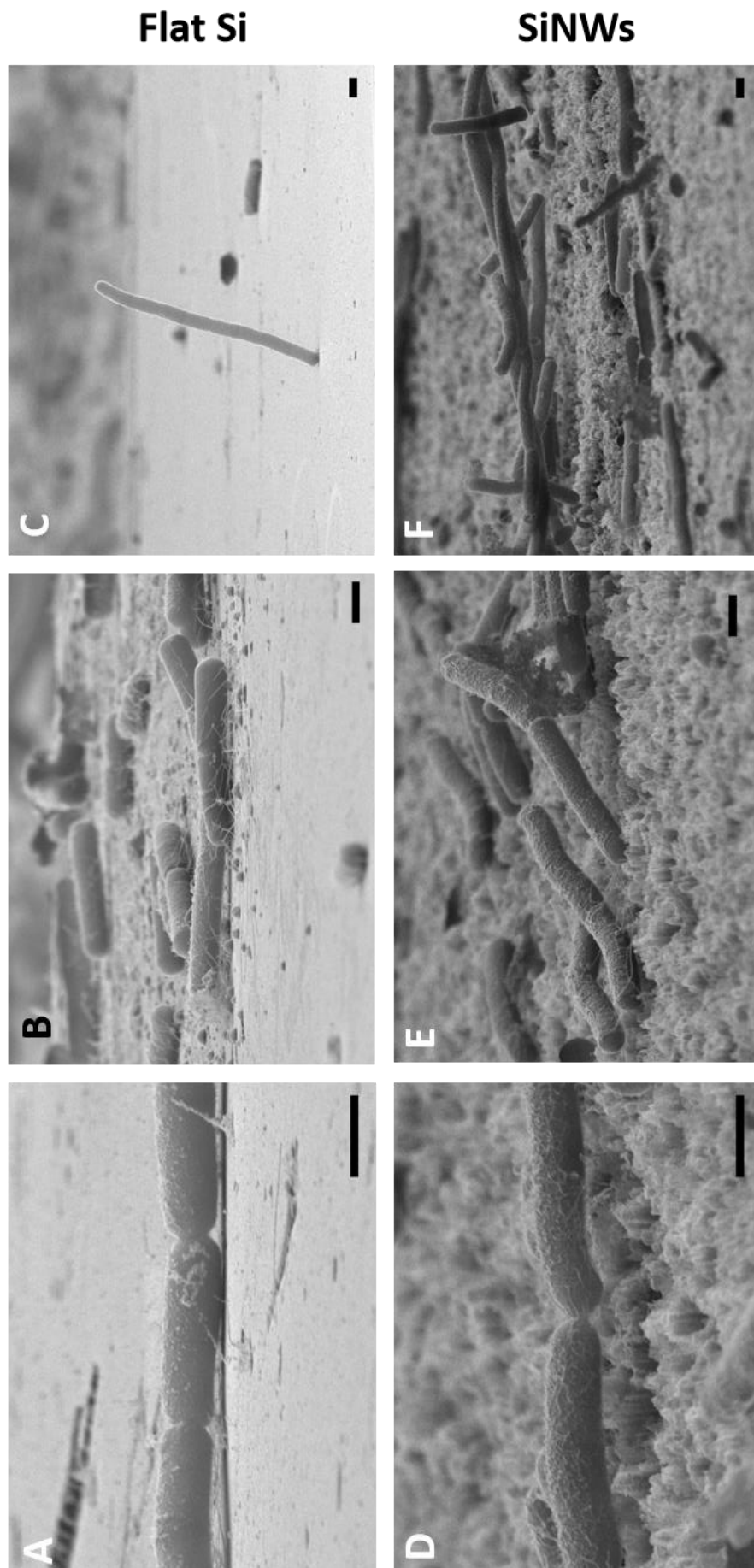


Fig. 5.3.10 Representative SEM images of *B. subtilis* cells adhering to flat Si (A, B, C) and SiNWs (D, E, F). Scale bars are 1 μm .

5.3.5 Attachment and division of *Caulobacter crescentus* on flat Si and SiNWs

C. crescentus is a non-pathogenic, Gram-negative, stalk-forming bacterium found typically in aquatic settings attached to substrates via an adhesive holdfast organelle located at the distal tip of the stalk [91]. The strain studied in this work, ATCC BAA2331, is a spontaneous S-layer negative variant of the strain CB2 (ATCC 15252) [92] and has previously been subject of studies on membrane lipid composition [93] and stalk development [94].

Fig. 5.3.11 shows representative SEM images of *C. crescentus* cells adhering to flat Si (**A, B, C**) and SiNWs arrays (**D, E, F**). The slower growth rate of this species compared to *E. coli* and *A. baumannii* [72] explains the less populated Si surfaces in this paragraph. Most cells are preserved in their upright position by the sample preparation process, **Fig. 5.3.11 A** clearly shows *C. crescentus* in S phase adhering to the flat Si by their stalk, while on SiNWs (**Fig. 5.3.11 D**) these protrusions seem to anchor to the cavities and the lateral walls of the peaks of the topographic surface, a conformation that in some cases (**Fig. 5.3.11 E**) causes *C. crescentus* cells to lay on parallel to the surface, with the stalk sank deeply in the cavities and the attached bacteria adapting to the uneven substrate. **Fig. 5.3.11 C**, taken with the microscope in upright configuration, shows a bacterium in G2 phase, with the stalked cell anchored to the surface while the swarmer cell, with the flagellum visible at its pole, is about to be separated by the ingrowing septum. Two dividing cells are visible in **Fig. 5.3.11 F**, adhering to SiNWs; in this case the stalked bacterium is in upright position and the flagellum of the swarmer cell freely moves in the surrounding environment. The following section of this chapter will furtherly investigate if the nanostructured surface affects the *C. crescentus* cell cycle.

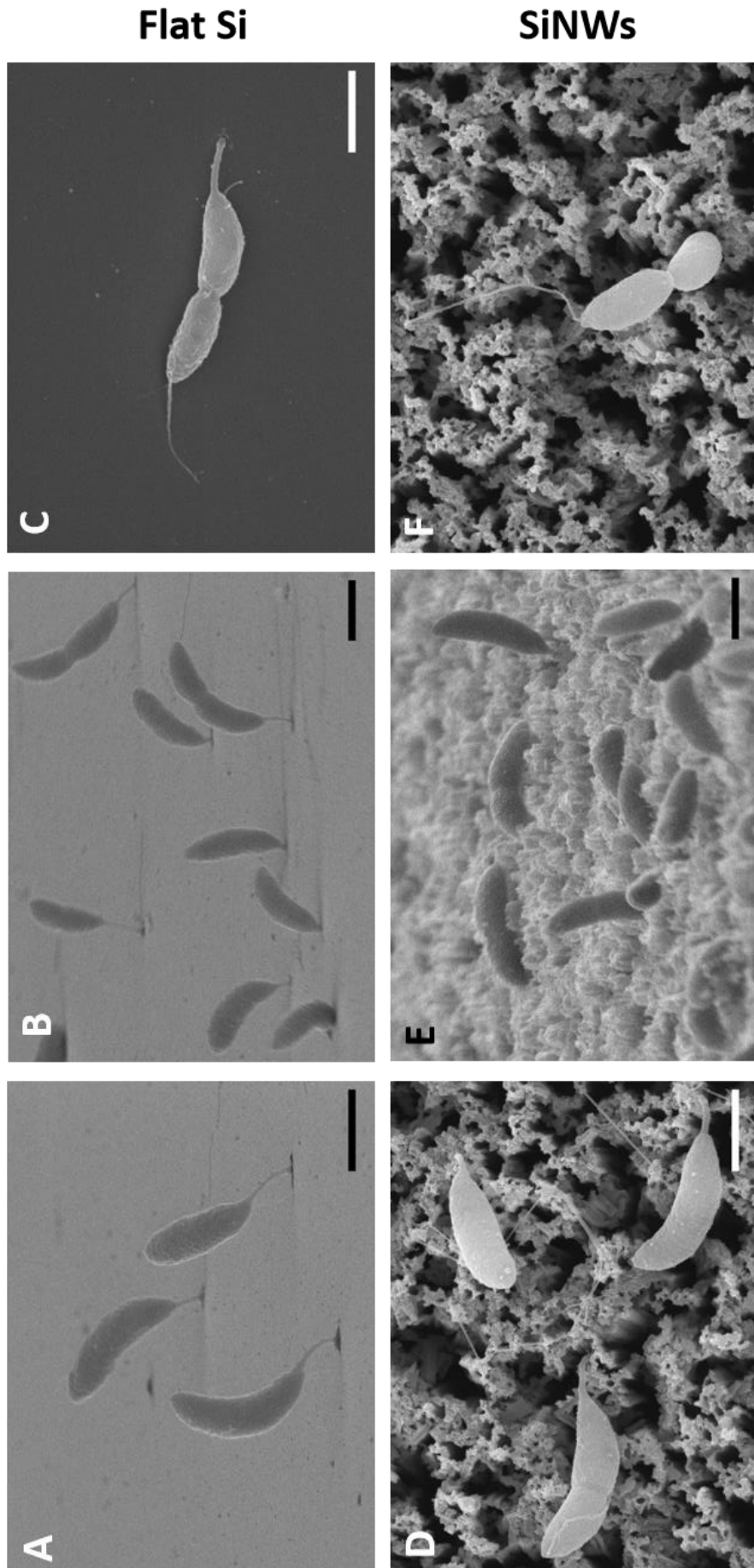


Fig. 5.3.11 Representative SEM images of *C. crescentus* cells attaching to flat Si (A, B, C) and SiNWs (D, E, F). Scale bars are 1 μm .

5.4 Division modes of rod-shaped bacteria at the surface

5.4.1 Effect of nanostructured Si on the division modes of *E. coli*, *A. baumannii* and *B. subtilis*.

The data discussed in the previous sections highlight similarities between the adhesion and growth of *E. coli*, *B. subtilis* and *A. baumannii* on flat Si and SiNWs. We hypothesised that after initial attachment mediated by pili and flagella, the majority of cells align parallel to the surface of both flat Si and SiNWs arrays in order to maximise the number of contact points and increase their detachment energy (**Fig. 5.4.2** above, **Fig 5.3.4 A and D**, **Fig 5.3.8 A and D**, **Fig 5.3.10 A and D**).

Interestingly, *E. coli*, *B. subtilis* and *A. baumannii* seem to display a wider range of attachment conformations on flat Si surfaces in comparison to the ones they assume on SiNWs arrays. We observed few cells capable of generating enough anchoring points to the substrate by adhering only via one of their poles (**Fig. 5.4.2** below, **Fig 5.3.3 B**, **Fig 5.3.4 B**, **Fig 5.3.7 C**, **Fig 5.3.8 C** and **Fig 5.3.10 B**). This conformation appeared to be less favoured on SiNWs arrays, as the lower number of available attachment points and the uneven topography lead to a relative lower number of cells adhering via one of their poles (**Fig 5.3.3 E**, **Fig 5.3.7 E** and **Fig 5.3.10 E**).

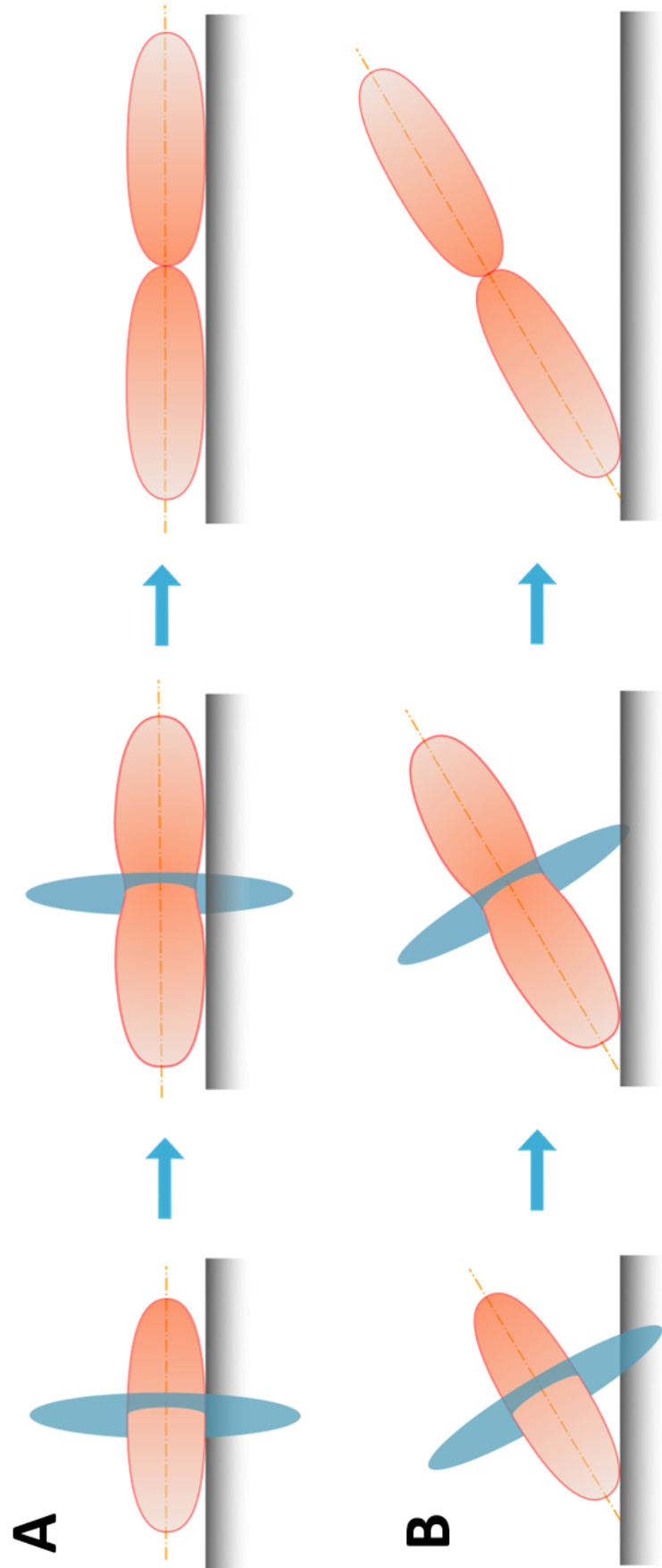


Fig. 5.4.1 Schematic representation of rod-shaped bacteria dividing on flat Si parallel to the surface **(A)** and tilted **(B)**.

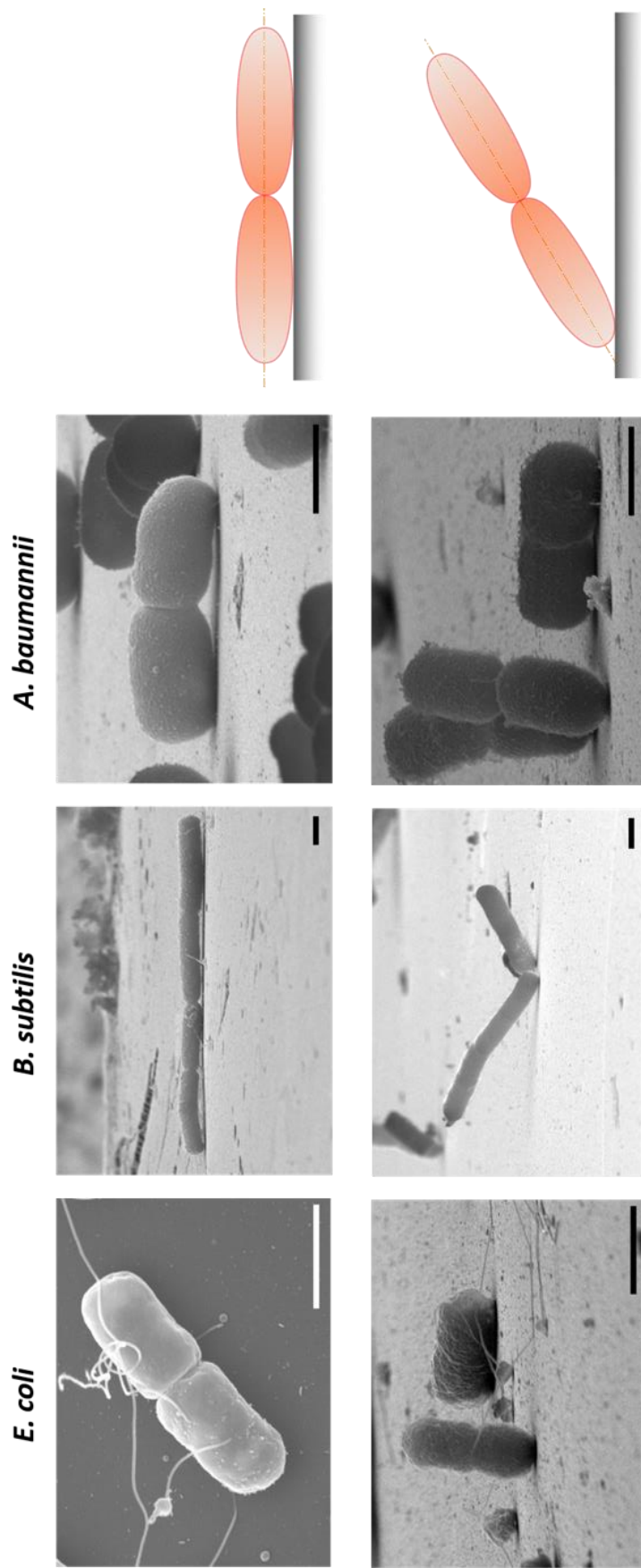
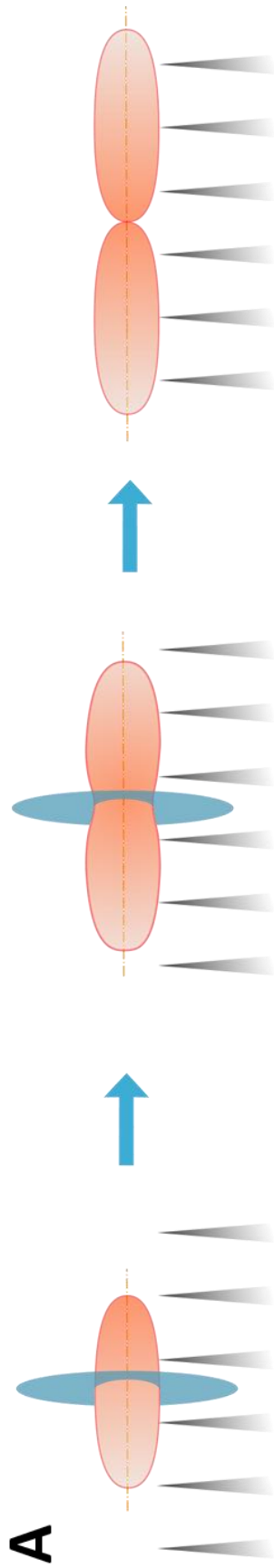
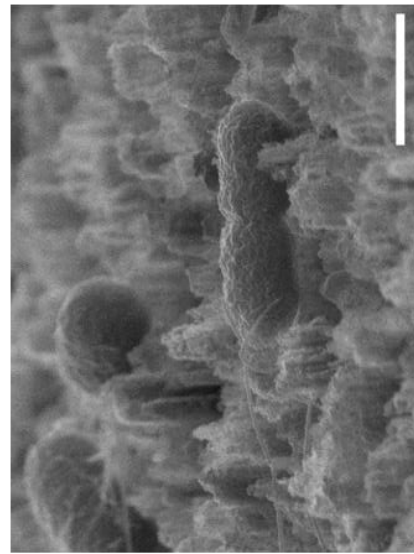


Fig. 5.4.2 SEM images and relative schematic representation of rod-shaped bacteria attached to flat Si dividing parallel to the surface (above) and out of plane (below). Scale bars are 1 μm .

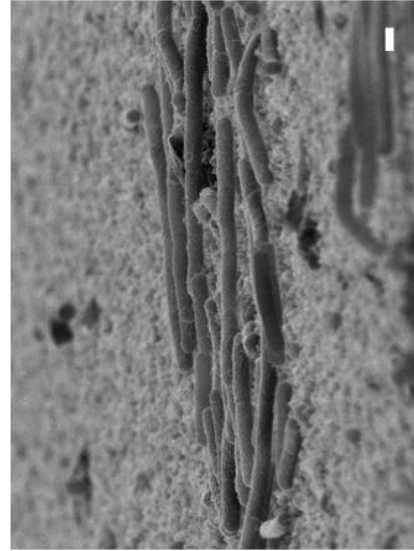
High magnification SEM images of *E. coli*, *B. subtilis* and *A. baumannii* cultured for 8 h on SiNWs show that only occasionally their division and growth are affected by the uneven topography of the nanostructured substrate. These findings are in contrast with the recent work of Jenkins *et al.* [60], in which the nanostructured surface induced cell impedance, which is suspected to reduce the capacity of bacteria to replicate, thus enhancing the antibiofilm properties of their nanopillar Ti surfaces. We observed in the previous chapter that the characteristic size of the *Staphylococci* (0.5 - 1 μm) often matches the one of the cavities of SiNWs arrays, allowing some cells to accommodate within the nanostructured features and restricting the available range of orientations of the division plane. In the case of *E. coli*, *B. subtilis* and *A. baumannii*, the cell length of 1-2 μm [50] prevents them from reaching the cavities of the SiNWs arrays, leading most bacteria to lie horizontally on the peaks of the nanostructured surface. This tendency was also observed by Serrano *et al.* in their 2015 work [59]. The orientation parallel to the substrate allows the cells to increase the number of contact points with the uneven surface, also due to a tendency of the bacteria to secrete a higher amount of short extracellular appendages when adhering to SiNWs arrays (**Fig 5.3.4 D**, **Fig 5.3.5 D** and **Fig 5.3.10 D**) in respect to flat Si (**Fig 5.3.4 A**, **Fig 5.3.5 A** and **Fig 5.3.10 A**). The orientation parallel to the surface plane, combined with the division in the direction of the polar axis (**Fig 5.4.3 A**), characteristic of rod-shaped bacteria, leads to the 2D structures we can observe in **Fig 5.4.3 B**, which display examples on how rod-shaped bacteria attachment adapt to the uneven topography of the nanostructured substrate, not allowing it to affect their characteristic polar growth and division process.



B *E. coli*



B. subtilis



A. baumannii

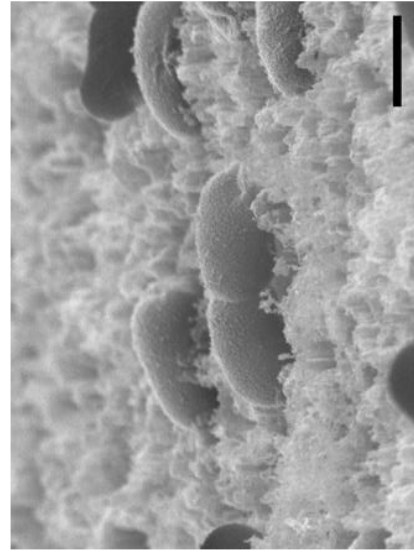


Fig. 5.4.3 Schematic representation of rod-shaped bacteria attached to SiNWs surfaces and their division effected by the uneven topography (A) SEM images of *E. coli*, *B. subtilis* and *A. baumannii* dividing on SiNWs (B). Scale bars are 1 μm .

5.4.2 Cell cycle of *Caulobacter crescentus* on nanostructured Silicon

C. crescentus possesses a unique growth cycle [48] and is often used as a model system for the study of bacterial differentiation [96, 97]. Unlike other species, *C. crescentus* differentiates during its cell cycle, prior to cell splitting with the synthesis of the flagellum, as a result of its asymmetric division which leads to the formation of a stalked and a swarmer cell (**Fig. 5.4.4 A**). The stalked sessile cell immediately initiates a second cell cycle, while the swarmer cell must initiate a new differentiation before attaching to a substrate and become a stalked cell [97].

Fig. 5.4.5 provides a detailed visualisation of the division process of *C. crescentus* on flat Si (**A, B, C**) and SiNWs arrays (**D, E, F**). **Fig. 5.4.5 A** and **D** display pre-divisional cells adhering to the surface via their stalk, which is a narrow elongation of the cell wall, constructed at the same location as the discarded flagellum [48]; **Fig. 5.4.5 A**, in particular, appears to show what may be the discarded flagellum laying on the surface next to the stalk. The attached cell displays a very light scar at the mid-cell, localising the septum in formation, and is going through the S phase that leads to the formation of two daughter chromosomes [48]. We can hypothesise that the cell in **Fig. 5.4.5 D** is in an earlier stage of this phase, due to the lack of a visible septum, the bacterium adheres to the nanostructured topography via its stalk, which anchors the cell to a cavity of the SiNW arrays, as schematised in **Fig. 5.4.4 B**. The septa in **Fig. 5.4.5 B** and **E** appear more pronounced, indicating that the bacteria are at a later stage of their division process, the swarmer cells although are yet to build their flagellum, suggesting that they are still in the DNA replication phase [48]. We hypothesise that the cells in **Fig. 5.4.5 C** and **F** have reached the G2 phase of the division process, which involves chromosome segregation and the formation of pili [48], the septa that divide the daughter cells in fact appear to have almost completed their ingrowth and the swarmer bacteria display a fully formed flagellum at the pole opposite the stalk. In the following stage, in which the daughter cells will be fully divided, the stalked one will immediately start a new reiteration of the S phase while the swarmer cell will find an anchoring point to the surface and form its stalk to initiate DNA replication and division [48].

Comparing the SEM images of the bacteria on flat Si and SiNWs, it appears evident that the unique cell cycle of *C. crescentus*, along with its attachment mechanism, are not affected by the local topography of the SiNWs. The cells show comparable morphology on both surfaces at different stages of their division process, indicating that their capability to differentiate is retained on the topographic SiNW surface.

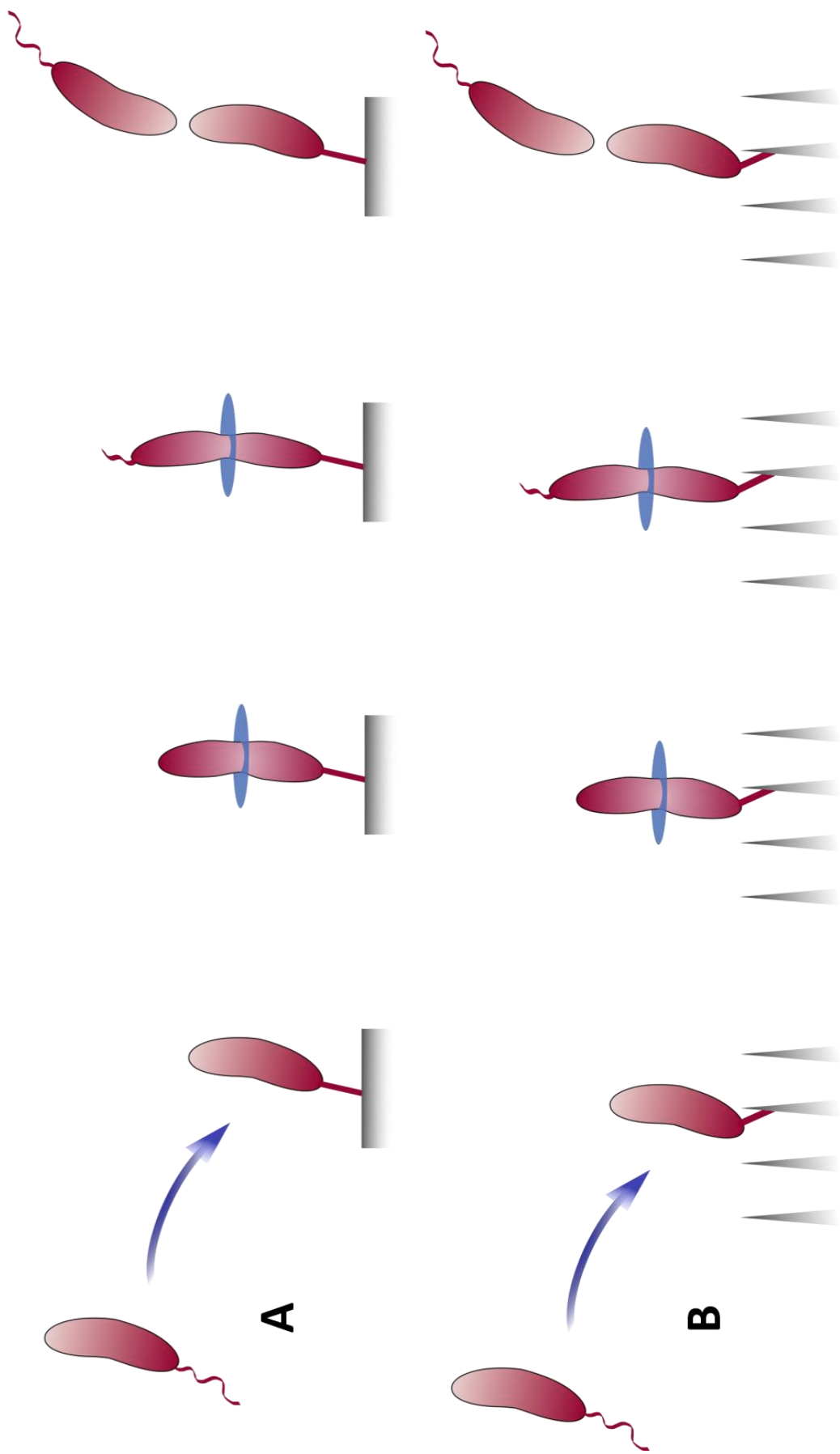


Fig. 5.4.4 Schematic representation of *C. crescentus* attaching and dividing on flat Si (A) and SiNWs (B).

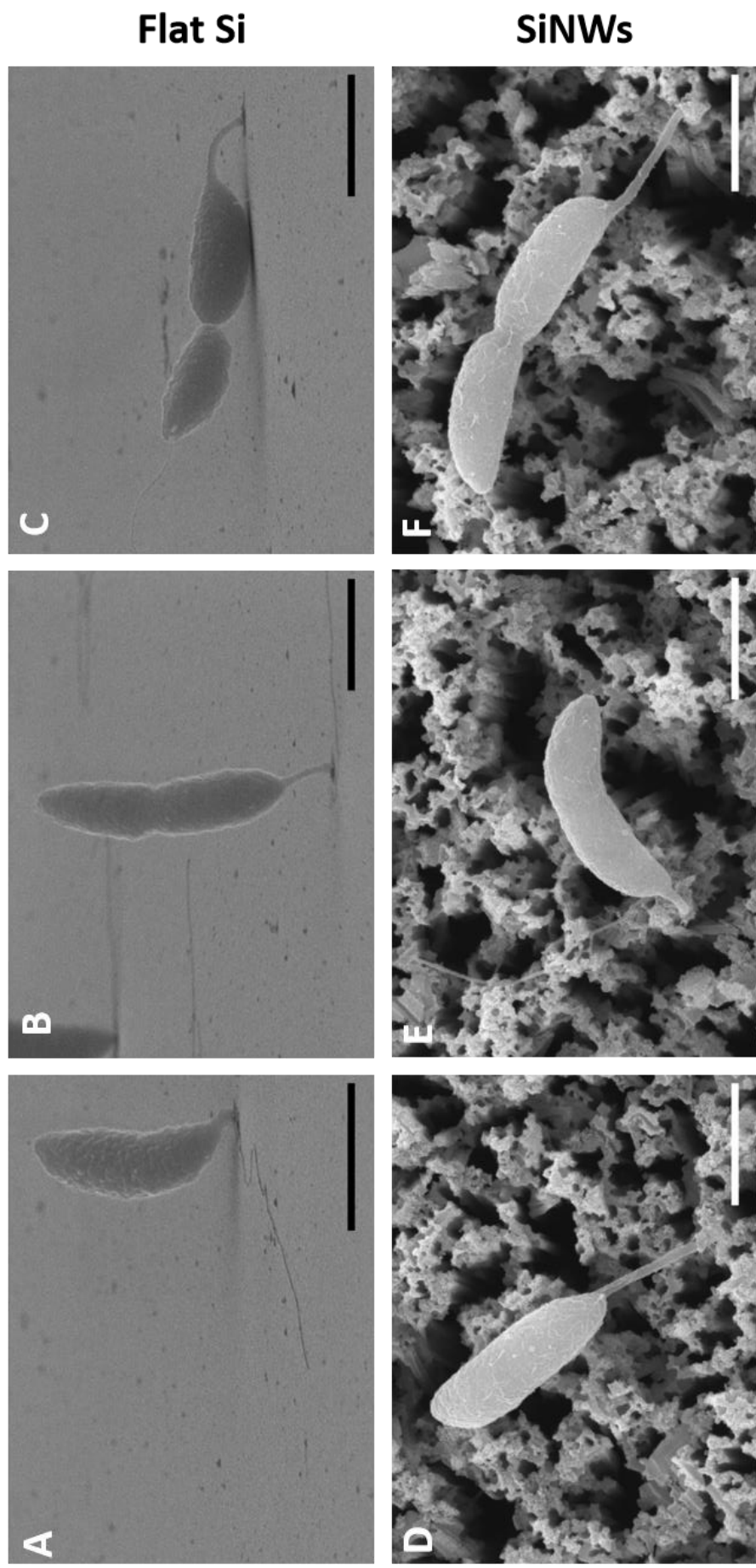


Fig. 5.4.5 Representative SEM images of *C. crescentus* cells dividing on flat Si (A, B, C) and SiNWs (D, E, F). Scale bars are 1 μm .

5.5 Conclusion

This chapter focused on the effect of nanostructured Si on the attachment and division of the rod-shaped bacteria *E. coli*, *B. subtilis*, *A. baumannii* and dedicated a section to the special case of *C. crescentus*. The morphology and division modes of the bacteria were analysed on SiNWs, which are Si surfaces functionalised with highly oriented filamentary Si crystals with ~100 nm diameter or less [98], shown to be biocompatible [99, 100]; flat Si wafers were used as control.

The analysis was based on high resolution SEM images acquired in tilted configuration, which allowed to investigate at the nanometer scale the cell morphology, the extracellular filaments protruding from the membranes and the attachment points of the bacteria to the substrates. We observed the cells making use of their short and long extracellular appendages to generate multiple contact points with the irregular topography of the SiNWs, often penetrating the cavities of the uneven substrate to strengthen the attachment.

Live/Dead assay and low-magnification SEM images showed that all bacterial species were able to adhere and proliferate on flat and nanostructured Si, which displayed no killing effect on the tested strains. High-magnification SEM images revealed a tendency of the cells to lay horizontally on SiNWs arrays, probably in order to maximise the number of attachment points with the surface. On flat Si, in a few cases, bacteria were able to anchor to the surface by only one of their poles, leading a division event with an upright orientation which caused the cells to organise in clusters, rather than to distribute evenly on the surface.

E. coli, *B. subtilis* and *A. baumannii* share similar division mode, which consists in elongation along the polar axis caused by peptidoglycan insertion, followed by formation of the FtsZ ring at the mid-cell, which leads to the separation of the two daughter cells at the septum. The cells were able to retain their classical growing mode on SiNWs, dividing via polar growth parallel to the surface as the majority of

the ones on flat Si, showing to be able to adapt to a nanostructured Si substrate offering fewer attachment points than a flat one.

A section of this chapter was dedicated to *C. crescentus*, a microorganism which possesses a unique growth cycle, differentiating prior to cell splitting with the synthesis of the flagellum. High-magnification SEM images showed the stalked cells adhering to the cavities of the uneven topography of the SiNWs, maintaining their characteristic morphology throughout the cell cycle and allowing this species to differentiate and proliferate on the nanostructured surface, unaffected by the local topography.

Our investigation on the division modes and attachment mechanisms of rod-shaped bacteria on SiNWs highlighted several key findings that could lead to a better understanding of the surface characteristics and topography that affect bacterial adhesion and proliferation. The ultimate goal of this study is to enable the engineering of advanced materials with controlled nanostructures, whose antimicrobial properties do not rely on antibiotics and with considerable potential biomedical applications.

5.6 Future Work

The SEM images in this chapter and the previous one display a qualitative assessment of the local surface topography effect on bacterial attachment. Based on the morphology and orientation of the cells, as well as their division modes, we hypothesised that *Staphylococci* adapt to the fewer attachment points available on the SiNWs by dividing in a wider range of orientations, which leads to a tendency of the colonies to develop perpendicular to the surface. In the case of rod-shaped bacteria, the cells adapt to the nanostructured Si substrates by lying and dividing horizontally, increasing the number of attachment points with the surface. *C. crescentus*, with its unique cell cycle, appears to be the species the most easily adapts to the local topography, with its flagella visibly adhering to the surface cavities.

In order to verify these assumptions, future studies on bacteria adhering to SiNWs would have to involve a microfluidic system with controllable flow conditions, often used in microbiology to culture eukaryotic cells for tissue engineering studies [101]. Grown in the same conditions as in chapters 4 and 5, the strains presented in this work would lead to comparable bacterial colonisation on both flat Si and SiNWs; the subsequent introduction of a laminar flow would allow to quantify the difference in shear stress (and therefore, energy) necessary for detachment. If the assumptions here proposed are correct, we would see a lower detachment energy on SiNWs for *S. aureus* than on flat Si, due to the tendency of cells to adhere to each other more than to the nanostructured topography, leading to upright colonies. An interesting aspect of the experiment would be to evaluate if the orientation parallel to the surface of the rod-shaped bacteria on SiNWs and, in some cases, the increase in membrane protrusions, would lead to a higher or lower detachment energy compared to flat Si. In the case of *C. crescentus*, if our assumptions are correct, we would not be expecting a significant difference in detachment energy depending on the tested substrates. A similar approach by Graham *et al.* [102] in 2013 lead to some interesting findings, with linear patterned Silicone surfaces showing great reduction in bacterial attachment in respect to flat substrates.

5.7 References

- [1] **Bacterial cell attachment, the beginning of a biofilm**
Palmer J, Flint S, Brooks J
J. Ind. Microbiol. Biotechnol. 34 (2007) 577–588
- [2] **Sticky Situations: Key Components That Control Bacterial Surface Attachment**
Petrova OE, Sauer K
J. Bacteriol. 194(10) (2012) 2413–2425
- [3] **Complexation, stabilization, and UV photolysis of extracellular and surface-bound glucosidase and alkaline phosphatase: implications for biofilm microbiota.**
Espeland EM, Wetzel RG
Microb. Ecol. 42 (2001) 572–585
- [4] **Evaluation of biohazards in dehydrated biofilms on foodstuff packaging**
Le Magrex-Debar E, Lemoine J, Gell MP, Jacquelin LF, Choisy C
Int. J. Food Microbiol. 55 (2000) 239–234
- [5] **Acid tolerance response of biofilm cells of *Streptococcus mutans***
McNeill K, Hamilton IR
FEMS Microbiol. Lett. 221 (2003) 25–30
- [6] **Human leukocytes adhere, penetrate, and respond to *Staphylococcus aureus* biofilms**
Leid JG, Shirtliff ME, Costerton JW, Stoodley P
Infect. Immun. 70 (2002) 6339–6345
- [7] **Biofilms in vitro and in vivo: do singular mechanisms imply cross-resistance?**
Gilbert P, Allison DG, McBain, AJ
J. Appl. Microbiol. 92 (2002) S98–S110
- [8] **Mechanisms of biofilm resistance to antimicrobial agents**
Mah TF, O'Toole GA
Trends Microbiol. 9 (2001) 34–39
- [9] **Bacterial Biofilms: From the Natural Environment To Infectious Diseases**
Hall-Stoodley L, Costerton JW, Stoodley P
Nat Rev Microbiol. 2(2) (2004) 95–108
- [10] **Microbial biofilms**
Costerton JW, Lewandowski Z, Caldwell DE, Korber DR, LappinScott HM
Annu. Rev. Microbiol. 49 (1995) 711–745
- [11] **Phosphorus limitation enhances biofilm formation of the plant pathogen *Agrobacterium tumefaciens* through the PhoR-PhoB regulatory system**
Danhorn T, Hentzer M, Givskov M, Parsek MR, Fuqua C
J. Bacteriol. 186 (2004) 4492–4501

[12] **Biofilm formation and dispersal under the influence of the global regulator CsrA of *Escherichia coli***

Jackson DW, et al
J. Bacteriol. 184 (2002) 290–301

[13] **Nutritional influences on biofilm development**

Bowden GHW, Li YH
Adv. Dent. Res. 11 (1997) 81–99

[14] **Microbial biofilms**

Costerton JW, Lewandowski Z, Caldwell DE, Korber DR, Lappin- Scott HM.
Annu. Rev. Microbiol. 49 (1995) 711–745

[15] **Adhesion and growth of bacteria at surfaces in oligotrophic habitats**

Marshall JC
Can. J. Microbiol. 34 (1988) 503–506

[16] **Influence of culture conditions on biofilm formation by *Escherichia coli* O157:H7**

Dewanti R, Wong ACL
Int. J. Food Microbiol. 26 (1995) 147– 164

[17] **Phenotypic characterization of *Streptococcus pneumoniae* biofilm development**

Allegrucci M, et al.
J. Bacteriol. 188 (2006) 2325–2335

[18] **Responses of marine bacteria under starvation conditions at a solid-water interface**

Humphrey B, Kjelleberg S, Marshall KC
Appl. Environ. Microbiol. 45 (1983) 43–47

[19] **Initial phases of starvation and activity of bacteria at surfaces**

Kjelleberg S, Humphrey BA, Marshall KC
Appl. Environ. Microbiol. 46 (1983) 978–984

[20] **Periodicity of cell attachment patterns during *Escherichia coli* biofilm development**

Agladze K, Jackson D, Romeo T
J. Bacteriol. 185 (2003) 5632–5638

[21] **SadB is required for the transition from reversible to irreversible attachment during biofilm formation by *Pseudomonas aeruginosa* PA14.**

Caiazza NC, O’Toole GA
J. Bacteriol. 186 (2004) 4476–4485

[22] ***Pseudomonas aeruginosa* displays multiple phenotypes during development as a biofilm.**

Sauer K, Camper AK, Ehrlich GD, Costerton JW, Davies DG
J. Bacteriol. 184 (2002) 1140–1154

[23] **Bacterial adhesion at the single-cell level**

Berne C, Ellison CK, Ducret A, Brun YV
Nat Rev Microbiol. 16(10) (2018) 616–627

- [24] **Bacterial Adhesion**
Geng J, Henry N
Springer, 1st Edition, 2011, 315–331
- [25] **Pathogenic *Escherichia Coli***
Kaper JB, Nataro JP, Mobley HL
Nat Rev Microbiol 2(2) (2004) 123-140
- [26] **Structure and Function of *Escherichia coli* Type 1 Pili: New Insight into the Pathogenesis of Urinary Tract Infections**
Schilling JD, Mulvey MA, Hultgren SJ
The Journal of Infectious Diseases 183(Suppl 1) (2001) 36–40
- [27] **Terminology of Bacterial Fimbriae, or Pili, and their Types**
Duguid JP, Anderson ES
Nature 215 (1967) 89–90
- [28] **Bacterial cell attachment, the beginning of a biofilm**
Palmer J, FlintS, Brooks J
J. Ind. Microbiol. Biotechnol. 34 (2007) 577–588
- [29] **Bacterial flagella explore microscale hummocks and hollows to increase adhesion**
Friedlander RS, et al.
Proc. Natl Acad. Sci. 110(14) (2013) 5624–5629
- [30] **Genetic analysis of *Escherichia coli* biofilm formation: roles of flagella, motility, chemotaxis and type I pili**
Pratt LA, Kolter R
Mol. Microbiol. 30 (1998) 285–293
- [31] **Obstruction of pilus retraction stimulates bacterial surface sensing**
Ellison CK, et al.
Science 358 (2017) 535–538
- [32] **Surface sensing and adhesion of *Escherichia coli* controlled by the Cpx-signaling pathway.**
Otto K, Silhavy TJ
Proc. Natl Acad. Sci. 99 (2002) 2287–2292
- [33] **A mechanical signal transmitted by the flagellum controls signalling in *Bacillus subtilis***
Cairns LS, Marlow VL, Bissett E, Ostrowski A, Stanley-Wall NR
Mol Microbiol. 90 (2013) 6–21
- [34] **Surface contact stimulates the just- in-time deployment of bacterial adhesins**
Li G, et al.
Mol. Microbiol. 83 (2012) 41–51

- [35] **Physiochemical properties of *Caulobacter crescentus* holdfast: a localized bacterial adhesive**
Berne C et al.
J. Phys. Chem. B 117 (2013) 10492–10503
- [36] **Division site selection in rod-shaped bacteria**
Bramkamp M, Van Baarle S
Current Opinion in Microbiology 12 (2009) 683–688
- [37] **FtsZ-ring structure associated with division in *Escherichia coli***
Bi EF, Lutkenhaus J
Nature 354 (1991) 161-164
- [38] **How to get (a)round: mechanisms controlling growth and division of coccoid bacteria**
Pinho MG, Kjos M, Veening JW
Nature Rev. Microb. 11 (2013) 601
- [39] **Negative membrane curvature as a cue for subcellular localization of a bacterial protein.**
Ramamurthi KS, Losick R
Proc. Natl Acad. Sci. 106 (2009) 13541–13545
- [40] **The *Bacillus subtilis* endospore: assembly and functions of the multilayered coat**
McKenney PT, Driks A, Eichenberger P
Nature Rev. Microb. 11 (2013) 33
- [41] **Essential Biological Processes of an Emerging Pathogen: DNA Replication, Transcription, and Cell Division in *Acinetobacter* spp.**
Robinson A, Brzoska AJ, Turner KM, Withers R, Harry EJ, Lewis PJ, Dixon NE
Microbiology and Molecular Biology Reviews 74 (2010) 273–297
- [42] **Coordination of cell division and chromosome segregation by a nucleoid occlusion protein in *Bacillus subtilis***
Wu LJ, Errington J
Cell 117 (2004) 915–925
- [43] **SlmA, a nucleoid-associated, FtsZ binding protein required for blocking septal ring assembly over chromosomes in *E. coli***
Bernhardt TG, De Boer PA
Mol. Cell 18 (2005) 555–564
- [44] **Noc protein binds to specific DNA sequences to coordinate cell division with chromosome segregation**
Wu LJ, et al.
EMBO J. 28 (2009) 1940–1952
- [45] **Polarity and the diversity of growth mechanisms in bacteria**
Brown PJB, Kysela DT, Brun YV
Semin. Cell Dev. Biol. 22(8) (2011) 790

- [46] **The tubulin homologue FtsZ contributes to cell elongation by guiding cell wall precursor synthesis in *Caulobacter crescentus***
Aaron M, Charbon G, Lam H, Schwarz H, Vollmer W, Jacobs-Wagner C
Mol Microbiol. 64 (2007) 938–952
- [47] **The cell shape proteins MreB and MreC control cell morphogenesis by positioning cell wall synthetic complexes.**
Divakaruni AV, Baida C, White CL, Gober JW
Mol Microbiol. 66 (2007) 174– 88
- [48] **Cell-cycle progression and the generation of asymmetry in *Caulobacter crescentus***
Skerker JM, Laub MT
Nature Rev. Microb. 326(2) (2004) 325-337
- [49] **Getting in the Loop: Regulation of Development in *Caulobacter crescentus***
Curtis PD, Brun YV
Microbiology And Molecular Biology Reviews 74(1) (2010) 1092-2172
- [50] **The interaction of cells and bacteria with surfaces structured at the nanometre scale**
Anselme K, Davidson P, Popa AM, Giazzon M, Liley M, Ploux L
Acta Biomaterialia 6 (2010) 3824–3846
- [51] **Probing bacterial electrosteric interactions using atomic force microscopy**
Camesano TA, Logan BE
Environ Sci Technol 34 (2000) 3354–3362
- [52] **Understanding bacteria**
Srivastava S, Srivastava PS
Kluwer Academic Publishers, 1st Editon, 2003
- [53] **Influence of wear and overwear on surface properties of Etafilcon a contact lenses and adhesion of *Pseudomonas aeruginosa*.**
Bruinsma GM, Rustema-Abbing M, de Vries J, Stegenga B, van der Mei HC, van der Linden ML, et al.
Invest Ophthalmol Vis Sci 43 (2002) 3646–3652
- [54] **Nanoengineered superhydrophobic surfaces of aluminum with extremely low bacterial adhesivity**
Hizal F, et al.
Appl Mat Interfaces 9(13) (2017) 12118–12129
- [55] **Fouling biofilm development: a process analysis.**
Characklis WG
Biotechnol Bioeng 23 (1981) 1923–1960
- [56] **Effects of substratum topography on bacterial adhesion.**
Scheuerman TR, Camper AK, Hamilton MA
J Colloid Interface Sci 208 (1998) 23–33

- [57] **Properties of the stainless steel substrate, influencing the adhesion of thermo-resistant streptococci**
Flint SH, Brooks JD, Bremer PJ
J Food Eng 43 (2000) 235–242
- [58] **Microbial response to surface microtopography: the role of metabolism in localized mineral dissolution**
Edwards KJ, Rutenberg AD
Chem Geol 180 (2001) 19–32
- [59] **Nanostructured medical sutures with antibacterial properties**
Serrano C, García-Fernández L, Fernández-Blázquez JP, Barbeck M, Ghanaati S, Unger R, Kirkpatrick J, Arzt E, Funk L, Turón P, Del Campo A
Biomaterials 52 (2015) 291-300
- [60] **Antibacterial effects of nanopillar surfaces are mediated by cell impedance, penetration and induction of oxidative stress**
Jenkins J, Mantell J, Neal C, Gholinia A, Verkade P, Nobbs AH, Su B
Nat Commun. 11(1) (2020) 1626
- [61] **Bacterial viability on chemically modified silicon nanowire arrays**
Susarrey-Arce A, Sorzabal-Bellido I, Oknianska A, McBride F, Beckett AJ, Gardeniers JGE, Raval R, Tiggelaar RM, Diaz Fernandez YA
J. Mater. Chem. B 4 (2016) 3104
- [62] **Influence of the surface topography of stainless steel on bacterial adhesion**
Medilanski E, Kaufmann K, Wick LY, Wanner O, Harms H
Biofouling 18 (2002) 193–203
- [63] **Multiple linear regression analysis of bacterial deposition to polyurethane coatings after conditioning film formation in the marine environment**
Bakker DP, Busscher HJ, van Zanten J, de Vries J, Klijnstra JW, Van der Mei HC
Microbiology 150 (2004) 1779–1784
- [64] **Effect of Micro- and Nanoscale Topography on the Adhesion of Bacterial Cells to Solid Surfaces**
Hsu LC, Fang J, Borca-Tasciuc DA, Worobo RW, Moraru CI
Applied and Environmental Microbiology 79(8) (2013) 2703–2712
- [65] **Enhancing the Bactericidal Efficacy of Nanostructured Multifunctional Surface Using an Ultrathin Metal Coating**
Tripathy A, Sreedharan S, Bhaskarla C, Majumdar S, Peneti SK, Nandi D, Sen P
Langmuir 33 (2017) 12569-12579
- [66] **Bactericidal activity of black silicon**
Ivanova EP, Hasan J, Webb HK, Gervinskas G, Juodkazis S, Truong VK, Wu AH, Lamb RN, Baulin VA, Watson GS, Watson JA, Mainwaring DE, Crawford RJ
Nat. Commun. 4 (2013) 2838

- [67] **Metal-Particle-Induced, Highly Localized Site-Specific Etching of Si and Formation of Single-Crystalline Si Nanowires in Aqueous Fluoride Solution**
Peng K, Fang H, Hu J, Wu Y, Zhu J, Yan Y, Lee ST
Chem. - A Eur. J. 12(30) (2006) 7942–7947
- [68] ***Caulobacter crescentus* (ATCC® BAA-2331™) – Culture method**
<https://www.lgcstandards-atcc.org/~media/602F8C14799E458FA8554BDB90801E4D.ashx>
(accessed 22nd September 2020)
- [69] **SYTO™ 9 Green Fluorescent Nucleic Acid Stain - ThermoFisher**
<https://www.thermofisher.com/order/catalog/product/S34854> (accessed 22nd September 2020)
- [70] **Mechanism and Use of the Commercially Available Viability stain, BacLight**
Stocks SM
Cytometry 61A(2) (2004) 189–195
- [71] **Propidium Iodide Nucleic Acid Stain**
<https://www.thermofisher.com/order/catalog/product/P1304MP?SID=srch-srp-P1304MP#/P1304MP?SID=srch-srp-P1304MP> (accessed on the 10th of September 2020)
- [72] **Surface topographical factors influencing bacterial attachment**
Crawford RJ, Webb HK, Truong VK, Hasan J, Ivanova EP
Adv. Colloid Interface Sci. 142 (2012) 179–182
- [73] **Chromosome Replication in *Caulobacter crescentus* Growing in a Nutrient Broth**
Iba H, Fukuda A, Okada Y
Journal Of Bacteriology 129(3) (1977) 1192-1197
- [74] **Integrated biphasic growth rate, gene expression, 2 and cell-size homeostasis behaviour of single *B. Subtilis* cells**
Nordholt N, Van Heerden JH, Bruggeman FJ
Current Biology 30 (2020) 1–10
- [75] **Measurement of the Unstable RNA in Exponentially Growing Cultures of *Bacillus subtilis* and *Escherichia coli***
SalslerV, Janin J, Levinthal C
J. Mol. Biol. 31 (1968) 237-266
- [76] **Relationship Between Glucose Utilization and Growth Rate in *Bacillus subtilis***
Baschnagel-Depamphili J, Hanson RS
Journal Of Bacteriology 98(1) (1969) 222-225
- [77] **Cell population heterogeneity during growth of *Bacillus subtilis***
Kearns DB, Losick R
Genes & Development 19 (2005) 3083–3094
- [78] **Diarrheagenic *Escherichia coli***
Nataro JP, Kaper JB
Clinical Microbiology Reviews 11(1) (1998) 142–201

- [79] **Draft Genome Sequence of *Escherichia coli* K-12 (ATCC 10798)**
Dimitrova D, Engelbrecht KC, Putonti C, Koenig DW, Wolfe AJ
Genome Announc. 5(27) (2017) e00573-17
- [80] **The Bacterial Cell Envelope**
Silhavy TJ, Kahne D, Walker S
Cold Spring Harbor Perspect. Biol. 2(5) (2010) a000414
- [81] **WHO publishes list of bacteria for which new antibiotics are urgently needed**
<https://www.who.int/news-room/detail/27-02-2017-who-publishes-list-of-bacteria-for-which-new-antibiotics-are-urgently-needed>
(accessed on the 11th of October 2020)
- [82] ***Acinetobacter baumannii*: Emergence of a Successful Pathogen**
Peleg AY, Seifert H, Paterson DL
Clin Microbiol Rev. 21(3) (2008) 538-582
- [83] ***Acinetobacter baumannii* outer membrane protein A targets the nucleus and induces cytotoxicity**
Choi CH, et al.
Cell. Microbiol. 10 (2008) 309–319
- [84] **Infections with *Acinetobacter calcoaceticus* (*Herellea vaginicola*): clinical and laboratory studies**
Glew RH, Moellering RC Jr., Kunz LJ
Medicine (Baltimore) 56 (1977) 79–97
- [85] **The Success of *Acinetobacter* Species; Genetic, Metabolic and Virulence Attributes**
Peleg AY, de Brij A, Adams MD, Cerqueira GM, Mocali S, Galardini M, et al.
PLoS ONE 7(10) (2012) e46984
- [86] **Attachment to and biofilm formation on abiotic surfaces by *Acinetobacter baumannii*: involvement of a novel chaperone-usher pili assembly system**
Tomaras AP, Dorsey CW, Edelmann RE, Actis LA
Microbiology 149 (2003) 3473–3484
- [87] **Sticking together: building a biofilm the *Bacillus subtilis* way**
Vlamakis H, Chai Y, Beauregard P, Losick R, Kolter R
Nat Rev Microbiol. 11 (2013) 157–168
- [88] **Giving structure to the biofilm matrix: an overview of individual strategies and emerging common themes**
Hobley L, Harkins C, MacPhee CE, Stanley-Wall NR
FEMS Microbiol. Rev. 39 (2015) 649–669
- [89] **The origins of 168, W23, and other *Bacillus subtilis* legacy strains**
Zeigler DR, Prágai Z, Rodriguez S, Chevreux B, Muffler A, Albert T, Bai R, Wyss M, Perkins JB
J Biotechnol. 190 (2008) 6983–6995

[90] **Characterization and optimization of *Bacillus subtilis* ATCC 6051 as an expression host**

Kabisch J, Thürmer A, Hübel T, Popper L, Daniel R, Schweder T
J Biotechnol. 163(2) (2013) 97-104

[91] **Identification, Isolation, and Structural Studies of Extracellular Polysaccharides Produced by *Caulobacter crescentus***

Ravenscroft N, Walker SG, Dutton GG, Smit J
J Bacteriol. 173(18) (1991) 5677-5684

[92] ***Caulobacter crescentus* (ATCC® BAA-2331™)**

https://www.lgcstandards-atcc.org/products/all/BAA-2331.aspx?geo_country=gb
(accessed 22nd September 2020)

[93] **Analysis of *Caulobacter crescentus* Lipids**

De Siervo AJ, Homola AD
J Biotechnol. 143(3) (1980) 1215-1222

[94] **The role of calcium in stalk development and in phosphate acquisition in *Caulobacter crescentus***

Poindexter JS
Archives of Microbiology 138 (1984) 140–152

[95] **Division site positioning in bacteria: one size does not fit all**

Monahan LG, Liew ATF, Bottomley AL, Harry EJ
Front. Microbiol. 5(19) (2014) 3

[96] **Bacterial differentiation**

Shapiro L, Agabian-Keshishian N, Bendis I
Science 173 (1971) 884-892

[97] **Generalized Transduction In *Caulobacter Crescentus***

Ely B, Johnson RC
Genetics 87 (1977) 301-309

[98] **Silicon Nanowires: A Review on Aspects of Their Growth and Their Electrical Properties**

Schmidt V, Wittemann JV, Senz S, Gösele U
Adv. Mater. 21(25–26) (2009) 2681–2702

[99] **Highly Efficient Biocompatible Single Silicon Nanowire Electrodes with Functional Biological**

Martinez JA, Misra N, Wang Y, Stroeve P, Grigoropoulos CP, Noy A
Pore Channels. Nano Lett. 9(3) (2009) 1121–1126

[100] **In Vitro Biocompatibility of N-Type and Undoped Silicon Nanowires**

Garipcan B, Odabas S, Demirel G, Burger J, Nonnenmann SS, Coster MT, Gallo EM, Nabet B, Spanier JE, Piskin E
Adv. Eng. Mater. 13(1–2) (2011) B3–B9

[101] **Microfluidic cell culture models for tissue engineering**

Inamdar NK, Borenstein JT

Current Opinion in Biotechnology 22(5) (2011) 681-689

[102] **Development of antifouling surfaces to reduce bacterial attachment**

Graham MV, Mosier AP, Kiehl TR, Kaloyerosa AE, Cady NC

Soft Matter 9 (2013) 6235-6244

Conclusions

Bacterial attachment and colonisation of surfaces play a critical role in the spreading of infections in humans, particularly when extended to medical devices. In this work, we presented two multidisciplinary approaches to investigate the bacteria-surface interactions and inhibit the first stages of bacterial colonisation at surfaces: the first approach consisted in the development of a novel post-fabrication modification method that allows to create a reservoir of biocide within the bulk of a biocompatible silicone-based polymer. The controlled release of the biocide within the supernatants showed high antimicrobial performance, both against planktonic and sessile Gram-positive and Gram-negative bacterial species, relevant to clinical infections.

The second approach involved the use of nanostructured Si surfaces to unravel the mechanisms that enable bacterial attachment and division at the surface. A wide range of bacterial species was investigated, encompassing different cell shapes and sizes, including spherical *Staphylococci* with distinct mechanism of cell division and the rod-shaped *Escherichia coli*, *Acinetobacter baumannii* and *Bacillus subtilis*, characterised by a division mode based on polar growth. A section was also devoted to *Caulobacter crescentus*, a species with a unique cell cycle and attachment mechanism to abiotic surfaces. Our findings provided important insights on the mechanisms that allow these bacteria to colonise and adapt to artificial nanotopographic substrates and on the effects of local topography on the cell division modes and biofilm formation at surfaces; this investigation opens new avenues to unravel bacteria-surface interactions at the nano-scale and to engineer nanopatterned surfaces with enhanced antibiofouling properties.

Throughout this thesis, a combination of surface chemistry, material science and advanced microbiology techniques was used to characterise the materials and the interaction between functional surfaces and bacterial cells, allowing the

identification of key features that control biofilm formation and paving the way for the development of advanced antimicrobial materials able to prevent bacterial attachment and colonisation on medical devices displaying hard and soft surfaces.

